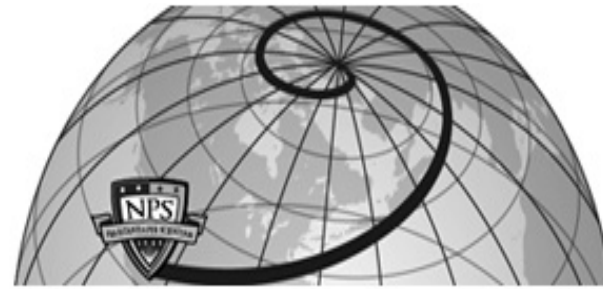




Institutional Archive of the Naval Postgraduate School



Calhoun: The NPS Institutional Archive

DSpace Repository

NPS Scholarship

Theses

2024-12

ADVANCED ALUMINUM ALLOY FABRICATION METHODS USING LIQUID METAL JET PRINTING AND EXPEDITIONARY USE OF METAL ADDITIVE MANUFACTURING IN THE FLEET

Vrtis, Zachary J.

Monterey, CA; Naval Postgraduate School

<https://hdl.handle.net/10945/73537>

This publication is a work of the U.S. Government as defined in Title 17, United States Code, Section 101. Copyright protection is not available for this work in the United States.

Downloaded from NPS Archive: Calhoun



<http://www.nps.edu/library>

Calhoun is the Naval Postgraduate School's public access digital repository for research materials and institutional publications created by the NPS community.

Calhoun is named for Professor of Mathematics Guy K. Calhoun, NPS's first appointed -- and published -- scholarly author.

Dudley Knox Library / Naval Postgraduate School
411 Dyer Road / 1 University Circle
Monterey, California USA 93943



NAVAL POSTGRADUATE SCHOOL

MONTEREY, CALIFORNIA

DISSERTATION

**ADVANCED ALUMINUM ALLOY FABRICATION METHODS
USING LIQUID METAL JET PRINTING AND
EXPEDITIONARY USE OF METAL ADDITIVE
MANUFACTURING IN THE FLEET**

by

Zachary J. Vrtis

December 2024

Dissertation Supervisor:

Ibrahim E. Gunduz

Distribution Statement A. Approved for public release: Distribution is unlimited.

THIS PAGE INTENTIONALLY LEFT BLANK

REPORT DOCUMENTATION PAGE			Form Approved OMB No. 0704-0188
<p>Public reporting burden for this collection of information is estimated to average 1 hour per response, including the time for reviewing instruction, searching existing data sources, gathering and maintaining the data needed, and completing and reviewing the collection of information. Send comments regarding this burden estimate or any other aspect of this collection of information, including suggestions for reducing this burden, to Washington headquarters Services, Directorate for Information Operations and Reports, 1215 Jefferson Davis Highway, Suite 1204, Arlington, VA 22202-4302, and to the Office of Management and Budget, Paperwork Reduction Project (0704-0188) Washington, DC, 20503.</p>			
1. AGENCY USE ONLY (Leave blank)	2. REPORT DATE December 2024	3. REPORT TYPE AND DATES COVERED Dissertation	
4. TITLE AND SUBTITLE ADVANCED ALUMINUM ALLOY FABRICATION METHODS USING LIQUID METAL JET PRINTING AND EXPEDITIONARY USE OF METAL ADDITIVE MANUFACTURING IN THE FLEET		5. FUNDING NUMBERS	
6. AUTHOR(S) Zachary J. Vrtis			
7. PERFORMING ORGANIZATION NAME(S) AND ADDRESS(ES) Naval Postgraduate School Monterey, CA 93943-5000		8. PERFORMING ORGANIZATION REPORT NUMBER	
9. SPONSORING / MONITORING AGENCY NAME(S) AND ADDRESS(ES) N/A		10. SPONSORING / MONITORING AGENCY REPORT NUMBER	
11. SUPPLEMENTARY NOTES The views expressed in this thesis are those of the author and do not reflect the official policy or position of the Department of Defense or the U.S. Government.			
12a. DISTRIBUTION / AVAILABILITY STATEMENT Distribution Statement A. Approved for public release: Distribution is unlimited.		12b. DISTRIBUTION CODE A	
13. ABSTRACT (maximum 200 words) <p>Metal additive manufacturing (M-AM) of high-end, 7XXX series aluminum alloys can allow unique function and high-performance with a variety of applications. Aluminum alloy 7075 and 7068 (AA 7075 and AA 7068) pose challenges during M-AM due to thermal cycles that cause hot cracking, which have been solved via the use of inoculants but with a degradation in mechanical properties. In this research, the liquid metal jet printing (LMJP) process was successfully used to print pure AA 7075 with superior mechanical properties. By using a high-temperature substrate, the LMJP process significantly reduces solidification and cooling rates during printing, eliminating hot cracking and producing fully dense, defect-free parts. After establishing a repeatable LMJP process for AA 7075, the zinc content of the AA 7075 feedstock was increased towards that of AA 7068 during printing, with improvements in the mechanical properties. The LMJP code parameters were adjusted to selectively reduce sample infill to optimize strength and weight for various applications. Further improvements in zinc addition and LMJP code parameters are needed to improve 7XXX aluminum printing capabilities. Outside of the laboratory, M-AM has the potential to provide value in contested logistics scenarios. Two containerized M-AM machines were successfully used during two Fleet exercises, but many logistics, training, and engineering challenges were identified and must be addressed in future exercises.</p>			
14. SUBJECT TERMS metal additive manufacturing, M-AM, aluminum alloy 7075, AA 7075, aluminum alloy 7068, AA 7068, liquid metal jet printing, LMJP, Battle Damage Assessment and Repair, BDA/R, contested logistics			15. NUMBER OF PAGES 217
16. PRICE CODE			
17. SECURITY CLASSIFICATION OF REPORT Unclassified	18. SECURITY CLASSIFICATION OF THIS PAGE Unclassified	19. SECURITY CLASSIFICATION OF ABSTRACT Unclassified	20. LIMITATION OF ABSTRACT UU

THIS PAGE INTENTIONALLY LEFT BLANK

Distribution Statement A. Approved for public release: Distribution is unlimited.

**ADVANCED ALUMINUM ALLOY FABRICATION METHODS USING LIQUID
METAL JET PRINTING AND EXPEDITIONARY USE OF METAL ADDITIVE
MANUFACTURING IN THE FLEET**

Zachary J. Vrtis
Lieutenant Commander, United States Navy
BSE, University of Pennsylvania, 2013
MSE, University of Pennsylvania, 2013

Submitted in partial fulfillment of the
requirements for the degree of

DOCTOR OF PHILOSOPHY IN MECHANICAL ENGINEERING

from the

NAVAL POSTGRADUATE SCHOOL
December 2024

Approved by:	Ibrahim E. Gunduz Department of Mechanical and Aerospace Engineering Dissertation Supervisor	Young W. Kwon Department of Mechanical and Aerospace Engineering Dissertation Chair
	Erick S. Alley Department of Mechanical and Aerospace Engineering	Troy Ansell Department of Mechanical and Aerospace Engineering
	Oleg A. Yakimenko Department of Systems Engineering	
Approved by:	Jarema M. Didoszak Chair, Department of Mechanical and Aerospace Engineering	
	James B. Michael Vice Provost of Academic Affairs	

THIS PAGE INTENTIONALLY LEFT BLANK

ABSTRACT

Metal additive manufacturing (M-AM) of high-end, 7XXX series aluminum alloys can allow unique function and high-performance with a variety of applications. Aluminum alloy 7075 and 7068 (AA 7075 and AA 7068) pose challenges during M-AM due to thermal cycles that cause hot cracking, which have been solved via the use of inoculants but with a degradation in mechanical properties. In this research, the liquid metal jet printing (LMJP) process was successfully used to print pure AA 7075 with superior mechanical properties. By using a high-temperature substrate, the LMJP process significantly reduces solidification and cooling rates during printing, eliminating hot cracking and producing fully dense, defect-free parts. After establishing a repeatable LMJP process for AA 7075, the zinc content of the AA 7075 feedstock was increased toward that of AA 7068 during printing, with improvements in the mechanical properties. The LMJP code parameters were adjusted to selectively reduce sample infill to optimize strength and weight for various applications. Further improvements in zinc addition and LMJP code parameters are needed to improve 7XXX aluminum printing capabilities. Outside of the laboratory, M-AM has the potential to provide value in contested logistics scenarios. Two containerized M-AM machines were successfully used during two Fleet exercises, but many logistics, training, and engineering challenges were identified and must be addressed in future exercises.

THIS PAGE INTENTIONALLY LEFT BLANK

TABLE OF CONTENTS

I.	INTRODUCTION.....	1
A.	MOTIVATION AND FOCUS	1
B.	OBJECTIVES	1
1.	Research Objectives.....	2
2.	Operational Objectives.....	3
C.	DISSERTATION LAYOUT	3
II.	BACKGROUND	5
A.	MATERIALS PROPERTIES OF ALUMINUM ALLOYS	5
1.	Crystal Structure and Miller Indices	7
2.	Aluminum Alloys	9
3.	Particle Strengthening Methods	14
4.	Heat Treatment and Precipitation Strengthening of 7XXX Series Aluminum Alloys.....	17
B.	MATERIALS CHARACTERIZATION AND TESTING.....	19
1.	Mechanical Testing	20
2.	Microscopy.....	24
3.	Energy-Dispersive Spectroscopy	27
4.	X-ray Diffraction.....	29
5.	Digital Radiography and Computed Tomography.....	31
6.	X-ray Nano-tomography	32
C.	OVERVIEW OF METAL ADDITIVE MANUFACTURING	33
1.	Metal Additive Manufacturing Methods	34
2.	Printer Control and Print Customization.....	42
3.	Metal Additive Manufacturing in the DON	45
III.	METHODOLOGY	49
A.	LIQUID METAL JET PRINTING	49
1.	Oxidation Control.....	51
2.	Aluminum Wire Preparation.....	56
3.	Variable Density Post Processor.....	64
B.	SAMPLE PREPARATION	68
1.	Heat Treatment	68
2.	Preparation of Samples for Microscopy	69
C.	MATERIALS TESTING	69
1.	Microhardness.....	70

2.	Tensile Testing.....	70
D.	MATERIALS CHARACTERIZATION	71
1.	Optical Microscopy.....	71
2.	Scanning Electron Microscopy and Energy-Dispersive Spectroscopy.....	72
3.	X-ray Diffraction.....	73
4.	DR and CT Scanning.....	74
5.	X-ray Nano-tomography	75
IV.	LIQUID METAL JET PRINTING OF ALUMINUM ALLOY 7075.....	77
A.	RESULTS AND DISCUSSION	77
1.	Materials Characterization.....	77
2.	Materials Testing	87
B.	PRELIMINARY FINDINGS.....	90
V.	LMJP OF PARTICLE-STRENGTHENED AA 7075	91
A.	RESULTS AND DISCUSSION	91
1.	Boron Nitride Nanobars.....	91
2.	Method 1: Pure Zn Strip Addition	92
3.	Method 2: Zn-enriched AA 7075 Wire Addition	99
B.	PRELIMINARY FINDINGS.....	107
VI.	GRADIENT INFILL OF ALUMINUM ALLOYS.....	109
A.	RESULTS / DISCUSSION.....	109
1.	Infill Droplet Placement	109
2.	Minimizing Infill Density	110
B.	PRELIMINARY FINDINGS.....	112
VII.	EXPEDITIONARY METAL ADDITIVE MANUFACTURING	113
A.	SALVAGE EXERCISE 2024.....	113
1.	Exercise Overview	114
2.	NPS Role in S24	116
3.	Training.....	117
4.	XSPEE3D Printing	119
5.	Lessons Learned.....	125
6.	Preliminary Findings.....	129
B.	TRIDENT WARRIOR 2024	130
1.	Exercise Overview.....	130
2.	NPS Role in TW24	132

3.	Training	132
4.	Snowbird Printing.....	134
5.	XSPEE3D Printing.....	137
6.	Materials Characterization.....	140
7.	Lessons Learned.....	146
8.	Preliminary Findings.....	148
VIII.	CONCLUSIONS	151
A.	RESEARCH OBJECTIVES	151
B.	OPERATIONAL OBJECTIVES	152
C.	FUTURE DIRECTIONS.....	154
1.	LMJP of AA 7075 and Zn-Enriched AA 7075	154
2.	Gradient Infill of Aluminum Alloys	154
3.	Expeditionary Metal Additive Manufacturing	154
APPENDIX A. ELEMX STANDARD OPERATING PROCEDURE.....		157
APPENDIX B. AA 7075 POLISHING AND ETCHING RECIPE		171
LIST OF REFERENCES		173
INITIAL DISTRIBUTION LIST		191

THIS PAGE INTENTIONALLY LEFT BLANK

X

LIST OF FIGURES

Figure 1.	Historical uses of aluminum	6
Figure 2.	FCC unit cell and crystal structure.....	7
Figure 3.	FCC close-packed directions and planes.	8
Figure 4.	Morphology of AA 7075 shows hot cracking and metallurgical bonding.	13
Figure 5.	Dislocation interactions with particles.....	15
Figure 6.	Summary of particle strengthening of metal alloys.	17
Figure 7.	Precipitates formed during T6 heat treatment of AA 7075.....	19
Figure 8.	Schematics and equation for the Vickers hardness test.	21
Figure 9.	Schematics and equation for Rockwell hardness test.	22
Figure 10.	Stress vs. strain curves of typical brittle (dashed) versus ductile (solid) materials.	23
Figure 11.	Yield stress and hardness relationship.....	24
Figure 12.	SEM and TEM architecture and SEM interactions.....	27
Figure 13.	EDS spectra of AA 7075 in terms of energy (KeV), truncated to show the lower energy peaks.	29
Figure 14.	Allowed reflections for cubic crystal systems.	31
Figure 15.	DR and CT scan formation schematics.....	32
Figure 16.	18-ID Full-Field X-ray imaging beamline (FXI) construction.	33
Figure 17.	Comparison of resolution, part complexity, cost, and part size among the common M-AM processes.	34
Figure 18.	Four steps of a MIM process.	35
Figure 19.	DED process schematics.....	36
Figure 20.	Overview of the cold spray process.	37
Figure 21.	L-PBF process and defects.....	38

Figure 22.	Additec ElemX printer overview.....	40
Figure 23.	Overview of ElemX thermal settings and cooling curves.	42
Figure 24.	Process flow of 3D printing.....	43
Figure 25.	Variable density prints from previous thesis research.	45
Figure 26.	USS BATAAN M-AM capability.	47
Figure 27.	ElemX print head and substrate temperature monitoring.	50
Figure 28.	Gen 1 containment.....	52
Figure 29.	Gen 2 containment.....	53
Figure 30.	Gen 3 containment.....	55
Figure 31.	Gen 4 containment.....	56
Figure 32.	Initial AA 7075 wire preparation.....	57
Figure 33.	AA 7075 spool EDS analysis.....	58
Figure 34.	NanoBarb™ additive used during AA 4008 printing.	59
Figure 35.	Zn powder addition rig.....	60
Figure 36.	Zn wire calculation and samples produced.	61
Figure 37.	Fracture surfaces of Zn-enriched samples showing indications of brittle fracture and discoloration.	62
Figure 38.	Zn-enriched wire production.....	64
Figure 39.	Droplet support and overlap during variable infill.	66
Figure 40.	Raster code and schematic for variable infill printing.	67
Figure 41.	Equipment for sample heat treatment.	69
Figure 42.	Mechanical testing devices in the NPS laboratory.	71
Figure 43.	Optical microscopy and porosity analysis.	72
Figure 44.	SEM and EDS in the NPS laboratory.	73
Figure 45.	Rigaku desktop x-ray diffractometer at the NPS laboratory.....	74

Figure 46.	X5000 DR / CT scanner at NPS laboratory.....	75
Figure 47.	200°C and 300°C sample optical microscopy.....	78
Figure 48.	400°C, 475°C, and 500°C sample optical microscopy.....	80
Figure 49.	Optical images and microscopy of AA 7075 test cubes at various substrate temperatures and successful AA 7075 prints.....	81
Figure 50.	CT scans of samples printed with 200–500°C substrate temperature.....	82
Figure 51.	EDS map comparison of AA 7075 wire and printed samples after T6 heat treatment.....	83
Figure 52.	EDS point analysis of AA 7075 samples after T6 heat treatment.	84
Figure 53.	SEM cross-sectional images of AA 7075 samples.	85
Figure 54.	XRD of AA 7075 samples.	85
Figure 55.	X-ray computed nano-tomography scans of AA 7075 samples.	86
Figure 56.	Microhardness of AA 7075 prints and standard plates.	88
Figure 57.	Stress-strain curves of printed AA 7075 tensile specimens at a substrate temperature of 475°C (dashed lines) and 500°C (solid lines).....	89
Figure 58.	Specific strength of printed AA 7075 compared to other alloys produced via AM methods.....	89
Figure 59.	SEM images of AA 4008 samples printed with NB additives.....	92
Figure 60.	SEM micrograph comparison for Zn-enriched AA 7075 (method 1).....	93
Figure 61.	EDS mapping of Zn-enriched AA 7075 (method 1).....	94
Figure 62.	EDS results for Zn-enriched AA 7075 (method 1).....	95
Figure 63.	XRD of Zn-enriched AA 7075 samples (method 1).....	96
Figure 64.	Microhardness measurements of AA 7075 and Zn-enriched AA 7075 (method 1).....	97
Figure 65.	Microhardness measurements of Zn-enriched AA 7075 (method 1).....	97

Figure 66.	Stress-strain curves of 3D printed tensile specimens of AA 7075 with a 500°C substrate (dashed lines) and Zn-enriched AA 7075 (method 1, solid lines).....	98
Figure 67.	Specific strength of Zn-enriched AA 7075 (method 1) compared to other alloys produced via AM methods.....	99
Figure 68.	CT scans of pure and Zn-enriched AA 7075 samples (method 2) printed with substrate temperature 500°C.....	100
Figure 69.	SEM micrograph comparison for Zn-enriched AA 7075 samples via both enrichment methods 1 and 2.....	101
Figure 70.	EDS mapping of Zn-enriched AA 7075 (method 2).....	102
Figure 71.	EDS results for Zn-enriched AA 7075 (method 2).....	103
Figure 72.	XRD of Zn-enriched AA 7075 samples (method 2).....	104
Figure 73.	Microhardness measurements of AA 7075 and Zn-enriched AA 7075 (method 2).....	105
Figure 74.	Microhardness measurements of Zn-enriched AA 7075 (method 2).....	105
Figure 75.	Stress-strain curves of 3D printed tensile specimens of AA 7075 with a 500°C substrate (dashed lines) and Zn-enriched AA 7075 (method 2, solid lines).....	106
Figure 76.	Specific strength of Zn-enriched AA 7075 (method 2) compared to other alloys produced via AM methods.....	107
Figure 77.	Results of initial droplet placement using modified G-code.	109
Figure 78.	Gradient infill prints with delays.	110
Figure 79.	Samples printed with DEM of 3.0.	111
Figure 80.	Samples printed with 5x5 search and collision kernel size.....	112
Figure 81.	The ship for S24, ex-TARAWA.	115
Figure 82.	XSPEE3D training during S24.	118
Figure 83.	Post-processing training during S24.	118
Figure 84.	XSPEE3D training for TW24.	119
Figure 85.	Space 5 repairs during S24.	120

Figure 86.	Space 1 flange repair during S24.....	121
Figure 87.	Space 1 cooler head repair details during S24.....	122
Figure 88.	Space 1 cooler head assembly and testing during S24.....	125
Figure 89.	XSPEE3D and SPEE3DCELL transportation methods.....	127
Figure 90.	JAMC focuses, details, key tests, and overview at TW 2024.....	131
Figure 91.	Training of personnel during TW24.....	133
Figure 92.	Snowbird training.....	134
Figure 93.	RO pump repair.....	135
Figure 94.	Snowbird case studies.....	137
Figure 95.	JLTV alignment puck.....	138
Figure 96.	XSPEE3D 316L SS print defects.....	139
Figure 97.	XSPEE3D AA 6061 prints.....	140
Figure 98.	Hardness and XRF analyses performed at Bear Machinery.....	141
Figure 99.	Test coupons from Snowbird printer.....	142
Figure 100.	Hardness results for 316L SS prints.....	143
Figure 101.	XRF results of all 316L SS prints.....	144
Figure 102.	Tensile testing results.....	145
Figure 103.	Specific strength comparison of 7XXX aluminum printed via LMJP....	152
Figure 104.	Successful prints during S24 and TW24.....	153

THIS PAGE INTENTIONALLY LEFT BLANK

LIST OF TABLES

Table 1.	Aluminum alloy series, description, and examples.	10
Table 2.	Elemental composition of A4008 / A356 and ElemX 4XXX series aluminum wire.	11
Table 3.	AA 7075 and 7068 comparisons.....	12
Table 4.	Specific strength of AA 7075, AA 7068, 316L stainless steel, and HY-80 steel.	12
Table 5.	Hardness testing methods.	20
Table 6.	Commonly used G-code commands.	44
Table 7.	Author's roles in Fleet exercises utilizing M-AM technologies.....	48
Table 8.	Summary of Zn-enriched AA 7075 samples (method 1).....	92
Table 9.	Summary of Zn-enriched AA 7075 samples (method 2).....	100
Table 10.	Summary of previous BDA/R exercises.....	114
Table 11.	Summary of S24 damaged spaces and repairs.	116
Table 12.	XSPEE3D printer specifications.	117
Table 13.	Materials properties comparison for 90–10 Cu Ni and SPEE3D Aluminum Bronze.	120
Table 14.	Properties of AMPCO-TRODE 10 and 46 electrodes.	123
Table 15.	Snowbird printer specifications.	134
Table 16.	Cost and Ao breakdown for Snowbird case studies.....	136
Table 17.	Wrought 316SS standard, XSPEE3D 316L SS powder, and Meltio 316L SS elemental composition comparison.....	146

THIS PAGE INTENTIONALLY LEFT BLANK

LIST OF ACRONYMS AND ABBREVIATIONS

AA 4008 / A356	Aluminum Alloy 4008 / Alloy 356
AA 6061	Aluminum Alloy 6061
AA 7068	Aluminum Alloy 7068
AA 7075	Aluminum Alloy 7075
AB	Aluminum Bronze
Additec	Additive Technologies Inc.
AdvM	Advanced Manufacturing
AES	Auger Electron Spectroscopy
Al	Aluminum
AM	Additive Manufacturing
Ao	Operational Availability
BDA/R	Battle Damage Assessment and Repair
BHR	ex-Bonhomme Richard
BNL	Brookhaven National Laboratory
BSE	Backscattered Electron
CAD	Computer-Aided Drafting
CAGR	Compound Annual Growth Rate
CAMRE	Consortium for Advanced Manufacturing Research and Education
CASREP	Casualty Report
CCD	Charge-Coupled Device
CG-62	USS CHANCELLORSVILLE
CLC-33	Combat Logistics Company 33
CONOPs	Concept of Operations
CT	Computed Tomography
Cu	Copper
DCM	Double Crystal Monochromator
DED	Directed Energy Deposition
DEM	Droplet Extrusion Multiplier
DLA	Defense Logistics Agency
DoD	Department of Defense
DOE	U.S. Department of Energy
DON	Department of the Navy
DR	Digital Radiography

EDO	Engineering Duty Officer
EDS	Energy-Dispersive Spectroscopy
FEDLOG	Federal Logistics
FXI	Full-Field X-ray Imaging
GAO	Government Accountability Office
GP Zones	Guinier-Preston Zones
HAZ	Heat Affected Zone
He	Helium
HRB	Rockwell B scale
HV	Hardness Vickers
ID	Infantry Division
JAMC	Joint Advanced Manufacturing Cell
JLTV	USMC Joint Light Tactical Vehicle
Li	Lithium
LMJP	Liquid Metal Jet Printing
L-PBF	Laser Powder Bed Fusion
LVSR	USMC Oshkosh Logistic Vehicle System Replacement
M-AM	Metal Additive Manufacturing
MCBH	Marine Corps Base Hawaii
MCM 11	USS GLADIATOR
Mg	Magnesium
MIG	Metal Inert Gas
MIM	Metal Injection Molding
MIU	Marine Innovation Unit
Mn	Manganese
N ₂	Nitrogen
NA	Numerical Aperture
NAB	Nickel Aluminum Bronze
NB	NanoBarb™
NDI	Non-Destructive Inspection
NSI	Northstar Imaging
NSLS-II	National Synchrotron Light Source II
OEM	Original Equipment Manufacturer
OIC	Officer in Charge
OOC	Out of Commission

PHNSY	Pearl Harbor Naval Shipyard
PMZ	Partially Melted Zone
RIMPAC	Rim of the Pacific Exercise
RO	Reverse Osmosis
S24	SALVAGE EXERCISE 2024
SCC	Stress Corrosion Cracking
SDS	Safety Data Sheet
SE	Secondary Electrons
SEM	Scanning Electron Microscopy
Si	Silicon
SINKEX	Sinking Exercise
SME	Subject Matter Expert
SOP	Standard Operating Procedure
SS	Stainless Steel
STL	Stereolithography
SWaRM	Ship Wartime Repair and Maintenance
TEM	Transmission Electron Microscopy
TIG	Tungsten Inert Gas
TW24	TRIDENT WARRIOR 2024
TXM	Transmission X-ray Microscopy
USA	United States Army
USAF	United States Air Force
USMC	United States Marine Corps
USN	United States Navy
UTS	Ultimate Tensile Stress
UXO	Unexploded Ordnance
VDPP	Variable Density Post Processor
WAAM	Wire Arc Additive Manufacturing
XRD	X-ray Diffraction
XRF	X-ray Fluorescence
Zn	Zinc

THIS PAGE INTENTIONALLY LEFT BLANK

ACKNOWLEDGMENTS

I have many wonderful people to thank for their support, mentorship, and assistance during my studies at NPS. First and foremost, thank you to my lovely wife, Dominique, for her unwavering love and support during the highs and lows over the past three years (but mostly highs!). Thank you to my amazing family, including my parents (Lori and Joe), Adam, and Monica, for the support and encouragement along the way. Additionally, I would like to extend a special thank you to the following:

- Dr. Emre Gunduz for the endless hours mentoring, teaching, and guiding me along the way as my advisor.
- Dr. Young Kwon for the great knowledge of the finite element method and for the wisdom and guidance as committee chair.
- Dr. Troy Ansell for your extreme patience with me in the lab learning how to use the XRD, SEM, and EDS in addition to serving on my committee.
- Dr. Erick Alley for the great solid mechanics and finite element methods class, the great trip / travel recommendations, and serving on my committee.
- Dr. Oleg Yakimenko for the great refresher and guidance in MATLAB coding, encouragement regarding my quest for my private pilot license, and serving on my committee.
- ENS Nik Kennedy, ENS Stephen Stokes, and ENS Sidney Hall-Smith for your help with AA 7075 printing and particle strengthening.
- ENS Victor Wang and LT Kristofer Misch for your help with custom infill printing.
- Mr. Anson Liu for the coding help with the variable density post processor.

- LT Mike Tisdall and LT Joel Hunter for all the hard work during SALVEX and TRIDENT WARRIOR 2024.
- Ms. Laurie Bliss for all the help around the office and her desire to make the MAE department an enjoyable place for us all.
- Mr. Forest Shaner for both the help at Building 230 and using the X5000.
- Mr. Rogelio Jacobo for his help and partnership while tinkering with the ElemX to successfully print AA 7075.
- Dr. Mika Mariusz at Additec for providing the AA7075 wire spool and for the helpful discussions.
- Dr. Tugba Isik for the help and expertise regarding x-ray nano-tomography scans at the FXI 18-ID beamline.
- Dr. Brian Bingham for your mentorship and guidance during my journey regarding robotics.
- CAMRE and Fleetwerx, particularly Mr. Chris Curran, Mr. Patrick Tucker, and Mr. Scott Cohick for all the work to make SALVEX and TRIDENT WARRIOR 2024 such a success.

This research was supported by the Consortium for Advanced Manufacturing Research and Education (CAMRE) and the Naval Innovation Exchange AM (NIX-AM) programs at NPS. In addition, this research used resources at the Full-Field X-ray Imaging (FXI) beamline (18-ID) of the National Synchrotron Light Source II, a U.S. Department of Energy (DOE) Office of Science by Brookhaven National Laboratory under Contract No. DE-SC0012704 and DOE grant PRJ1009594.

I. INTRODUCTION

A. MOTIVATION AND FOCUS

Three-dimensional (3D) printers are becoming common items to find in businesses and even homes. However, these printers are almost all for polymers, which operate at low temperatures with minimal footprints, support equipment, and power requirements. Also, polymer prints are usually ready for use immediately after printing (i.e., no post-processing is required). In contrast to polymer printing, a review of Xometry's website states 3D printers for metal, or metal additive manufacturing (M-AM) methods, are more challenging to adapt for industrial use, largely due to the requirement to certify the metal has the required materials properties [1]. Metal printers fall into several different categories based on the method of joining and the feedstock, and most of them are fairly expensive and require specialized training to operate [1]. According to the literature surrounding 3D printing, polymer printers can normally print a wide range of products whereas metal printers are usually optimized for a couple of metallic alloys, and they are often unable to print others due to large differences in the melting and boiling points, thermal conductivity, and composition among different alloys. Additionally, the product of a metal printer often requires extensive post-processing, including removal from the substrate, machining of the final surfaces, and heat treatment—which can add several days to the process and often require more specialized training. Gunduz of the Naval Postgraduate School (NPS) notes that M-AM can have a large impact due to the unique advantages of 3D printing—namely the ability to rapidly and cost-effectively produce small scale parts for niche applications [2]. For the Department of Defense (DoD) and Department of the Navy (DON), this capability is critical as many weapons systems and platforms rely on metal parts with long supply lead times or enormous costs. Therefore, research into M-AM techniques to produce key alloys for use on DoD and DON units is of paramount importance.

B. OBJECTIVES

M-AM is still an evolving technology with lots of active research occurring, but it is also immediately relevant to real world operations. Similarly, the goal of this research

was to produce high-end aluminum alloy systems using applicable M-AM techniques in the laboratory and improve M-AM techniques currently being used in the Fleet. As a result, this dissertation has three research and two operational objectives.

1. Research Objectives

These alloys, particularly aluminum alloy 7075 (AA 7075) and aluminum alloy 7068 (AA 7068), are of high importance to the DoD and DON because they are both aerospace grade aluminum alloys used in key aircraft structural components. Sokoluk et. al observes that both alloys have been historically used since the 20th century in airframe construction, but both alloys are notoriously difficult to weld due to cracking issues along and within the welds [3]. The study, in addition to many others, notes that since many M-AM processes are highly analogous to welding, these alloys are also very challenging to produce via M-AM for the same reasons [3], [4], [5], [6]. These studies state that AA 7075 and 7068 have been successfully printed using M-AM techniques, but not without the addition of additives which result in inferior materials properties [3], [4], [5], [6]. The laboratory research objectives are as follows:

- Print AA 7075 samples with comparable properties to that of the wrought alloy. Characterize and mechanically test the samples to verify fully dense, crack-free, full-strength fabrication.
- Identify and successfully utilize additives while printing AA 7075 to improve the materials properties beyond those achieved by pure AA 7075 via particle strengthening methods. Characterize and mechanically test the samples to verify additives were successfully incorporated and probe the microstructure to understand how the additives interacted with AA 7075.
- Design and print custom infill aluminum components to further optimize strength-to-weight ratio. Initial printing to be done with aluminum alloy 4008 (AA 4008) to lay the groundwork for accomplishing with AA 7075.

2. Operational Objectives

In the Era of Great Competition, the U.S. Navy faces unprecedented ship and submarine construction and repair challenges. M-AM provides an option to accelerate battle damage repair in addition to normal ship and submarine repair and construction timelines. NPS was invited to participate in two exercises—Salvage Exercise (SALVEX) 2024 and TRIDENT WARRIOR (TW) 2024—that involved the use of M-AM techniques. However, the scope of the two exercises were very different. SALVEX 2024 was designed to simulate the repair of battle damage to a capital ship. The objective of TW 2024, on the other hand, was to design and implement a Joint Advanced Manufacturing Cell (JAMC) to rapidly identify, print, and certify parts for all DoD components. The operational objectives are as follows:

- Utilize a M-AM technique for a simulated battle damage repair, where the part drawing is unavailable, and the original part is damaged beyond repair. The printed parts should be post-processed and retested to the maximum extent possible.
- Utilize various M-AM techniques to design, print, and certify parts for as many DoD components as possible. Certification shall be conducted both at NPS and locally to expedite the timeline to verify a part is suitable for use.

C. DISSERTATION LAYOUT

This dissertation applies both laboratory and operational research to the advancement of M-AM. Chapter II (Background) provides the necessary information for the reader to grasp the important concepts explored, both in the laboratory and in the field. Chapter III (Methodology) contains the laboratory procedures used for the research chapters to follow, except for the methodology for Chapter VI. Chapters IV–VI contain the research accomplished in the laboratory. Chapter VII contains the research accomplished during the exercises. Chapter VIII provides the overall conclusions from both areas and discussion on how they relate back to the objectives of this work as well as future directions.

THIS PAGE INTENTIONALLY LEFT BLANK

II. BACKGROUND

The previous chapter defined the motivation for the laboratory and operational research performed during this dissertation. All the laboratory research objectives involve the production of advanced aluminum alloys via M-AM processes. Therefore, an introduction of the applicable materials science of the aluminum alloys under investigation is required, to include aluminum alloy compositions and materials properties, dispersion and precipitation strengthening, and heat treatment methods. Next, the techniques used to explore the material properties of aluminum are discussed, to include tensile testing, microhardness, x-ray diffraction (XRD), optical microscopy, scanning electron microscopy (SEM), energy-dispersive spectroscopy (EDS), digital radiography (DR), computed tomography (CT) scanning, and nano-tomography.

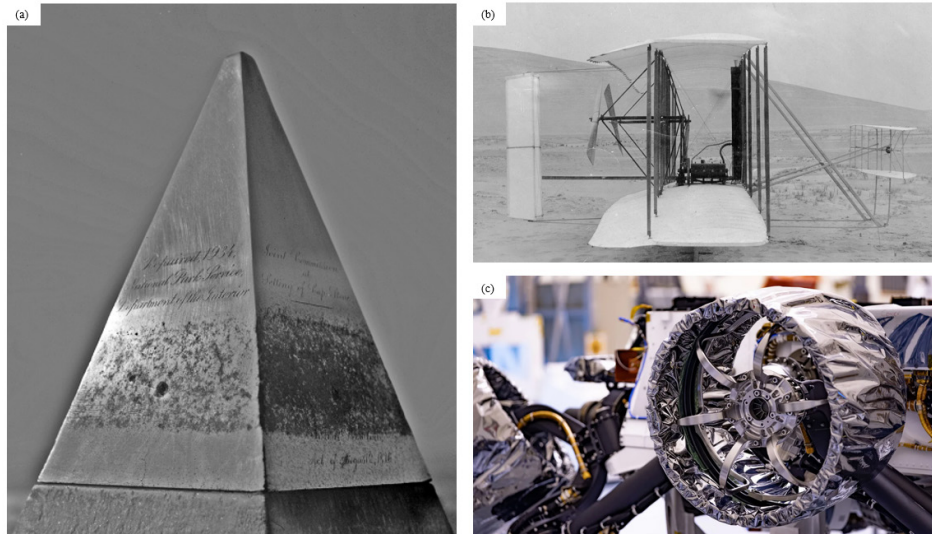
With the necessary background regarding materials characterization of aluminum alloys covered, an overview of M-AM with a specific description of the operating principles of the Additec (formerly Xerox) ElemX liquid metal printer shall be discussed. The printer control system including the G-code used by the ElemX is discussed since the modification of the code enabled the production of custom infill specimens. The magnetohydrodynamic forces utilized for metal droplet formation in the ElemX provide the ability to precisely control the cool down rate—they shall be discussed because it is this unique feature that allows for the successful printing of AA 7075 and zinc-enriched AA 7075.

Finally, a description of current and future operational impacts of M-AM on the DON and DoD is provided to set the scene for the expeditionary M-AM work and research done as part of the SALVEX 2024 and TW 2024 exercises in the spring and summer of 2024.

A. MATERIALS PROPERTIES OF ALUMINUM ALLOYS

Aluminum is everywhere in the industrial world due to its abundance (third most common element in the Earth's crust) and excellent materials properties, particularly its strength, density (weight), recyclability, and corrosion resistance [7], [8]. However, despite this abundance, aluminum was once more valuable than gold [6]. In fact, Napoleon III of France is known as one of the first proponents of aluminum, and he showcased that belief by

turning France's entire stock into cutlery that only certain guests used while the others used "regular" gold utensils [9]. In 1884, aluminum exploded to national prominence in the United States when it was used to construct the first pyramidal cap of the Washington Monument [10]. The reason for the high cost is aluminum bonds readily with other elements, and it is not found in a pure state in nature (like most other metals) because it is normally found in Bauxite or a similar aluminum oxide compound [11]. With the invention of the Hall-Heroult process in 1886, the cost of aluminum was substantially reduced, making it readily available for the coming aerospace industry [11]. The Wright Flyer flew in 1903, less than 20 years after the discovery, in no small thanks to the use of aluminum for the four-cylinder engine used as its powerplant [9]. Since then, aluminum has been used in virtually all other aircraft designed, to include many components of spacecraft [12]. The use of aluminum in the industrial world expanded throughout the 20th century and shows no signs of slowing—the aluminum market is forecast to expand at a 2.03% compound annual growth rate (CAGR) thanks to its heavy use for electric vehicles, solar panels, batteries, and aircraft/spaceship [13]. Figure 1 highlights the evolution of the use of aluminum from its humble beginnings to the current space exploration age of today.

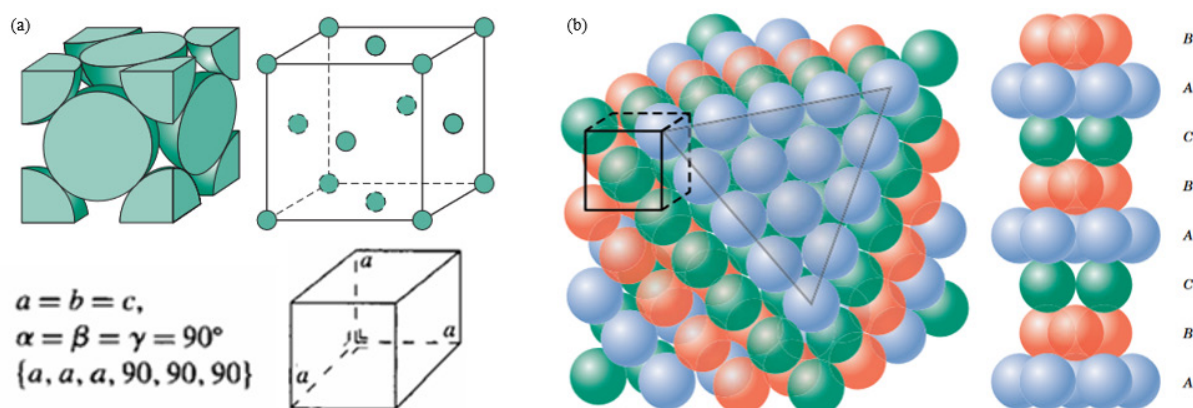


(a) Original Washington Monument cap. Adapted from [14]; (b) Wright Flyer engine block. Adapted from [15] (c) Wheels of the Mars 202 rover, Perseverance, that are machined out of aluminum. Adapted from [12].

Figure 1. Historical uses of aluminum.

1. Crystal Structure and Miller Indices

Aluminum, like other metallic elements, is a crystalline material, composed of an orderly array of stacked atoms which form a crystal lattice [16]. The crystal structure of a material is important since many properties depend upon it, such as tensile strength, ductility, and hardness, to name a few [16], [17]. Crystal lattices fall into two different classes—Bravais and non-Bravais lattices—with the difference being all lattice points in a Bravais lattice are equivalent, but not so for non-Bravais lattices [18]. A Bravais lattice is a combination of the crystal lattice and a symmetric array of lattice points; in three dimensions, only 14 Bravais lattices are possible, in three dimensions, from the seven possible crystal lattices: cubic, trigonal, tetragonal, hexagonal, orthorhombic, monoclinic, and triclinic [19]. “A Bravais lattice is a mathematical description that shows how space can tessellate infinitely by translation,” but without a crystal basis it has no physical meaning [20]. Of the cubic crystal lattices, three Bravais lattices are possible—simple cubic, body-centered cubic, and face-centered cubic [20]. The FCC crystal structure, shown in Figure 2a, is one variant of the cubic crystal system where all sides are the same length and all interior angles are 90° [21]. All aluminum alloys have FCC crystal structure which is the crystal structure that allows the highest atomic packing factor of 0.74 (Figure 2b) [22].



(a) FCC unit cell showing equivalent side lengths and all angles of 90° . Adapted from [16].
(b) FCC crystal structure showing close packing planes in ABCABCABC stacking sequence. Adapted from [20].

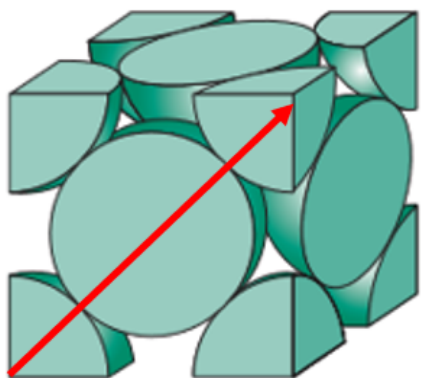
Figure 2. FCC unit cell and crystal structure.

Planes and directions within the FCC lattice (and all lattices for that matter) are defined using a system called Miller indices. In [23], Ohl states that individual crystallographic planes are written in the form $(h k l)$ and a family of planes, where all planes are equivalent by symmetry, are written in the form $\{h k l\}$. Similarly, individual crystallographic directions are denoted $[h k l]$, a family of directions is written as $\langle h k l \rangle$ [23]. A reliable means of determining crystallographic directions and planes is crucial because it allows for determining crystal lattice parameters, such as the distance between planes [24]. This distance can be calculated and simplified based on FCC lattice symmetry ($a = b = c$) [24]. For the FCC lattice, the close-packed planes and directions are summarized in Figure 3, with six close-packed directions corresponding to four close-packed planes [24]. Of note, a “bar” over the top of an index number indicates a negative value.

$$\frac{1}{d_{hkl}} = \sqrt{\frac{h^2}{a^2} + \frac{k^2}{b^2} + \frac{l^2}{c^2}} \quad (1)$$

$$d_{hkl} = \frac{a}{\sqrt{h^2 + k^2 + l^2}} \therefore \frac{1}{d_{hkl}} = \frac{(h^2 + k^2 + l^2)}{a^2} \quad (2)$$

For Equations 1 and 2, $d_{hkl} \equiv$ distance between crystallographic planes, $h, k, l \equiv$ crystallography plane index, and $a, b, c \equiv$ crystal lattice parameters.



Close Packed Directions:

$$\begin{aligned} \langle 110 \rangle &= [1\bar{1}0], [01\bar{1}], [10\bar{1}], \\ &[110], [101], [011] \end{aligned}$$

Close Packed Planes:

$$\{111\} = (111), (\bar{1}\bar{1}1), (1\bar{1}\bar{1}), (11\bar{1})$$

Adapted from [16], [23].

Figure 3. FCC close-packed directions and planes.

Close-packed planes and directions have the greatest planar density, and together they form slip systems within a material [16]. Slip is the process by which a material plastically deforms and is the “sliding displacement along a plane of one part of a crystal relative to the rest of the crystal under the action of shearing forces” [25]. Slip occurs by the motion of dislocations, which can be either edge, screw, or mixed and are defined as the mismatch of crystal planes due to a missing row of atoms [26]. In metallic materials, slip occurs by the motion of dislocations, and the most favorable pathway for dislocation motion is along the close-packed directions within close-packed planes, which is {111} <110> for the FCC crystal system [16]. However, dislocations cannot always move along slip planes during deformation due to the presence of other dislocations, particles, or other barriers, and these interactions all contribute to the material’s mechanical properties [16], [27].

2. Aluminum Alloys

Aluminum by itself, like many other elements, has poor mechanical properties and is not particularly useful in the pure state. It is through the addition of other elements in small amounts, a process known as alloying, that imparts aluminum alloys with remarkable materials properties. A review of the literature identifies two general categories of aluminum alloys—cast and wrought [28], [29]. Cast alloys are melted and poured into a molding to form the desired shape, whereas wrought alloys are worked into the desired shape using tools [30]. Wrought aluminum alloys, which make up ~85% of alloys, are both heat treatable and non-heat treatable in addition to being worked vice cast [28], [29]. Heat treatable wrought alloys contain silicon (Si), copper (Cu), zinc (Zn), and magnesium (Mg) in lower concentrations than normally found in cast alloys [28]. The addition of alloying elements and proper processing, including heat treatment, results in a much stronger metal than before the additions and treatments [31]. Aluminum alloys have continued to evolve over the 20th century, becoming stronger and lighter, with alloys tuned for certain uses, as shown in Table 1. Due to their favorable mechanical properties and applicability to the DON, wrought aluminum alloys are the focus for the laboratory research.

Table 1. Aluminum alloy series, description, and examples.

Alloy Series	Description	Example
1000	Mostly pure aluminum (Al) with superior corrosion resistance (99% minimum Al)	99% pure Al
2000	Primary alloying elements: Cu and lithium (Li) Uses: aerospace components	2195 (0.8–1.2% Li and 3.7–4.3% Cu)
3000	Primary alloying element: Manganese (Mn) Uses: cookware, heat exchangers, and soda cans	AA 3003 (1.1–1.5% Mn)
4000	Primary alloying element: Silicon (Si) Uses: filler material for welding / brazing	A356 and AA 4008 (6.5–7.5% Si)
5000	Primary alloying element: Magnesium (Mg) (not heat treatable) Uses: transportation, tanks, vessels, and bridges	AA 5052 (2.2–2.8% Mg)
6000	Primary alloying elements: Mg and Si Uses: structural components	AA 6061 (0.4–0.8% Si, 0.7% Fe, 0.8–1.2% Mg)
7000	Primary alloying element: Zn Uses: aerospace and competitive automotive and sporting equipment	AA 7075 (1.2–2.0% Cu, 2.1–2.9% Mg, 5.1–6.1% Zn)

Adapted from [32], [33], [34], [35], [36], [37], [38].

4XXX series aluminum alloys use Si as the primary alloying element to lower the overall density and improve the castability [39]. Some 4XXX series also contain Mg, which improves the alloy by allowing it to be age hardened [40]. Historically, 4XXX series alloys have been the most used in M-AM, mostly due to its ease of castability and lack of oxidation at elevated temperatures, to include the Additec ElemX liquid metal jet printer, and a comparison of the alloy used in the printer to Al4008 (A356) is shown in Table 2 [41]. Despite their ease of production and oxidation resistance, A356 only has an ultimate tensile strength (UTS) and strain to failure (ductility) of 228 MPa and 3.5%, which is significantly lower than that of higher end aluminum alloys [16]. Attempts have been made to improve the materials properties of this alloy system via incorporation of precipitates and grain refinement; improvements in UTS have been realized, but not so in ductility [42]. Due to these limitations, use of 4XXX series aluminum for DoD and DON applications is limited.

Table 2. Elemental composition of A4008 / A356 and ElemX 4XXX series aluminum wire.

Aluminum Alloy 4008 / A356								
Element	Si	Mg	Fe	Ti	Cu	Mn	Zn	Al
wt%	6.5–7.5	0.25–0.45	0.2	0.2	0.2	0.1	0.1	bal.
ElemX 4XXX Series Aluminum Wire								
Element	Si	Mg	Fe	Ti	Cu	Mn	Zn	Al
wt%	7	0.4	0.08	0.08	< 0.01	< 0.01	< 0.01	bal.

Adapted from [43].

On the other hand, aluminum alloy 7XXX series has many DoD and DON applications due to their extremely high strength-to-weight ratio and corrosion resistance [44]. AA 7075, originally developed in the 1940s, has seen widespread application in the fabrication of aircraft fuselages, wings, and other key structural components [45], [46], [47]. After proper heat treatment, AA 7075 has a higher strength-to-weight ratio than any type of steel [48]. As the need for stronger and lighter materials increased, research into the 7XXX series continued throughout the 20th century with the development of AA 7068 by Kaiser Aluminum in the 1990s in response to the request from the ordnance industry for an aluminum alloy with higher tensile strength than AA 7075 [49], [50]. From a review of the literature, AA 7075 and 7068 have very similar compositions with the major differences being the higher Cu and Zn and the lower Fe and Cr present in AA 7068 versus AA 7075 (Table 3) [16], [37], [49], [50], [51], [52], [53]. The nominal UTS of AA 7068 is ~130 MPa higher than that of AA 7075, and, as expected, it has a lower ductility of 5% compared to 11% of AA 7075 [49]. Vickers hardness of both alloys is similar—185 for AA 7075 compared to 200 for AA 7068 [50]. By increasing the Zn concentration of AA 7075 by 2 wt% to that of AA 7068, the UTS can be improved to 662 MPa with a slight degradation in the ductility to ~4% [54]. This is due to the formation of more precipitates in the alloy, which is discussed in greater detail in the next section [54]. Due to their high UTS and low density (2.81 g/cm³ for AA 7075 and 2.85 g/cm³ for AA 7068), a huge advantage of these alloys is specific strength, which is calculated via Equation 3 [55].

Specific strength of AA 7075 and 7068 compared to some common steel alloys is shown in Table 4.

$$\text{Specific Strength} \left(\text{MPa} * \frac{\text{cm}^3}{\text{g}} \right) = \frac{\text{UTS (MPa)}}{\text{Density } \left(\frac{\text{g}}{\text{cm}^3} \right)} \quad (3)$$

Table 3. AA 7075 and 7068 comparisons.

Aluminum Alloy 7075										
Element	Si	Mg	Fe	Ti	Cu	Mn	Zn	Cr	Zr	Al
wt%	≤ 0.4	2.1– 2.9	≤ 0.5	≤0.2	1.2–2.0	≤ 0.3	5.1– 6.1	0.18– 0.28	≤ 0.05	bal.
UTS (MPa)	550–570		Hardness (HV)			185		Ductility (%)	11	
Aluminum Alloy 7068										
Element	Si	Mg	Fe	Ti	Cu	Mn	Zn	Cr	Zr	Al
wt%	≤ 0.12	2.2– 3.0	≤ 0.15	≤0.1	1.6–2.4	≤ 0.1	7.3– 8.3	≤ 0.05	0.05– 0.15	bal.
UTS (MPa)	683–703		Hardness (HV)			200		Ductility (%)	5	

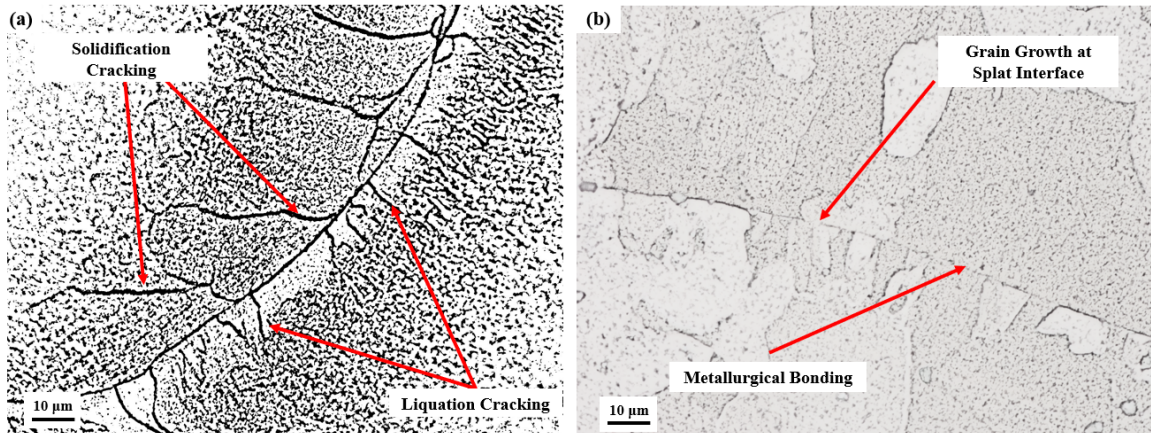
Adapted from [16], [37], [49], [50], [51], [52], [53].

Table 4. Specific strength of AA 7075, AA 7068, 316L stainless steel, and HY-80 steel.

Materials Property	AA 7075	AA 7068	316L Stainless Steel (Meltio XY)	HY-80
UTS (MPa)	550 – 570	683 – 703	643	827
Ductility (%)	9 – 11	5 – 9	38	17 – 20
Density (g/cm ³)	2.81	2.85	8.0	7.75
Specific Strength	202.85	246.67	80.375	106.71

Adapted from [16], [49], [51], [52], [56], [57].

AA 7075 and 7068 are both susceptible to hot cracking (i.e., hot tearing), which makes them difficult to weld and to produce via M-AM techniques [5], [58], [59], [60]. During welding or M-AM of AA 7075 and 7068, the solid grows in a morphology depending on the cooling and solidification rates that are typically very high around the fusion zone [59], [61]. AA 7075 and 7068 have high thermal expansion coefficients of $\sim 24 \mu\text{m}/\text{m}\cdot^\circ\text{C}$, which makes the alloys susceptible to solidification cracking [59]. The solidus temperature is approximately 520–530°C for the AA 7075 alloy, but incipient melting occurs at 477°C in a limited amount around precipitates that form lower melting point eutectics [62], [63]. The liquidus temperature is around 628–635°C depending on the exact composition [63]. In the terminal solidification stages, microsegregation occurs due to solute rejection, which enriches the interdendritic and intercellular liquid with solute [61]. This leaves just enough liquid to weaken the material that is under tension during solidification and cooling, which causes hot cracking as shown in Figure 4a-b [59], [64].



(a) Typical M-AM morphology at splat interface showing solidification and liquation cracking and (b) proper grain growth and bonding

Figure 4. Morphology of AA 7075 shows hot cracking and metallurgical bonding.

Liqation cracking is another type of defect observed for aluminum alloy 7XXX series within the partially melted zone (PMZ) adjacent to the melt pool during welding or previously deposited splats during M-AM processes [59], [64]. During welding and M-AM, columnar grains grow from the PMZ and heat affected zone (HAZ), producing crack-

susceptible grain structures [59], [61]. One way to eliminate hot cracking on AA 7075 is to preheat the substrate during processing (at least above 260°C), which has been shown to reduce the temperature gradient and cooling rate with no crack formation during M-AM processes, resulting in good metallurgical bonding and grain growth across splats [6]. In addition to hot cracking defects, AA 7075 and 7068 are both susceptible to loss of alloying elements, particularly Zn and Mg, during welding or M-AM processes [65]. This is due to the low boiling points of Zn (907°C) and Mg (1,091°C), which are much lower than Al (2,470°C) and Cu (2,562°C) and close to the solidus of AA 7075 and 7068 [66], [67]. If alloy processing temperatures are too high, large pores from degasification of Zn and Mg can result and significantly degrade the mechanical properties of the alloy [58], [59], [67], [65].

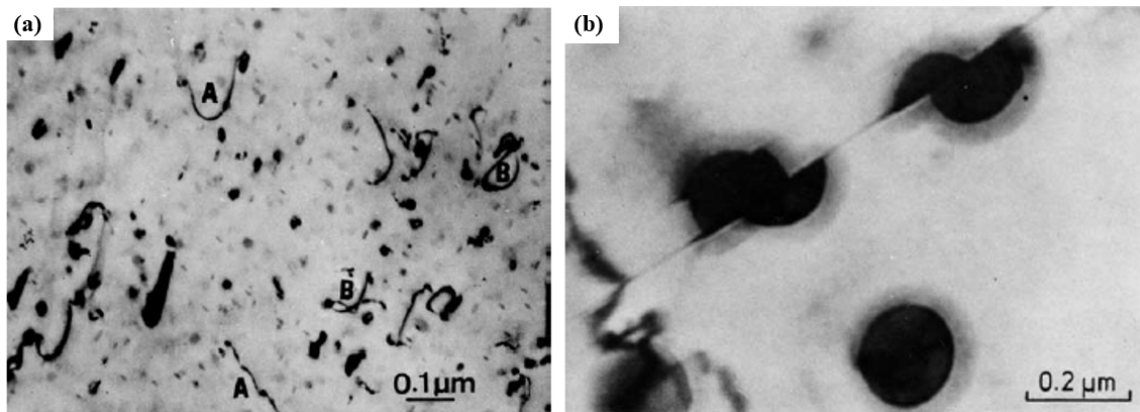
3. Particle Strengthening Methods

A common method of improving the strength of an alloy is particle strengthening, which occurs via the addition of dispersoids or precipitates. Meyers and Chawla identify several key differences between the two methods, but the major differentiation between them is precipitates are formed from the original alloy whereas dispersoids are a different elemental composition than the original alloy [27]. For dispersion strengthening, insoluble particles are introduced into the matrix through a processing method such as powder metallurgy, oxidation, or oxide break-up to a volume fraction of 3–4% maximum [27], [68]. They go on to discuss pros and cons – one huge advantage of dispersion strengthening is temperature stability—there is no risk of losing the dispersoids during large temperature swings which is favorable for many industrial applications [27]. The second method of particle strengthening is known as precipitation strengthening, where heat treatment is used to generate particles of a different phase in the matrix [69]. These particles are composed of the same elements but in different proportions, also called intermetallics, and are formed in a precipitation hardening process as follows:

- Solid solution treatment: the alloy is heated above the solvus temperature to produce a homogeneous single-phase structure by dissolving any secondary phases [70].

- Quenching: this step is crucial and often has strict time limits to preserve the solid solution and prevent undesirable phase formation [69].
- Aging: after quenching, the alloy is heated to and maintained at “a temperature below the solvus in order to provide the thermal energy required for a precipitate to form” throughout the alloy matrix [70].

Both dispersion and precipitation strengthening improve the mechanical strength of a material by impeding dislocation motion, forcing them to bow around or cut through the particles (Figure 5) [68], [71].



(a) Dislocations pinned by precipitates within an alloy and (b) precipitates sheared by the passage of a dislocation. Adapted from [27].

Figure 5. Dislocation interactions with particles.

As discussed, dislocations in a material move through the matrix when it is plastically deformed. Meyers and Chawa observe that particles dispersed throughout the metal matrix affect the movement of dislocations when the material is put under stress, thus improving a material’s strength [27]. There are two main mechanisms by which particles accomplish this:

1. The particles interpenetrate the slip plane of the dislocations and cannot be cut by dislocation motion [27].

2. The particles are subject to shear by the dislocation flow in the slip planes and are cut by dislocation motion [27].

For case 1, dislocations moving through a metal encounter the particles and sufficient stress must be applied to bend the dislocation around the impenetrable particles, as shown in Figure 6a [27]. The dislocation line must have a critical stress applied to bow around the particles, leaving behind a dislocation ring around the bypassed particles [72]. The stress needed to bow a dislocation line is given by the Orowan Equation [27]:

$$\tau \approx \frac{Gb}{2r} = \frac{Gb}{x} \quad (4)$$

In Equation 4, τ \equiv shear stress, G \equiv shear modulus of the material, b \equiv the burgers vector of the dislocation, and $2r$ \equiv the distance between two particles, which is simplified to x . The addition of the particles improves the yield stress of the material:

$$\tau_y \approx \tau_m + \frac{Gb}{x} \quad (5)$$

In Equation 5, τ_y \equiv the yield stress of the material and τ_m \equiv the critical shear stress for yielding in the metal matrix in the absence of a particle [27].

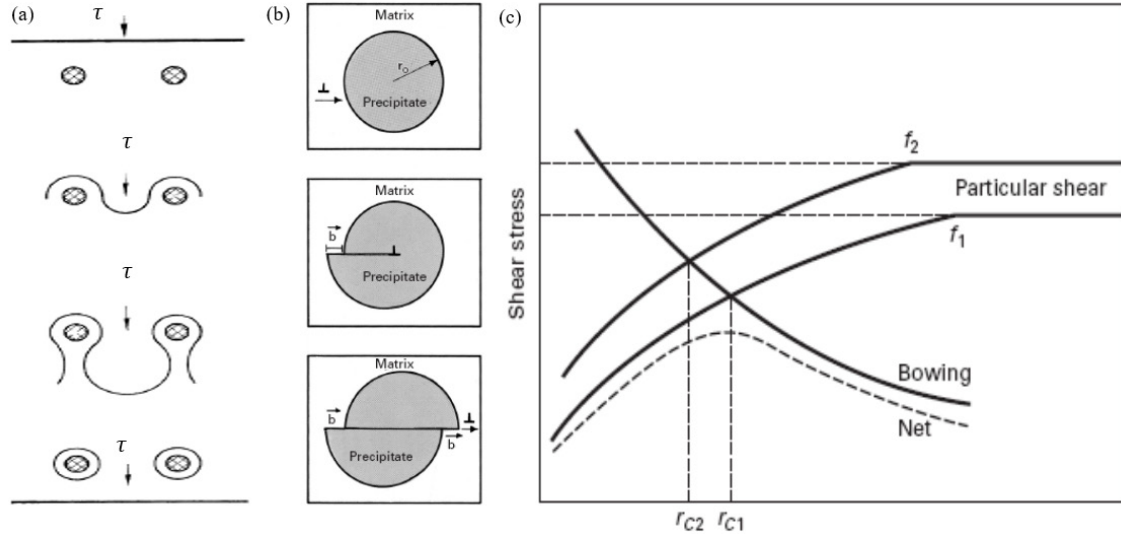
For case 2, the particles in the matrix are sheared if the stress to shear a particle is less than that of Equation 4 to bow around the particle (Figure 6b) [27]. For precipitation hardened alloys, the size and volume fraction of a precipitate changes as the alloy is heat treated; shear stress is thus dependent upon both the size and volume fraction of the precipitates [27]:

$$\tau \propto \sqrt{rf} \quad (6)$$

In Equation 6, r \equiv the particle radius and f \equiv the particle volume fraction.

As an alloy is aged, volume fraction increases but eventually reaches a plateau; however, the particle size continues to increase in a phenomenon known precipitate coarsening [27]. Therefore, whether the dislocations bow around or cut through a

precipitate depends upon the distribution, size, and spacing of precipitates as shown in Figure 6c [27].



(a) Dislocation looping around particles, (b) particle shearing by dislocations, and (c) graphical depiction of particle strengthening showing the relationship between stress and particle size. Adapted from [27].

Figure 6. Summary of particle strengthening of metal alloys.

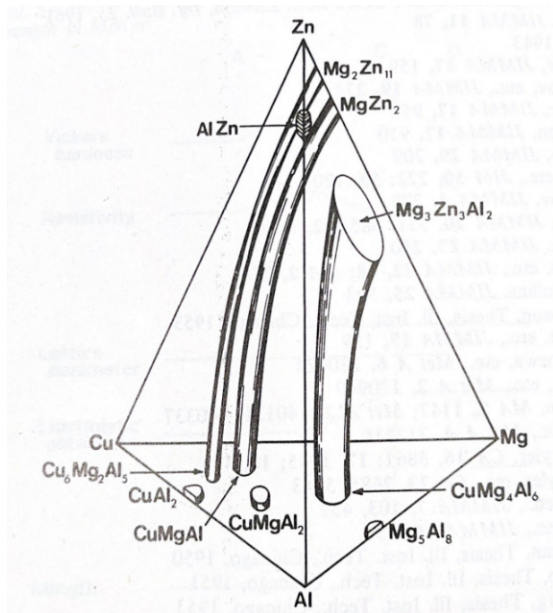
4. Heat Treatment and Precipitation Strengthening of 7XXX Series Aluminum Alloys

Both AA 7075 and 7068 alloy are age hardened in a 3 step age hardening process during the T6 temper [73], [74]. The procedure for T6 treatment of AA 7075 varies slightly across the literature, but generally consists of solutionizing at $\sim 480^{\circ}\text{C}$ for 1–2 hours, rapid quenching in water, and finally age hardening at $\sim 121^{\circ}\text{C}$ for 24–48 hours [70], [75]. The final age hardening process provides the high strength of AA 7075 and 7068 by permitting the formation of nanoscale precipitates of η (MgZn_2) from Guinier-Preston (GP) zones via the following process [76], [77], [78]:



In Equation 7, $\text{SS} \equiv$ solid solution, $\text{GP} \equiv$ GP zones, and η' and $\eta \equiv$ precipitates.

GP zones are metastable, and the aging process basically replaces those zones with the η' and finally the η phase [78]. The result is a finely distributed structure of intermetallics, primarily of η , but also including $Mg(Al, Cu, Zn)_2$ (with Al and Cu substitutions for Zn within η phase lattice), Al_2CuMg (S), Al_7Cu_2Fe (ω), Al_2Cu , Mg_2Si , $Mg_3Zn_3Al_2$, and other phases that can form during the heat treatment process (Figure 7) [6], [79]. The high strength of AA 7075 (~550–570 MPa UTS) comes from the primary phase nanoscale precipitates of η that form during aging but comes at the cost of high susceptibility to stress corrosion cracking (SCC) and reduced ductility [27]. If a proper T6 heat treatment is not performed, the η starts to break down and form coarser precipitates, significantly reducing the mechanical properties of the alloy [80]. Additionally, the presence of iron (Fe) in AA 7075 leads to the formation of ω as well as Al_3Fe ; these precipitates tend to be coarser, do not refine during heat treatment, and require thermomechanical processing to improve the properties of the alloy [81]. It is possible for precipitates within AA 7075 and 7068 alloys to consist of multiple intermetallics due to their heterogeneous nucleation from insoluble Fe-rich ω phase [82]. Due to the wide range of precipitates formed during T6 heat treatment, AA 7075 and 7068 are susceptible to localized corrosion, including peripheral pitting (trenching), intergranular, and exfoliation corrosion due to the formation of galvanic couples within the alloy [81], [82]. The precipitates Al_7Cu_2Fe , Al_3Fe , Al_2Cu act as cathodes whereas Mg_2Si , Al_2CuMg , and $MgZn_2$ act as anodes to the Al matrix, and localized corrosion can develop where a galvanic couple is formed between anodic and cathodic precipitates in close proximity [82].



Source: [79].

Figure 7. Precipitates formed during T6 heat treatment of AA 7075.

B. MATERIALS CHARACTERIZATION AND TESTING

According to the ASM International, materials characterization is defined as testing and analyses performed to ascertain the macro, micro, and surface composition and structure of materials which all contribute to a material's properties and performance [83]. The analyses performed in this dissertation shall be discussed, and they are divided into mechanical testing, elemental composition analysis, and imaging categories. For mechanical testing, hardness and tensile testing are performed to obtain hardness, UTS, and ductility. XRD, x-ray fluorescence (XRF), and EDS are both used to determine the elemental composition. Specimens are imaged via optical microscopy and SEM to ascertain the microstructure. Non-destructive inspection (NDI) techniques are used to study the internal structure of specimens to look for porosity, cracks, and other defects which can lead to premature failure. Digital radiography (DR), computed tomography (CT), and x-ray nano-tomography are used to probe the interior of specimens to investigate the microstructure and look for defects.

1. Mechanical Testing

Several key values are used to ascertain a material's mechanical performance: hardness, tensile strength, and ductility. Struers, a leading provider of materials testing devices, states hardness testing on metallic specimens is performed via either the Rockwell, Vickers, Brinell or Knoop test [84]. All the major hardness tests operate using the same basic principle—a hardened indenter with a specific shape and size is pushed into the surface of a specimen using a known force, and the size of the resulting indentation is measured [85]. A summary of these tests is provided in Table 5; since aluminum and steel alloys are the focus of this research, both Vickers and Rockwell hardness tests are the appropriate tests to ascertain specimen hardness [27].

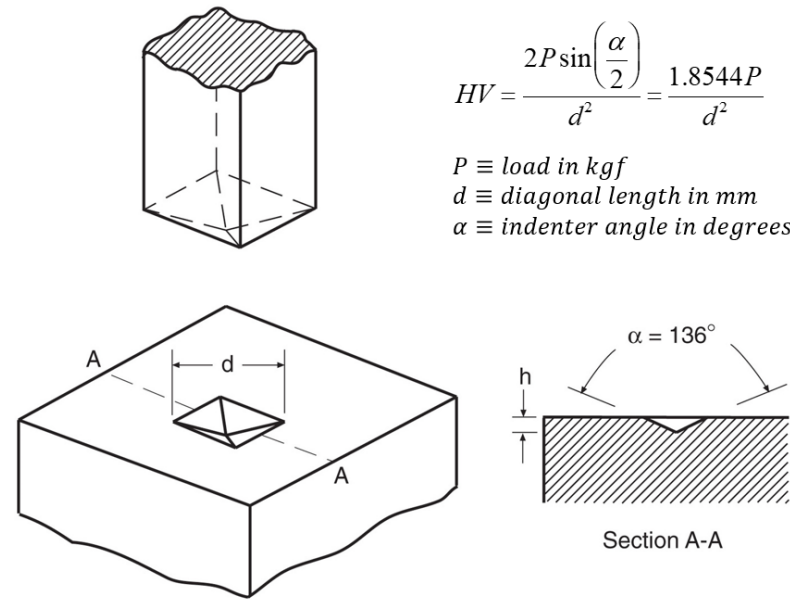
Table 5. Hardness testing methods.

Hardness Test	Base Equation	Shape	Uses
Brinell	$HB = \frac{P}{\pi D \times depth}$ $= \frac{2P}{\pi D(D - \sqrt{D^2 - d^2})}$		Acceptance testing for commercial products; best for coarse or rough surfaces
Vickers	$HV = \frac{2P \sin(\frac{\alpha}{2})}{d^2} = \frac{1.8544P}{d^2}$		Wide range of loads allow for testing of all solid materials
Rockwell	$HR = N - \left(\frac{d}{D} \right)$		Fast test developed for production control, primarily for metallic materials.
Knoop	$HKN = \frac{14.228P}{L^2}$		Brittle materials, thin parts, and coatings

Adapted from [27], [85], [86], [87], [88], [89].

The Vickers hardness test utilizes an optical measuring system and a diamond indenter with an angle between the faces of 136° which is used based upon the limitations of spherical indenters used in the Brinell and some Rockwell tests (Figure 8) [27]. One of the major advantages of the Vickers test is one indenter can be used for a wide range of material, regardless of its hardness [88]. Hardness test results from the Vickers test are reported in the form of “XXX HV YY.Y” where XXX is the three digit hardness number and Y.Y is a two or three digit number which corresponds to the load applied during the

test in kilograms of force (kgf) [27]. So, a test result of 185 HV 1.0 would correspond to a hardness of 185 with a 1.0 kgf load applied [27]. For the laboratory research in this dissertation, the Vickers hardness test 1.0 (HV 1.0) was used for AA 7075, and HV 2.0 was used for Zn-enriched AA 7075 due to the higher expected hardness.

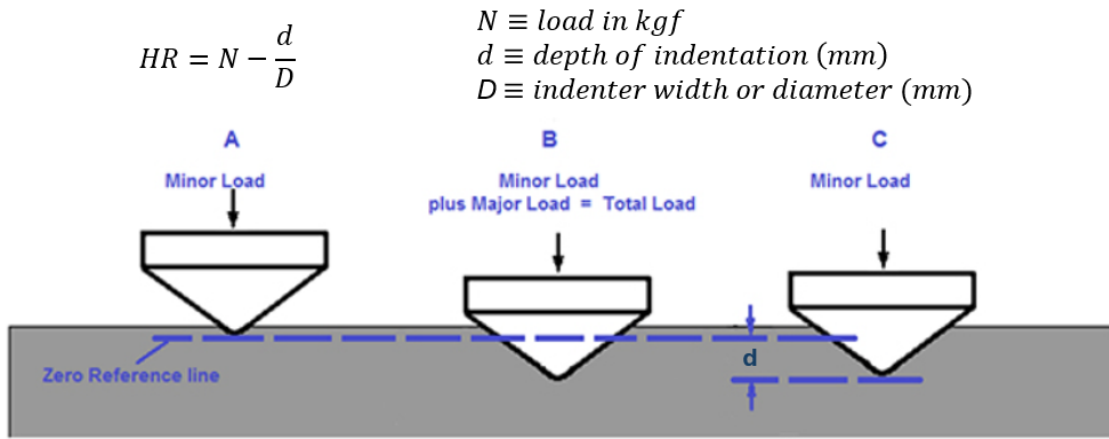


Adapted from [27], [85].

Figure 8. Schematics and equation for the Vickers hardness test.

For the operational research in this dissertation, the Rockwell B hardness test was used based upon its simplicity. According to Struers, there are 30 different scales possible for the Rockwell test based on five different indenters and six possible applied loads [87]. The appropriate Rockwell scale is selected based upon the anticipated hardness of the material [87]. The Rockwell scale for 316L stainless-steel specimens is the B scale, which utilizes a 1.587 mm diameter steel ball and 100 kgf for the major load [27]. In lieu of an optical measuring system such as the Vickers test, the Rockwell test uses a dial system to measure the difference in depth of indentation between a known minor and major load [86], [90]. The depth of indentation is then read off the dial as the difference between major and minor loads, as shown in Figure 9 [86], [90]. For Rockwell testing, it is imperative to meet the following precautions for accurate and reproducible results [27]:

- Clean and well seated indenter to ensure dimensions are as close to the specified value as possible.
- Clean and oxide free surface finish—incremental sanding with sandpaper is sufficient.
- Sample should be mounted such that the surface is flat and perpendicular to the indenter.
- Sample thickness should be at least 10 times the depth of the indentation.
- Sample test points should be spaced out at least 3–5 times the indenter diameter to ensure no biased results from strain hardening of the surface from previous tests.
- Speed should be as close as similar as possible across all tests.



Adapted from [86], [90].

Figure 9. Schematics and equation for Rockwell hardness test.

Tensile testing is performed to determine a specimen's tensile strength and ductility. In metallurgical testing, the crucial product of tensile testing is a stress-strain curve, which has a distinct shape based on whether the material tested is brittle or ductile (Figure 10) [16], [27], [85]. Brittle materials experience very little, if any, elongation before

failure, whereas ductile materials normally exhibit a significant amount of elongation at approximately the same stress [16]. Engineering stress and strain differ from true stress and strain in that the latter account for the elongation of the material being tested [85]. The relationships between engineering and true stress and strain are as follows (assuming no volume change during deformation) [85]:

$$\sigma_t = (1 + \varepsilon_e)\sigma_e \quad (8)$$

$$\varepsilon_t = \ln(1 + \varepsilon_e) \quad (9)$$

In Equations 8 and 9, σ_e \equiv engineering stress, ε_e \equiv engineering strain, σ_t \equiv true stress, and ε_t \equiv true strain.

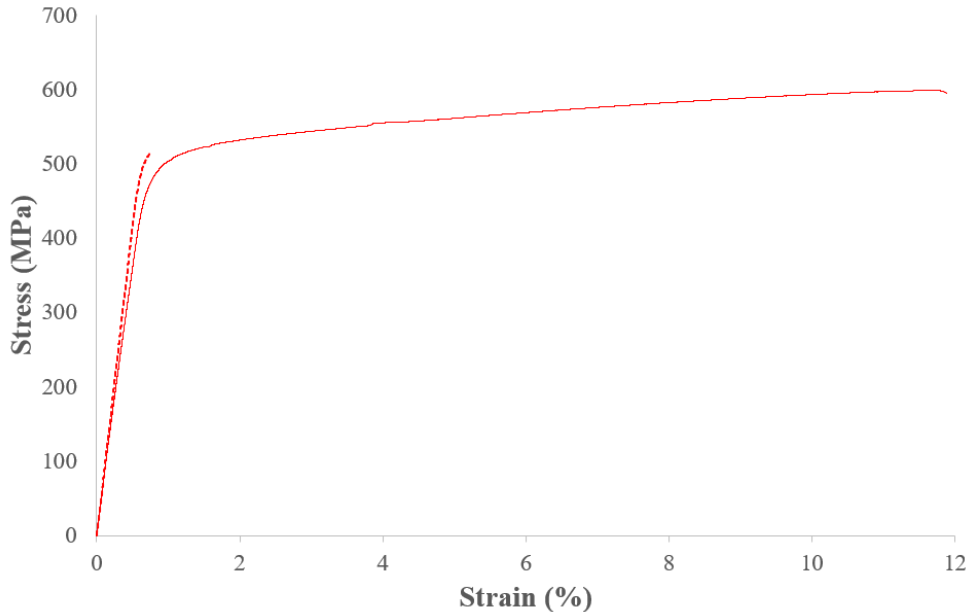
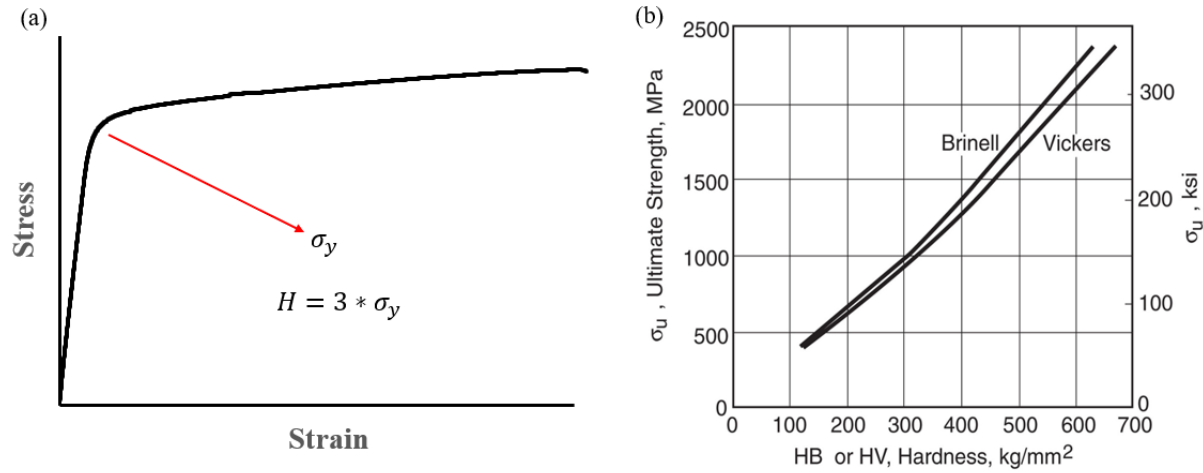


Figure 10. Stress vs. strain curves of typical brittle (dashed) versus ductile (solid) materials.

In [27], Meyers and Chawla present a key characteristic of the stress-strain curve, known as the yield point, which occurs at the yield stress (σ_y) and is defined as the transition point from elastic to plastic behavior, or “the minimum stress at which a solid will undergo deformation or plastic flow without a significant increase in the load or

external force.” For ductile materials, the yield point occurs early in the tensile test with fracture occurring at a much later time after elongation and necking (Figure 11a) [27]. For brittle materials, yield stress is usually rapidly followed by UTS and failure [27]. Another key relationship observed during mechanical testing of steels is the one between hardness and UTS, shown in Figure 11b [27].



(a) Stress-strain curve showing yield stress and hardness relationship and (b) correlation between UTS and hardness. Adapted from [27], [91].

Figure 11. Yield stress and hardness relationship.

2. Microscopy

Both optical and SEM were utilized to image samples in this research. Both techniques shall be briefly discussed. Preparation for both optical microscopy and SEM is similar and consists of the following general steps [92]:

- Mounting—samples are mounted in epoxy using a puck or die system to keep the sample stable and flat during imaging and for ease of follow-on preparation steps.
- Grinding—mounted samples are gradually sanded using increasingly fine sandpaper to remove all scratches and surface defects.

- Polishing—after the incremental grinding is completed, a series of polishing steps with a fine polishing agent (usually diamond or alumina with particle size of 1–5 microns) is performed to leave the sample with a mirror-like finish.
- Etching—the surface of the sample is exposed to a chemical agent, which preferentially attacks higher energy sites of the surface (such as grain boundaries, topographical features, and precipitates). The result is a surface with these features that are much more readily visible via microscopy.

a. Optical Microscopy

Optical microscopy is a useful tool for a variety of fields, including medical sciences, geology, and materials science. In [92], Brandon and Kaplan explain optical microscopy is a tool suitable for investigating only the surface of metallic samples metals since they are normally opaque to visible light. Etching can be essential for imaging metal alloys to highlight grain boundaries and precipitates of interest, but care must be taken not to over etch the surface, which can remove these features requiring additional sample preparation [92]. The numerical aperture (NA) of an optical microscope is “a measure of its ability to gather light and resolve fine specimen detail at a fixed object distance” [93]. NA is dependent upon the refractive index of the medium and angular aperture [93]. Optical microscopy resolution is limited to ~0.3 microns (half the wavelength of visible light), and a higher resolution comes at the expense of depth of field which is defined as the distance over which the object remains in focus [92]. Optical microscopes inherently have poor depth of field [92], [93].

b. Scanning Electron Microscopy

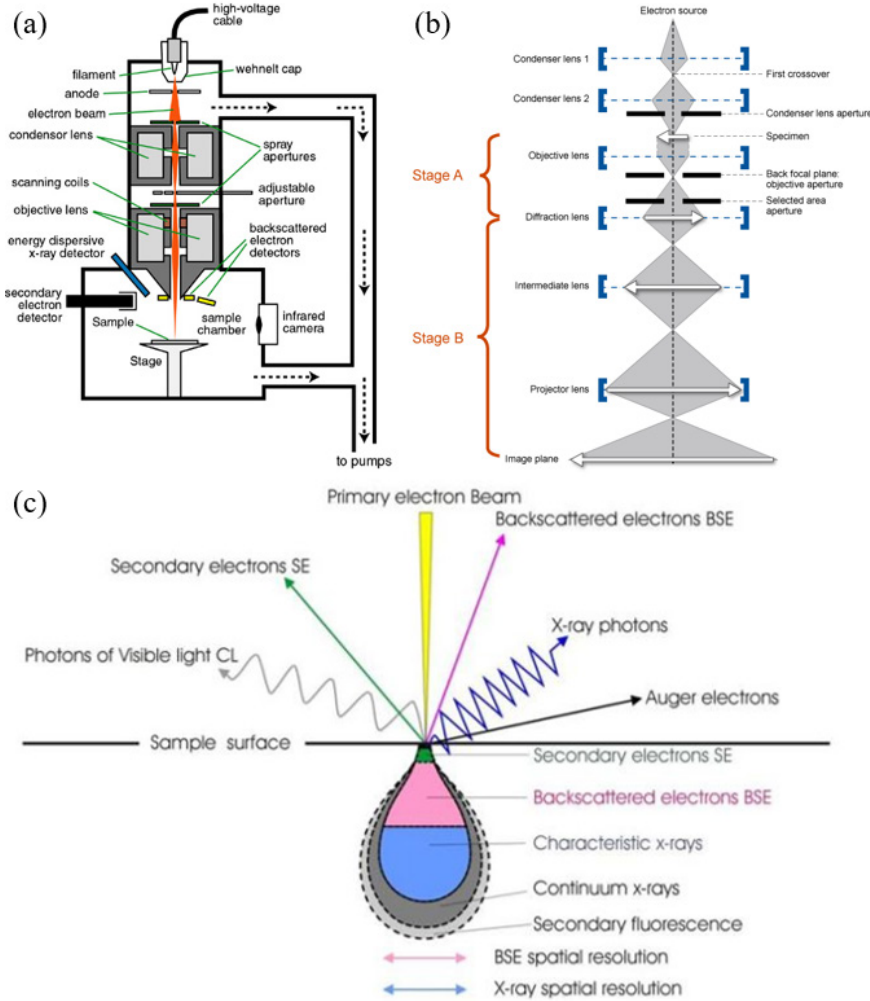
Electron microscopy is divided into two primary categories: SEM and transmission electron microscopy (TEM). Ansell of the Naval Postgraduate School (NPS) explains how electrons are excited from a source, focused into a beam, and accelerated through a vacuum onto a sample surface during SEM (Figure 12a) [94]. Therefore, SEM provides an image

based on electrons from the surface or near to the surface of a sample [92], [94]. On the other hand, a TEM utilizes transmitted electrons to provide data regarding the crystal structure, morphology, and stress state of a material [95]. TEM produces 2D images of the sample and is capable of nearly 50 million times magnification (compared to 1–2 million times for SEM) using lenses positioned below the sample (Figure 12b) [95].

Both the current and voltage of the electron beam can be varied by the operator and have an important role in the types of information collected from the sample [92]. Unlike optical microscopy, the resolution and depth of field of SEM is determined by signals obtained from the area scanned by the electron beam, and those signals are the result of the following [96]:

- Secondary Electrons (SE)—ejected from inelastic collisions with the sample surface. They provide topographical information and are more prevalent at lower electron energy. Auger electrons are a type of secondary electron that can be used to ascertain the surface chemistry of a sample via Auger Electron Spectroscopy (AES) [92], [97]
- Backscattered electrons (BSE)—ejected from elastic collisions with the sample surface. BSE provide compositional information about the sample, to include layers below the surface which is useful for identifying different phases or precipitates due to a difference in contrast on the SEM image [92].
- X-ray photons—ejected from the sample after a beam electron displaces an orbital electron, forcing another electron to de-excite to fill the vacancy [98]. The x-ray energy or wavelength is correlated to the element from which it was ejected, allowing the elemental composition of the sample to be determined, and giving them the name characteristic x-rays [92].

To capture the above signals, SEMs contain several common signal detectors arranged around the electron beam gun to capture them [92]. Figure 12c provides a visual aid of the types of interactions that occur when a sample surface is struck by the electron beam in a SEM.



(a) Primary components of a SEM. Adapted from [94], [99]. (b) Primary components of a TEM. Adapted from [100], [101]. (c) Interaction of the SEM electron beam with a sample surface and the products that result from it. Adapted from [94], [102]

Figure 12. SEM and TEM architecture and SEM interactions.

3. Energy-Dispersive Spectroscopy

To reiterate, x-ray are one of the products from the interaction of the electron beam and sample within SEM. Brandon and Kaplan discuss the importance of x-rays to materials characterization in [88]; the term characteristic x-ray is used since they have a very specific wavelengths or energies and are named K, L, M, or N depending on the orbital of the displaced electron. Collection of characteristic X-rays is dependent on electron beam energy, which must be carefully optimized to be high enough to ensure a sufficient volume

of the sample is excited and ejects x-rays but not too high otherwise the detector can become flooded with Bremsstrahlung radiation [92]. A good thumb rule is beam energy should be higher than the K excitation value of the heaviest element of interest, but lower than four times the threshold energy for x-ray excitation, which is when the signal-to-noise ratio starts to decrease [92]. Another reason to limit beam energy is loss of resolution—if a specific feature of a sample is the intended target, then a high beam energy may capture x-rays from both the target and surrounding region, which can lower the accuracy of the analysis [92]. EDS is a technique used in conjunction with SEM where the characteristic x-rays are collected and analyzed as function of energy (KeV) or wavelength (nm) to determine the elemental composition of a sample [92]. A typical EDS spectrum of AA 7075 in terms of energy is shown in Figure 13. If performed without a set of certified standards, the elemental composition from EDS is a standardless quantitative analysis [103]. Another source of concern regarding the accuracy of the EDS analysis (and one that can be amended via the use of a known standard) is fluorescent radiation, which is the secondary excitation of neighboring elements by the characteristics x-ray during its emission from the sample [92]. In addition, the accuracy of the EDS results depends on the following:

- The sample is polished and flat [104].
- The sample is homogeneous and infinitely thick compared to the interaction volume of the electron beam and sample [104].
- Appropriately selected electron beam current and voltage [92].

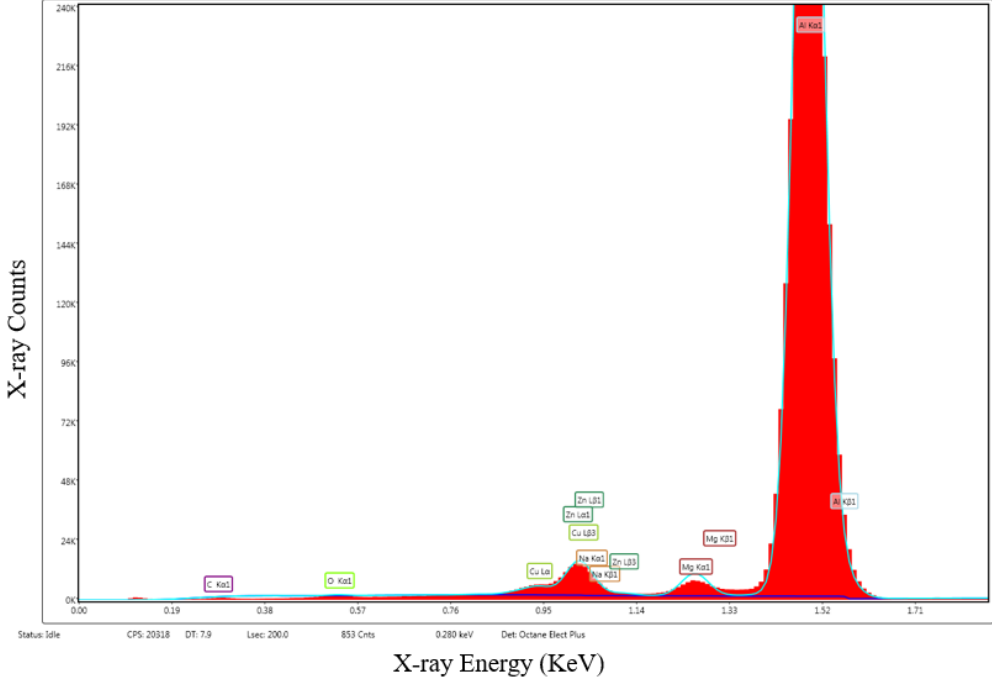


Figure 13. EDS spectra of AA 7075 in terms of energy (KeV), truncated to show the lower energy peaks.

4. X-ray Diffraction

In [19], [98], Ansell discusses the important role of XRD—a material’s crystal structure is critical to most of its materials properties and is determined from the diffracted radiation intensity plotted against a diffraction angle to form a XRD spectrum. When exposed to x-ray radiation, the atoms in a crystalline material scatter the radiation elastically at certain angles to the incident beam, and the scattering angle and intensity are functions of the wavelength, radiation, and crystal structure [105]. The chemical composition of the material can be inferred from the XRD spectrum if the primary element is known and by matching the other peaks from known standards [105]. The base equation for XRD is known as Bragg’s law, which relates the incident x-ray wavelength, lattice spacing, and diffraction angle [105]. The integer n in Bragg’s law is also called the order of reflection, and the spacing between lattice planes can be written as $\frac{d_{hkl}}{n}$ corresponding to the lattice plane with Miller indices $(nh nk nl)$ [105]. As a result, Bragg’s law can be

rewritten to reflect that the lattice spacing corresponds to a specific order (Equations 10 and 11) [105].

$$n\lambda = 2dsin\theta \quad (10)$$

$$\lambda = 2d_{hkl}sin\theta \quad (11)$$

In Equations 10 and 11, λ \equiv incident x-ray length, n \equiv order of reflection, d \equiv lattice spacing, and θ \equiv diffraction angle.

With Bragg's Law defined, it is now possible to correlate diffracted x-rays with the measured angle and discern lattice spacing, but not all reflections are permitted based on the geometry of the material [98]. Reflected x-rays interact both constructively and destructively with one another, and the result is allowed and disallowed reflections for each Bravais lattice [92], [105]. By rearranging Equation 11 and combining with Equation 1, a relation between the diffraction plane indices and the lattice parameter of the cubic crystal system is derived (Figure 14). In [19], a list of reflections for the various cubic crystal systems and the equation for determining the lattice spacing and lattice parameter for each system is developed (also shown in Figure 14). This diffraction spectrum or pattern is normally compared to known spectrums to identify the material by assessing the degree of fit and assigning confidence based on it [105].

$$\frac{\sin^2\theta}{(h^2 + k^2 + l^2)} = \frac{\sin^2\theta}{s} = \frac{\lambda^2}{4a^2}$$

Simple Cubic:

$s = 1, 2, 3, 4, 5, 6, 8, 9, 10, 11, 12, 13, 14, 16, 17, 18, 19, 20\dots$

BCC:

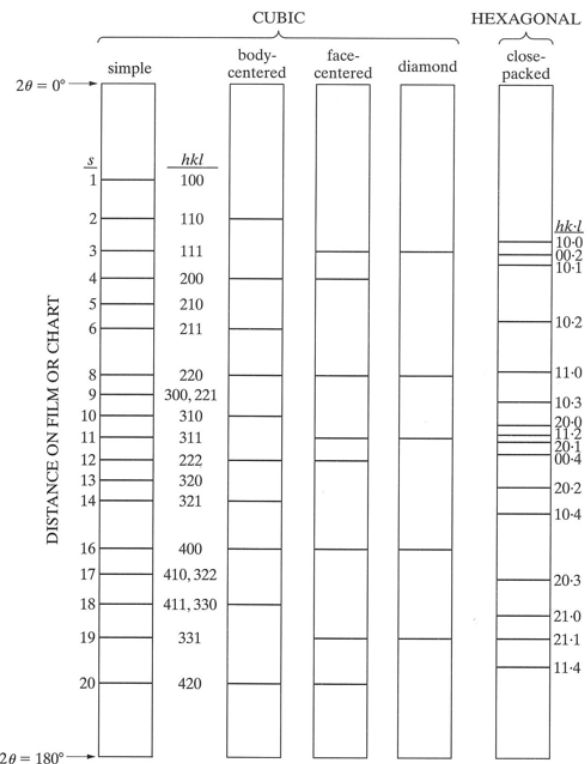
$s = 2, 4, 6, 8, 10, 12, 14, 16, 18, 20\dots$

FCC:

$s = 3, 4, 8, 11, 12, 16, 19, 20\dots$

Diamond Cubic:

$s = 3, 8, 11, 16, 19\dots$



Bragg's Law modified to identify the s -values and known peak locations for cubic crystal systems. Adapted from [105].

Figure 14. Allowed reflections for cubic crystal systems.

5. Digital Radiography and Computed Tomography

Digital radiography (DR) and computed tomography (CT) scanning are both NDI methods for inspecting a material for quality assurance, failure analysis, process control, and internal defects [106], [107]. DR is a two-dimensional scan that utilizes an x-ray tube and flat panel detector to capture scans of an object in real-time [101]. A CT scan is a three-dimensional rendering of the interior and exterior of an object that is constructed from hundreds or thousands of DR scans taken while the object is slowly rotated 360° in front of the flat panel detector [101]. As a result, a CT scan takes much longer to construct, but the ability to see the interior volume of an object allows for detection of porosity, cracking, and other internal flaws in a material [101]. A schematic showing similar setup, but different results, for DR and CT processes is shown in Figure 15.

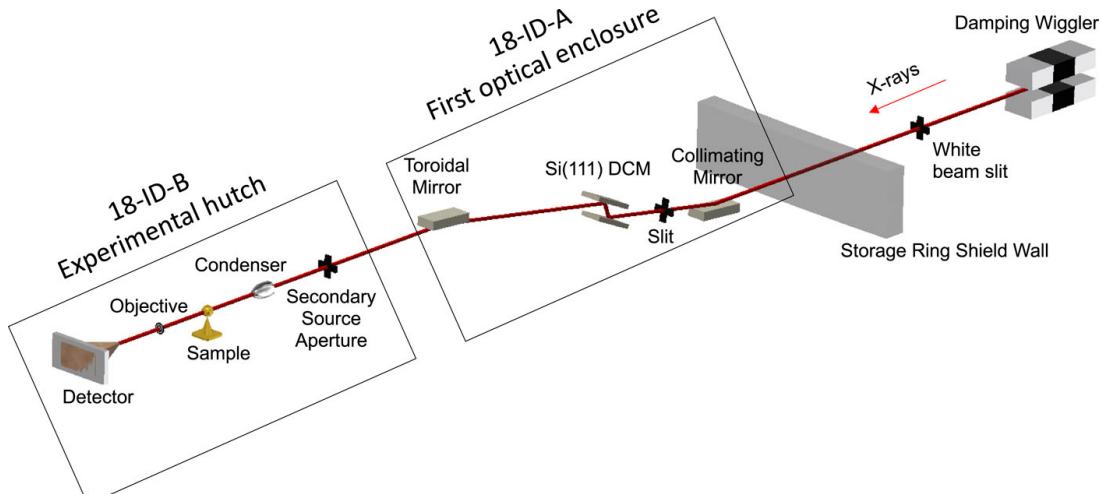


Schematic showing the formation of a (a) DR scan vice a (b) CT scan with the x-ray tube, object, flat panel detector, and computer system. Adapted from [107].

Figure 15. DR and CT scan formation schematics.

6. X-ray Nano-tomography

Nano-tomography, as its name suggests, is a form of CT that uses x-rays, but with resolutions on the nanometer vice micrometer scale. Unlike a traditional CT system, The 18-ID Full-field X-ray Imaging beamline (FXI) at the National Synchrotron Light Source-II (NSLS-II) incorporates more than just an x-ray source, target, and detector which allows for much higher resolution [108], [109]. Whereas a traditional CT system uses an x-ray tube, the FXI utilizes a 100 mm-period damping wiggler (DW100) as the x-ray source [110]. Following the wiggler is a collimating mirror to focus the x-rays into the necessary energy bandwidth for measurements, a Si (111) double crystal monochromator (DCM), toroidal mirror, aperture, condenser, sample stage, objective and final detector, shown in Figure 16 [111]. The detector at the end is a transmission x-ray microscope (TXM) with an x-ray energy range 4.5–15 keV range which achieves a spatial resolution of 30 nm [110].

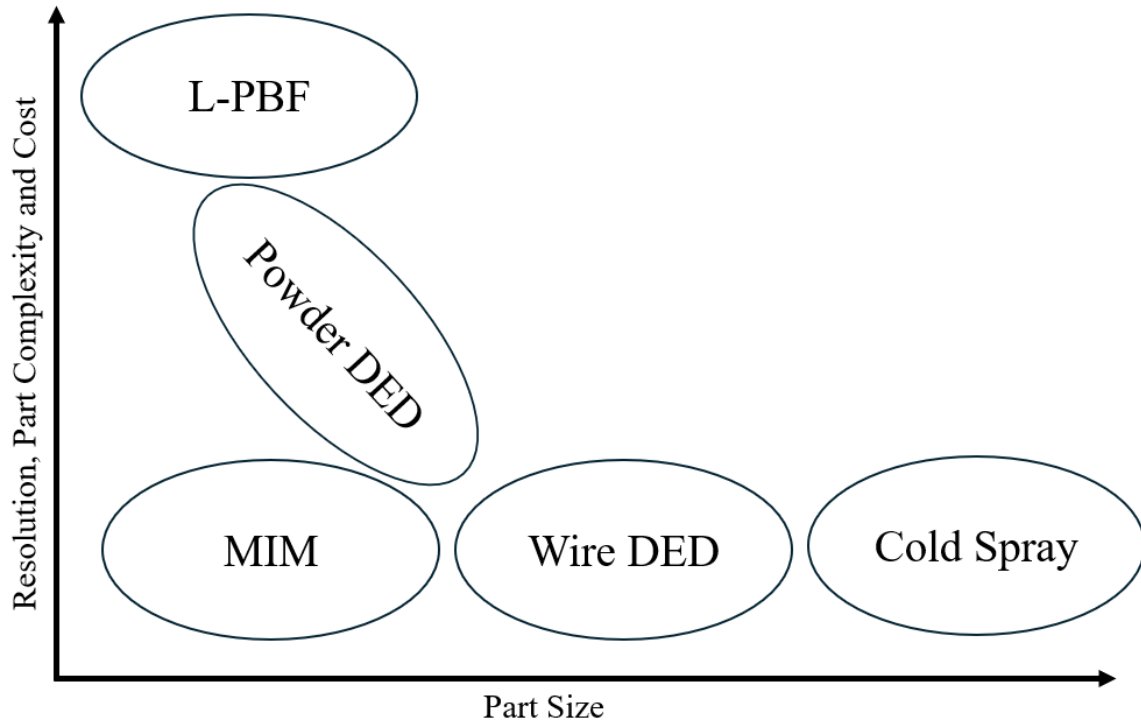


Source: [111].

Figure 16. 18-ID Full-Field X-ray imaging beamline (FXI) construction.

C. OVERVIEW OF METAL ADDITIVE MANUFACTURING

Metal additive manufacturing (M-AM) has rapidly evolved from a tool for prototyping to an established method to print complete components for a variety of applications [112]. M-AM has been used with steels, aluminum, titanium, and nickel alloys and has significantly decreased part costs at low part production numbers, allowing rapid development cycles while matching a range of size and resolution requirements [112], [113]. The advantages of M-AM over traditional fabrication processes include complete material utilization, reduced assembly steps, the ability to produce complex geometries, and the timely production of critical, one-off parts needed for urgent repairs [44]. The last advantage is particularly valuable to the military and defense sectors—such parts are often not readily available from the original equipment manufacturer (OEM) and cannot be produced because it would be cost-prohibitive. According to the literature, M-AM parts have been used for closed-cycle liquid rocket motors, high-temperature turbine blades, and lightweight CubeSat components [114], [115], [116]. Biomedical applications such as metal implants can benefit from total geometric control to form biomimetic bone-like structures [117]. Four major categories of M-AM are as follows: metal injection molding (MIM), directed energy deposition (DED), gas dynamic cold spray (cold spray), and laser powder bed fusion (L-PBF) [66], which are summarized in Figure 17.

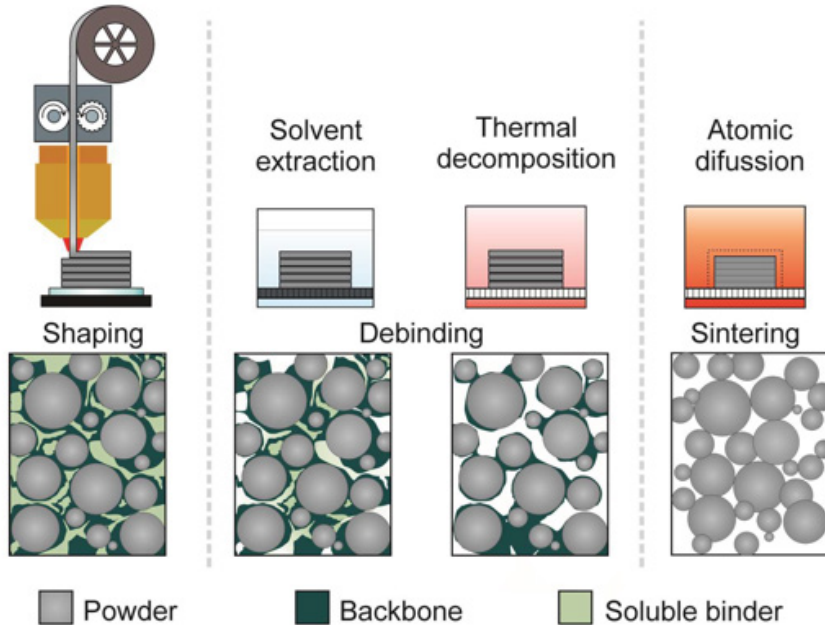


Adapted from [118].

Figure 17. Comparison of resolution, part complexity, cost, and part size among the common M-AM processes.

1. Metal Additive Manufacturing Methods

Now that a brief overview of M-AM has been provided, the four main categories and the method used in the laboratory research shall be discussed in further detail. In [119], [120], MIM methods are characterized by a four step process—mixing, injection molding, debinding, and sintering (Figure 18)—and are advantageous due to their ability to produce small and complex parts at reduced costs. Metal is mixed in with a binding agent to form a rod feedstock which is then injected into a crucible at high pressure to form the initial part geometry [121]. After printing, the binding agent is removed via the debinding and sintering process, and the part shrinks by 20–30% to a final density of ~97% [121].

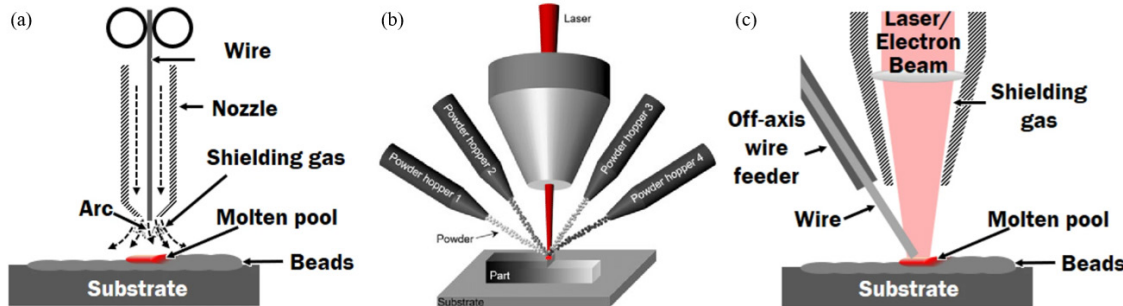


Source: [122].

Figure 18. Four steps of a MIM process.

DED systems utilize powder or wire as the feedstock and either an arc / plasma, laser, or electron beam to melt the feedstock during deposition, as seen in Figure 19a [122], [123]. A type of DED called wire arc additive manufacturing (WAAM) is a versatile and low-cost method of M-AM because it utilizes a wire arc to fuse metallic wire to a base plate, making it highly analogous to arc welding processes [46], [123], [124]. WAAM is also advantageous due to its high deposition rate and large build volume, allowing for building large structures on short lead times [46]. Deposition rates of several kg per hour are achievable for aluminum with both high energy and materials savings [125]. Lasers are a common heat source for DED processes with systems that are designed to melt either powder or wire feedstock [126]. Laser DED with powder feedstock offers improved resolution over WAAM, but at the expense of speed and cost [126]. Newer powder DED systems have multiple powder streams, allowing for the printing of a component with multiple alloys without having to swap out the feedstock (Figure 19b) [121]. Another challenge associated with powder-based systems is health concerns—powders are usually $< 100 \mu\text{m}$ in size and thus require careful control to avoid health, environmental, and

explosion hazards [127]. By using wire instead of powder (Figure 19c), DED systems can eliminate the hazards associated with powder and also realize important cost savings since powders are generally much more expensive than wire feedstock [128].



Schematics of (a) WAAM (adapted from [129]), (b) powder DED (adapted from [121]), and (c) wire DED processes (adapted from [129]) showing the feedstock, heat source, and deposition.

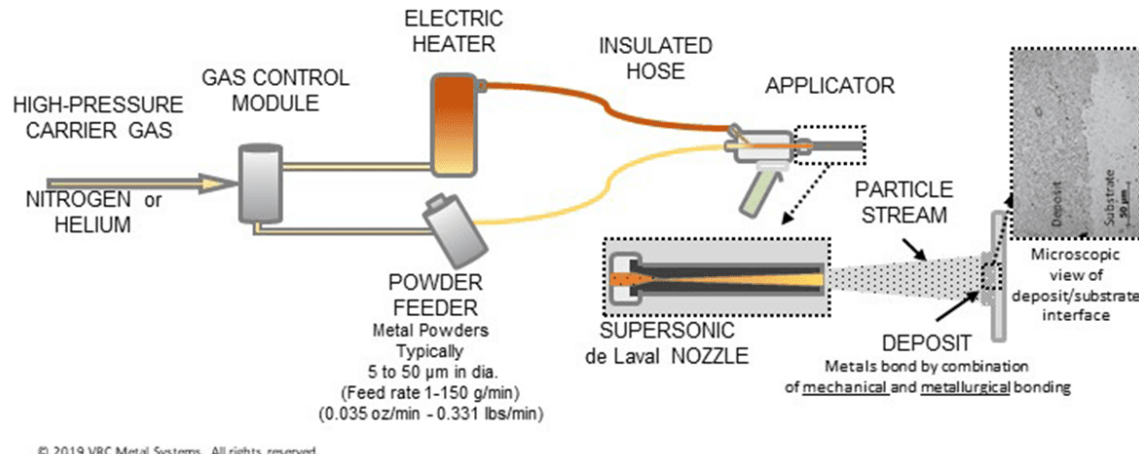
Figure 19. DED process schematics.

Cold spray is a low temperature process where metal powders are bonded to a substrate and itself via kinetic energy; the powders are slightly heated to 300–500°C and accelerated to supersonic speeds through a de Laval converging-diverging nozzle before impact with the print area (Figure 20) [130], [131]. To successfully bond, the metal powders must be accelerated to the critical velocity, which is a function of the powder's material properties, process gas used, nozzle used, and distance to the substrate [130], [132], [133]. The two process gases most used are nitrogen (N_2) and helium (He); N_2 is favorable due to its lower cost and availability, but He is favorable due to improved deposition and properties with certain alloys [134]. However, cold spray using compressed air is possible and a much cheaper and logically easier alternative [134]. Cold spray is of interest to the DON due to its ease of application and improved corrosion resistance when applied to surfaces, particularly in a marine environment [130].



THE COLD SPRAY PROCESS

SUPersonic Particle Deposition

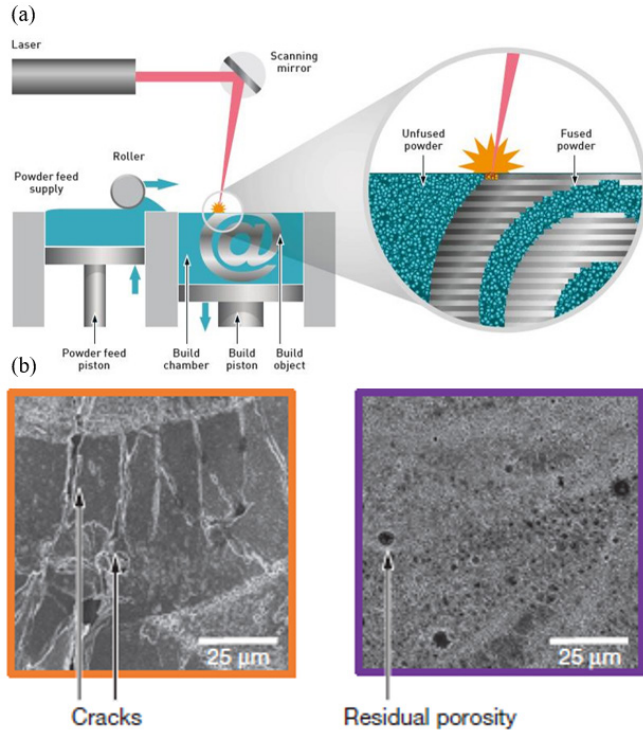


© 2019 VRC Metal Systems. All rights reserved.

Source: [135].

Figure 20. Overview of the cold spray process.

The most common process of M-AM is L-PBF, which utilizes lasers and very fine powders to build parts by sequentially depositing a fresh powder layer, using the laser to fuse the powder to create the new layer on top of the one, and then repeating the process (Figure 21a) [67], [136], [137]. Current state-of-the-art systems that use L-PBF processes can produce $\sim 150 \mu\text{m}$ feature sizes with layer heights down to $30 \mu\text{m}$ using very fine powders [136]. L-PBF systems are well suited to produce Inconel 718, stainless steel 316, and titanium alloys [136]. Although the build rates are low and build sizes are limited, there are many applications that are suitable for L-PBF [67], [112], [136]. However, the thermal cycles introduced by rapid laser rastering cause undesirable cooling rates that can lead to hot cracking, porosity, and warping in many light metal alloys, particularly 7XXX series aluminum alloys (Figure 21b) [5], [67], [136], [138].



(a) Schematic of a typical L-PBF system showing laser, roller, powder deposition process, build chamber, and powder fusion process. Adapted from [139]. (b) Common defects found in 7XXX aluminum alloys from L-PBF processes. Adapted from [5].

Figure 21. L-PBF process and defects.

In addition, elements with low boiling points such as Zn and Mg, both of which are present in high concentration within 7XXX series aluminum alloys, tend to vaporize under the laser beam and cause degradation of the alloy [58], [59], [67]. Si, titanium carbide, and other additives have been successfully employed to print crack-free AA 7075 via LBPF systems, but the modified alloy has inferior materials properties to that of the pure alloy [4], [5], [60], [140]. Another way to counteract the loss of volatile alloying elements, particularly Zn and Mg, is by enriching the feedstock with excess quantities of those elements [66]. One way of overcoming the challenge of solidification and liquation cracking using L-PBF is heating the substrate to arrest the normally high cool down rates, but this can be undesirable due to powder sintering, reactivity, and safety / health concerns [141]. It is highly desirable to be able to print pure AA 7075 at high resolution with no additives or other alloying components, but the methods previously described are currently unable to do so.

Unlike MIM, DED, and L-PBF processes, the liquid metal jet printing (LMJP) process can be used to 3D print AA 7075 alloy at full strength and ductility. Unlike L-PBF techniques, the high local temperatures from laser spot interaction with powder surfaces is avoided, which minimizes vaporization of Mg and Zn [136], [141]. The M-AM printer used in this research is the Additec (formerly Xerox) ElemX, shown in Figure 22a. The ElemX uses a 9.07 kg (20 lb.) aluminum wire spool as the feedstock, which is fed into a resistively heated crucible and melted. Pulsed external electric pulses are applied to the melt pool by a coil surrounding the crucible, inducing currents in the melt pool without direct contact [142]. The induced currents interact with the external magnetic field from the coil which pushes the material through a graphite nozzle via Lorentz forces [142]. The result is a jet of molten droplets of ~0.5 mm diameter traveling at speeds up to 3 m/s that form splats upon impact with the heated substrate. The system has a constant argon flow rate of 7 L/min fed at the top of the crucible that protects the melt pool and flows out around surrounding the graphite nozzle with an opening of 0.5 mm. After printing is complete, the samples are submerged in water and readily come off the plate due to thermal contraction without the need for machining. A schematic representation of the ElemX printer and droplet deposition is shown in Figure 22b-d.

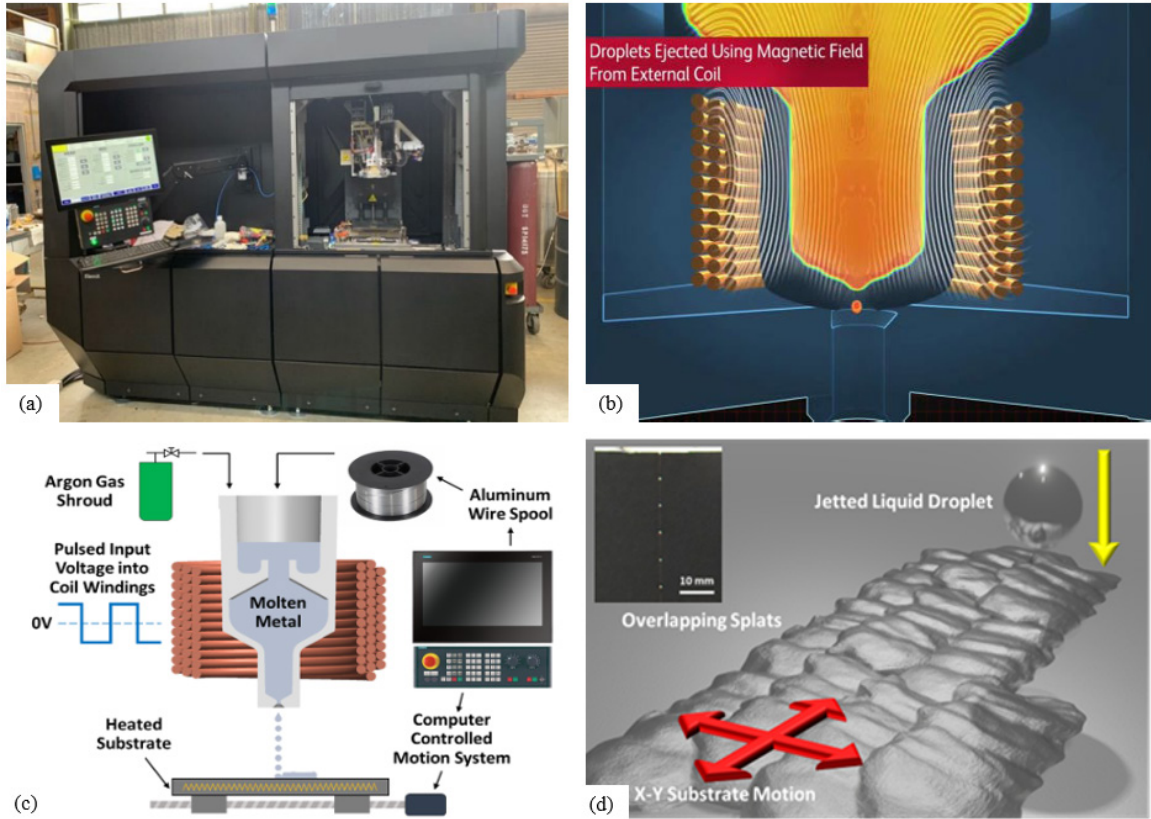


Figure 22. Additec ElemX printer overview.

A printer crucible temperature setpoint of 775°C maintains the nozzle temperature at ~700°C and substrate temperature setpoint of 575°C maintains the substrate temperature at ~500°C, both of which are monitored during printing (Figure 23a-b). The nozzle temperature is crucial to minimize Zn losses and alloy degradation while still providing sufficient margin above the AA 7075 liquidus temperature of 635°C. Using a simple model assuming 1D heat transfer via conduction (Figure 23c), the thermal history of splats was estimated as a function of substrate temperature [144]. The interface temperature of the splat was calculated using the heat conduction and energy conservation equations (Equations 12 – 14) [144]. For most of the print, the droplets are deposited on the part rather than the substrate, so the thermal properties of the substrate alloy were used [144]. From the graphs of the splat thermal history (Figure 23d), only a substrate temperature of

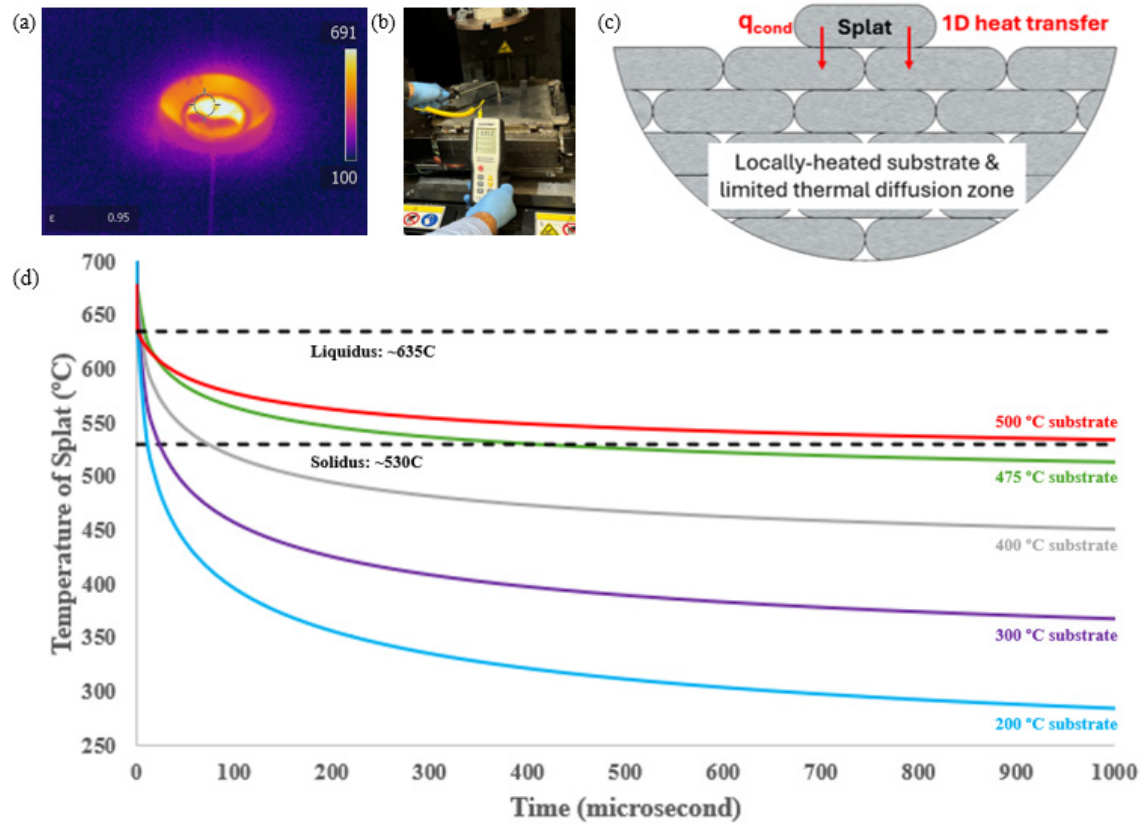
500°C maintains interface temperature (from Equation 14) above the solidus temperature for a prolonged period. Therefore, the lower cooling rate of the droplets on the 500°C substrate should result in good metallurgical bonding throughout the microstructure with no hot cracking [142].

$$T(x, t) - T_d = \frac{\Lambda_0}{\sqrt{\pi Dt/8}} e^{-2x^2/Dt} \quad (12)$$

$$\Lambda_0 = \frac{\rho_1 C_{pl}}{\rho_s C_{ps}} \delta (T_m - T_i) \quad (13)$$

$$T(0, t) = \frac{\frac{\rho_1 C_{pl}}{\rho_s C_{ps}} \delta T_m + \sqrt{\pi Dt/8} T_d}{\frac{\rho_1 C_{pl}}{\rho_s C_{ps}} \delta + \sqrt{\pi Dt/8}} \quad (14)$$

In Equations 12–14, D ≡ the thermal diffusivity of the part, t ≡ time, T_d ≡ temperature of the substrate (assumed to be the same as the part temperature), T_m ≡ is the melting point of the droplet, $T(0, t)$ ≡ the interface temperature between splat and part (assumed to be temperature of the whole splat due to the fast heat diffusivity), ρ_l ≡ density of droplet, ρ_s ≡ density of the part, C_{pl} ≡ the specific heat capacity of the metal droplet, C_{ps} ≡ the specific heat capacity of the part, and δ is the thickness of the splat.



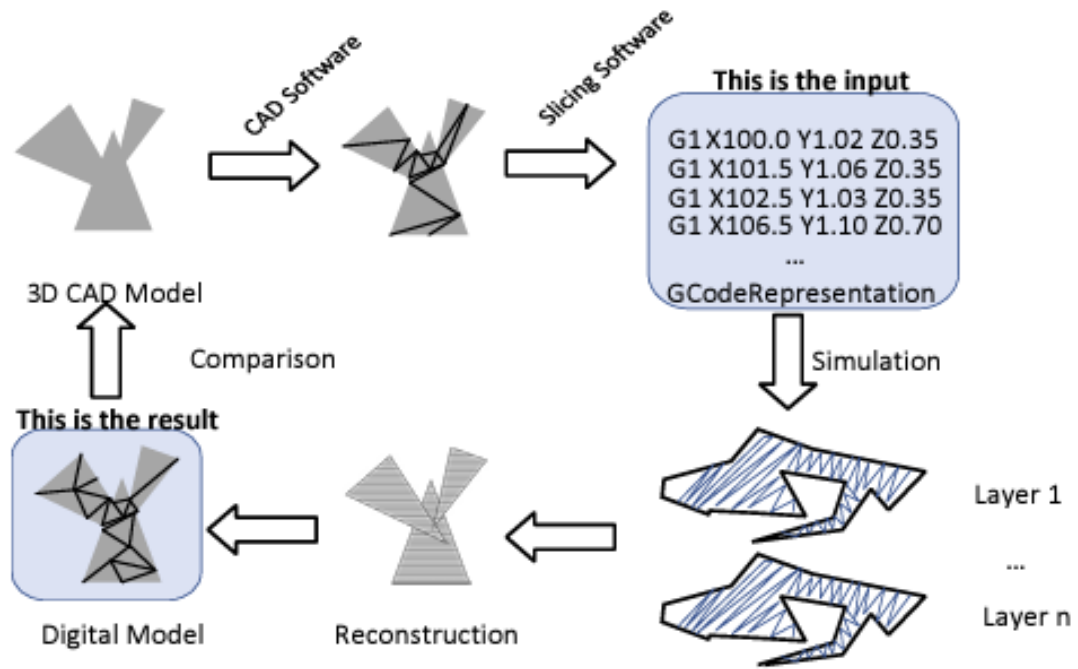
(a) Printer nozzle temperature measured with an infrared camera. (b) Substrate temperature measurement using a contact probe. (c) Thermal losses to the substrate. (d) Estimated cooling curves for substrate temperatures of 200–500°C.

Figure 23. Overview of ElemX thermal settings and cooling curves.

2. Printer Control and Print Customization

The starting point of any 3D print operation is the generation of the object to be printed. In [145], Brown et. al. describe methods of obtaining the object, including a traditional drawing approach using computer-aided drafting (CAD) software, such as SolidWorks or Fusion 360, or rendering into a printable file with the aid of a 3D scanner. The end requirement is a stereolithography (STL) file, which is the input for the next step of the printing process called slicing [145]. The slicer software splits the 3D mesh into multiple horizontal layers which are iteratively printed starting with the initial layer on the printer substrate [146]. Subsequent layers are printed on the initial layer until the print is complete as shown in Figure 24 [146]. During the slicing process, the 3D object STL file is converted into geometric code, also called G-code [147]. G-code are preparatory codes

for CNC machines and 3D printers, and they provide instructions to the machines on movement, speed, angle, position, feed rate,, and many more depending on the type of machine [148].



Source: [146].

Figure 24. Process flow of 3D printing.

In addition to G-code, many CNC and 3D printer machines utilize miscellaneous or machine code (M-code), which covers all auxiliary functions the machine executes that are not covered by G-code [149]. In total, there are over 100 G-codes (G0–G99) and 100 M-codes (M0–M99), but not all machines are compatible with all these codes. Both G-code and M-code positions can be interpreted in both absolute and relative coordinates. Commonly used G-code and M-code commands for printing movements are shown in Table 6.

Table 6. Commonly used G-code commands.

Command	Format	Notes
G0 (rapid move) / G1 (linear move)	G{0/1} X{xxx} Y{yyy} Z{zzz} E{eee} F{fff}	X, Y, Z ≡ print location (mm) E ≡ extruder position (mm) F ≡ feedrate (mm/min)
G4 (dwell)	G4 P{ppp}	P ≡ dwell time in milliseconds
M0 (stop or unconditional stop) / M1 (sleep or conditional stop)	M{0/1} P{ppp} or S{sss}	P ≡ time to wait in milliseconds S ≡ time to wait in seconds

Adapted from [150].

According to [151], the ElemX printer and its slicing software, Builder, use absolute positioning with the XY origin located at the center of the substrate, z origin at the top surface of the substrate, and E origin is located at the wire position when starting a print job. The M1 code resets the E position to zero before a layer change. Additionally, the absolute E position of a movement is cumulative, and the extrusion amount is the difference in E from the previous state [151]. When the E position of a state is modified, all future E positions must be offset by ΔE to maintain future movement's original extrusion amounts [151]. ΔE is defined as the total modification of E position until the next E position reset (M1) [151]. ΔE can be positive or negative. Future movements' E position will add ΔE to retain all future original extrusion amounts [151].

In Builder, the user can change printing settings such as infill percentage, speed, and resolution in the slicer software to develop the final G-code for a print, which is in the code called MPF [151]. The MPF file is post-processed by the ElemX printer host workstation into another compatible format called SPF in layer chunk sizes defaulting to five. The SPF file is interpreted by the printer and translated to physical printing movements. ElemX Builder generated MPF files contain G-code comments prefixed with “;.” These comments can include descriptions of feature types and print settings [151].

Feature types provide information on the structural or printing intent of the following G-code until a new feature type is found [151].

The LMJP process of the ElemX allows for printing unique geometries, including hollow aluminum parts that can float in water. The size of the ejected aluminum droplet is set during the calibration step of ElemX startup, but it can be manually changed by the operator during a print ranging from $\sim 250\text{--}500\ \mu\text{m}$ [151]. Doing so is usually not recommended since jetting can become unstable. However, the ability to vary the droplet size opens the door to printing part with customized infills. ElemX Builder currently does not have an option for variable density infill in user defined regions; therefore, previous research to print parts with variable density infill involved a series of prints with infill manually set by the operator [152], [153]. Examples of variable infill prints accomplished via a series of print steps are shown in Figure 25.



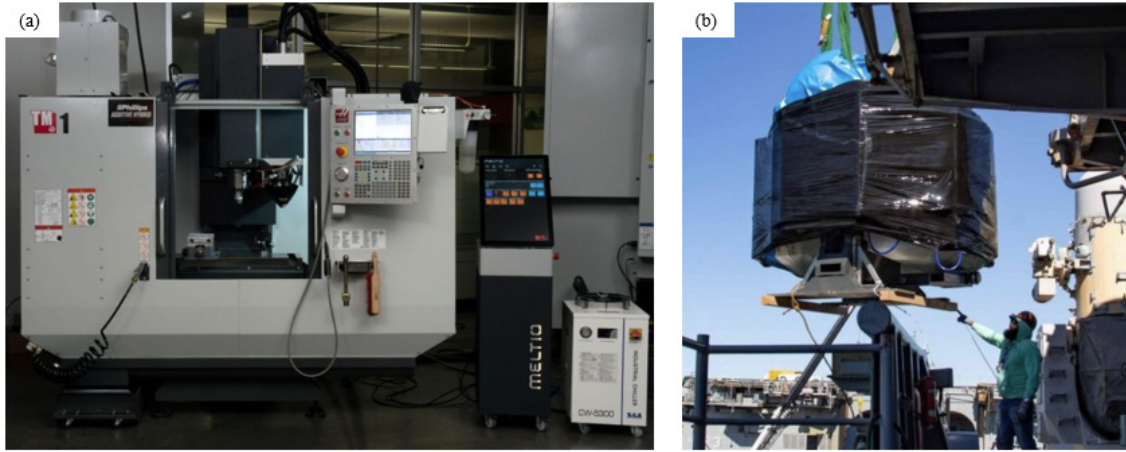
Adapted from [152], [153].

Figure 25. Variable density prints from previous thesis research.

3. Metal Additive Manufacturing in the DON

M-AM is an important technology to help expedite both the repair and construction of ships and submarines for the DON. Multiple U.S. defense media outlets claim accelerating both is absolutely critical in the Era of Great Competition—the DON needs to produce two VIRGINIA class and one COLUMBIA class submarine per year on top of the requirement to maintain the current Fleet [154]. Unfortunately, the DON has challenges meeting the

peacetime maintenance requirements for the current Fleet. According to recent GAO reports, all of the repair activities across the DON saw a combined 38,900 days of delays which equates to the loss of the operational availability (Ao) of approximately 15 ships or submarines from 2014 to 2020(Ao is a metric used to quantify the readiness of platforms by the DON) [155], [156]. With no specialized teams, ships, or facilities specifically for battle damage repair, the DON would rely on the shipyards and repair activities for any such repairs, which would only exacerbate the delay seen right now [155], [156]. Therefore, it is imperative for the Navy to embrace M-AM and other technologies to both improve the performance in shipyards and repair facilities while simultaneously developing battel damage repair capabilities [154]. Another huge advantage of M-AM is the ability to push repair capabilities to individual ships via expeditionary, containerized machines to allow for ships to print repair parts as needed. By using such machines, the DON can help reduce the pressure on the supply system and overcome the “tyranny of distance” by allowing ships to quickly print and machine what they need to stay in the fight. A success story highlighted by U.S. defense media is the installation of a Haas TM1 machine with a Meltio print head aboard the USS BATAAN in January 2023 (Figure 26) [157], [158]. The TM1 combines a 5-axis subtractive machining capability with the Meltio laser wire DED print head, allowing the machine to print and machine 316L stainless steel (SS) [157], [158]. In August 2023, DON sailors and civilians worked together to perform a crucial repair on BATAAN’s deballasting system, saving both money and Ao and demonstrating the value of having M-AM technologies onboard ships [159].



(a) Haas TM1 platform with 5-axis subtractive capability and a Meltio print head. Adapted from [157]. (b) The same machine being craned aboard for installation aboard USS BATAAN in early 2023. Adapted from [157], [158].

Figure 26. USS BATAAN M-AM capability.

To underscore the current importance of educating military officers in the future role of M-AM in the DON, NPS invested heavily in experimenting with M-AM technologies in expeditionary environments. To do so, NPS participated in two Fleet exercises—SALVAGE EXERCISE 2024 (S24) and TRIDENT WARRIOR 2024 (TW24). The author’s involvement in both exercises is summarized in Table 7. S24 solely used M-AM in addition to post-processing and subtractive technologies for BDA/R. TW24 focused on identifying and producing critical parts for the joint force through the establishment of a JAMC with a focus on parts meeting the following criteria [160]:

- Long lead time in the supply system.
- High cost due to scarcity.
- High cost due to the need to buy the next higher assembly.

Table 7. Author's roles in Fleet exercises utilizing M-AM technologies.

Date Range	Exercise	Role
May 20–June 3, 2024	S24	XSPEE3D subject matter expert (SME)
July 5–11, 2024	TW24	Lead NPS student at JAMC to establish initial battle rhythm. SME for M-AM and materials characterization
July 17–26, 2024	TW24	Lead NPS student and XSPEE3D SME

III. METHODOLOGY

The laboratory research was performed using processes that are categorized as follows: liquid metal jet printing, sample preparation, materials testing, and materials characterization.

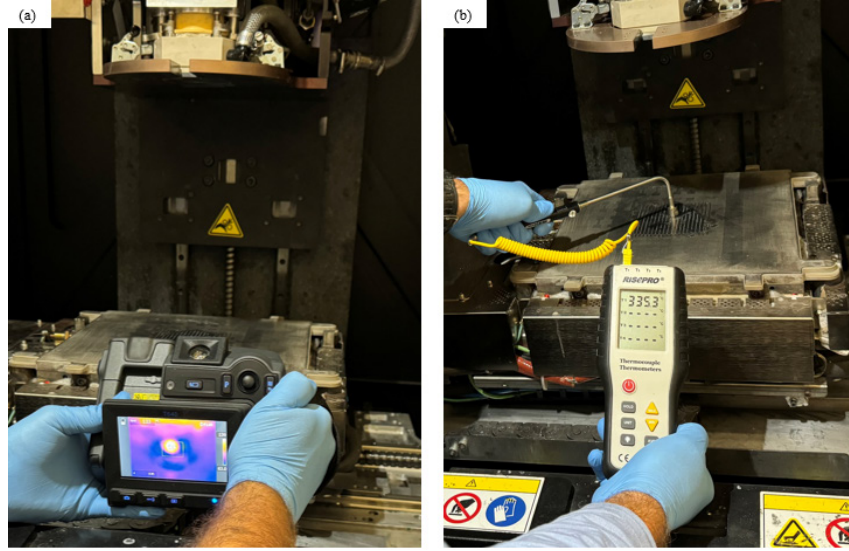
A. LIQUID METAL JET PRINTING

The laboratory research for this dissertation was performed using the Additec (formerly Xerox) ElemX, a printer based on the LMJP process. AA 7075 wire from the 9.07 kg (20 lb.) spool was installed on the ElemX, melted in the crucible, and ejected onto the heated substrate into the desired geometry. LMJP with the ElemX is accomplished via five important steps:

- Startup: aluminum alloy wire spool installation, print head nozzle preparation and installation, and auxiliary support systems (chill water, argon, and low-pressure air) aligned.
- Burn in: after startup, the “burn in” program is run to prepare the graphite nozzle for printing operations by ensuring the nozzle tip is wetted and ejecting aluminum droplets in a straight, steady stream.
- Calibration: after burn in, the “calibration” program is run to measure the amount of aluminum ejected after 10,000 pulses. The droplet size is then adjusted to only eject 1.45 ± 0.05 g of aluminum per 10,000 pulses.
- Printing: after calibration, the desired print, an MPF file, is loaded into the printer queue and started.
- Cooldown and shutdown: printed parts are removed from the substrate via thermal shock after submergence in water and the printer head and substrate is cooled down.

A full standard operating procedure (SOP) for the ElemX is contained in Appendix A with much greater detail on the 5 steps outlined above. Printer head and substrate temperature

setpoints during printing were set to obtain the desired nozzle temperature of $\sim 700^{\circ}\text{C}$ and substrate temperature of $\sim 500^{\circ}\text{C}$. The actual nozzle and substrate temperatures were verified during printing using a FLIR T640 infrared camera (working distance of 300 mm and a frame rate of 30 Hz) and a Risepro temperature probe (maximum rated temperature of 600°C), respectively, as shown in Figure 27.



(a) FLIR T640 camera used to verify nozzle temperature and (b) Risepro temperature probe used to verify substrate temperature during printing.

Figure 27. ElemX print head and substrate temperature monitoring.

The feedstock of the ElemX is a spool of aluminum wire; the printer is optimized for A356 / AA4008, but the research of this dissertation was mostly centered on printing AA 7075 with and without additives. Two major challenges were encountered during the printing of this alloy that shall be elaborated on more thoroughly:

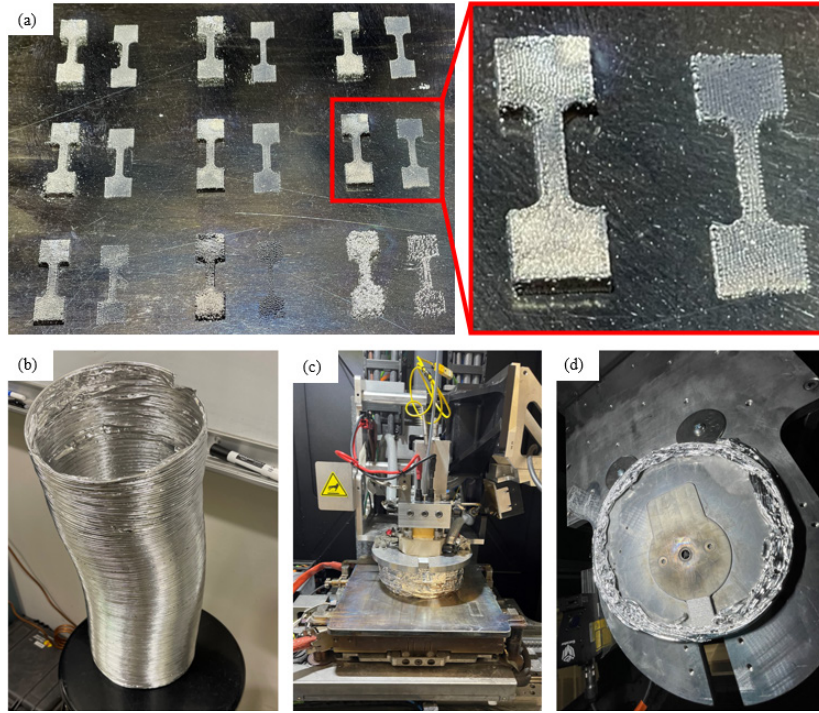
- Oxidation control during AA 7075 printing operations.
- Sourcing a reliable feedstock for printing both pure AA 7075 and with additives incorporated.

1. Oxidation Control

As previously stated, the ElemX LMJP was designed and optimized to print the A356 / AA 4008 alloy. Therefore, there was no need for an enclosed build volume with atmospheric control; a constant flow of argon from the print head with the droplets was sufficient. Unlike AA 4008 and A356, AA 7075 is very sensitive to oxidation, particularly at higher temperatures. Since the ElemX does not have an enclosed build chamber, an additional Kapton shroud was built around the print head to prevent oxidation of the part during printing. The shroud proved successful at both withstanding the high substrate temperatures and for trapping argon over the print area—the argon level was measured to be ~99% within the shroud using a handheld tester (Forensics Detectors, FD-311-Ar).

a. *Gen 1 Containment—Stove Piping*

The first attempts to print miniature tensile specimens identified the oxidation concern shown in Figure 28a, which were printed with no attempt to create an atmospheric containment system. In addition, these specimens were printed with AA 7075 wire fragments before the AA 7075 wire spool was obtained. By continuously opening the print head to feed in wire strips, the oxidation of the samples was exacerbated. The first attempt to control the atmosphere around the samples during printing involved commercially procured stove piping that was attached to the underside of the ElemX print head, as shown in Figure 28b–d. Although the material was able to withstand the high substrate temperatures and did not introduce any foreign contamination into prints, the piping sections were single use only and did not adequately exclude oxygen from the print area during testing. Additionally, the stove pipe sections were compressed so much that the wire frame of the material was scouring and gouging the ElemX substrates and not allowing for reuse. Tensile and microhardness results of the samples were well below expected values for AA 7075 and are not included in this study. In fact, many of the samples were weak enough to break by hand and tensile testing was not possible or necessary.



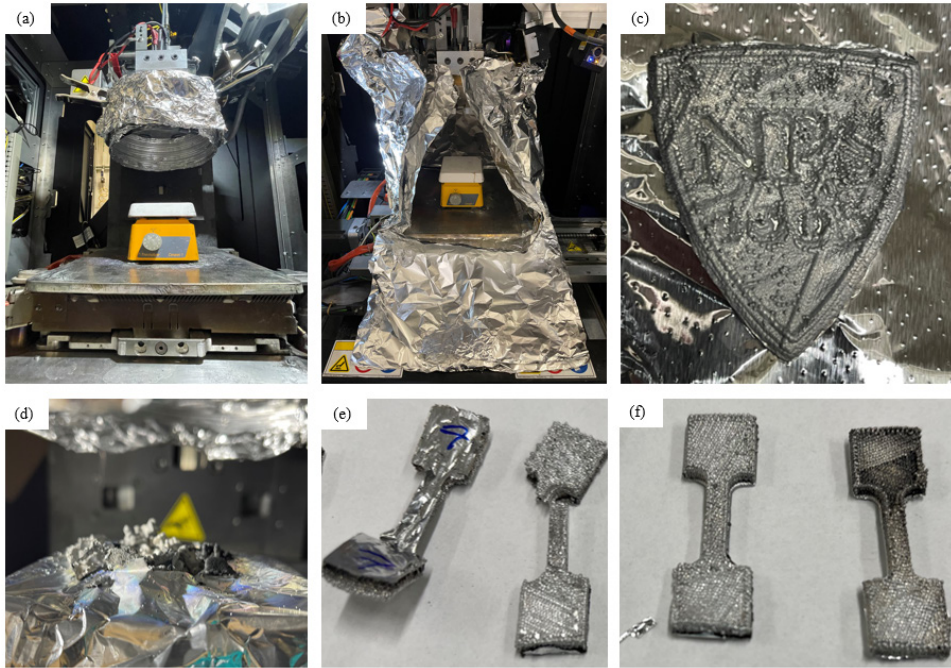
(a) Oxidation of AA 7075 miniature tensile specimens and (b–d) Gen 1 argon containment fabricated from commercially procured stove piping

Figure 28. Gen 1 containment.

b. Gen 2 Containment—Custom Substrate

After the unsuccessful attempts with the Gen 1 containment, a different approach was needed to better control the atmosphere and eliminate oxidation of AA 7075 prints. For the Gen 2 design, a custom substrate was fabricated by permanently attaching a small laboratory hot plate to the top of a decommissioned ElemX substrate as seen in Figure 29a–b. The hot plate had its own plug for power, so the substrate heater of the ElemX was not needed, which vastly decreased the time required to prepare the ElemX for printing samples. However, the main advantage and rational for the Gen 2 design was the hot plate was small enough to fit within the stove piping utilized in the Gen 1 containment. By keeping the hot plate inside the stove piping and wrapping the substrate and print head in aluminum foil, the theory was sufficient argon would be trapped to produce a noticeable reduction in oxidation of the AA 7075 prints. Since the surface of the hot plate was ceramic, it was not possible to print directly to the hot plate for fear of damaging it, and a method was needed to safely remove samples for analysis. Therefore, a variety of different hot plate surfaces were investigated to include

thicker steel plates and aluminum foil with stability on the hot plate the main challenge. Ultimately, aluminum foil was selected due to the ease of molding the foil around the hot plate to secure it as well as its high thermal conductivity. However, printing on foil (and on all other surfaces) introduced serious defects into the prints since it tended to shift and distort during printing as seen in Figure 29c–e. Additionally, the oxidation of AA 7075 was reduced, but not eliminated as seen by the darkening of the tensile specimens in Figure 29f. Follow-on printing and atmospheric testing with an argon probe confirmed that argon levels were elevated, but not high enough to sufficiently exclude oxygen from the immediate print area. Therefore, a better containment system was needed.



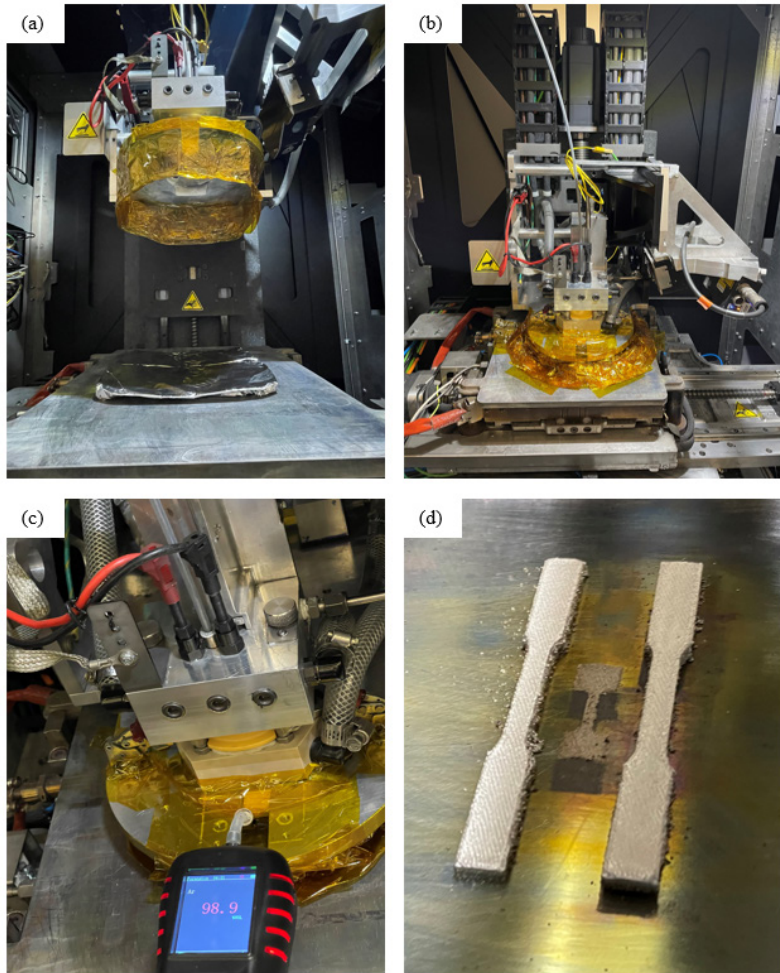
(a–b) Gen 2 argon containment and (c–f) samples produced utilizing the Gen 2 system.

Figure 29. Gen 2 containment.

c. ***Gen 3 Containment—Kapton Tape Shroud***

The Gen 2 containment showed a slight improvement in atmosphere control, but the smaller hot plate proved unsuitable for use since larger parts could not be produced. High temperature Kapton tape, able to withstand the expected substrate temperatures of 475–500°C

for short periods of time, was procured. The tape was wrapped around the print head such that the adhesive would not encounter the substrate and generate fumes which would be both a hazard to the ElemX operator and possibly introduce containments into the prints. The tape was used to cover all gaps on the top of the print head and was formed into a compressive shroud that would ride along the substrate during printing, ensuring maximum argon containment, as shown in Figure 30a–b. Atmospheric testing with an argon probe showed nearly 99% argon in the print area was sustained during printing at all areas immediately underneath the print head, as shown in Figure 30c. As a result, samples were printed to the sizes specified in ASTM B557M-15 with no evidence of oxidation due to the success of oxygen reduction from the printing area (Figure 30d). However, the nickel coated bronze plate that was the original substrate supplied by the manufacturer proved to be incapable of heating higher than 475°C despite raising the setpoint of the heater controller to the maximum limit of 600°C. These substrates were only able to hit the required temperatures on the first two or three uses. Exposure to high temperatures and subsequent quenching to remove samples caused warping of the substrates. The warping resulted in uneven contact with the underlying substrate heater, resulting in lower substrate temperatures, as well as undesirable warping in the samples. Temperatures higher than 475°C were needed to print AA 7075 to full strength, requiring a substrate able to repeatedly heat up to that temperature without warping.



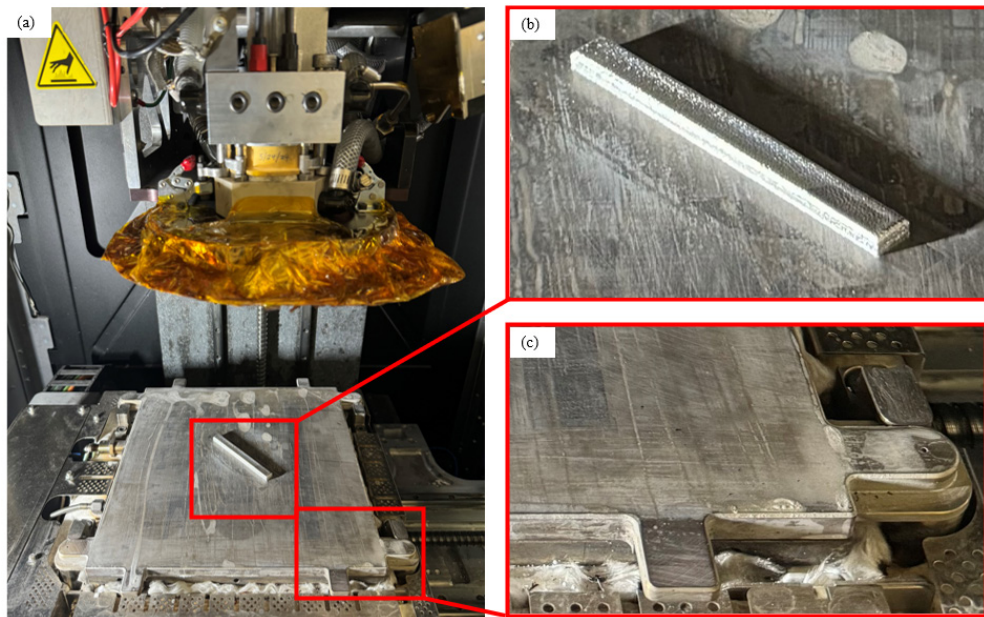
(a–b) Gen 3 argon containment, (c) high argon concentration under the Kapton tape shroud, and (d) high quality samples produced.

Figure 30. Gen 3 containment.

d. Gen 4 Containment—Kapton Tape and Steel Substrate

The Gen 3 containment finally overcame the challenges of printing samples to the dimensions required by ASTM B557M-15 for tensile testing. However, the warping and lower temperature limits of the nickel coated bronze substrates were obstacles to printing AA 7075 samples to full tensile strength and ductility. A stainless-steel substrate and improved substrate heating system was acquired through Additec, which had the dual benefits of a faster heat up rate and higher temperature limit. The new stainless-steel (SS) substrates, used in conjunction with the Kapton tape shroud in Gen 3, produced high quality samples free of oxidation and warping as seen in Figure 31a–b. The new substrates are

distinguishable from the older ones by the four metal tabs around the perimeter (two in front and two in back) that also permitted easier substrate removal and quenching (Figure 31c). Use of the stainless-steel substrate required the application of an adhesion layer prior to printing; the residue from this layer was easily removed after each print via mechanical filing and sanding.



(a) Gen 4 argon containment, (b) high quality samples produced, and (c) closer view of stainless-steel substrate.

Figure 31. Gen 4 containment.

2. Aluminum Wire Preparation

The second challenge of printing AA 7075 was obtaining satisfactory feedstock for the ElemX. This challenge was significant since AA 7075 is not an easily weldable wire; as a result, it is not stocked by many suppliers. Various methods of producing suitable AA 7075 feedstock were explored which was good practice for the later work of incorporating additives into the alloy later in the work.

a. AA 7075 Wire Preparation

AA 7075 wire was originally made from commercially sourced AA 7075 plate from Kaiser Aluminum and McMaster-Carr. The aluminum plates were 0.8 mm (0.031 in) thick and were cut into thin aluminum wires or strips using a metal shear in the machine shop. The nominal diameter of the provided AA 4008 wire from Additive Technologies Inc. (Additec) is 1.5 mm (0.059 in); by using a thinner plate, a safe margin was provided to ensure the cut wire strips would fit through the print head feed port and not cause a jam. Before cutting, the plate was cleaned with acetone and P500 sandpaper to remove any surface impurities. Wires were also cleaned post cutting with acetone and kimwipes to remove any debris from the metal shear. AA 7075 plate and wires as well as the mechanical shear used to produce them are shown in Figure 32. However, printing full size test specimens in accordance with ASTM B557M-15 were not possible using this method due to the inability to add more wire strips during the printing [161], [162]. Also, jetting noticeably degrades as the melt pool volume drops within the crucible, leading to poor prints.



(a) AA 7075 plate and wires and (b) the mechanical shear with a plate staged for cutting

Figure 32. Initial AA 7075 wire preparation.

However, these problems were overcome by sourcing a spool of AA 7075 wire from Additec. The material used was Alcoa commercial AA 7075 wire with a diameter of 0.889 mm (0.035 in) supplied by Additec in a 9.07 kg (20 lb.) spool for use with the ElemX

printer. Wire samples were melted in the printer and tested for microhardness following T6 heat treatment to verify the alloy met the specifications for AA 7075. The wire consisted of Al (balance, wt.%), Zn (6.05%), Mg (2.43%), Cu (1.77%), Cr (0.69%), Fe (0.44%), Si (0.29%), Mn (0.34%), and Ti (0.48%) by EDS analysis (Figure 33). With a spool of AA 7075 available, specimens were printed to the requirements of ASTM B557M-15 for subsize specimens [161].

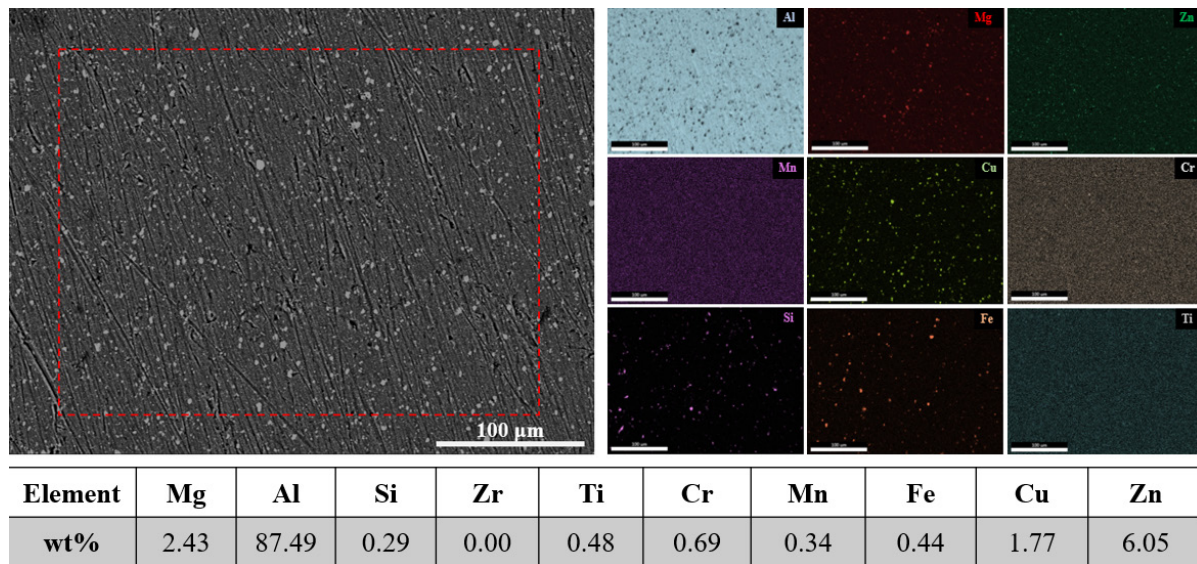


Figure 33. AA 7075 spool EDS analysis.

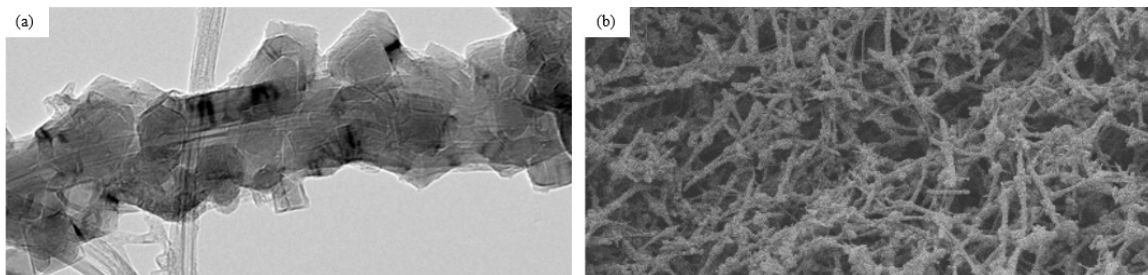
b. Additives with AA 7075

Once pure AA 7075 samples were successfully printed, the focus of the research shifted to incorporating additives into the AA 7075 to enhance the materials properties of the printed samples.

(1) Boron-Nitride Nanobars

The first additive considered for incorporation into AA 7075 during LMJP was a boron-nitride nanotube product supplied by BNNano. The powder, known as NanoBarbTM (NB), consists of a nanotube comprised of boron and nitrogen atoms with projections resembling rock-candy, which allows for easy connections within the matrix material

similar to rebar in concrete (Figure 34a–b). NB was identified as a good candidate for incorporation into the AA 7075 matrix, but significant challenges were encountered trying to produce viable specimens with NB powder. Ultimately, incorporation of NB powder into AA7075 during LMJP was abandoned in lieu of more promising alloy enhancements.

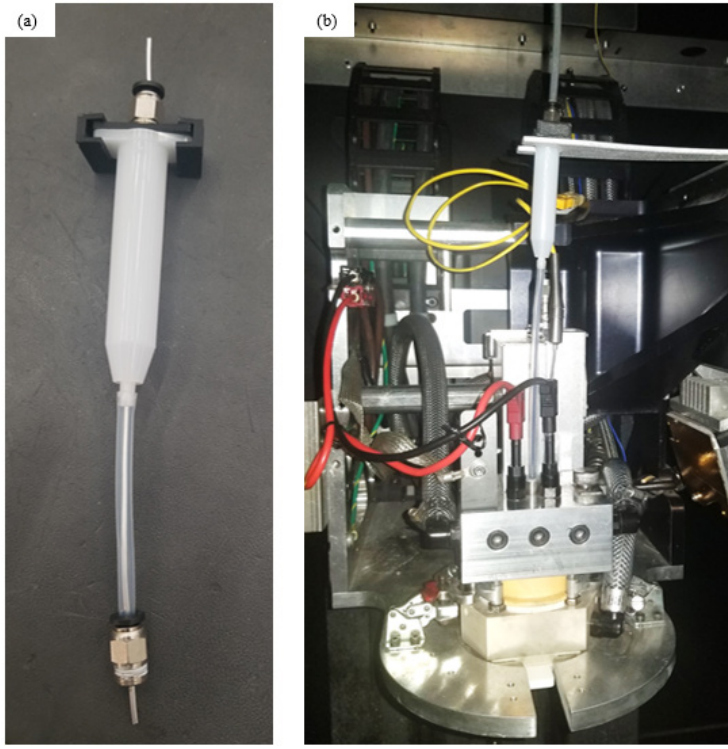


(a) TEM and (b) SEM views of the NanoBarbTM product. Adapted from [163], [164].

Figure 34. NanoBarbTM additive used during AA 4008 printing.

(2) Zn addition via Wire and Powder

To attain near-AA 7068 mechanical properties, Zn was added to AA 7075 during LMJP. Both Zn powders and Zn wires were explored. Zn powder was added to the crucible without interrupting the print process by incorporating a syringe holding a large amount of the material over the print head, as shown in Figure 35. The amount of powder was estimated by noting the beginning and ending levels in the syringe, and calculating the added mass based on the volumetric change of the syringe. However, Zn powder addition was ruled out because the samples printed using this method were extremely brittle, most likely due to inconsistent Zn dispersal throughout the print volume.



(a) syringe with aluminum wire protruding at top and bottom and (b) syringe installed above ElemX head for Zn powder addition. Adapted from [165].

Figure 35. Zn powder addition rig.

Next, strips of pure Zn were added to the crucible. Zn strips were cut using the shear shown in Figure 32b and weighed to determine the mass. The Zn strips were carefully trimmed to produce the exact mass needed to raise the Zn content of the AA 7075 feedstock. The mass of Zn needed was calculated based on the higher weight percentage of Zn in AA 7068, as shown in Figure 36a. Initially, smaller, disproportionate tensile specimens were printed since no additional AA 7075 wire was added to the reservoir during printing, so the total size of the print was severely limited by the degradation of the jetting as the reservoir emptied. Once the method produced some results, the subsize tensile specimen from ASTM B557M-15 was proportionally scaled to produce a specimen mass of approximately 9 g total, which corresponds to the mass of a full crucible's worth of molten aluminum [161]. The two sizes of Zn-enriched AA 7075 tensile specimens printed are shown in Figure 36b. Zn was manually added at the beginning of each specimen printing per the following methodology:

- Burn in and calibration completed with the AA 7075 wire spool to verify good jetting.
- Wire feed was disabled, and the crucible level was lowered by ~3 mm for Zn addition.
- A Zn wire of 198 mg was added to the reservoir.
- Wire feed was enabled, and the crucible level was raised to full for printing using the AA 7075 wire spool
- Test jetting for 5 seconds to ensure Zn was adequately mixed into the crucible followed by immediate printing to minimize Zn loss due to vaporization.

(a)
 AA 7075: 5.1 – 6.1 wt% Zn
 AA7068: 7.3 – 8.3 wt% Zn

$$\text{Minimum Zinc: } 9 \text{ g} * 0.051 = 459 \text{ mg Zn}$$

$$\text{Maximum Zinc: } 9 \text{ g} * 0.061 = 549 \text{ mg Zn}$$

$$\text{Minimum Zinc: } 9 \text{ g} * 0.073 = 657 \text{ mg Zn}$$

$$\text{Maximum Zinc: } 9 \text{ g} * 0.083 = 747 \text{ mg Zn}$$

$$\text{Minimum Addition: } 657 - 549 = 108 \text{ mg Zn}$$

$$\text{Maximum Addition: } 747 - 459 = 288 \text{ mg Zn}$$

$$\text{Average: } 198 \text{ mg Zn}$$



(a) Zn wire mass calculation based on the difference in Zn content between AA 7075 and 7068 and (b) enriched Zn test specimens produced using the Zn wire addition methodology.

Figure 36. Zn wire calculation and samples produced.

Adding Zn wire produced several samples with improved tensile strengths, but many of the produced samples failed prematurely during testing. Upon visual examination of the samples and fracture surfaces following tensile testing, brittle fracture surfaces and areas of discoloration were noted (Figure 37); one possible explanation is nonhomogeneous

distribution of Zn within the molten Al which was confirmed via mechanical testing. Therefore, a better way of ensuring a more uniform Zn distribution was needed.

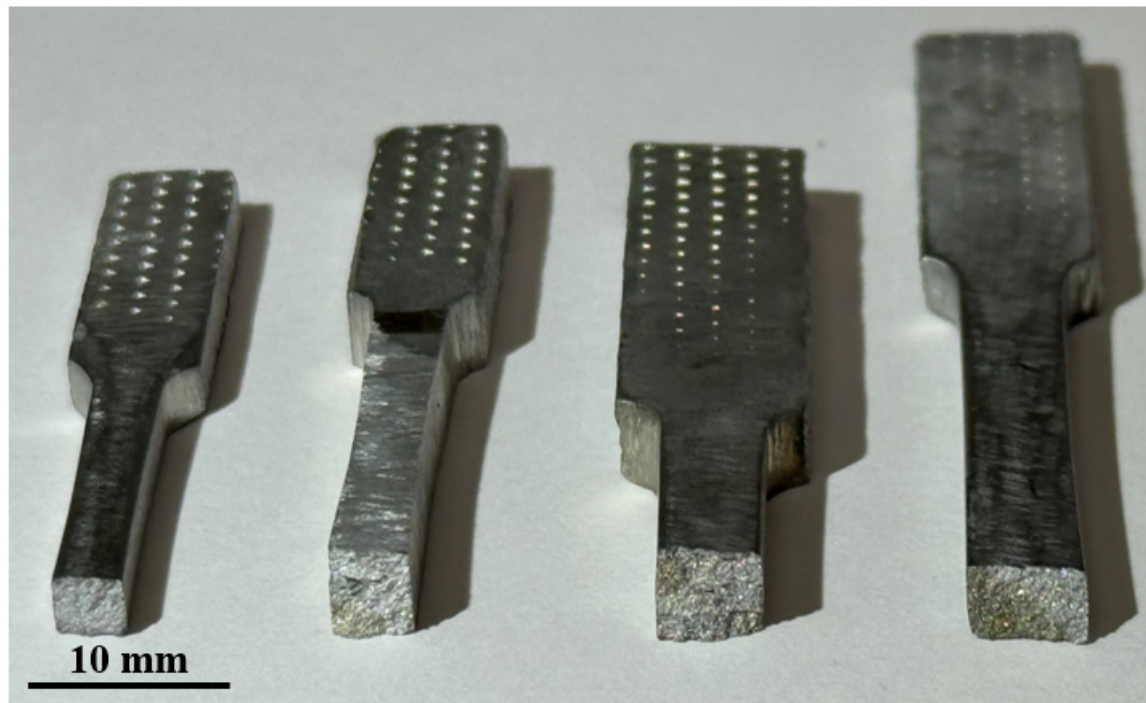


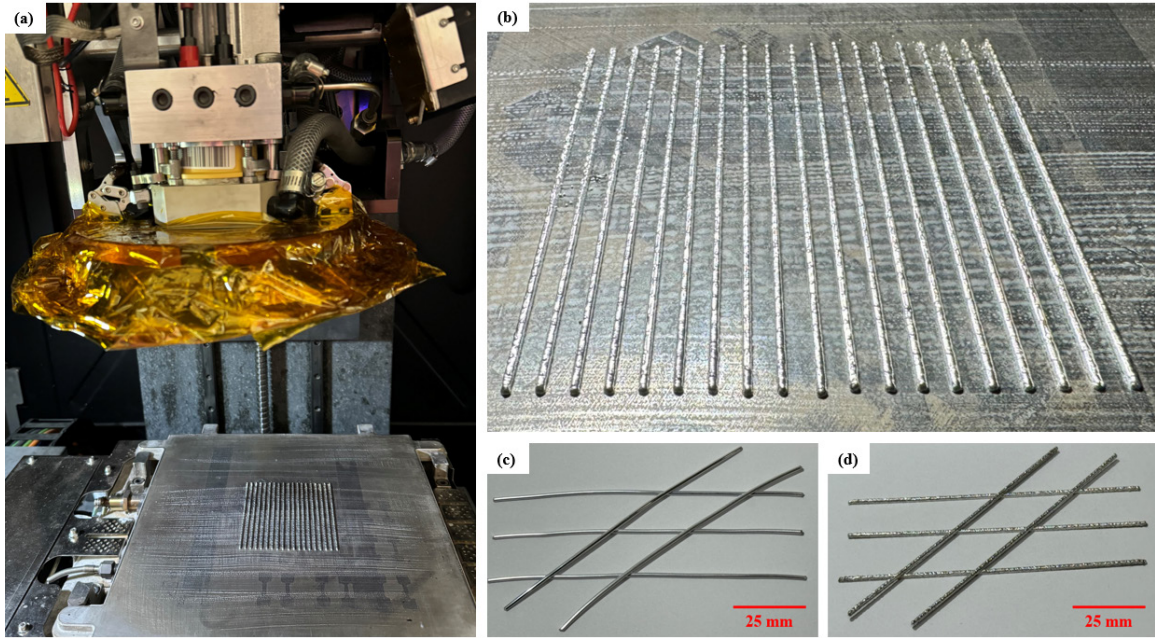
Figure 37. Fracture surfaces of Zn-enriched samples showing indications of brittle fracture and discoloration.

(3) Printing Zn-enriched AA 7075 Wire

Following the marginally successful results of adding a wire of pure Zn to the ElemX prior to printing, a better method of raising the Zn content was needed to improve both the materials properties and consistency of the process. Zn-enriched AA 7075 wires were printed using the ElemX using the same methodology as above for Zn addition to the crucible with a Gen 4 containment and AA 7075 temperatures setpoints, as shown in Figure 38a–b. The wires were designed with dimensions of 100 mm length and 1.25 mm diameter to ensure the wires would have the same or slightly smaller diameter as that of the stock wire to ensure jams would not occur during printing, as shown in Figure 38c–d. After printing and removal from the substrate, the wires were sanded with P500 grit sandpaper to remove any contaminants from the substrate and cleaned with kimwipes and an air gun.

Specimens were then printed to the subscale tensile specimen specification using the following methodology:

- Burn in and calibration completed with the AA 7075 wire spool to verify good jetting.
- Wire feed was disabled, and the crucible level was lowered by ~3 mm for Zn addition.
- Zn-enriched AA 7075 wire added to refill the reservoir to full.
- Test jetting for five seconds to ensure Zn was adequately mixed into the crucible.
- Commenced printing the specimen, but at 30% frequency. This frequency was chosen based on a stable droplet pattern and a slow enough speed to allow for manual feeding of enriched Zn wires to maintain reservoir level at roughly the same level throughout the printing process.
- Due to the lower Zn expected at the onset of the print, the lower layers were filed off prior to final machining into the desired tensile specimen geometry before heat treatment.



(a–b) ElemX printer with Zn-enriched wires on the substrate, (c) close-up of the feedstock wire, and (d) close-up of the printed wires.

Figure 38. Zn-enriched wire production.

3. Variable Density Post Processor

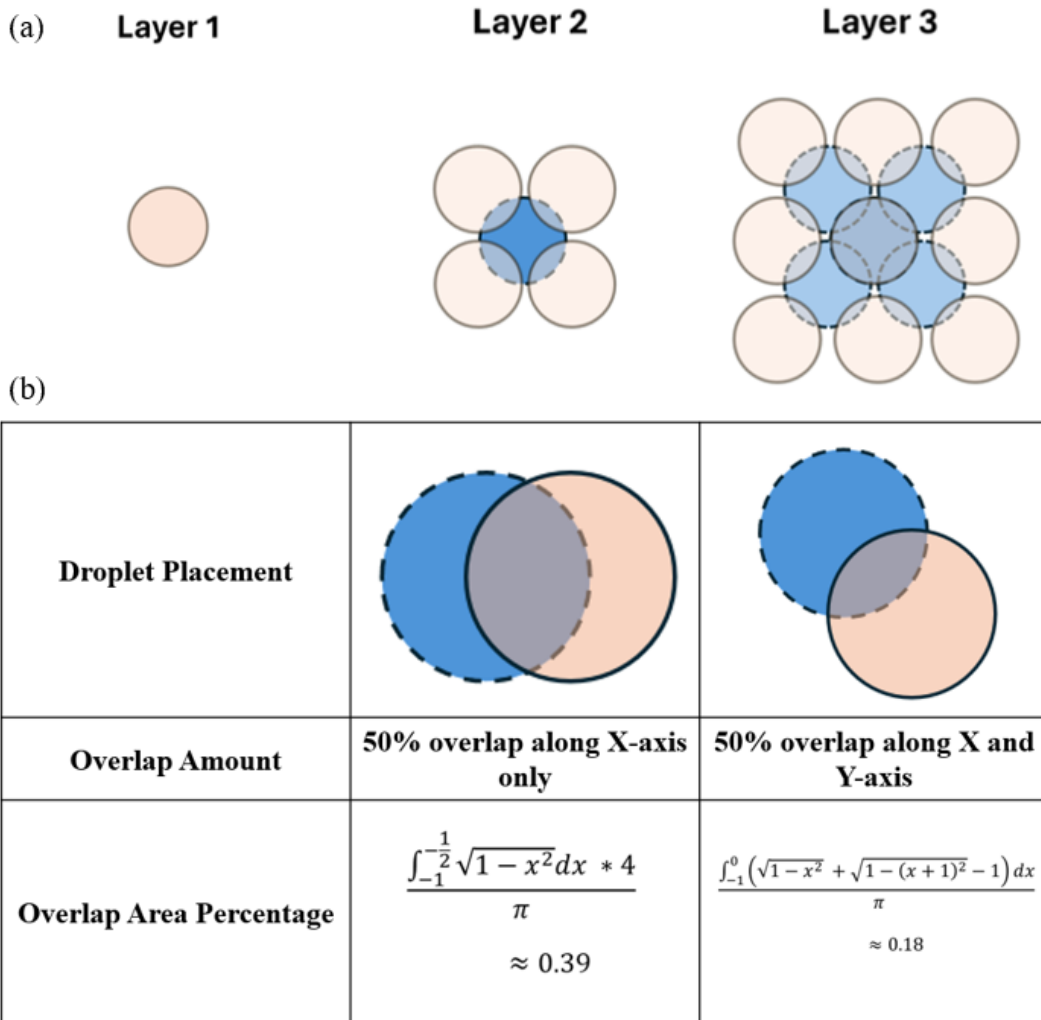
To print variable infill samples as a single print, a Variable Density Post Processor (VDPP) to identify and reduce the infill density in a local region was designed using Python. The post processor operates on MPF style G-code, which is the output of the ElemX Builder slicer software. The user controls the modification by defining a rectangular cuboid with coordinates and a target density. The VDPP identifies reads G-code line by line from the start of a file. The last found feature type is used to define the current command's feature type. When a G0 or G1 command is found, the X, Y, Z, and E parameters are stored to describe the intended end state of that command. The intended start state of a command is the end state of the previous command. The difference in E position between the current and previous states directly represents the amount of material evenly extruded over the current move.

a. Infill Droplet Placement

First, the ability to deposit a droplet upon a printed droplet from the previous layer was tested. Depending on the infill pattern generated by the slicer, not all infill movements may pass over a droplet on the previous layer. Achieving a lower target infill density requires extruding a percentage of the original infill mass—which is directly related to the extrusion amount. If an infill movement does not have suitable locations to extrude enough mass, another infill movement on the same layer can extrude additional mass to make up the difference. ElemX Builder and other slicers generate G-code in “islands,” and each island is a disconnected region to print on an individual layer.

b. Minimizing Infill Density

To reduce the density of the object in a controllable manner, G-code commands from Builder must be modified and/or skipped. The feature type and path of the G-code command is checked to determine if it should be modified. The VDPP checks if current printing feature type is “infill” and determines if the line segment drawn between the start and end points of the movement intersect a user defined bounding box. A movement that intersects the bounding box is split into separate movements on both sides of the intersection. If both infill feature type and intersection(s) are found, the movement data is stored in a queue in memory for further modification. Otherwise, the read command is written to the output as-is with E adjustments. The top layer of a variable density region must have 100% density to ensure that the original layers above the region are supported. Thus, the variable density region must increase in density towards the top of the region to get adequate density. Every droplet that is not touching a wall can support at least four droplets on top (in 2D space) with a 50% overlap along the X and Y axes. Based on 50% overlap along X and Y, total overlap of circular droplet is estimated at 18–39%, as shown in Figure 39.



(a) ElemX stacking schematic showing overlap of circular droplets and (b) overlap area percentage calculation of 18 and 39% for circular droplets.

Figure 39. Droplet support and overlap during variable infill.

The converted droplets of subsequent modified density layers' movements are evaluated for support by checking if the droplets overlap droplets on the previous layer. A NxN kernel can be used to find overlaps while avoiding overlaps in the raster of the previous layer. Initially, a raster spacing of $\frac{1}{2}$ droplet width and 3x3 kernel size was tested for both overlaps and overbuilds (search and collision, respectively), which allowed actual overlaps percentages of 100% (same location), 39% (1 axis), and 18% (2 axes, diagonal) per the calculations in Figure 39. Next, a raster spacing of $\frac{1}{4}$ droplet width and a 5x5 kernel size was tested for both, increasing resolution and allowing for droplet placement with $\frac{3}{4}$

X/Y overlaps. The corners of the rectangular kernel were excluded by applying a corner radius to the larger kernel since they have smaller overlap areas. Both kernel sizes and the code used to generate them are shown in Figure 40. Following printing, all promising samples were sectioned in half using a band saw to determine if the gradient infill code was successful.

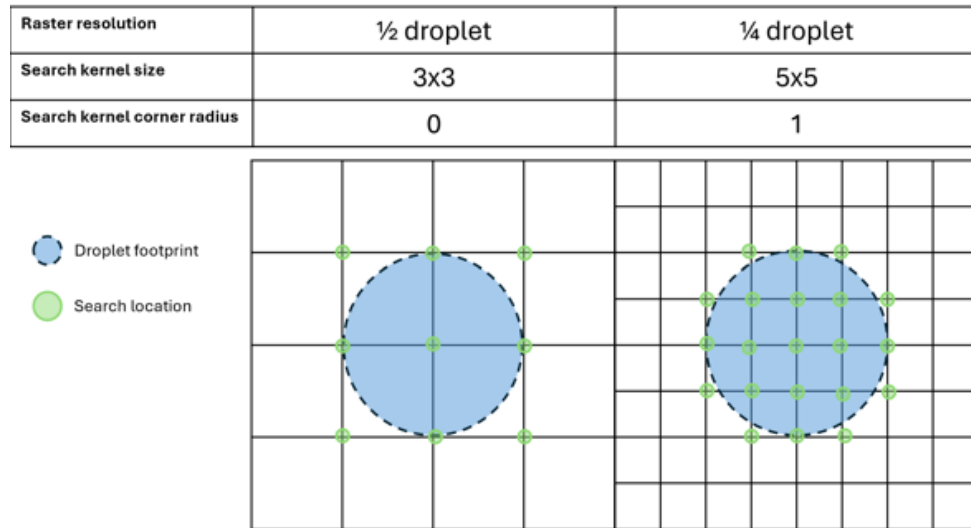
(a)

```
# DROPLET
DROPLET_WIDTH = 0.510 #mm
#DROPLET_OVERLAP_PERC = 0.5 #%
DROPLET_RASTER_RESOLUTION_PERC = 0.5 #% of droplet width
DROPLET_RASTER_SUPPORTED_SEARCH_KERNEL_SIZE = 3 # in raster index widths (must be odd numbers)
DROPLET_RASTER_SUPPORTED_SEARCH_CORNER_RADIUS = 0 # in raster index widths
DROPLET_RASTER_COLLISION_SEARCH_KERNEL_SIZE = 3
DROPLET_RASTER_COLLISION_SEARCH_CORNER_RADIUS = 0
```

(b)

```
# DROPLET
DROPLET_WIDTH = 0.510 #mm
#DROPLET_OVERLAP_PERC = 0.5 #%
DROPLET_RASTER_RESOLUTION_PERC = 0.25 #% of droplet width
DROPLET_RASTER_SUPPORTED_SEARCH_KERNEL_SIZE = 5 # in raster index widths (must be odd numbers)
DROPLET_RASTER_SUPPORTED_SEARCH_CORNER_RADIUS = 1 # in raster index widths
DROPLET_RASTER_COLLISION_SEARCH_KERNEL_SIZE = 5
DROPLET_RASTER_COLLISION_SEARCH_CORNER_RADIUS = 1
```

(c)



(a) 3x3 kernel search and collision raster code, (b) 5x5 kernel search and collision raster code, and (c) schematic showing the increase in search locations due to improving raster resolution.

Figure 40. Raster code and schematic for variable infill printing.

B. SAMPLE PREPARATION

After printing, all aluminum specimens required minor filing and sanding to remove surface imperfections that could serve as stress concentrations in accordance with standard filing best practices [166]. Next, a T6 heat treatment was performed to obtain the desired materials properties. Specimens destined for examination via optical microscopy or SEM were mounted in epoxy, sanded and polished before examination. In most cases, mechanical testing was performed prior to preparation for microscopy.

1. Heat Treatment

All the samples underwent a T6 heat treatment procedure consisting of a series of temperature soaks using two furnaces. First, a solutionizing treatment with a soak time of 2 hours at 480°C was performed in a Thermo Scientific Lindberg Blue M furnace, shown in Figure 41a, followed by a rapid quench in distilled water at 25°C. After removal from the water bath, samples were dried and placed into an MTI Corporation Gravity Convection Oven, shown in Figure 41b, for precipitation hardening treatment at 121°C for 24 hours followed by a rapid quench in distilled water at 25°C before final preparation for testing. Samples were wrapped in aluminum wire as shown in Figure 41c to ensure the quenching times requirements of AMS 2771 were met following the solutionizing heat treatment step [167].



(a) Thermo Scientific Lindberg Blue M furnace used for the solutionizing step, (b) MTI Corporation Gravity Convection Oven used for the precipitation hardening step, and (c) wire wrap method utilized to ensure quenching timelines were met.

Figure 41. Equipment for sample heat treatment.

2. Preparation of Samples for Microscopy

Microstructure cubes were prepared for mounting in a two-part Buehler Sampl-Kwick™ Fast Cure Acrylic epoxy resin. Following visual inspection, two cubes at each temperature were mounted in epoxy in an as-printed state, and two others were subjected to T6 temper and then mounted in epoxy. Once cured, all mounted samples were sanded progressively with P800, P1000, P1500, P2500, and P4000 silicon carbide sandpaper before polishing with 1 µm alumina and distilled water. After all investigations via SEM and EDS were complete, the samples were prepared for optical microscopy. To do so, the samples were etched with Keller's Etch (5 mL HNO₃, 3 mL HCl, 2 mL HF, and 190 mL H₂O) for approximately 30 seconds before optical microscopy to reveal the microstructure. A summary of the preparation methodology for all aluminum alloy specimens is included in Appendix B.

C. MATERIALS TESTING

Mechanical testing of samples was performed, and the results were compared to the values for the wrought alloy. Of note, mechanical testing was performed in parallel with

materials characterization for efficiency purposes and to ensure time was not wasted preparing samples for microscopy that did not have satisfactory mechanical properties.

1. Microhardness

All samples were hardness tested to ensure alloy degradation due to Zn loss did not occur during the LMJP process. A Struers DuraScan system with a diamond indentation tip was used as shown in Figure 42a. Printed samples of AA 7075 in post-solutionized and post-T6 condition were tested alongside a known AA 7075 standard from Kaiser Aluminum. All AA 7075 samples were tested with Vickers hardness measurements, specifically HV 1.0. All Zn-enriched AA 7075 samples were tested with Vickers hardness measurement HV 2.0 due to the expected higher hardness of Zn-enriched AA 7075.

2. Tensile Testing

Tensile specimens were printed to ASTM B557M-15 standard for subsize specimens and were filed and sanded with P600 and P2500 silicon carbide sandpaper to remove surface inconsistencies that could lead to stress concentrations and premature failure. Tensile tests were performed on an Instron model 5982 equipped with a 100-kN load cell as shown in Figure 42b. Samples were held using wedge-style grips and tested until fracture. All testing was done in accordance with ASTM B557M-15 and E8M. Crosshead speed was calculated in accordance with ASTM E8M section 7.6.4.3 [168]. Strain was measured using an Instron clip-on extensometer at the center of the gauge section. The strain rates were in the range 0.015 ± 0.003 mm/mm/min for all the tests. The load cell calibration and accuracy were verified by testing AA4008 and AA7075 alloy wrought coupons before testing of the 3D printed specimens.



(a) Struers DuraScan that was used for all microhardness testing and (b) Instron 5982 that was used for all tensile testing.

Figure 42. Mechanical testing devices in the NPS laboratory.

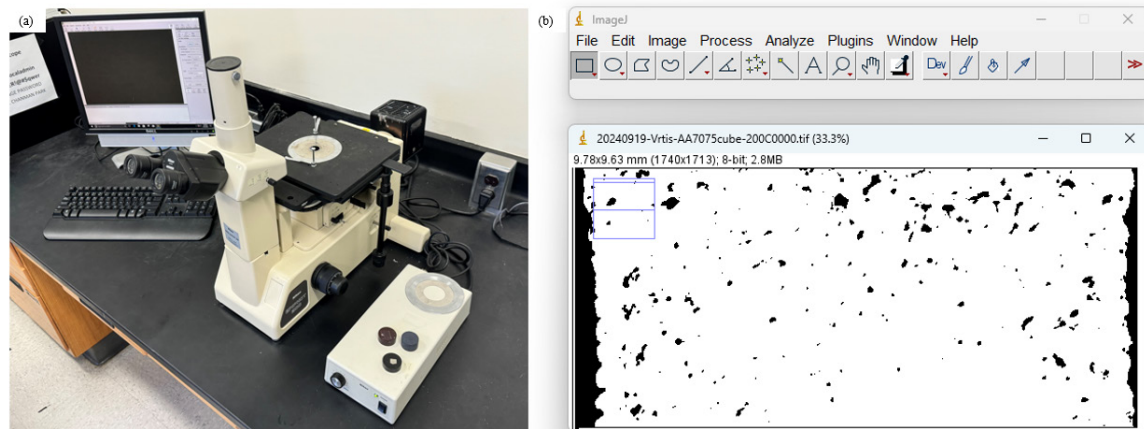
D. MATERIALS CHARACTERIZATION

After mechanical testing, suitable samples were prepared per the methodology in III.B.2 and analyzed via a variety of characterization methods. Some samples, such as lower substrate temperature test cubes, were prepared solely for materials characterization with no mechanical testing performed. Mechanical testing and materials characterization were performed in parallel to the maximum extent possible for efficiency.

1. Optical Microscopy

After etching, samples were imaged using a Nikon Epiphot 200 inverted optical microscope to examine the microstructure (Figure 43a). Samples with substrate temperatures ranging from 200–500°C were all imaged to investigate the effect of substrate temperature on microstructure and porosity. After capturing images via optical

microscopy, the images were analyzed via ImageJ software to determine the porosity (Figure 43b).

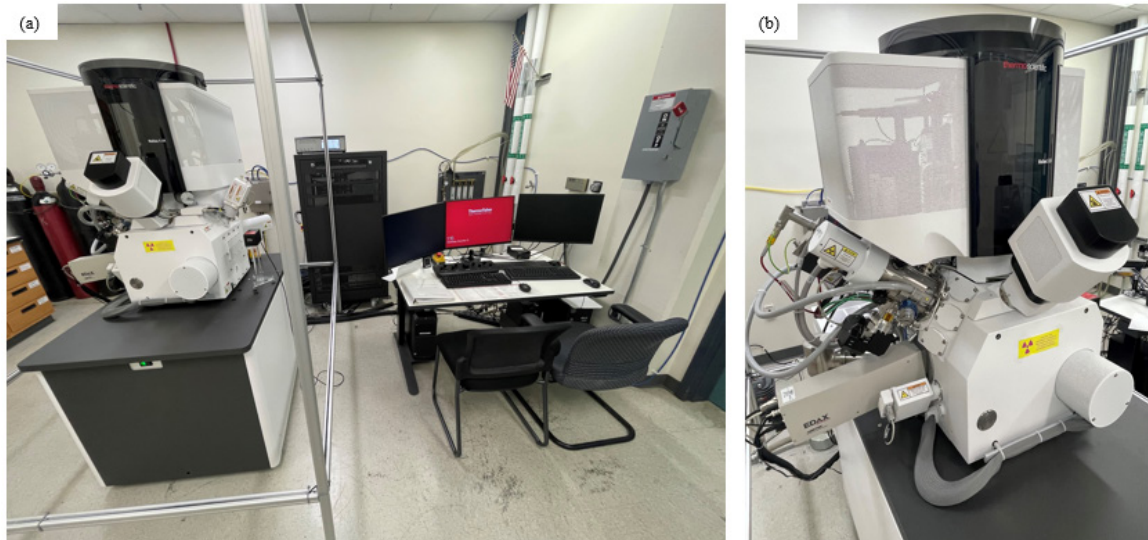


(a) Nikon Epiphot 200 inverted optical microscope and (b) ImageJ toolbar with an image being adjusted for porosity analysis.

Figure 43. Optical microscopy and porosity analysis.

2. Scanning Electron Microscopy and Energy-Dispersive Spectroscopy

The FEI Helios 5 UX SEM (Figure 44a) and EDAX Ametek EDS instrument (Figure 44b) were used to image and determine the elemental composition of various samples. BSE images with 1,000–10,000 \times magnification were captured to show the precipitates within the AA 7075 matrix. EDS analysis was performed at beam voltage and current of 20 kV and 1.6 nA and in both point and mapping modes to verify the presence of precipitates in AA 7075. 20 kV and 1.6 nA were selected to ensure sufficient excitation of the K α x-rays for Zn, the heaviest element expected within AA 7075, and sufficient penetration for a representative measurement of the sample.



(a) Layout of the Helios SEM and control center in the NPS laboratory and (b) close-up of the EDS instrument where it mates into the SEM.

Figure 44. SEM and EDS in the NPS laboratory.

3. X-ray Diffraction

The Rigaku Miniflex 600 desktop XRD was used to ascertain the crystal structure of various samples (Figure 45a). The sample holder utilized was the ASC-6 rotary sample holder (Figure 45b), which was used to ensure proper sample height within the instrument during analysis. Spectra for samples were collected for 2θ values of 30° – 80° since that is the range over which the precipitates of interest within AA 7075 should have peaks. The XRD spectra peaks were compared to the known spectrum of AA 7075 to confirm peaks corresponding to the precipitates were present. XRD and EDS data were compared to ensure agreement and confirm the presence of the expected precipitates within the samples.

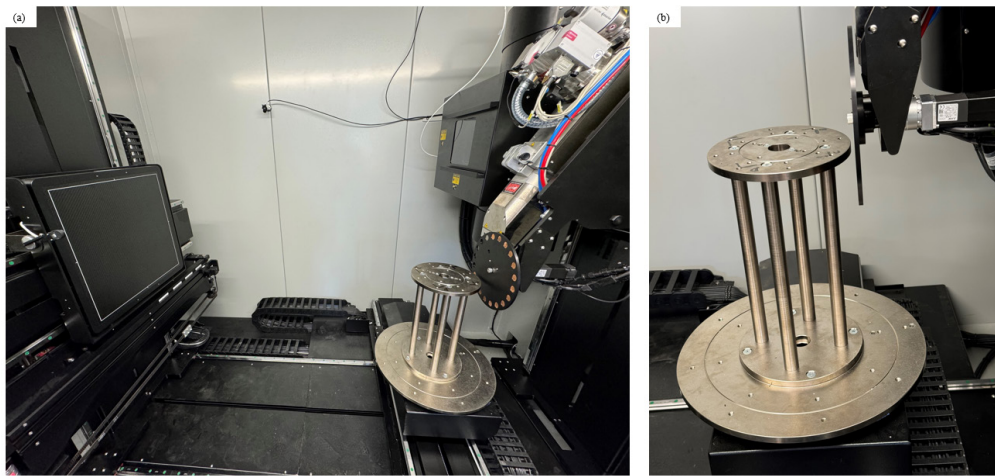


(a) Rigaku x-ray diffractometer and (b) ASC-6 rotary sample holder inside the detection chamber.

Figure 45. Rigaku desktop x-ray diffractometer at the NPS laboratory.

4. DR and CT Scanning

AA 7075 sample cubes, printed with substrate temperatures of 200°C, 300°C, 400°C, 475°C, and 500°C, were investigated via CT scan with the Northstar Imaging (NSI) X5000 DR/CT scanner (Figure 46). All cubes were imaged using 100 kV, 180 μA, low gain, 6 frames per second, and a zoom factor of 9.75, which resulted in an effective pixel pitch of 15.38 μm. These settings were empirically determined to provide the highest possible resolution within the existing mechanical limitations of the X5000 machine. NSI software was used to process the CT scans and identify / label representative cross-sections of each sample to show internal porosity and defects. Unfortunately, the NSI software does not provide a function to automatically calculate porosity; therefore, a series of six representative cross-section scans were analyzed via ImageJ software and an average porosity was determined for each substrate temperature.



(a) Inside the cabinet of the X5000 DR / CT scanner showing the (left to right) detector, sample stage, and x-ray tube and (b) close-up of the sample stage showing the sample stage as close to the x-ray source as possible to maximize magnification by minimizing aperture.

Figure 46. X5000 DR / CT scanner at NPS laboratory.

5. X-ray Nano-tomography

Synchrotron x-ray nano-tomography was conducted at the Full-field X-ray Imaging beamline (FXI, 18-ID) at National Synchrotron Light Source II (NSLS-II) of Brookhaven National Laboratory (BNL) [169]. The energy of the incident X-ray was set to 8.0 keV. The sample was measured in a fly-scan mode with a rotation range of 180° and exposure time of 100 ms. The images were captured using a lens-coupled charge-coupled device (CCD) detector with a binning of 2×2, resulting in an effective pixel size of 40.0 nm. The nano-tomography data was reconstructed using Tomopy with gridrec algorithm [170]. The images were stacked and analyzed using ImageJ Fiji.

THIS PAGE INTENTIONALLY LEFT BLANK

IV. LIQUID METAL JET PRINTING OF ALUMINUM ALLOY 7075

This chapter is under peer-review for publication in Additive Manufacturing. The text and figures have been modified for better applicability within the chapter. The relevant literature review, introduction, and methodology was covered in Chapters II and III. In this chapter, materials characterization and testing data for AA 7075 samples printed at a variety of substrate temperatures are presented. Both materials characterization and testing were performed in parallel for efficiency. For materials characterization, 5 mm test cubes were 3D printed at substrate temperatures of 200–500°C to study the effect of substrate temperature and T6 heat treatment on the print quality, splat morphology and possible hot cracking. Tensile specimens were printed at substrate temperatures of 475°C and 500°C to perform materials testing.

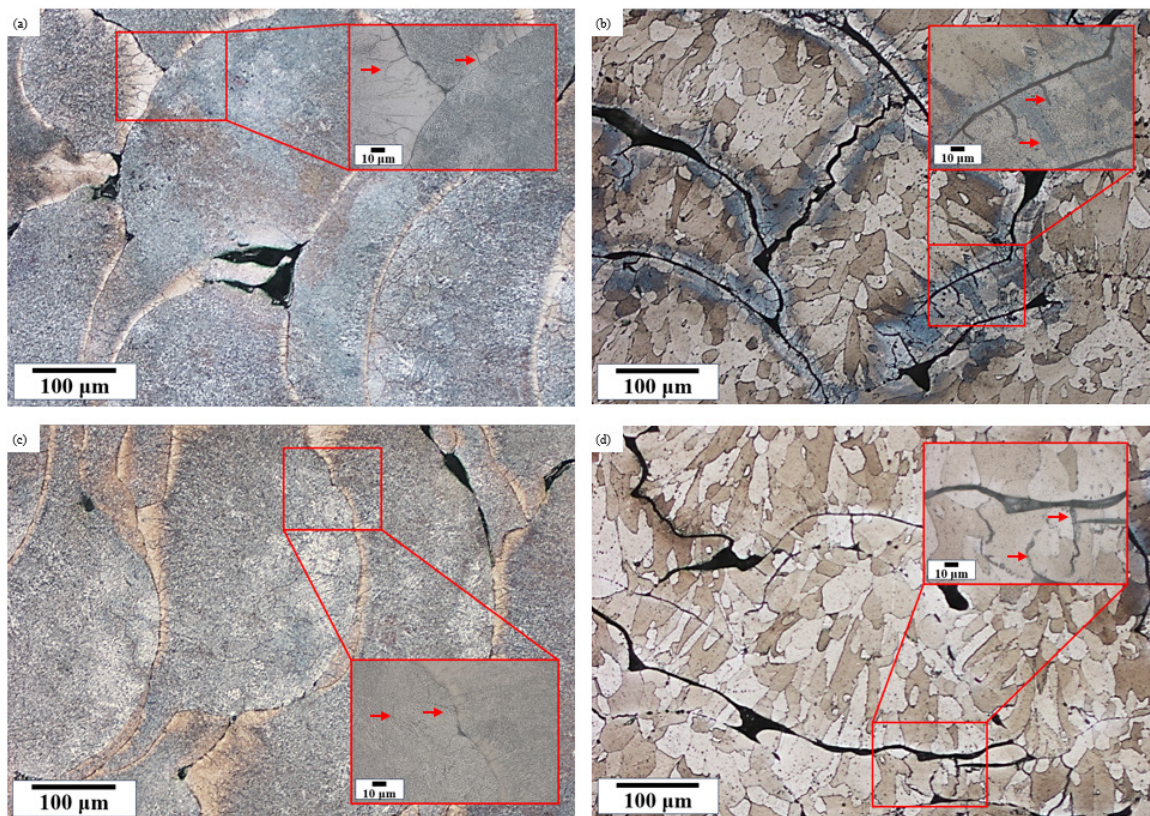
A. RESULTS AND DISCUSSION

Materials characterization shall be discussed followed by materials testing on AA 7075 samples.

1. Materials Characterization

In the as-printed and post T6 samples in Figure 47a–d, both solidification and liquation cracking were prevalent at substrate temperatures of 200°C and 300°C. The samples had fine grains with dendritic structures due to rapid cooling rates below the solidus curve from the thermal model. As a result, droplets are not adequately spread out upon impact with the substrate or previous deposition, and spherical droplets vice splats are formed. Due to the formation of spherical droplets, these parts had a significant amount of porosity estimated to be 12% for 200°C substrate and 5% for 300°C substrate using cross-sectional micrographs arising from gaps as the splats are partially solidified before fully spreading. This causes overbuilding due to the increased thickness of the splats, resulting in a rough, uneven surface as seen in Figure 49a. The splat boundaries also showed poor metallurgical bonding as evidenced by the large gaps between the clearly visible droplets and lack of grain growth between droplets. The red inset boxes in Figure

47 show extensive solidification and liquation cracking (red arrows), occurring within the droplets and adjacent to droplet boundaries, respectively. These process conditions were not suitable both on account of microstructure (i.e., cracks) and morphology (porosity and overbuilding).

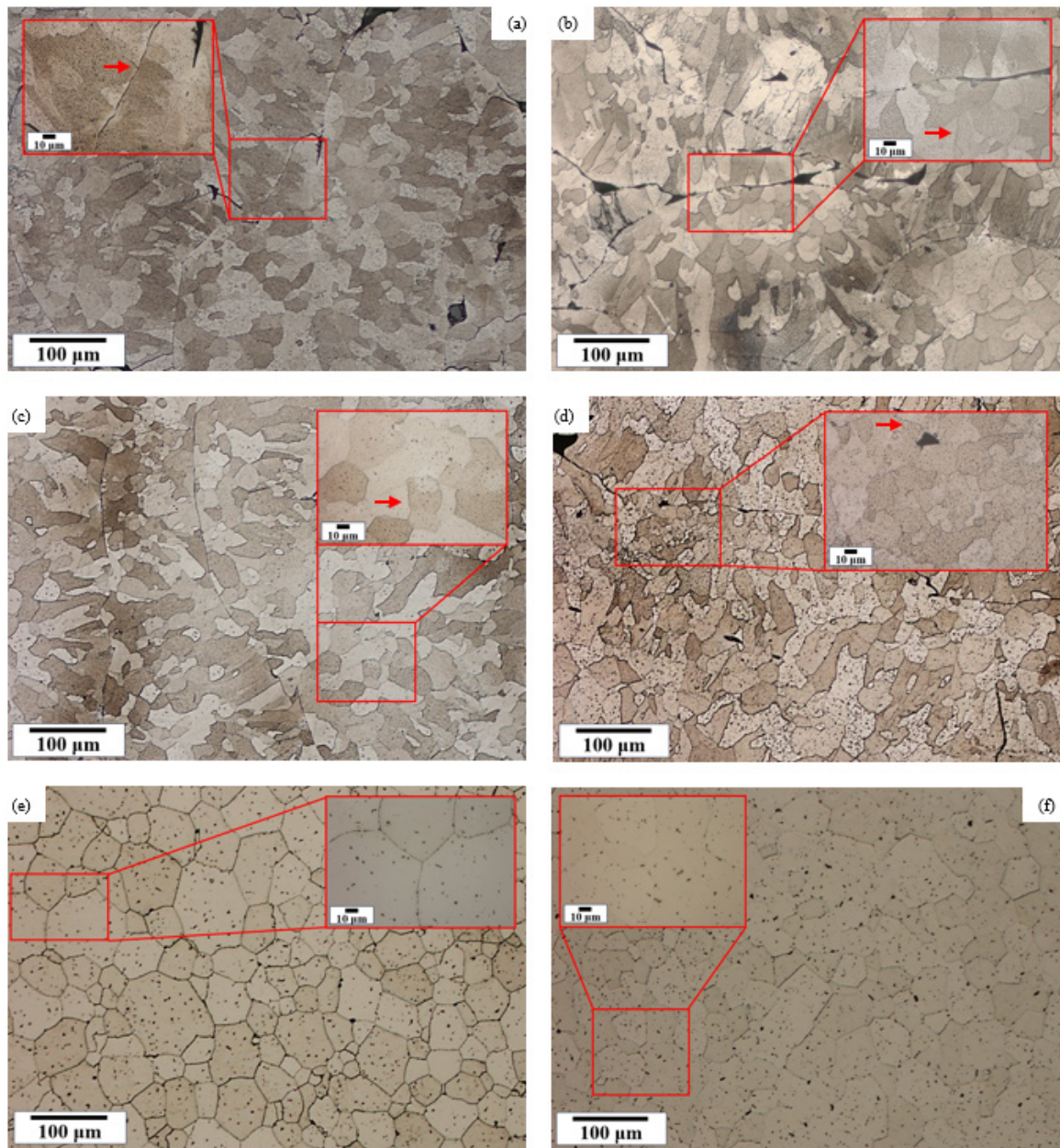


(a) 200°C sample as printed and (b) 200°C sample post T6 showing significant solidification and liquation cracking as well as a porosity of ~12%. (c) 300°C sample as printed and (d) 300°C sample post T6 showing slightly better cracking and porosity of ~5%.

Figure 47. 200°C and 300°C sample optical microscopy.

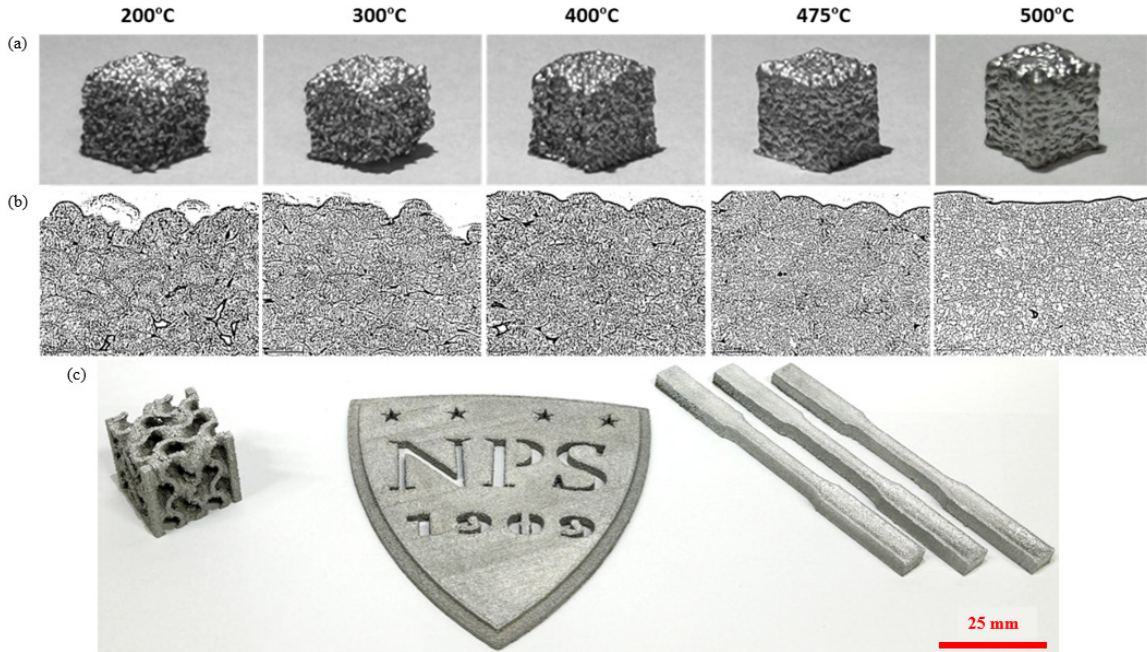
At 400°C, fewer solidification and liquation cracks were visible, identified by the red arrows in Figure 48a-b. The morphology still showed significant porosity (> 5%) due to the solidification rates that prevented the splats from filling the gaps as well as overbuilding, similar to the lower temperature samples. At substrate temperature of 475°C, minimal hot cracks in the inset red box, lower porosity (<5%), and equiaxed recrystallized grains were observed (Figure 48c-d). This is due to the reduced cooling rates that allow

droplets to fully spread out, forming splats vice spherical droplets, which both fill the gaps and prevents hot cracking. Only the 500°C sample had no porosity or cracks that could be detected with an overall excellent metallurgical bonding (Figure 48e–f). The samples with substrate temperatures above 400°C had coarse grains because the original grains were replaced with recrystallized grains that grew in-situ during printing due to the high substrate temperatures. Only samples above 400°C show extensive grain growth across the interfaces, though the lower substrate temperatures result in porosity and incomplete splat spread that causes overbuilding as seen on the test cubes in Figure 49a-b. Samples printed with a substrate temperature of 500°C are shown in Figure 49c, which no evidence of oxidation, warping, and very slight overbuilding indicating fully dense, defect-free printing.



(a) 400°C sample as printed and (b) 400°C sample post T6 showing lower solidification and liquation cracking in addition to lower, but still present, porosity. (c) 475°C sample as printed and (d) 475°C sample post T6 showing minimal cracking and voids. (e) 500°C sample as printed and (f) 500°C sample post T6 showing no detectable cracking or voids via optical microscopy.

Figure 48. 400°C, 475°C, and 500°C sample optical microscopy.



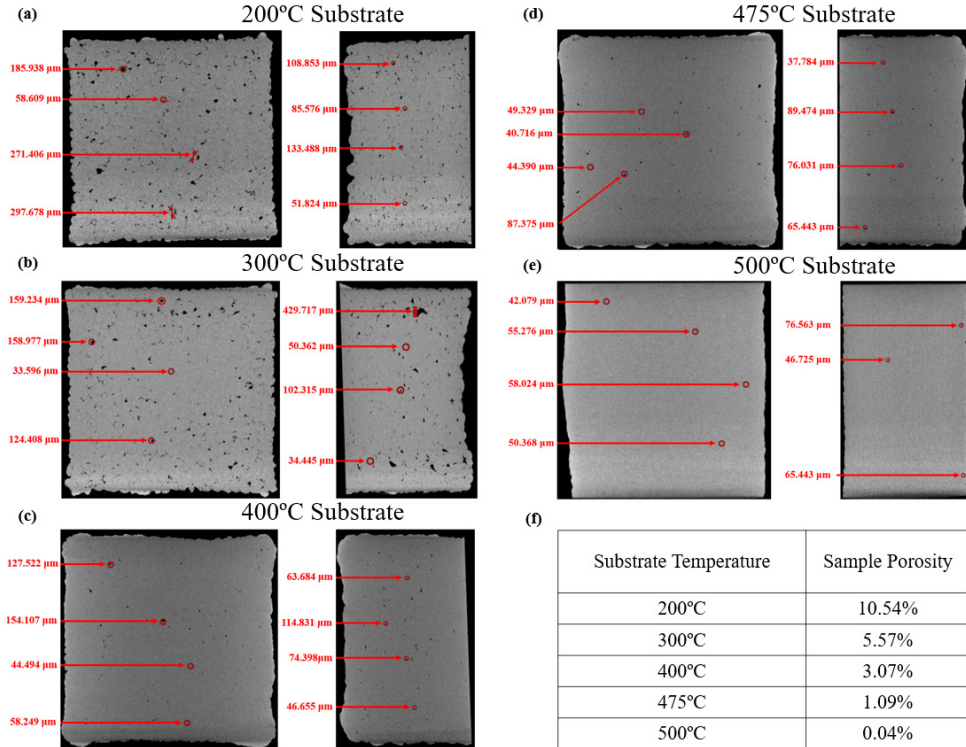
(a) 5 mm test cubes printed at substrate temperatures of 200–500°C and the corresponding microstructures, showing a dome-like top due to rapid splat freezing and overbuilding except for the 475–500°C samples. (b) Cross-sections of the samples show a reduction in porosity with increasing substrate temperature. (c) Complex gyroid, NPS shield, and tensile specimens printed at substrate temperature 500°C.

Figure 49. Optical images and microscopy of AA 7075 test cubes at various substrate temperatures and successful AA 7075 prints.

The solutionizing treatment at 480°C (from the T6 heat treatment in Chapter III.B.1) caused grain recrystallization and growth for the lower temperature samples, 200 °C and 300 °C, whereas for the >400°C samples, the microstructure looked similar to the as-printed condition as the substrate temperatures were above recrystallization temperatures. During aging at 121°C, very fine nanoscale precipitates of MgZn₂ (which cannot be resolved with optical microscopy) form where only larger secondary precipitates are visible. All the T6 heat-treated samples showed reduced cracking compared to as-printed parts, indicating that these cracks can possibly be healed at the solutionizing temperature of 480 °C. However, this did not improve the metallurgical bonding at the splat interfaces or porosity.

In addition to optical microscopy, samples were analyzed using the X5000 CT scanner. All samples were scanned with the same settings (Chapter III.D.4) and compared to one another (Figure 50). The porosity of each substrate temperature was calculated via

ImageJ and compares closely with the values determined via optical microscopy. Defect size and abundance both shrank as substrate temperature was increased, reaching a maximum defect size of ~60 µm and 0.04% porosity at substrate temperature 500°C.

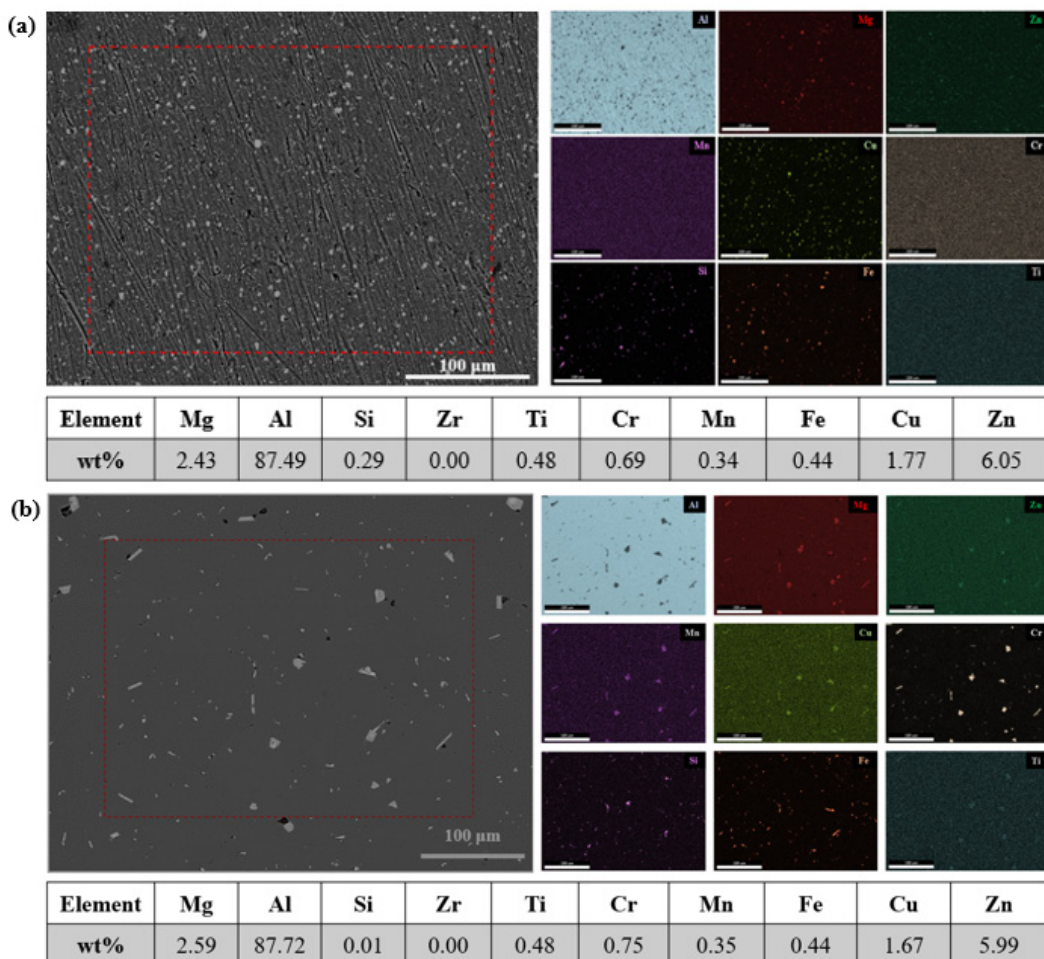


(a) 200°C substrate with 10.54% porosity and defects up to ~300 µm. (b) 300°C substrate with 5.57% porosity and defects up to ~160 µm. (c) 400°C substrate with 3.07% porosity and defects up to ~155 µm. (d) 475°C substrate with 1.09% porosity and defects up to ~90 µm. (e) 500°C substrate with 0.04% porosity and defects up to ~60 µm. (f) Summary of the sample porosity for all substrate temperatures.

Figure 50. CT scans of samples printed with 200–500°C substrate temperature.

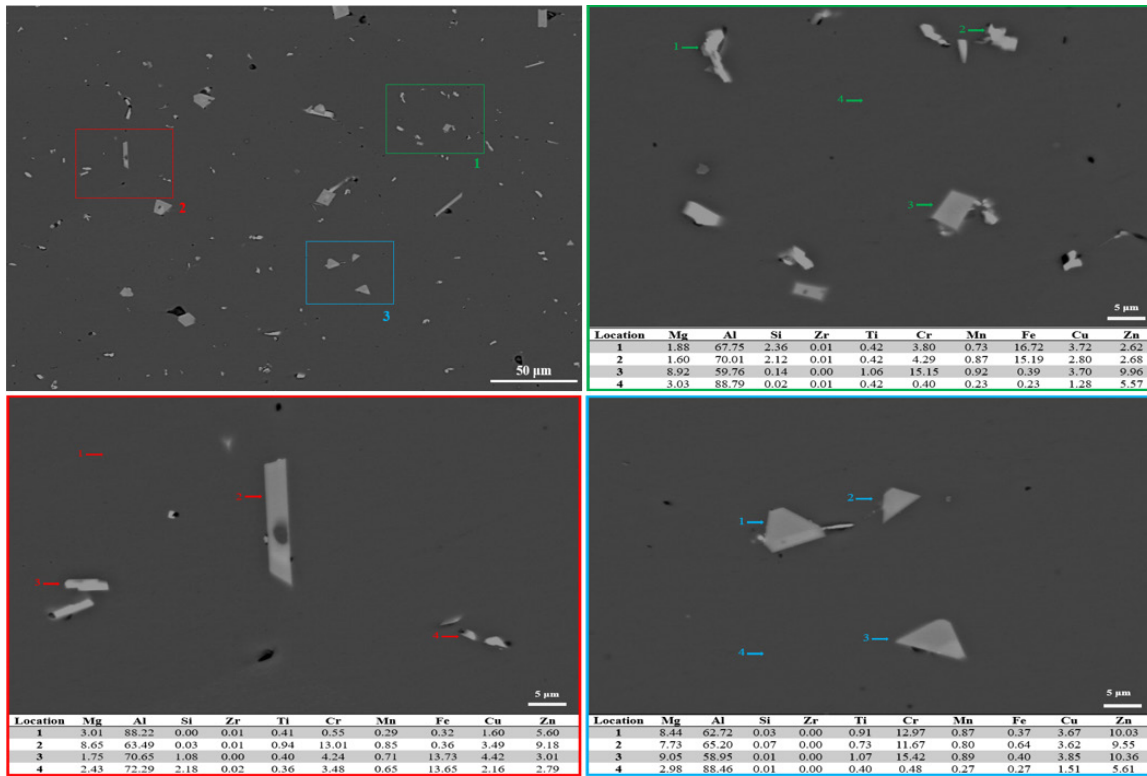
A standardless quantification via EDS mapping of the printed AA 7075 samples and the AA 7075 feedstock wire was performed with no major differences between the elemental compositions observed; this indicates the alloy composition is not significantly affected during printing (Figure 51). Most importantly, this indicates Mg and Zn were not lost due to vaporization during printing. η precipitates are not visible due to their small size, but their presence is indicated by both Mg and Zn homogeneously distributed throughout the EDS map. A BSE image from the 3D-printed sample with EDS point

analysis is shown in Figure 52. The intermetallics identified are most likely ω indicated by Fe-rich precipitates, S with Cu-rich Fe-poor precipitates, and $\text{Al}_2\text{Mg}_3\text{Zn}_3$ precipitates with high Cr content (due to the high Cr content of the feedstock). Overall, almost all precipitates had elevated levels of Fe compared to the average composition. It should be noted that none of the compositions match the exact stoichiometric values for these phases out of hundreds of EDS measurements performed, most likely due to fluorescent x-rays from neighboring precipitates in the sample.



(a) EDS map of AA 7075 feedstock wire and (b) EDS map of printed AA 7075 samples.

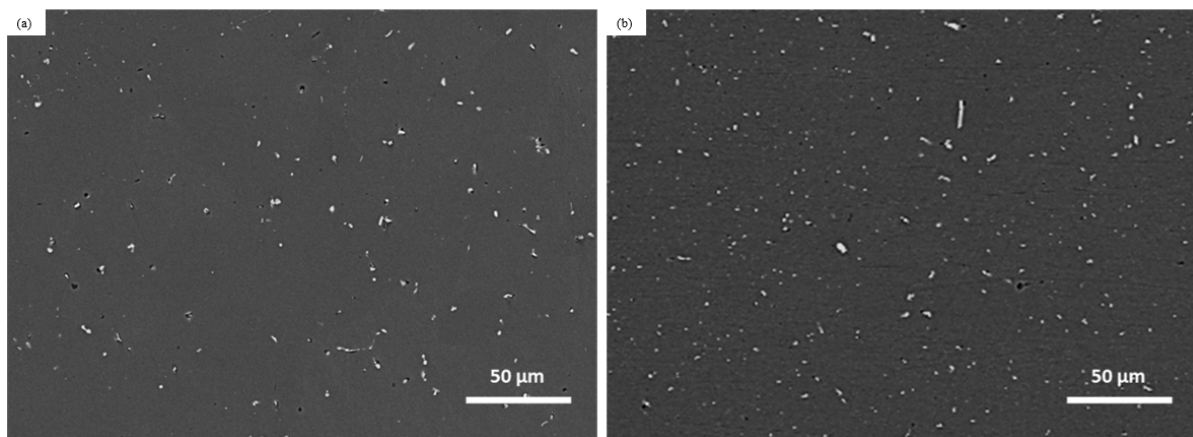
Figure 51. EDS map comparison of AA 7075 wire and printed samples after T6 heat treatment.



(top left) SEM micrograph of AA 7075 at 1000x magnification, which was reproduced from Figure 51b with EDS sites marked. (remainder) Sites 1–3 present EDS results showing likely S, ω , and $\text{Al}_2\text{Mg}_3\text{Zn}_3$ precipitates.

Figure 52. EDS point analysis of AA 7075 samples after T6 heat treatment.

The distribution of these secondary phase particles can be seen from a comparison of samples as-printed vice after T6 heat treatment from SEM imagery shown in Figure 53. The precipitates are initially coarse and mostly located around grain boundaries. The T6 heat treatment causes dissolution and the creation of a solid solution during the solutionizing step followed by reprecipitation of finer precipitates during the artificial aging step as expected. Neither SEM nor EDS provide definitive proof of the η phase due to its small size. XRD analysis (Figure 54) shows the existence of peaks corresponding to the phases MgZn_2 (η)/ $\text{Mg}(\text{Al}, \text{Cu}, \text{Zn})_2$, $\text{Al}_7\text{Cu}_2\text{Fe}$ (ω), and Al_2CuMg (S) in the reference stock alloy and the 3D-printed sample.



SEM cross-section image of (a) as-printed AA 7075 sample and (b) T6 heat-treated samples showing the more uniformly redistributed secondary phase precipitates.

Figure 53. SEM cross-sectional images of AA 7075 samples.

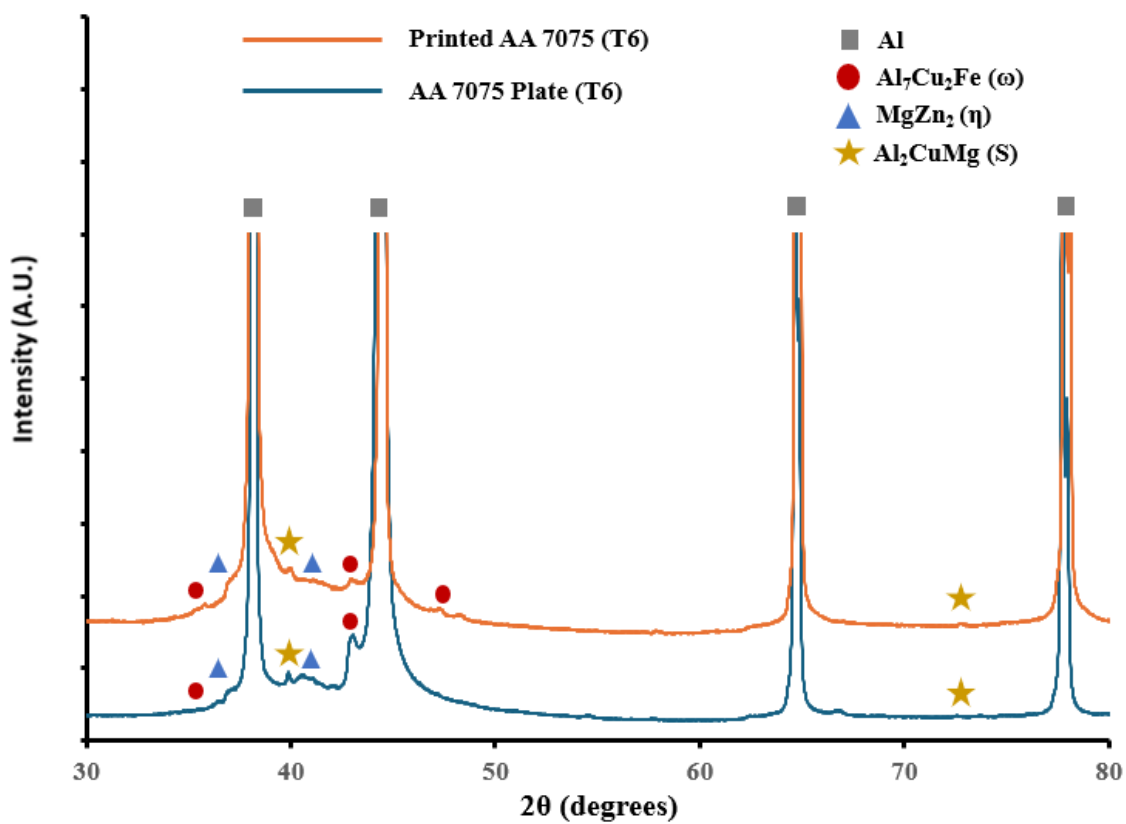
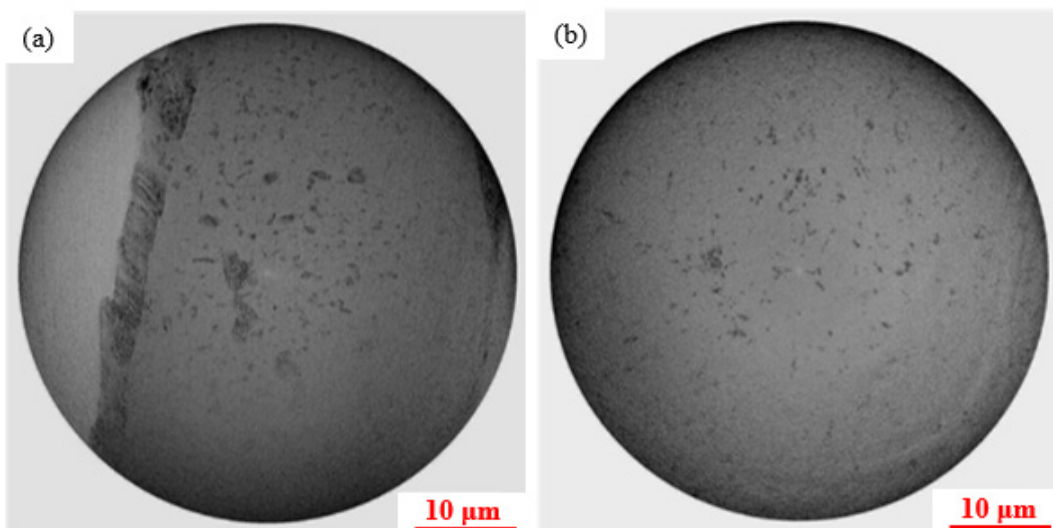


Figure 54. XRD of AA 7075 samples.

To further investigate the microstructure of the printed samples, x-ray computed nano-tomography at a resolution of 40 nm/pixel at Brookhaven National Laboratory 18-ID FXI beamline with a field of view of $50 \times 40 \mu\text{m}^2$ was used. Figure 55 shows snapshots from 80 slices merged to a depth of 3.2 μm for as-printed and T6 heat-treated samples to observe precipitates and investigate their distribution. Although the x-ray contrast of the precipitates can, in theory, be used to estimate the types of phases when supplemented with XRD and EDS analysis, it was difficult to distinguish between these three phases based on only contrast in nano-CT, as some of the x-ray imaging artifacts tend to affect contrast as well at material boundaries where density changes abruptly for the very fine precipitates.



X-ray computed nano-tomography scans for (a) as-printed and (b) T6 heat-treated printed samples for a substrate temperature of 475 C. Both scans are comprised of 80 slices combined to show the particles within a depth of 3.2 μm that shows distribution of coarser precipitates.

Figure 55. X-ray computed nano-tomography scans of AA 7075 samples.

There were a few types of fine and coarse precipitates that could be distinguished in the as-printed samples (Figure 55a). The finer, sub-micron precipitate structures were not clearly visible in the SEM images (Figure 53), nor in single snapshots from the CT scans, where only the grain boundaries could be distinguished. As recrystallization and grain growth occur during printing, insoluble precipitates might have remained in their

original locations resulting in the observed distribution. In addition, there were coarse precipitates with sizes up to a few microns, located primarily on grain boundaries. These precipitates all have higher density compared to the aluminum matrix based on contrast and likely have varying amounts of Mg, Cu, Fe and Zn indicating co-existence of S, η and the insoluble ω phases as shown by the EDS point analysis.

The initial structure of these precipitates changed after the T6 heat treatment, where the microstructure transformed into uniformly distributed sub-micron precipitates with no larger precipitates remaining (Figure 55b). The SEM and EDS analysis showed the same phases but their extended morphology and denser arrangement within boundaries suggest their nucleation and growth is affected by the prior microstructure. It is possible that 3D printed parts uniquely benefit from the local rapid solidification rates that produce finer insoluble precipitates that remain after heat treatment, which would improve mechanical strength as well as corrosion resistance. In essence, the printing process combines rapid solidification with consolidation.

2. Materials Testing

Microhardness measurements of the standard AA 7075 alloy and 3D printed samples after solutionizing at 480°C for 2 hours and after the full T6 heat treatment were measured to verify alloy quality. Vickers Hardness (HV1) values for all the printed samples are consistent with the standard values and reach a value of 78.74 ± 2.67 after solutionizing and 185.60 ± 3.50 HV1 after the T6 treatment (Figure 56), indicating no degradation or loss of Mg or Zn during printing. The microhardness of samples produced at all substrate temperatures was very consistent, but the tensile results were not due to extensive hot cracking and voids at substrate temperatures below 500°C.

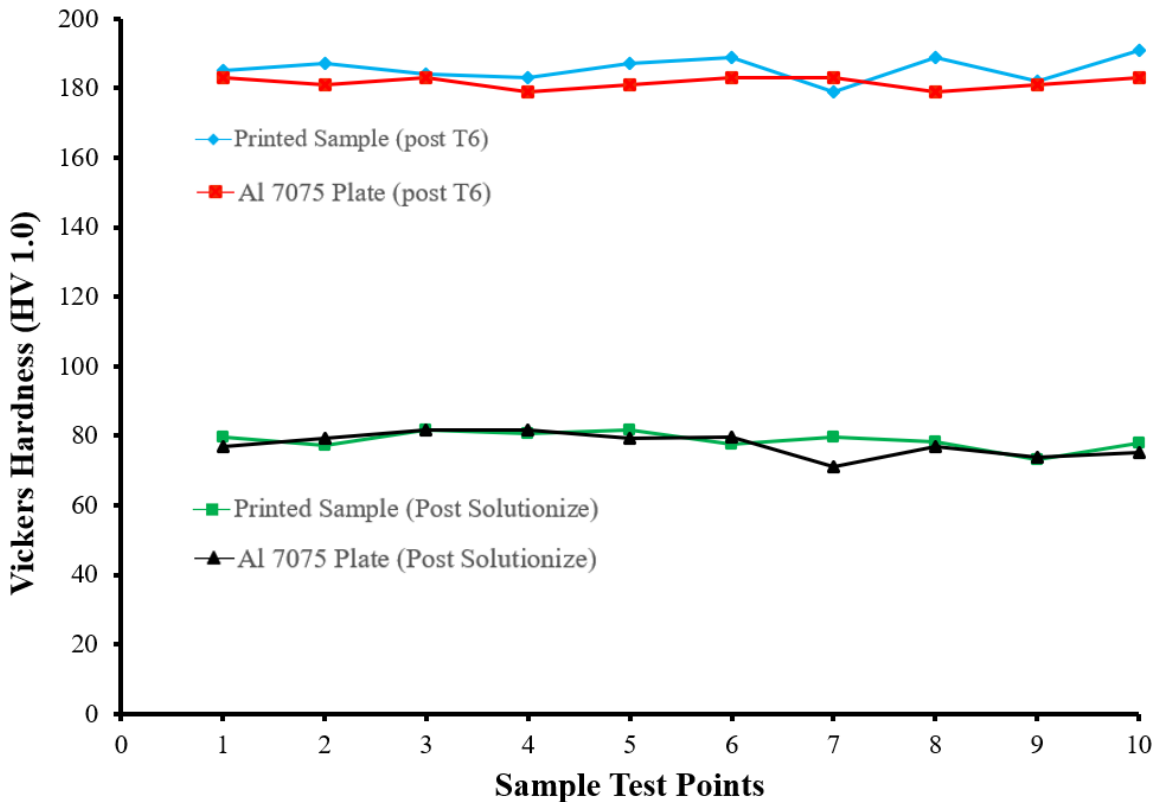


Figure 56. Microhardness of AA 7075 prints and standard plates.

The tensile test results are shown in Figure 57 for the 475°C and 500°C samples. The measured ultimate tensile strength and strain 58to failure values were $\sigma_{true} = 503.49 \pm 8.16$ MPa and $\varepsilon_{fail} = 0.74 \pm 0.01$ for the 475°C substrate and $\sigma_{true} = 593.22 \pm 8.05$ MPa and $\varepsilon_{fail} = 10.05 \pm 1.35$ for the 500°C substrate. The results for the 500°C samples match or exceed the nominal values for AA 7075. The samples printed with a substrate temperature of 475°C had tensile strengths approaching those of AA 7075 but had low ductility, most likely due to porosity and hot cracking. All the other samples at substrate temperatures lower than 475°C had even lower tensile strength and ductility, although they all had a nominal microhardness value of ~180 (HV1). At a substrate temperature of 500°C, the average ductility was comparable to the wrought alloy. The specific strength of the printed AA 7075 samples was calculated, and the value was calculated to be in the range of titanium alloys produced by M-AM (Figure 58).

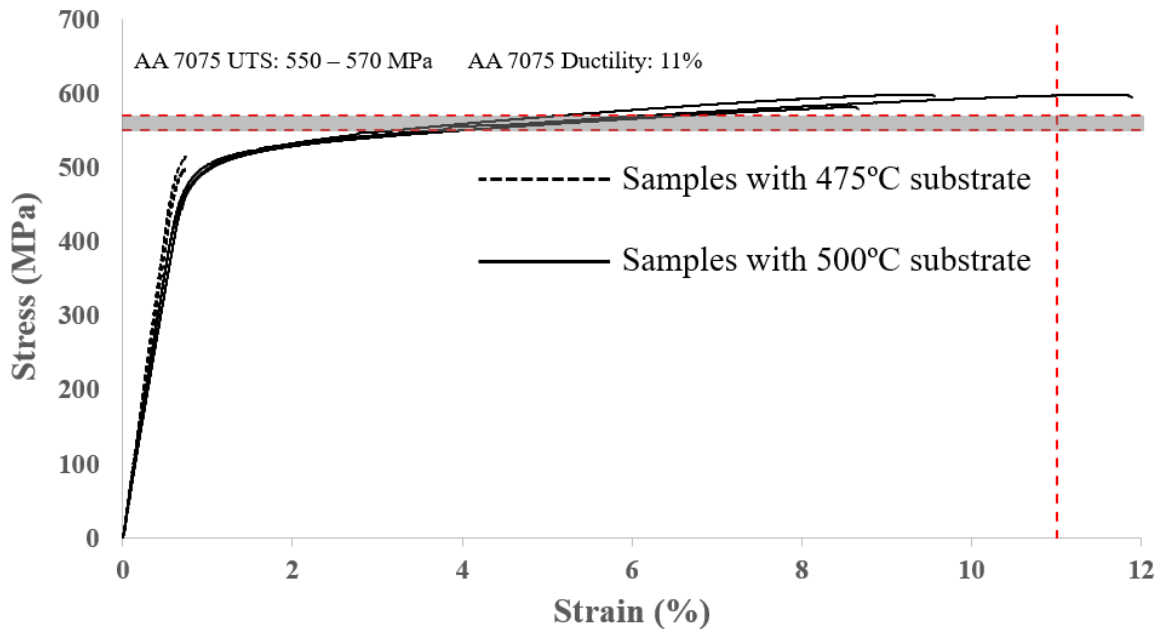
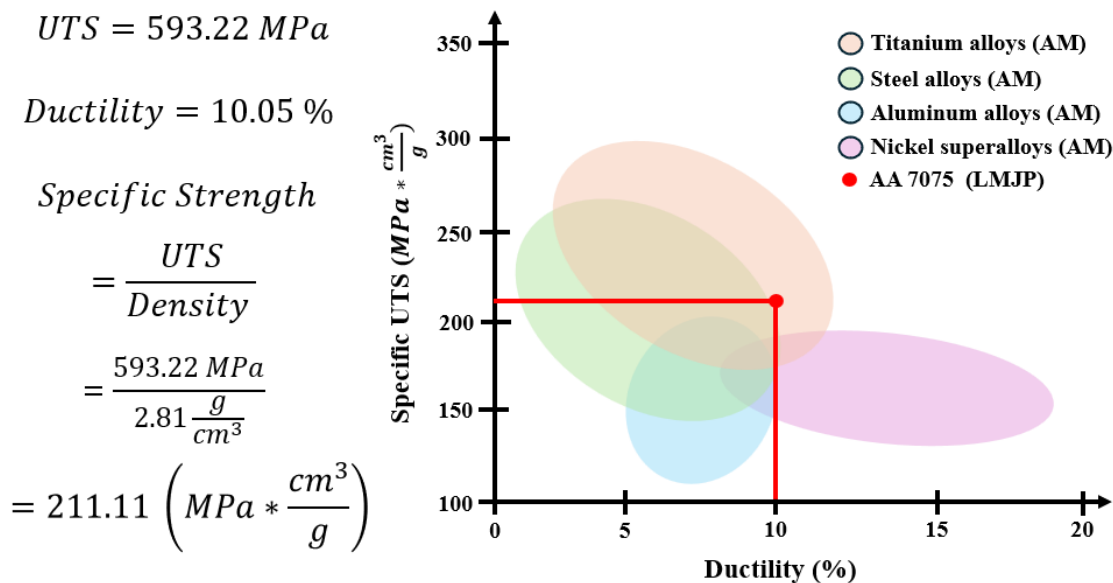


Figure 57. Stress-strain curves of printed AA 7075 tensile specimens at a substrate temperature of 475°C (dashed lines) and 500°C (solid lines).



Adapted from [55].

Figure 58. Specific strength of printed AA 7075 compared to other alloys produced via AM methods.

B. PRELIMINARY FINDINGS

Pure AA7075 parts were printed at full strength and at high resolution in this study using LMJP with no crack formation and minimal porosity at optimal process conditions. The part geometry and surface finish have sufficient consistency with only slight dimensional variations from print to print, but all parts conform to the model dimensions within ~5%. The results show that elevated substrate temperatures from 200 – 500°C produce samples with fewer hot cracks and pores as temperature increases. A substrate temperature of 500°C is required to minimize hot cracking, as well as to allow enough time for splat spreading to fill the gaps to produce fully dense parts. The average ultimate tensile strength of the printed parts that underwent T6 heat treatment exceeded the wrought alloy specifications at an average UTS and ductility of 593.22 MPa and 10.05%, respectively. The requirement of a high substrate temperature imposes limits on the types of M-AM approaches that can be used to print hot cracking susceptible alloys – a process such as L-PBF would not be able to safely approach these levels of preheating. The lower overall process temperature of LMJP also prevents loss of volatile elements such as Zn and Mg, commonly observed during L-PBF. The LMJP process shows promise as a reliable means to produce alloys that require a controlled cooldown rate to eliminate hot cracking.

V. LMJP OF PARTICLE-STRENGTHENED AA 7075

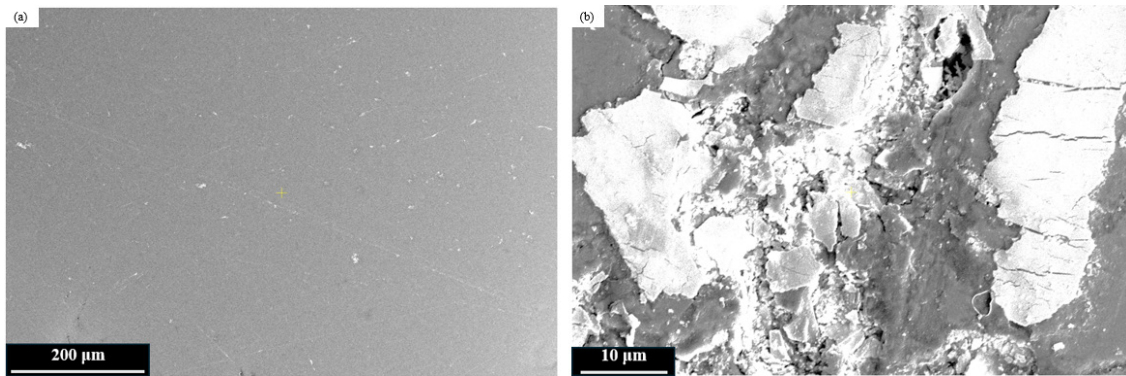
The research in this chapter builds upon the successful printing of pure AA 7075 samples in the previous chapter. The relevant literature review, introduction, and methodology are covered in Chapters II and III. In this chapter, materials characterization and testing data from particle-strengthened AA 7075 samples are presented. Both materials characterization and testing were performed in parallel for efficiency. Tensile specimens were printed for both materials characterization and testing due to the limitations placed on printing Zn-enriched AA 7075 as described in Chapter III.

A. RESULTS AND DISCUSSION

After the success of printing AA 7075 with the ElemX, the LMJP method was explored to produce aluminum alloys with superior properties to AA 7075 via particle strengthening. First, the results of dispersion strengthening with NB are discussed, although the results were disappointing. Adding Zn to raise alloy concentrations to that of AA 7068 was the next method explored, with better results obtained. For NB addition, only materials characterization shall be discussed. For both Zn addition methods, the materials characterization and testing are presented.

1. Boron Nitride Nanobars

Initially, dispersion strengthening with NB into the AA 7075 alloy during ElemX printing was explored. However, NB proved to be immiscible within AA 4008 when tested before attempting to incorporate into AA 7075. The powder tended to clump together in the crucible, causing the print to fail due to nozzle blockage. Additionally, evidence of clumping was visible during examination of printed specimens (Figure 59a–b). Therefore, no mechanical testing was performed since satisfactory samples were not obtained.



(a) ElemX samples with NB incorporated into the print at 500x and (b) 6,500x magnification showing clustering of NB within the AA 4008 matrix. Adapted from [171].

Figure 59. SEM images of AA 4008 samples printed with NB additives.

2. Method 1: Pure Zn Strip Addition

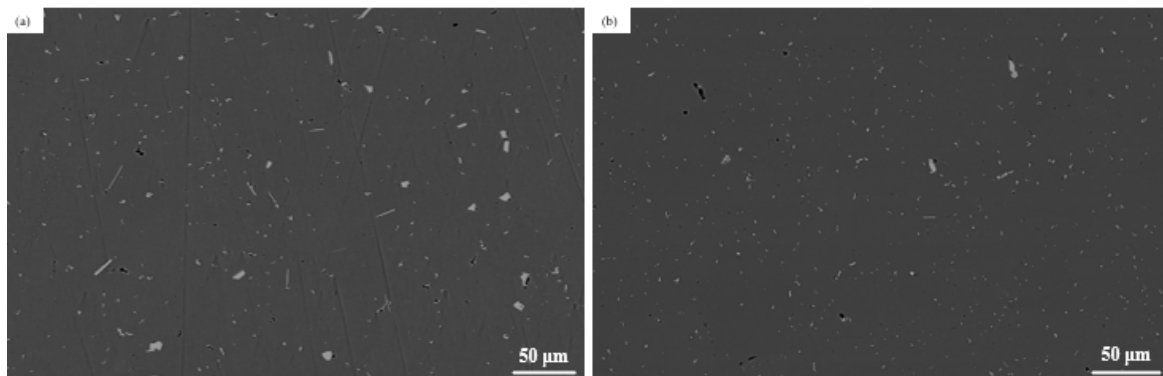
The first method to raise the Zn content of the printed AA 7075 samples was to add a strip of pure Zn as described in Chapter III.A.2.b.(2). The mass of the Zn wire was calculated to ensure the final Zn weight percentage (wt% Zn) of the sample was within the AA 7068 Zn range of 7.3 – 8.3 wt% Zn. A significant problem with this addition scheme was consistency; only four samples with properties approaching those of AA 7068 were obtained out of a total of 72 total samples—a success rate of only 5.6%. The properties of the four best samples are summarized in Table 8. Although these results were promising, they were still not quite to the expected levels for an increase of 2 wt% Zn from the literature (662 MPa and 4%, respectively). Materials characterization via SEM, EDS, and XRD were performed to look for reasons as to why these results fell short of the expected values.

Table 8. Summary of Zn-enriched AA 7075 samples (method 1)

Sample / Date	Heat Treatment	Microhardness (HV2)	UTS (MPa) / Ductility (%)
5/7/2024 #4	T6	201.11 ± 7.72	600.62 / 5.53
5/7/2024 #6	T6	197.80 ± 5.19	607.70 / 6.76
5/9/2024 #1	T6	197.0 ± 3.03	619.74 / 5.83
6/17/2024 #2	T6	198.56 ± 4.24	648.74 / 8.20
Average		198.56 ± 5.32	$619.20 \pm 18.37 / 6.58 \pm 1.04$

a. Materials Characterization

Except for the four samples in Table 8, all other samples were very brittle with low UTS values; upon visual inspection of the fracture surface, yellow and discolored areas were observed on unsatisfactory samples (Figure 37). Following sample preparation in accordance with Appendix B, the four samples in Table 8 were examined via SEM (BSE) to ensure sufficient distribution of precipitates. SEM micrographs of a Zn-enriched sample compared to a pure AA 7075 sample are shown in Figure 60. Long, needle-like precipitates were observed in all four Zn-enriched AA 7075 samples, but not in pure AA 7075.

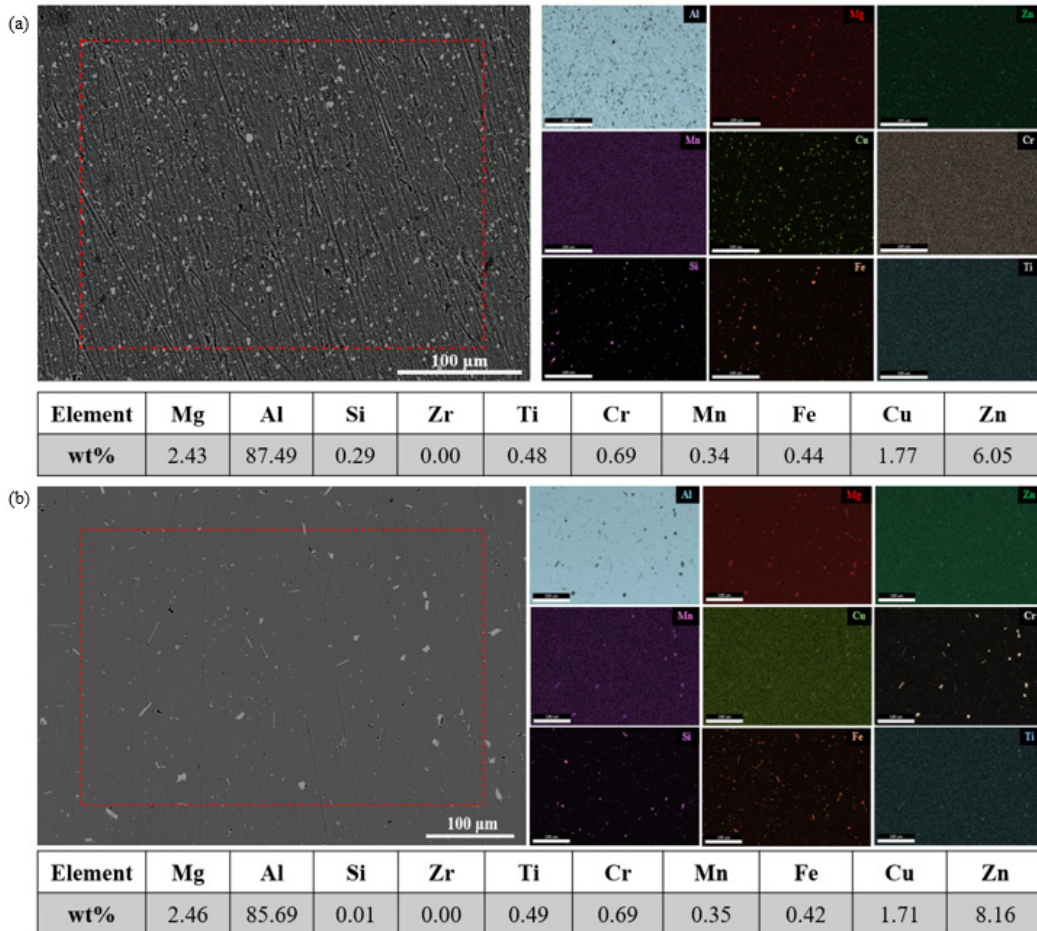


SEM micrographs of (a) Zn-enriched AA 7075 and (b) pure AA 7075 at 1000x magnification, showing similar distribution of precipitates throughout the aluminum matrix.

Figure 60. SEM micrograph comparison for Zn-enriched AA 7075 (method 1).

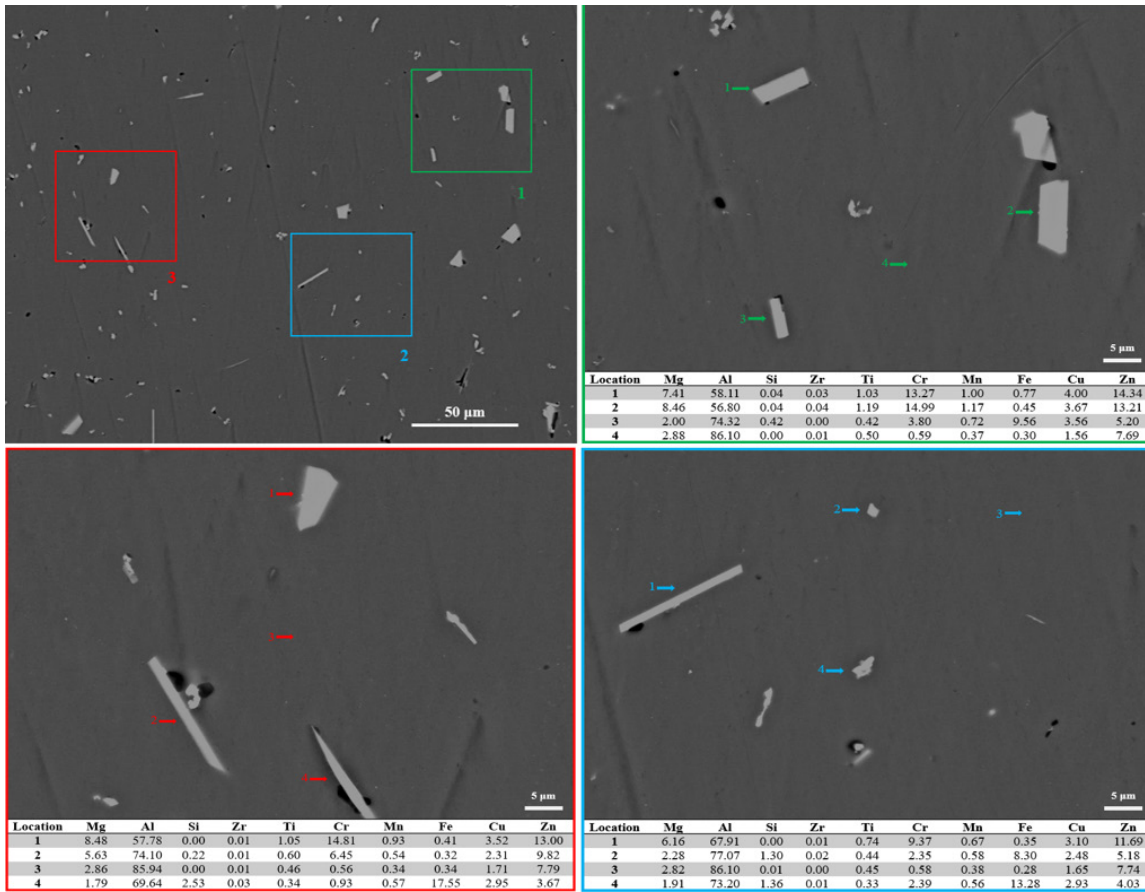
The needle-like precipitates contain elevated Mg, Fe, Cu, and Zn concentrations. In general, the stoichiometry of the precipitates did not exactly match, which is due to fluorescent radiation from other parts of the alloy besides the targeted precipitate during EDS. The presence of these precipitates is most likely due to the excess Zn added during the printing process. A standardless quantification using EDS mapping showed the alloy contained 8.16 wt% Zn, suggesting that Zn enrichment was successful when compared to the AA 7075 feedstock (Figure 61). Additionally, Mg and Zn are homogeneously distributed throughout EDS map and no Mg losses due to vaporization occurred. As with the AA 7075 printed samples, ω indicated by Fe-rich precipitates, S with Cu-rich Fe-poor precipitates, and $\text{Al}_2\text{Mg}_3\text{Zn}_3$ precipitates with high Cr content were identified via EDS

point analysis (Figure 62). Mg and Si are co-located in the EDS map in Figure 61b, which could correspond to the Mg_2Si precipitate.



(a) EDS map of AA 7075 feedstock wire and (b) EDS map of printed Zn-enriched AA 7075 (method 1) samples.

Figure 61. EDS mapping of Zn-enriched AA 7075 (method 1).



(top left) SEM micrograph of Zn-enriched AA 7075 at 1000x magnification, which was reproduced from Figure 61b with EDS sites marked. (remainder) Sites 1–3 present EDS results showing likely S, ω , and $\text{Al}_2\text{Mg}_3\text{Zn}_3$ precipitates in addition to higher Zn content in the matrix.

Figure 62. EDS results for Zn-enriched AA 7075 (method 1).

XRD analysis was relied upon to provide further proof of η precipitates as well as other intermetallics. The XRD spectrum shows peaks corresponding to the η , ω , and S precipitates (Figure 63). Interestingly, the peaks corresponding to all precipitates are higher than those observed from pure AA 7075. A peak corresponding to the S phase at 2θ value of $\sim 68^\circ$ is identified in the Zn-enriched AA 7075 (method 1) sample, but not in either the printed AA 7075 or the reference AA 7075 alloy. Similarly, more peaks corresponding to the η phase are seen at 2θ values of ~ 42 and 58 . The XRD spectrum for the Zn-enriched AA 7075 (method 1) shows evidence that Zn enrichment successfully increased the distribution of η precipitates and should result in improved mechanical properties.

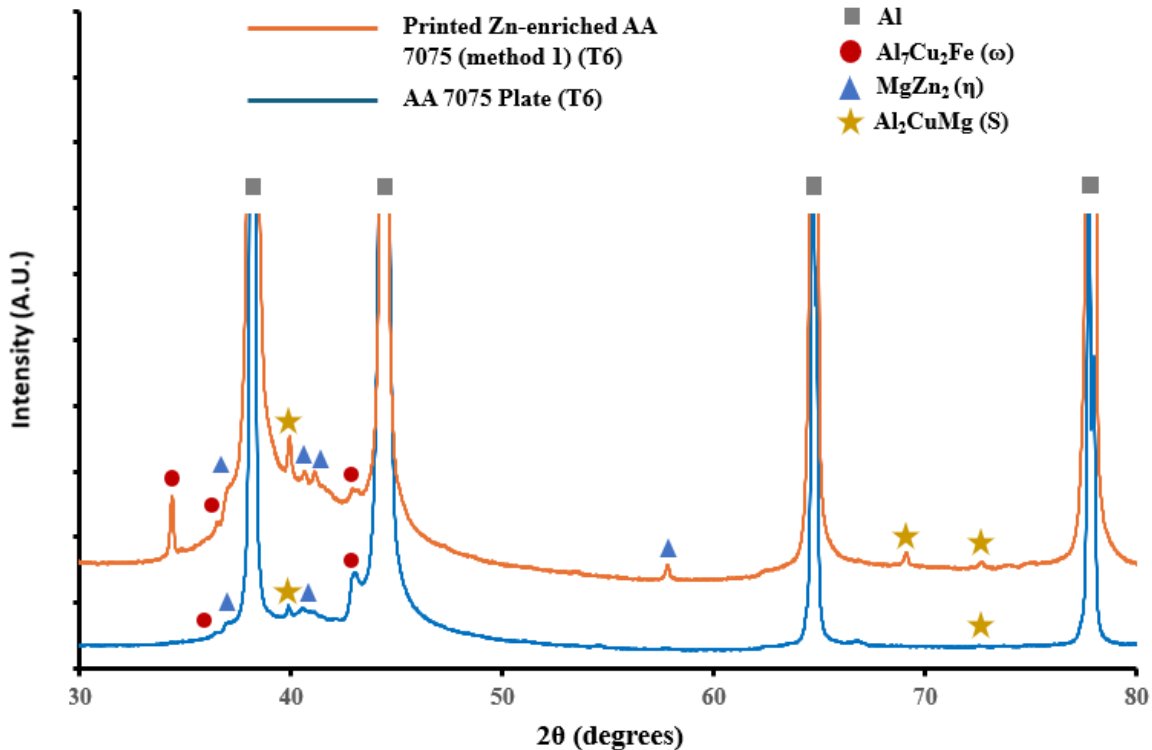


Figure 63. XRD of Zn-enriched AA 7075 samples (method 1).

b. Materials Testing

After T6 heat treatment, microhardness measurements of the Zn-enriched AA 7075 (method 1) samples were taken to verify alloy quality. Vickers Hardness (HV2) tests were performed on these samples due to the expected higher hardness from the Zn addition. Microhardness results across all four samples were 198.56 ± 5.32 , which was near the expected value of 200 for AA 7068. This indicates no degradation of the alloy or Zn loss during printing at $\sim 700^\circ\text{C}$. All sample points from the samples with Zn addition had higher hardness values than those of just AA 7075 (Figure 64). However, there was a higher distribution of the microhardness data, particularly for samples 1 and 2, compared to that of the AA 7075 plate and samples (Figure 65). The higher distributions of samples 1 and 2 suggest nonhomogeneous mixing of Zn within the alloy when added to the ElemX print head, partially corroborating the observations shown in Figure 37.

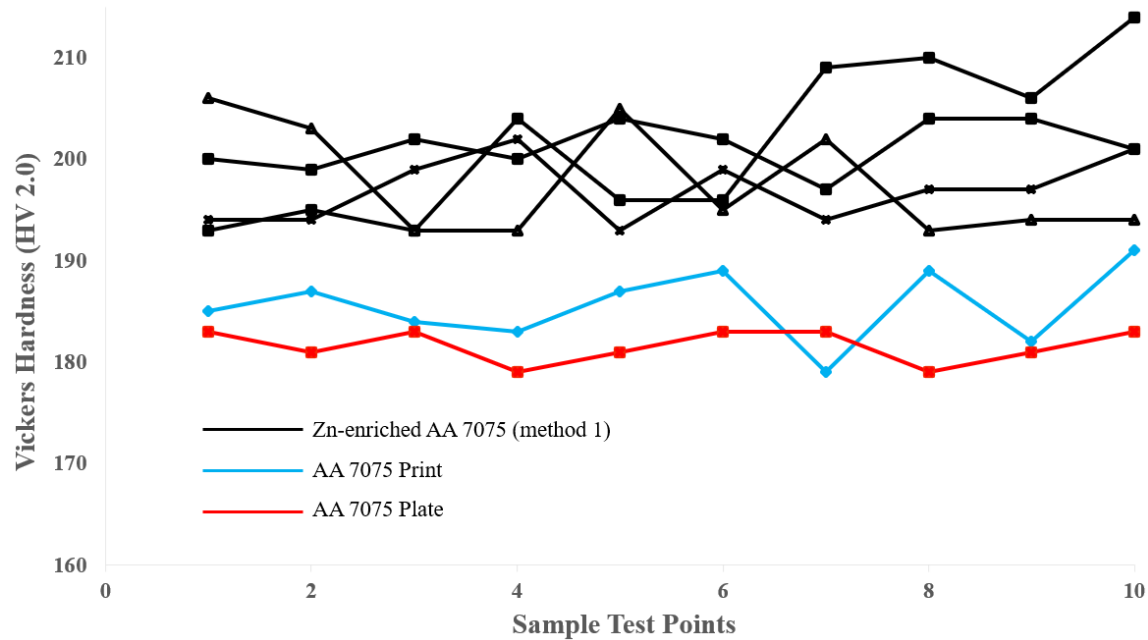


Figure 64. Microhardness measurements of AA 7075 and Zn-enriched AA 7075 (method 1).

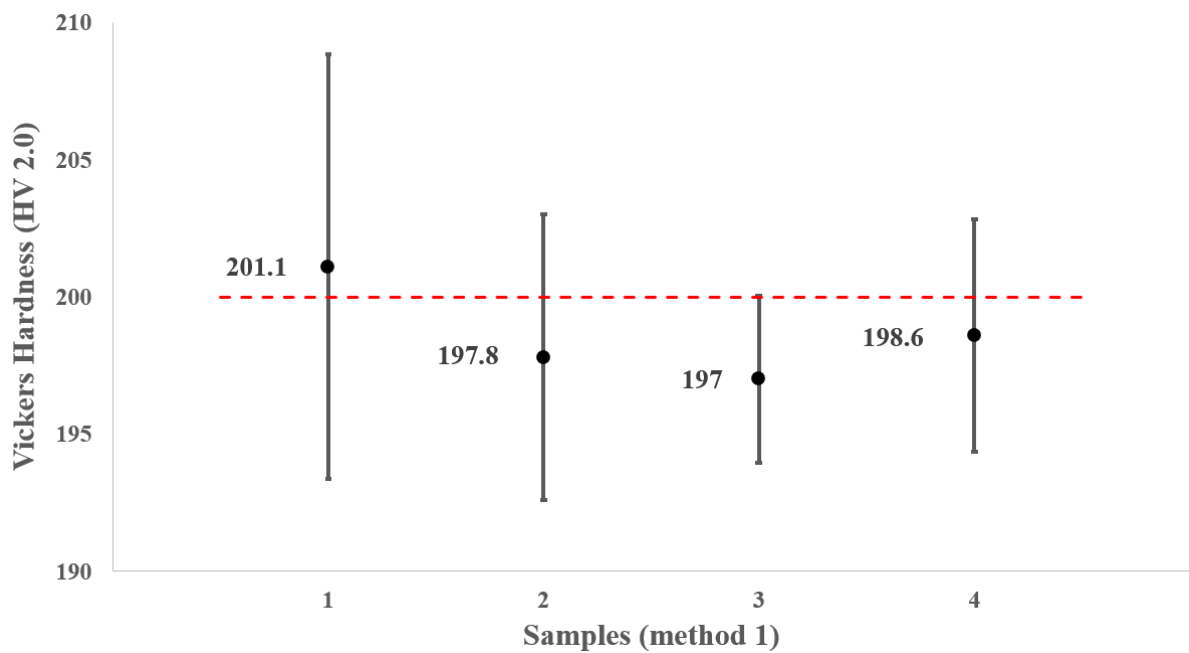


Figure 65. Microhardness measurements of Zn-enriched AA 7075 (method 1).

The tensile test results are shown in Figure 66 for the pure AA 7075 samples with substrate temperature 500°C versus the Zn-enriched AA 7075 (method 1) samples. The measured UTS and ductility values for the Zn-enriched AA 7075 (method 1) samples were $\sigma_{true}^{method\ 1} = 619.20 \pm 18.37$ MPa and $\varepsilon_{fail}^{method\ 1} = 6.58 \pm 1.04$ %, respectively. The red dashed lines displayed on Figure 66 lie at the nominal UTS and ductility values of AA 7068. Although the UTS of the Zn-enriched AA 7075 (method 1) samples were all above the pure AA 7075 samples, the UTS was still well below that of AA 7068. Additionally, the ductility of all Zn-enriched AA 7075 (method 1) samples was below both the pure AA 7075 samples and AA 7068 specification. The specific strength of the Zn-enriched AA 7075 (method 1) samples was calculated, and the value was calculated to be between the ranges of steel and titanium alloys produced by M-AM due to the lower ductility compared to pure AA 7075 (Figure 67).

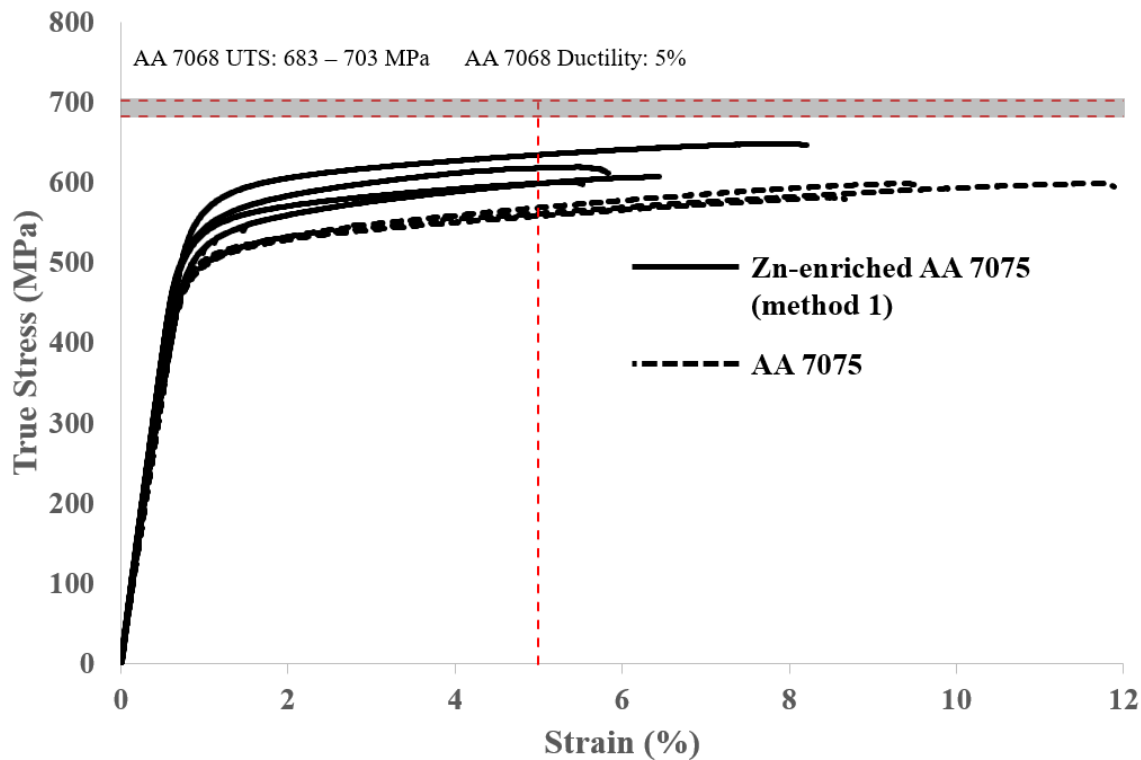


Figure 66. Stress-strain curves of 3D printed tensile specimens of AA 7075 with a 500°C substrate (dashed lines) and Zn-enriched AA 7075 (method 1, solid lines).

$$UTS = 619.20 \text{ MPa}$$

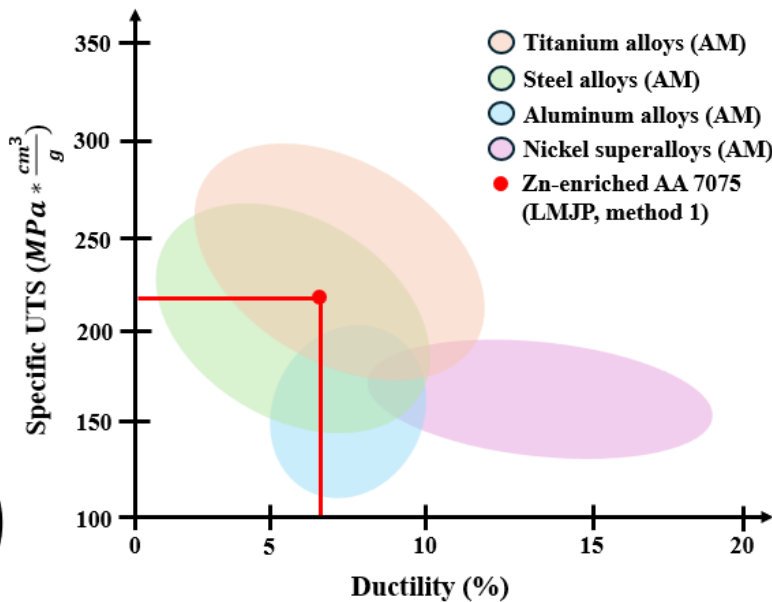
$$\text{Ductility} = 6.58 \%$$

Specific Strength

$$= \frac{UTS}{\text{Density}}$$

$$= \frac{619.20 \text{ MPa}}{2.85 \frac{\text{g}}{\text{cm}^3}}$$

$$= 217.26 \left(\text{MPa} * \frac{\text{cm}^3}{\text{g}} \right)$$



Adapted from [55].

Figure 67. Specific strength of Zn-enriched AA 7075 (method 1) compared to other alloys produced via AM methods.

3. Method 2: Zn-enriched AA 7075 Wire Addition

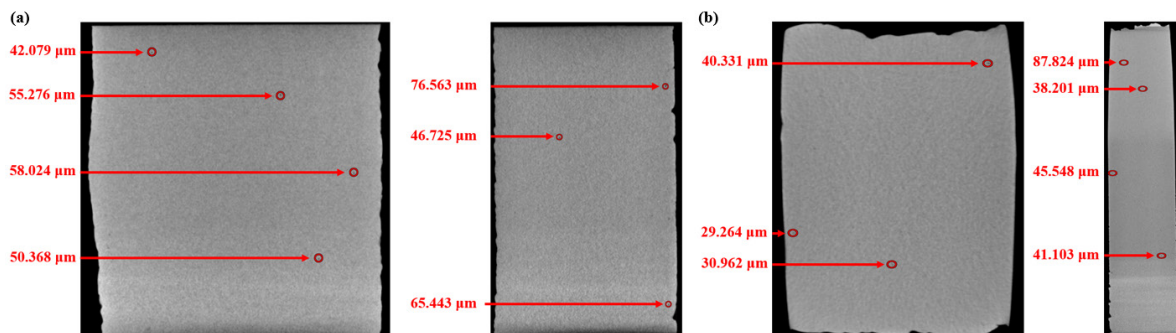
The second method to raise the Zn content of the printed AA 7075 samples was via the addition of a wire printed with an elevated Zn content, as described in Chapter III.A.2.b.(3). Much more consistent results were obtained using this methodology—50% of the samples produced were satisfactory (four out of eight)—and those samples are summarized in Table 9. The results show significant improvement over method 1, with ~25 MPa improvement in UTS and almost double the ductility (~6% improvement). UTS results fell a little short, but the ductility results were well above the expected values for an increase of 2 wt% Zn from the literature (662 MPa and 4%, respectively). Materials characterization via SEM, EDS, and CT scans were performed to understand these results.

Table 9. Summary of Zn-enriched AA 7075 samples (method 2).

Sample / Date	Heat Treatment	Microhardness (HV2)	UTS (MPa) / Ductility (%)
8/2/2024 #1	T6	196.3 ± 3.52	656.01 / 13.84
8/2/2024 #3	T6	198.1 ± 1.37	651.68 / 13.57
8/17/2024 #2	T6	200.0 ± 3.46	645.07 / 11.34
8/17/2024 #3	T6	199.2 ± 2.68	626.07 / 8.30
Average		198.4 ± 3.21	$644.77 \pm 11.45 / 11.76 \pm 2.22$

a. Materials Characterization

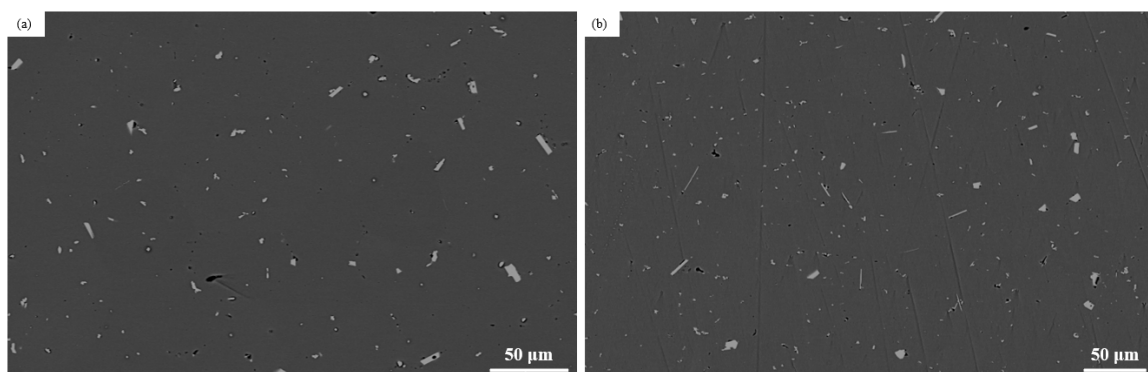
A Zn-enriched AA 7075 (method 2) sample was examined via CT scan to determine if the sample was free of major internal defects with low porosity. The Zn-enriched AA 7075 (method 2) sample porosity was measured to be 0.05% compared to 0.04% for pure AA 7075 samples; therefore, a substrate temperature of 500°C is a sufficiently high temperature to eliminate hot cracking and porosity even with an elevated Zn content. Representative cross-section scans of both pure AA 7075 and Zn-enriched AA 7075 (method 2) in Figure 68 show similar ranges in defects in addition to very similar porosity percentages.



Side-by-side comparison of (a) pure AA 7075 sample printed with a 500°C substrate temperature and (b) Zn-enriched AA 7075 (method 2) sample also printed with a 500°C substrate temperature.

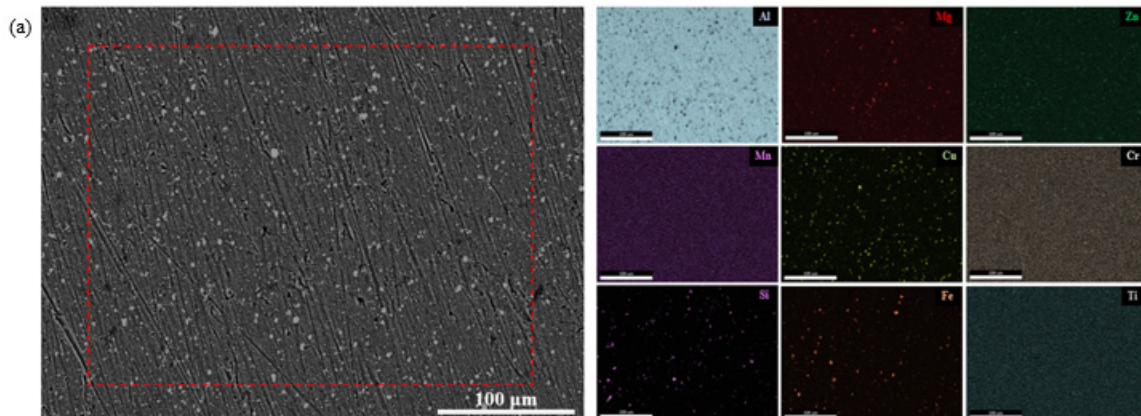
Figure 68. CT scans of pure and Zn-enriched AA 7075 samples (method 2) printed with substrate temperature 500°C.

Following sample preparation in accordance with Appendix B, the four samples in Table 9 were examined via SEM (BSE). The Zn-enriched AA 7075 (method 2) samples show adequate distribution of precipitates; however, the longer, needle-like precipitates were not observed (Figure 69). The likely reason for the lack of those precipitates is a lower Zn concentration, which was confirmed to be 6.70 wt% via a standardless quantification using EDS mapping (Figure 70). As with method 1, Mg and Zn are homogeneously distributed throughout EDS map and no Mg losses due to vaporization occurred. From EDS point analysis in Figure 71, precipitates corresponding to ω (Fe-rich), S (Cu-rich, Fe-poor), and $\text{Al}_2\text{Mg}_3\text{Zn}_3$ (high Mg, Zn, and Cr). As with method 1, Mg and Si appear to be co-located in the EDS map in Figure 70b, which could correspond to the Mg_2Si precipitate. Based on SEM and EDS observations and measurements, the Zn content of samples from method 2 is lower than samples from method 1, but there are still the expected precipitates for AA 7075. Therefore, the mechanical properties of Zn-enriched AA 7075 (method 2) are expected to be similar or superior to Zn-enriched AA 7075 (method 1).

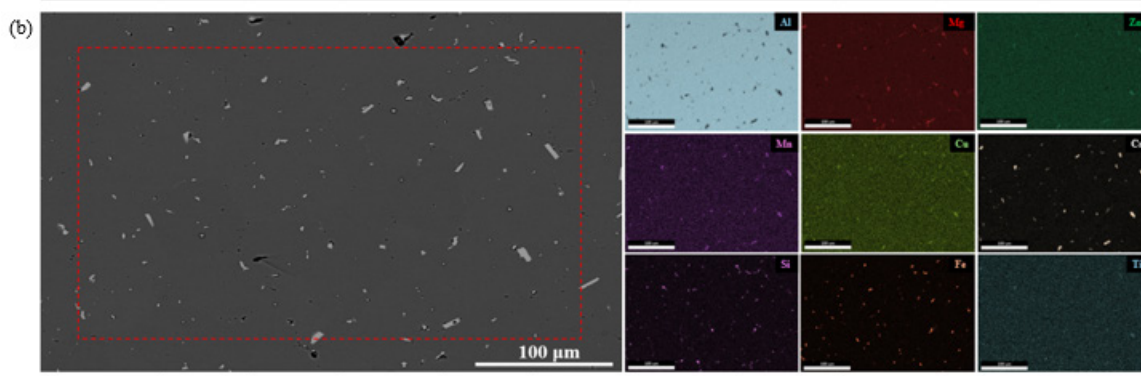


SEM micrographs of (a) Zn-enriched AA 7075 (method 2) and (b) Zn-enriched AA 7075 (method 1) at 1000x magnification, showing similar distribution of precipitates throughout the aluminum matrix.

Figure 69. SEM micrograph comparison for Zn-enriched AA 7075 samples via both enrichment methods 1 and 2.



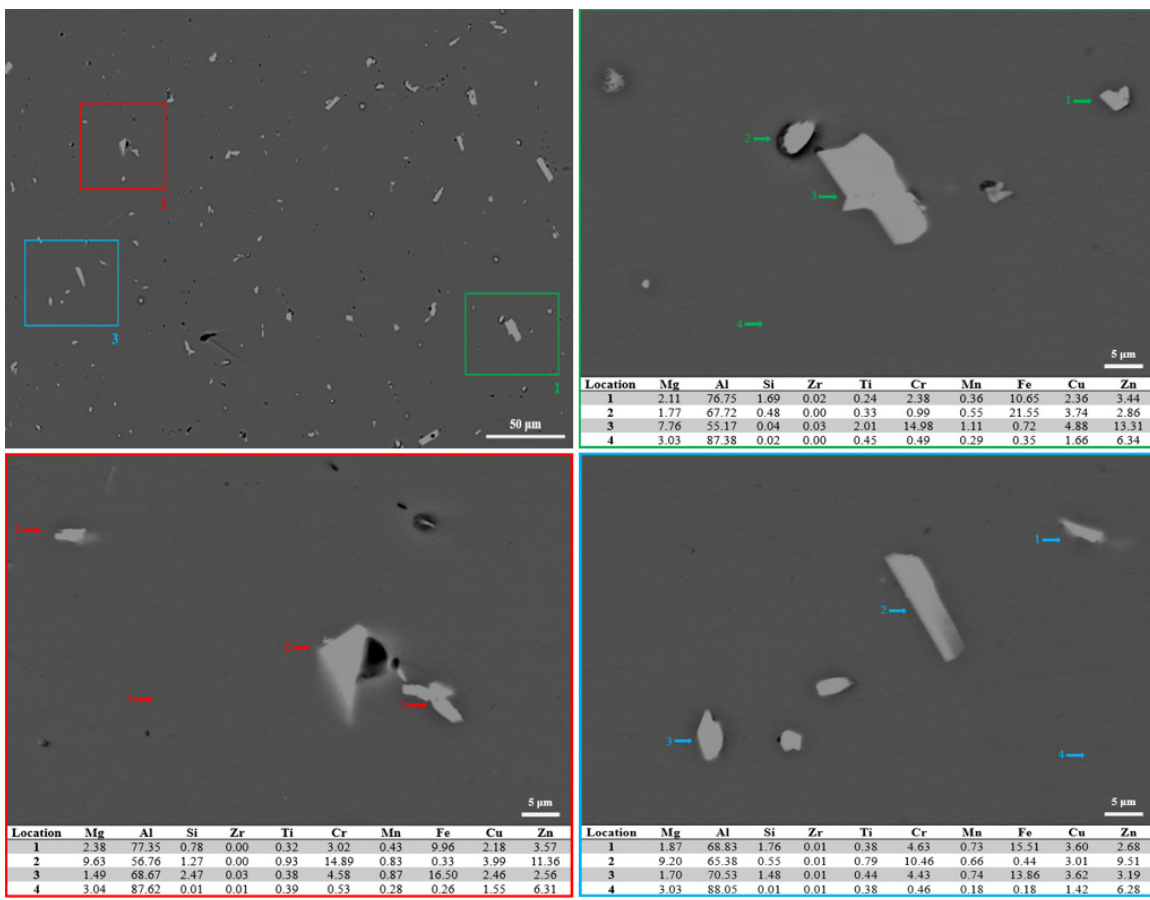
Element	Mg	Al	Si	Zr	Ti	Cr	Mn	Fe	Cu	Zn
wt%	2.43	87.49	0.29	0.00	0.48	0.69	0.34	0.44	1.77	6.05



Element	Mg	Al	Si	Zr	Ti	Cr	Mn	Fe	Cu	Zn
wt%	2.66	86.56	0.06	0.00	0.56	0.77	0.41	0.48	1.80	6.70

(a) EDS map of AA 7075 feedstock wire and (b) EDS map of printed Zn-enriched AA 7075 (method 2) samples.

Figure 70. EDS mapping of Zn-enriched AA 7075 (method 2).



(top left) SEM micrograph of Zn-enriched AA 7075 at 1000x magnification, which was reproduced from Figure 69a with EDS sites marked. (remainder) Sites 1–3 present EDS results showing likely S, ω , and $\text{Al}_2\text{Mg}_3\text{Zn}_3$ precipitates in addition to higher Zn content in the matrix.

Figure 71. EDS results for Zn-enriched AA 7075 (method 2).

As before, XRD analysis was relied upon to provide further proof of η precipitates as well as other intermetallics. Peaks corresponding to the η , ω , and S precipitates at the same 2θ values are identified (Figure 72). Like method 1, the peaks corresponding to all precipitates in method 2 are higher than those observed from pure AA 7075, and the extra peaks corresponding to the S and η phases are also present. The XRD spectrum for the Zn-enriched AA 7075 (method 2) shows evidence that Zn enrichment via method 2 was also successful at increasing the distribution of η precipitates and should also result in improved mechanical properties.

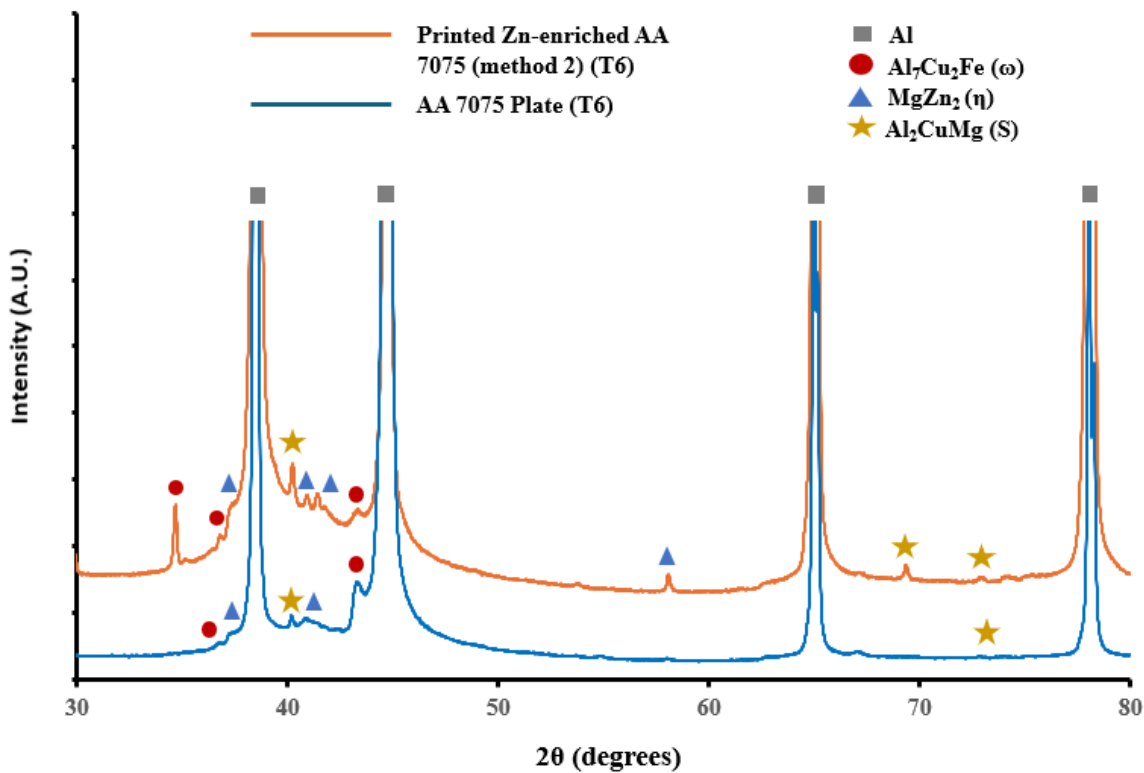


Figure 72. XRD of Zn-enriched AA 7075 samples (method 2).

b. Materials Testing

After T6 heat treatment, microhardness measurements (HV2) of the Zn-enriched AA 7075 (method 2) samples were taken to verify alloy quality. Like method 1, all points from method 2 samples had higher microhardness values than those of pure AA 7075 (Figure 73). Microhardness results across all four samples were 198.4 ± 3.21 , which is similar to method 1 (198.56 ± 5.32) and near the expected value of 200 for AA 7068 (Figure 74). The lower distribution of hardness values for the Zn wire samples suggests a more thorough mixing of Zn within the alloy is achieved when the Zn is initially added to the alloy and the resulting Zn-enriched wires are used as the feedstock.

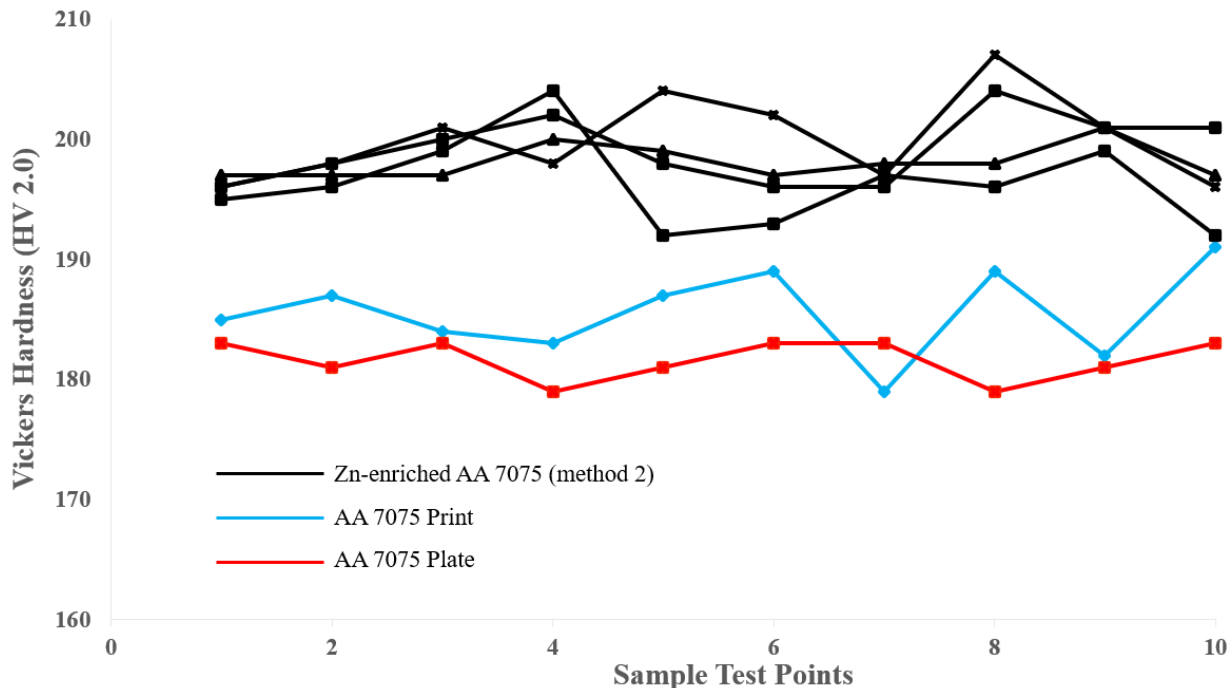


Figure 73. Microhardness measurements of AA 7075 and Zn-enriched AA 7075 (method 2).

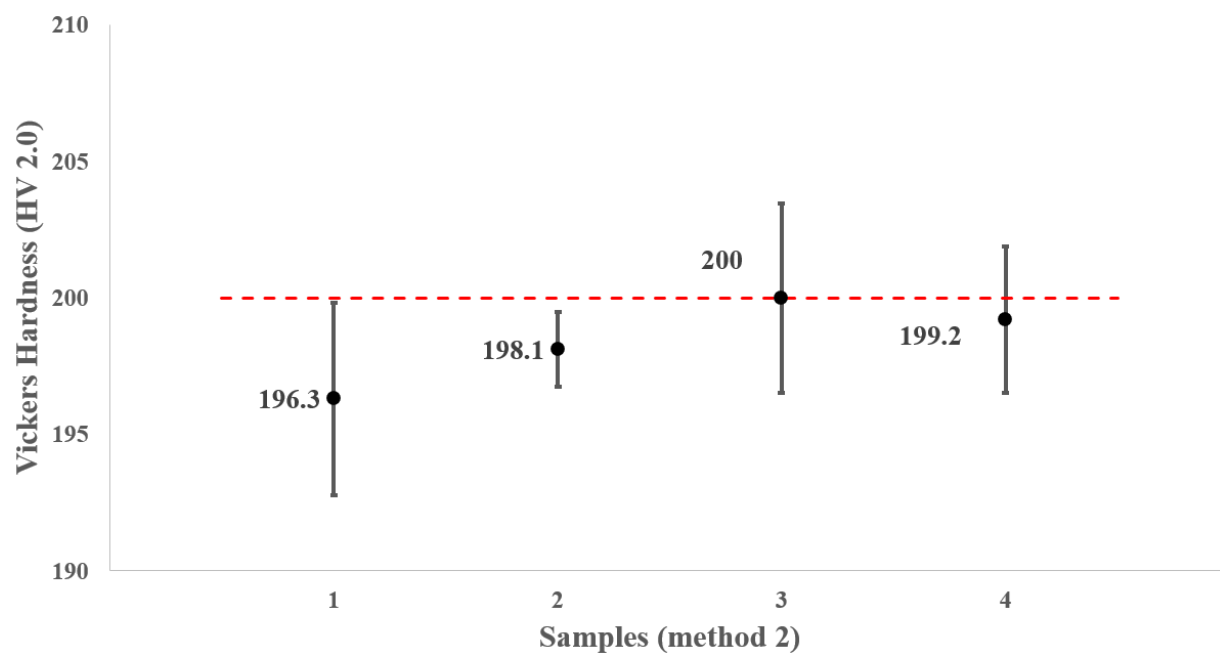


Figure 74. Microhardness measurements of Zn-enriched AA 7075 (method 2).

The tensile test results are shown in Figure 75 for the pure AA 7075 samples with substrate temperature 500°C versus the Zn-enriched AA 7075 (method 2) samples. The measured UTS and ductility for the Zn-enriched AA 7075 (method 2) samples were $\sigma_{true}^{method\ 2} = 644.77 \pm 11.45$ MPa and $\varepsilon_{fail}^{method\ 2} = 11.76 \pm 2.22$ %, respectively. The UTS and ductility of the Zn-enriched AA 7075 (method 2) samples were all above the pure AA 7075 samples, but the UTS was still below that of AA 7068. Zn enrichment is sufficient to improve AA 7075 mechanical properties, but not enough to match those of AA 7068. The specific strength of the Zn-enriched AA 7075 (method 2) samples was calculated, and the value was calculated to be at the edge of the range for titanium alloys produced by M-AM due to the higher UTS and ductility compared to pure AA 7075 (Figure 76).

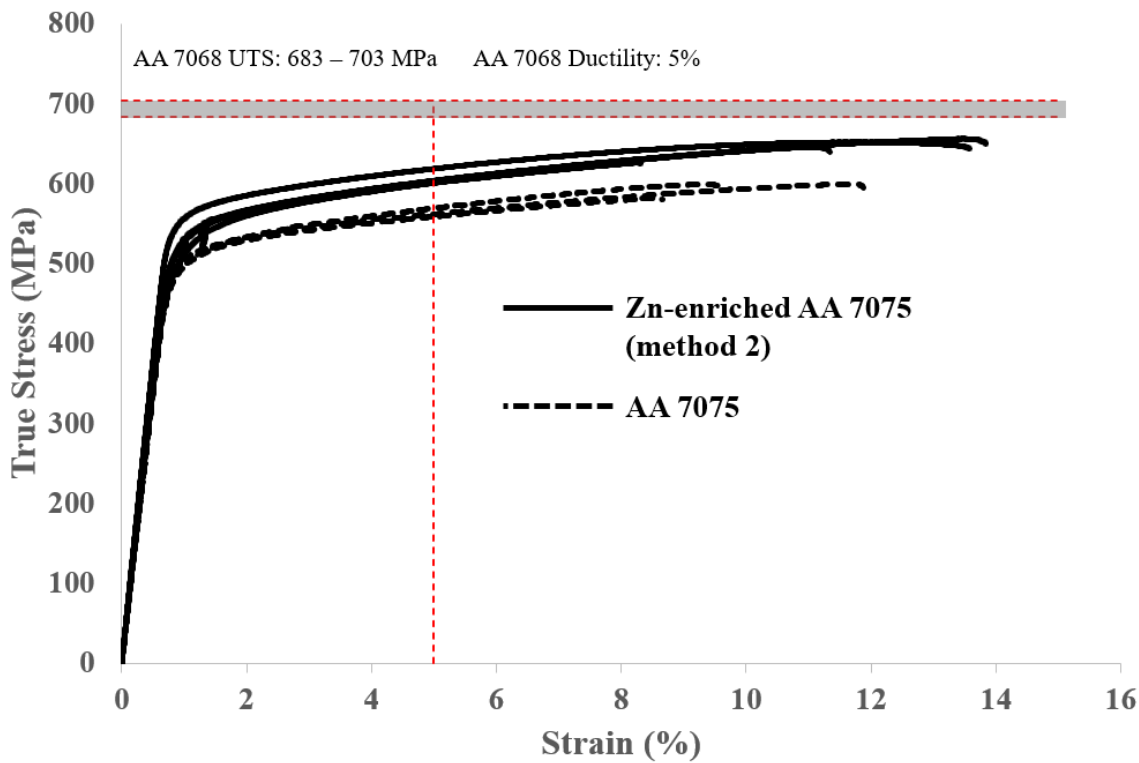


Figure 75. Stress-strain curves of 3D printed tensile specimens of AA 7075 with a 500°C substrate (dashed lines) and Zn-enriched AA 7075 (method 2, solid lines).

$$UTS = 644.77 \text{ MPa}$$

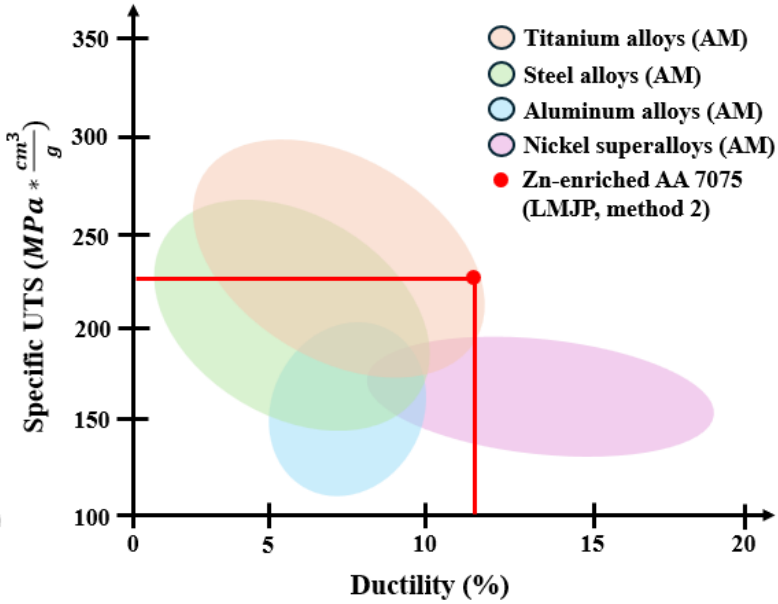
$$\text{Ductility} = 11.76 \%$$

Specific Strength

$$= \frac{UTS}{\text{Density}}$$

$$= \frac{644.77 \text{ MPa}}{2.85 \frac{\text{g}}{\text{cm}^3}}$$

$$= 226.24 \left(\text{MPa} * \frac{\text{cm}^3}{\text{g}} \right)$$



Adapted from [55].

Figure 76. Specific strength of Zn-enriched AA 7075 (method 2) compared to other alloys produced via AM methods.

B. PRELIMINARY FINDINGS

Particle strengthening of AA 7075 achieved a mix bag of results. No mechanical testing was achieved with NB addition due to difficulties printing samples. Zn enrichment of AA 7075 via method 1 produced four samples with UTS superior to pure AA 7075, but with lower ductility. However, the other 68 samples printed via method 1 had poor UTS and ductility. Zn enrichment of AA 7075 via method 2 produced four samples with both UTS and ductility superior to pure AA 7075. The average mechanical properties of the four best Zn-enriched AA 7075 samples from method 1 and 2 are summarized below.

- Method 1: Microhardness (HV2) = 198.56 ± 5.32 , $\sigma_{true}^{method\ 1} = 619.20 \pm 18.37 \text{ MPa}$, $\varepsilon_{fail}^{method\ 1} = 6.58 \pm 1.04$, and specific strength = 217.26
- Method 2: Microhardness (HV2) = 198.4 ± 3.21 , $\sigma_{true}^{method\ 2} = 644.77 \pm 11.45 \text{ MPa}$, $\varepsilon_{fail}^{method\ 2} = 11.76 \pm 2.22$, and specific strength = 226.24

Both method 1 and 2 samples were printed at a substrate temperature of 500°C, further demonstrating the importance of a high substrate temperature to a crack and

porosity-free microstructure for 7XXX series aluminum alloys. Method 2 provided superior Zn mixing, producing Zn-enriched AA 7075 with materials properties nearly equivalent to that of previous research via Zn enrichment (662 MPa and 4%) and approaching AA 7068 (683–703 MPa and 5%). The ductility of the method 2 samples exceeded that of the previous research, indicating Zn mixing within the AA 7075 was successful and uniform. Once again, high substrate temperatures were demonstrated to be key to successfully producing hot cracking susceptible alloys via the LMJP process, which has not been demonstrated via any other M-AM process.

VI. GRADIENT INFILL OF ALUMINUM ALLOYS

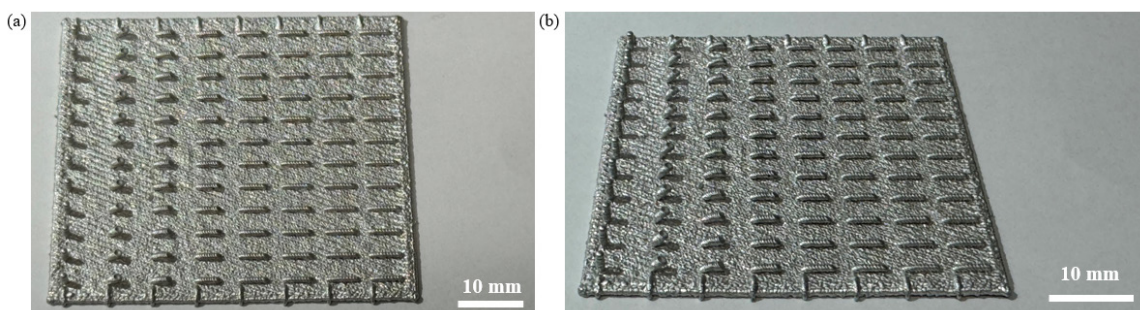
In this chapter, the results of printing variable infill AA 4008 samples by modification of the G-code output of the ElemX Builder slicer software is discussed. The research in this chapter builds upon the successful printing sparse infill aluminum components using multiple, nested printing operations by former students ENS Victor Wang and LT Kristofer Misch. The relevant literature review, introduction, and methodology are covered in Chapters II and III. The results of printing accomplished using a custom code to modify the G-code output of the ElemX printer are presented in this chapter. However, the results are qualitative and based on observation only since the code has not been perfected to be able to print parts suitable for mechanical testing.

A. RESULTS / DISCUSSION

The results of tuning the infill droplet placement and minimizing infill density were qualitatively assessed to determine the efficacy of the code for modifying the ElemX prints.

1. Infill Droplet Placement

Initial testing with a code to modify the infill of a printer was deliberately simple before moving to a more complex geometry. After printing a 50 mm x 50 mm test substrate, droplets were stacked at various angles from vertical (90°) to horizontal (0°) to demonstrate proper operation of the code, as shown in Figure 77.

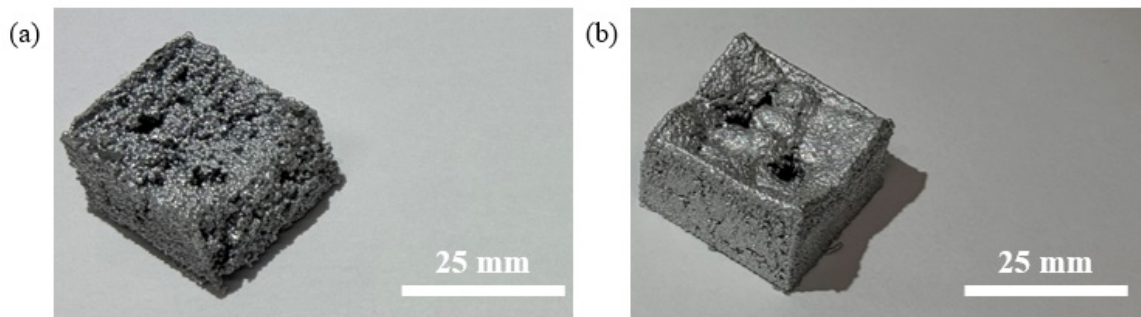


Overhead view of a 50 mm x 50 mm test substrate showing stacked droplets and (b) an angled view to show the change in stack angle achieved.

Figure 77. Results of initial droplet placement using modified G-code.

2. Minimizing Infill Density

Following the results of droplet placement, the same technique was applied to a 25 mm x 25 mm x 10 mm test cube with a designed gradient infill. Initially, a delay either before or after the gradient infill was tested to inform follow-on experimentation. The two best results came from the no delay and delay before cases, shown in Figure 78. However, both samples were too delicate to section with a band saw so no information on the gradient infill was obtained besides a very sunken top roof structure and porous-looking sides.



No delay and (b) delay before gradient infill prints

Figure 78. Gradient infill prints with delays.

To address the sunken roof of the initial gradient infill prints, a modification to the code to incorporate a droplet extrusion multiplier (DEM) was incorporated. DEM was applied to the E parameter during gradient infill to increase the amount of aluminum extruded during those print operations. However, an increase in DEM, although successful in raising the top of the infill to the perimeter, did not result in uniform, consistent results as shown in Figure 79.

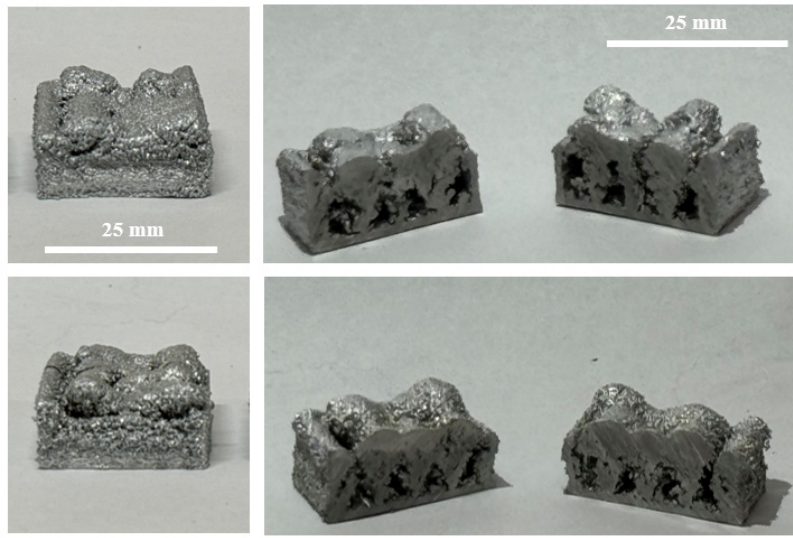
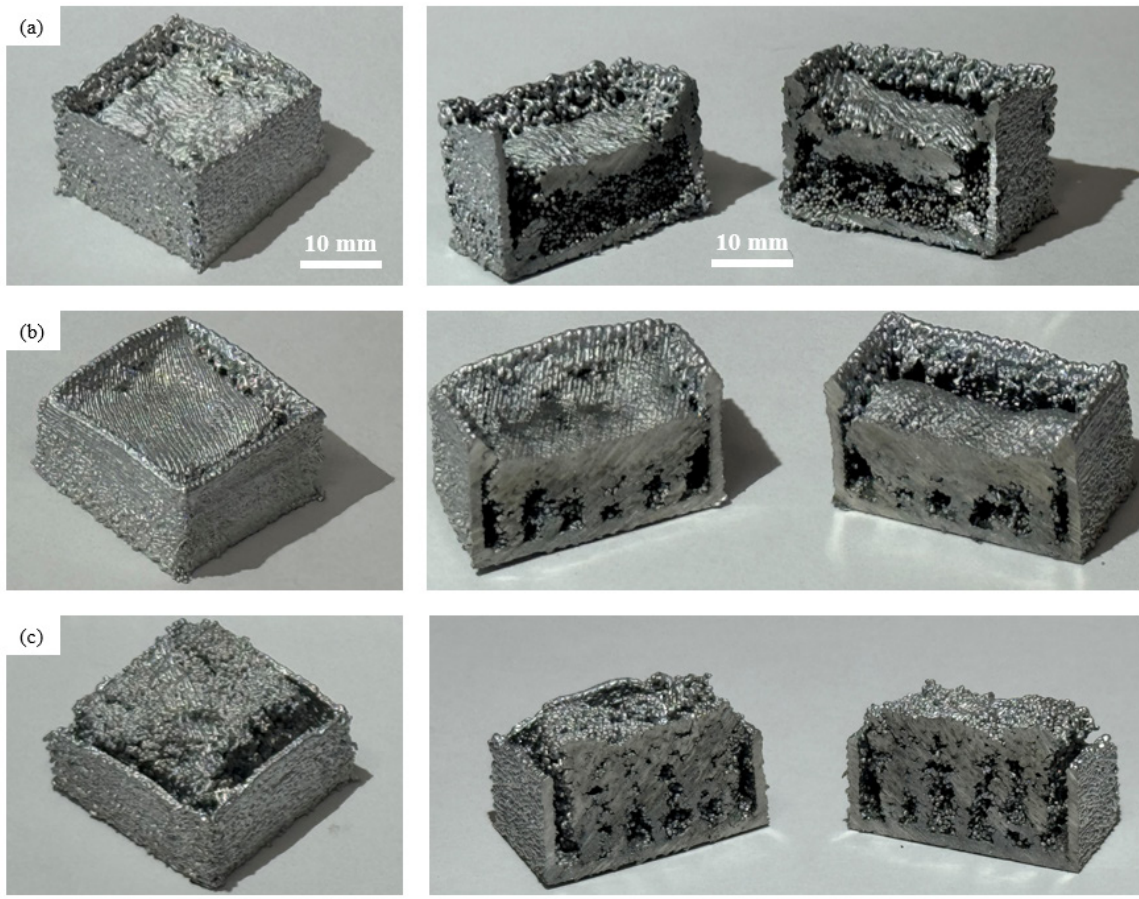


Figure 79. Samples printed with DEM of 3.0.

Since print modification solely with DEM was insufficient, the NxN search and collision kernels were implemented to achieve more reproduceable results. During testing using 3x3 kernels, overlapping along just the X or Y axis showed poor overhang performance, and diagonal overlapping droplets failed to stack upwards, instead settling into the voids between previous droplets. Therefore, a higher resolution kernel for both search and collision (5x5) and a corner radius of 1 were implemented. The changes resulted in improved infill and less of a sunken roof, and results improved as DEM was increased from 0.5 to 1.0, as shown in Figure 80.



Samples printed with 5x5 search and collision kernel size and a corner radius of 1 with DEM of (a) 0.5, (b) 0.75, and (c) 1.0.

Figure 80. Samples printed with 5x5 search and collision kernel size.

B. PRELIMINARY FINDINGS

Using custom G-code modification software, the ability to print samples with variable infill was demonstrated. Using a combination of DEM and search/collision kernels, samples with variable infill were produced, but not consistently or with any mechanical integrity. Further tuning of the code and parameters is required to optimize the performance and to truly produce quality variable infill parts like the ones produced with multiple printing operations (Figure 25). Additionally, a means of quantifying the amount of infill must be explored to determine how closely the printed sample compares to the variable infill target of the code.

VII. EXPEDITIONARY METAL ADDITIVE MANUFACTURING

Parts of this chapter were previously published by *The Phalanx* [160]. The text and figures have been modified for better applicability within the chapter. The relevant literature review, introduction, and methodology was covered in Chapters II and III. Two exercises, SALVAGE EXERCISE 2024 and TRIDENT WARRIOR 2024, provided invaluable experience to the DON for the use of M-AM for BDA/R and contested logistics.

A. SALVAGE EXERCISE 2024

One of the great applications of M-AM is in Battle Damage Assessment and Repair (BDA/R). To streamline all lines of effort around BDA/R, the Navy has developed the Ship Wartime Repair and Maintenance (SWaRM) concept of operations (CONOPs). One of the classic historical BDA/R case studies is that of the USS Yorktown repair during World War II (WWII). Fleet Admiral Nimitz is infamous for telling the incredulous shipyard workers they had three days to fix all the damage incurred by the aircraft carrier during the Battle of the Coral Sea [172]. All repairs were successfully completed, perhaps not to the original condition, but satisfactory for at sea operations just in time for the Battle of Midway. Since WWII, the Navy has not had many opportunities to exercise BDA/R concepts, which was a major finding of a Government Accountability Office (GAO) report to Congress on June 2, 2021 [155]. As a result, the Navy has designed and executed various BDA/R exercises to regain proficiency in this critical area.

BDA/R exercises have been performed on a variety of Navy platforms, including both commissioned and decommissioned warships. The first such exercise was performed on the ex-Bonhomme Richard (BHR) while she was under tow for final scrapping in Brownsville, Texas in 2021. The BHR fire and her subsequent loss was a large driving factor behind the DON's emphasis on BDA/R; since then, the EDO community has taken advantage of all opportunities to demonstrate BDA/R and validate the SWaRM CONOPs, as summarized in Table 10. So far, BDA/R exercises have provided invaluable experience with unexploded ordnance (UXO) disposal, underwater cutting and welding at sea, cofferdam installation and dewatering, repair patch design and installation, and emergency towing and dry docking

operations [173], [174], [175], [176], [177], [178]. However, M-AM techniques have yet to be tested during a BDA/R scenario despite their capability to produce one of a kind, custom metal parts that are not readily available through the supply chain.

Table 10. Summary of previous BDA/R exercises.

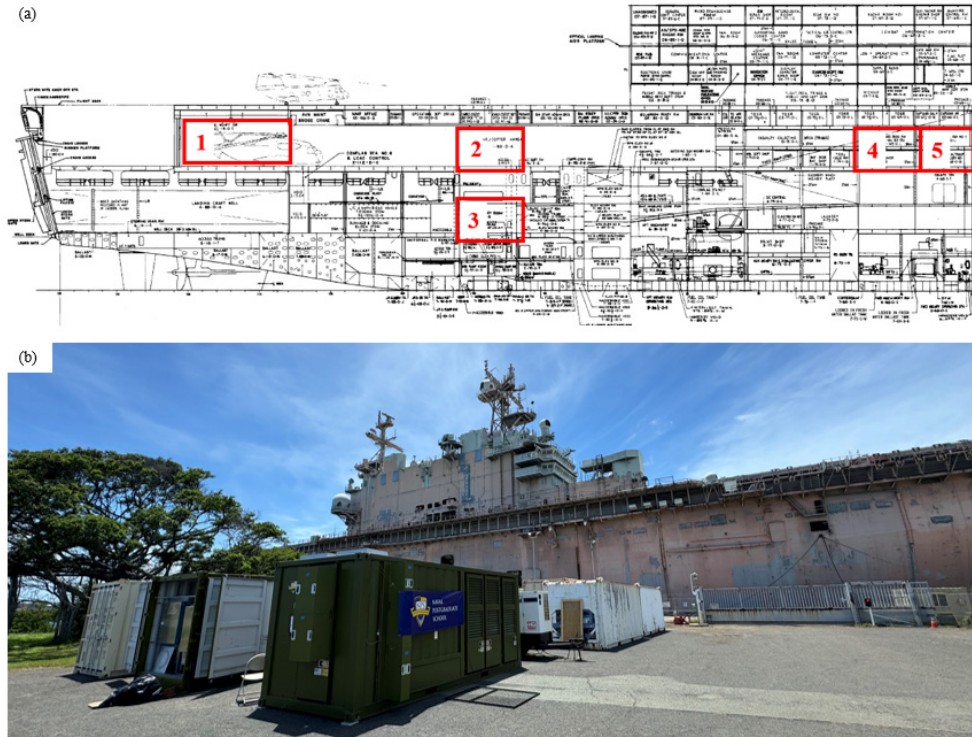
Date	Platform	Repairs and Capabilities Demonstrated
26 May–03 June 2021	ex-USS BONHOMME RICHARD	Underwater welding and cutting, emergency patch design and install, emergency dewatering.
30 December 2021–26 May 2022	USS CHANCELLORSVILLE (CG-62)	Emergent dry docking to repair the port shaft due to a real casualty during operations.
21 March–04 April 2022	ex-USS BOONE	Underwater patching and welding, cutting, rigging, at sea diving and damage assessment
19–28 June 2022	ex-USS DENVER	Human effects explosive testing, Unexploded ordnance (UXO) identification and removal, confined space diving, repair patch welding, emergency dewatering and towing.
21–23 May 2023	USS GLADIATOR (MCM 11)	UXO identification and removal, cofferdam installation, dewatering, underwater patch installation, towing

Adapted from [173], [174], [175], [176], [177], [178].

1. Exercise Overview

Building on the previous exercises to validate the SWaRM CONOPS, S24 was envisioned as the next iteration in the DON’s BDA/R exercise series. Pearl Harbor Naval Shipyard (PHNSY) and NAVSEA 05 took the lead for exercise planning, and an opportunity to conduct S24 on the ex-TARAWA was identified. The ex-TARAWA was designated as the ship for the upcoming sinking exercise (SINKEX) in Rim of the Pacific Exercise (RIMPAC) 2024, making it the perfect place to damage some key ship systems and experiment with new repair methods. S24 was timed for late May–early June 2024 on a not-to-interfere schedule with RIMPAC 2024. The ex-TARAWA was mechanically damaged in several compartments in a simulated battle scenario, and the ship was turned over to the exercise team to evaluate the damage and repair the ship in the most expeditious way possible. The compartments that

received “battle damage” are identified as 1–5 in Figure 81a and are described in detail in Table 11 [160]. Exercise participants were given very specific timelines to produce the required repairs or parts based on a deadline to get the ex-TARAWA underway to join combat operations. After receiving simulated battle damage, the ex-TARAWA was shifted to a pier at Ford Island, which is where the exercise took place as seen in Figure 81b with the XSPEE3D and SPEE3D Cell set up in the foreground. The other participants in the exercise set up their machines and equipment, most of which were containerized as well, either on the pier next to ex-TARAWA or in the vicinity of the XSPEE3D and SPEE3D Cell. Since NPS was already slated for TW24 participation, the support of S24 presented an opportunity to demonstrate the potential of M-AM for BDA/R.



(a) Side view of ex-TARAWA showing the five damaged areas. Adapted from [179]. (b) Ex-TARAWA at the Ford Island pier with XSPEE3D and SPEE3D Cell in the foreground.

Figure 81. The ship for S24, ex-TARAWA.

Table 11. Summary of S24 damaged spaces and repairs.

Space Number	Space name	Damage
1	Port Diesel Generator	Seawater cooling system for the generator set
2	Port Hangar AFFF	Hangar firefighting and AFFF supply systems
3	Port Hangar Door Hydraulics	Gasket damage to hydraulic pump and accumulator
4	Hangar Bay	Bullet holes in decking
5	Machine Shop	Cable bundles and support brackets cut

2. NPS Role in S24

For S24, the ex-TARAWA was moored on Fox pier, Ford Island, Joint Base Pearl Harbor Hickam, and all M-AM and other machinery was staged pier-side around the ex-TARAWA. The exercise leadership communicated that larger repair parts (> 20 kg) would need to be produced from a variety of metal alloys. Based on these criteria, the XSPEE3D cold spray metal printer was selected due to its ability to print with a variety of metal alloys at high speeds and large sizes. A summary of the printer's specifications is provided in Table 12. In addition to its production flexibility, the XSPEE3D is designed within the same dimensions as a 20-foot, standard height and width, shipping container which was anticipated to significantly reduce the logistical complexity of transporting the machine to forward deployed areas. In addition to the XSPEE3D, the parent company (SPEE3D) provided the SPEE3DCell, a containerized post-processing system including a Tormach 1100 3-axis CNC mill, drill press, and heat treatment ovens, to Ford Island to work in conjunction with the XSPEE3D. SPEE3D also sent two technical representatives to Ford Island to help support the exercise. NPS sent three students, including the author, to Ford Island to supervise the training of Naval reservists and civilians in the operation of the XSPEE3D machine and work with NAVSEA 05 and PHNSY to identify and print repair parts for the ex-TARAWA.

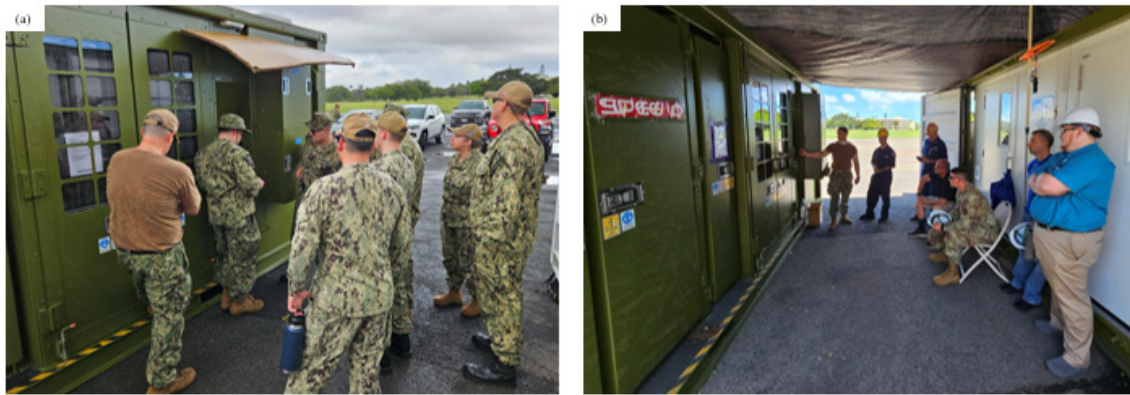
Table 12. XSPEE3D printer specifications.

Print Specification	Value
Metal alloys available for printing	Copper, 316L SS, aluminum alloy 6061 (AA6061), aluminum bronze (AB), and nickel aluminum bronze (NAB)
Build Volume	900 mm x 700 mm
Weight Limit (maximum part size)	40 kg
Deposition Rate	100 g/min (maximum)
Deposit Size	6 mm
Power Requirements	3 phase, 415 V, 80 A

Adapted from [180].

3. Training

Naval reservists from around the country were assigned to support S24. The first week of the exercise was intended to train these sailors on the operations of the XSPEE3D and SPEE3DCell. However, due to some logistics issues that will be covered in greater detail later in this report, the training of sailors occurred later in the first week and bled over into the second week as well. In total, 17 sailors were trained during S24, as shown in Figure 82. Due to the time constraints placed on the exercise to simulate an expeditionary repair needed in wartime, the main operators of XSPEE3D and SPEE3DCell during S24 were NPS students and SPEE3D contractors. Some of the prints from S24 did require post-processing that were beyond the capabilities of the SPEE3DCell's machines. Therefore, training value was provided to an additional group of reservists and civilians. In particular, the cooler head assembly required flange facing and re-drilling of the flange holes, which were performed by sailors trained to use equipment provided by Mactech and NAVSEA 05T as seen in Figure 83.



Naval reservists and civilians being trained by (a) LT Michael Tisdall during week 1 and (b) LT Joel Hunter during week 2 of S24.

Figure 82. XSPEE3D training during S24.



Naval reservists were trained and operated the (a) flange facing and (b) 3-axis lathe to finish the main component of the cooler head assembly for SALVEX 2024

Figure 83. Post-processing training during S24.

Following the completion of S24, the XSPEE3D and SPEE3DCell were both transported to Marine Corps Base Hawaii (MCBH) Kaneohe Bay to join the JAMC that was established. Both machines were set up at Combat Logistics Company 33 (CLC-33), and a group of three Marines were trained as operators. The Marines were trained on all XSPEE3D operations over a period of three days as shown in Figure 84, and their training culminated in printing a bracket for a USMC 7-ton truck. The bracket was chosen as a suitable part for M-

AM production since it frequently breaks during routine operations and has a long lead time in the supply system.



Marines assigned to CLC-33 performing (a) printing, (b) powder loading, and (c) barrel alignment operations on the XSPEE3D.

Figure 84. XSPEE3D training for TW24.

4. XSPEE3D Printing

During S24, the XSPEE3D was utilized to print parts for systems 1 and 5 listed in Table 11 [160]. From space 1, a flange from the sea water piping system and the sea water/freshwater cooler head were damaged beyond repair and required replacement. From space 5, the brackets supporting a cable bundle in the overhead were damaged beyond repair and two new brackets were required. Aluminum bronze was selected as the desired material for the flange and cooler head from space 1. The original components were made of 90–10 copper nickel alloy, and the two alloys have similar properties as shown in Table 13. Both alloys have excellent corrosion resistance and machinability, making both ideal for use in many types of marine applications [181], [182]. The materials selection for the brackets for the cable bundle was not a critical factor in their design; therefore, to minimize machine down time for powder replacement, the brackets were also printed from aluminum bronze. All aluminum bronze components were heat treated in accordance with the following procedure:

1 hour at 400°C, air cool, 14 hours at 1000 °C, 2.5 hours at 900 °C, and quench in 5% soluble oil [183]. The brackets printed for the cable bundle support are shown as installed in space 5 in Figure 85.

Table 13. Materials properties comparison for 90–10 Cu Ni and SPEE3D Aluminum Bronze.

Property	90-10 Cu Ni	SPEE3D Aluminum Bronze
Composition	Ni (10.5%), Fe (1.5%), Mn (0.75%), Cu (bal.)	Si (<0.1%), Mg (<0.1%), Al (7-8%), other (<0.15%), Cu (bal.)
0.2% Yield Stress (MPa)	105	165 (XY and Z)
UTS (MPa)	300	350 (XY) and 300 (Z)
Elongation (%)	30	16 (XY0 and 9 (Z)

Adapted from [181], [182].

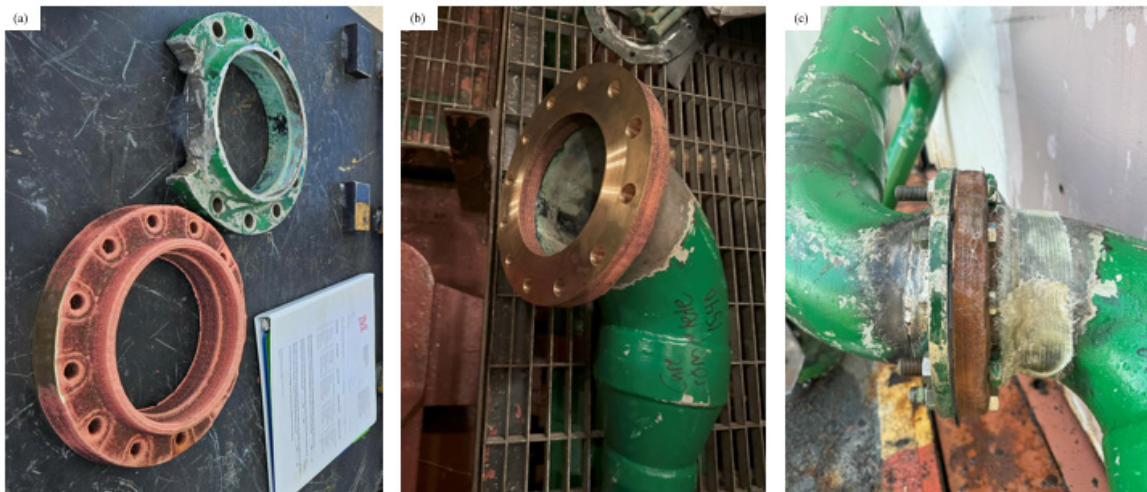


(a) Forward and (b) aft brackets for supporting cable bundle inside space 5.

Figure 85. Space 5 repairs during S24.

Space 1 of the ex-TARAWA saw most of the repairs conducted utilizing the XSPEE3D. The first component was the flange from the sea water system which was mechanically damaged during the beginning stage of S24 [160]. As seen in Figure 86a, the

flange was damaged beyond repair and a new component was required to be produced from aluminum bronze to closely match the original material of 90/10 copper nickel [160]. The new flange was printed, heat-treated, and installed in the system in place of the original flange as seen in Figure 86b [160]. The piping system was then tested to operating pressure (0.31 MPa or 45 PSI), but hydrostatic test pressure (0.42 MPa or 61 PSI) was not reached due to leakage from the flange to pipe bond, which was performed with an epoxy treatment and resin patches as seen in Figure 86c [160]. However, the leakage was due to a failure of the epoxy seal, not the flange, and the leakage rate of 1 gal/min at operating pressure was deemed acceptable to allow ex-TARAWA to get underway for combat operations.



(a) Side-by-side comparison of the legacy and printed flange. Adapted from [160]. (b) Printed flange installed on piping junction. Adapted from [160]. (c) Hydrostatic test of printed flange in the system.

Figure 86. Space 1 flange repair during S24.

The cooler head in space 1 was unable to be printed as one assembly due to the location of the cooler inside the space and the configuration of the cooler head as shown in Figure 87a [160]. Therefore, the cooler head was designed to be assembled from four separate aluminum bronze parts which would then be joined together to produce the replacement cooler head [160]. Unfortunately, the XSPEE3D was inoperative for the last three days of S24, and the root cause was the failure of a lava seal on the powder feeder tube assembly as

shown in Figure 87b. The lava seal is designed for one time use (it destructively fails when installed to create a seal) and is composed of alumina. Therefore, it was not possible to print or fabricate a spare lava seal with the equipment at S24. However, the parts printed before the XSPEE3D became inoperative were able to be utilized to produce a cooler head that matched the legacy part closely as shown in Figure 87c.



Figure 87. Space 1 cooler head repair details during S24.

During the fit-up shown in Figure 87c, it became apparent that extensive welding and other joining operations would be required. Extra aluminum bronze pieces with the same

thickness as the cooler head body were salvaged from a previous print, and the pieces were hand forged into the correct shape by heating to 900°C and hammering into shape before quenching in 5% oil per the heat treatment procedure. With those final pieces complete, the cooler head was ready to be assembled. Tungsten Inert Gas (TIG) welding was identified as the preferred joining method to complete the assembly, but two major challenges were encountered. First, TIG welding of aluminum bronze is not commonly performed by the welders at S24, and the best filler material is AMPCO-TRODE 10 electrode which was not readily available. Second, the timeline to perform all the TIG welding required to complete the assembly was over a day, but the ex-TARAWA was scheduled to get underway within 12 hours. Since AMPCO-TRODE 10 was not available on Oahu and could not be procured in time to meet the exercise timeline, the next best filler rod, AMPCO-TRODE 46, was procured for use. AMPCO-TRODE 10 and 46 are very similar in terms of composition as mechanical properties, as shown in Table 14, and the only concern for using 46 was the nickel content creating a galvanic couple with aluminum. However, the risk of a galvanic couple was dismissed due to the nature of S24; in reality, galvanic corrosion would be a minor concern for a wartime repair.

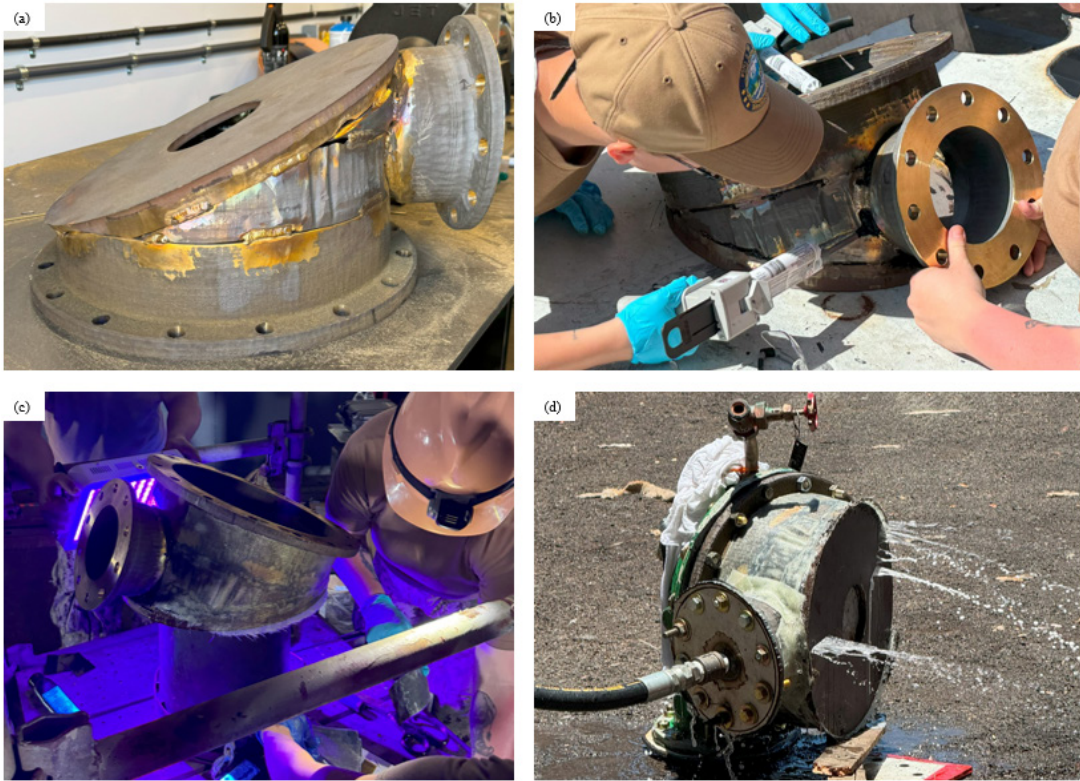
Table 14. Properties of AMPCO-TRODE 10 and 46 electrodes.

Electrode	AMPCO-TRODE 10	AMPCO-TRODE 46
Composition	Al (6.5-9%), Fe (0.5-5%), Si (1.5% max), Cu (bal.)	Al (8.5-9.5%), Fe (3-6%), Ni (4-5.5%), Mn (0.5-3.5%), Si (1.5% max), others (0.5% max) Cu (bal.)
0.2% Yield Stress (MPa)	241	400
UTS (MPa)	531	683
Elongation (%)	27	22

Adapted from [184], [185].

To meet the underway deadline, the welders were able to tack weld the pieces together to form the skeleton of the cooler head assembly as seen in Figure 88a [160]. While the tack welding was being performed, the engineering team looked at alternative joining methods.

3M Scotch-Weld Structural Adhesive and SUNREZ UV-curable resin patches were applied around and on top of the tack welds to complete the assembly; the tensile strength of the adhesive and resin patches was 7.00 MPa (1,015 PSI) and ~6.89 MPa (~1,000 PSI), respectively. The risk in using these products was deemed acceptable based on the 0.31 MPa (45 PSI) operating pressure of the cooler head. As seen in Figure 88b–c, naval reservists applied both the adhesive and resin patches to complete the cooler head assembly after receiving training [160]. After the final assembly was completed, the cooler head was tested at operating pressure (0.31 MPa or 45 PSI) with minor leaks observed [160]. The cooler head was then tested to 135% operating pressure of 0.42 MPa (61 PSI) with ~ $\frac{1}{4}$ gal/min leakage observed and finally to failure as seen in Figure 88d, which occurred at 0.69 MPa (100 PSI, 220% operating pressure) [160]. The decision to pressure test until failure was made to determine if the joints or the components printed from the XSPEE3D would fail first. As expected, the top piece of the cooler head failed due to having a lower wall thickness since it was an incomplete print. Overall, the cooler head was deemed acceptable for the simulated wartime repair since minor leaks at operating pressure would not preclude the ex-TARAWA from getting underway for combat operations.



(a) TIG tack welds holding the assembly together, (b–c) sailors applying structural adhesive and resin patches to reinforce tack welds, and (d) hydrostatic test of the cooler head. Adapted from [160].

Figure 88. Space 1 cooler head assembly and testing during S24.

5. Lessons Learned

Many lessons learned were captured during the execution of S24 despite the overall success of the exercise. Where possible, those lessons were applied as TW24 progressed.

a. Logistics

Logistics challenges plagued the NPS team during S24. Both the XSPEE3D and SPEE3DCell require 400 volt, 3-phase power, with a maximum current capacity of 80 amps each. During initial planning, the NPS support team requested a 250 kW electric generator to satisfy this requirement with an allowance for other accessories, such as additional lighting. A 250 kW generator was not available from the facilities contractor supporting the exercise, so organizers provided the team with a 350 kW generator. This generator was unusable due to the low operating load of both machines (around 75 amps

continuous load). Had it been used; the generator would have been mechanically damaged from light loading in a matter of hours. To overcome the power issues the team sourced a 150 kW generator from Naval Facilities Command Pearl Harbor and staggered the use of XSPEE3D and SPEE3DCell to avoid exceeding the generator's rated capacity. This temporary resolution allowed the team to set up, calibrate and test XPSEED and SPEE3DCell before the commencement of the exercise events.

Transportation of the machines was also a significant issue. XSPEE3D has a gross weight near 11,793.40 kg (26,000 lb.) making it just light enough to be lifted by a 14-ton capacity forklift, however these forklifts are large and difficult to source. The weight of XSPEE3D also exceeded the maximum loading per square foot of Fox Pier, where ex-TARAWA was moored. This required that the machines be set up in a dirt-lot near the end of the pier, a considerable distance from the infrastructure built by PHNSY and NAVSEA 05 for the administration of the exercise (offices, relief areas, drinking water, etc.). XSPEE3D was inadvertently placed on uneven ground, with a high point supporting the center of the structure, leaving the corners unsupported. The hogging strain created by this support arrangement created enough deformation in the structure that access doors were stuck closed and misaligned. To remedy this, two of the four corners of the machine were raised up and shimmed to level the structure. The container jack and shims used were provided with SPEE3DCell, and without them the delay in setting up would have been more significant.

Both PHNSY and Defense Logistics Agency (DLA) were unable to provide transportation of both machines to MCBH Kaneohe Bay after the conclusion of S24. However, this provided an opportunity to demonstrate USN-USMC cooperation and the compatibility of both machines for shipping via USMC Oshkosh Logistic Vehicle System Replacement (LVSR). Instead of crane/forklift onto a normal flatbed truck for transportation, as seen in Figure 89a during XSPEE3D shipping from NPS to Oahu, both machines were loaded onto USMC LVSRs for transportation to MCBH Kaneohe Bay as seen in Figure 89b. Transporting via LVSR required both machines to tilt up to 45°, requiring addition internal storage precautions. Upon arrival at MCBH Kaneohe Bay, both machines were inspected and found to be fully operational.



(a) Machine transport via flatbed truck from NPS to PHNSY and (b) transport via USMC LVSR from Ford Island to MCBH Kaneohe Bay.

Figure 89. XSPEE3D and SPEE3DCELL transportation methods.

b. Environmental

During the planning process for S24, environmental concerns were discussed because the well-being of both the environment and the operators were very important to exercise stakeholders, and the recent mishap at the Red Hill fuel depot has further heightened scrutiny of any event that has the potential to cause environmental harm in the State of Hawaii. During the planning phase, the health of personnel both on and off ex-TARAWA was discussed, as well as the impact on the surrounding community. The NPS and SPEE3D team communicated early and often that XSPEE3D uses metal powder as the feedstock for printing, but, despite those efforts, the environmental shop of both PHNSY and the base had some concerns regarding the printer operation on Ford Island. Specific concern was directed at the human interaction with metal powders containing nickel compounds and the certified emissions of XSPEE3D's chamber air evacuation system. Only after providing the safety data sheet (SDS) for all the metal powders to be used during S24 did the environmental shop allow printer operations to commence. Environmental problems were resolved early in the second week of the exercise, and the machines were ready for use in time to support the main portion of the exercise.

c. Training

Because of the delays mentioned due to logistics and environmental challenges, training scheduled for the first week had to be adapted to exclude practical demonstrations

on XSPEE3D. LT Mike Tisdall, from the NPS Team, trained 17 U.S. Navy Reserve Sailors on the operation of XSPEE3D using the manufacturer's provided training materials and static displays of the machine. One of the critical pieces of the training process is the practical demonstration of skills learned in the administrative training portion. Because of the operational delays experienced, this practical demonstration could not be completed until the exercise events were underway during week two. LT Joel Hunter, LCDR Zachary Vrtis, Mr. Matthew Harbridge and Mr. Mark Bashor were the primary operators of XSPEE3D and SPEE3DCell during the exercise, with the U.S. Navy Reserve component assisting them or operating the machines under supervision.

d. Larger Prints

The sea water/freshwater cooler head in space 1 was one of the largest and most challenging parts printed in the field by a XSPEE3D system. The original request from the engineering team was to produce the cooler head as one print. The NPS and SPEE3D Team explained to the engineering team that the geometry of the cooler head made a single print process not possible. Supports are not generated by the XSPEE3D during printing, so the cooler head was designed to be a four-part assembly requiring a fit-up and joining process after printing and heat treatment [160]. As discussed previously, significant difficulties were encountered sourcing the correct electrode for TIG welding the assembly together. Thankfully, the 3M Scotch-Weld Structural Adhesive and SUNREZ UV-curable resin patches were already at the exercise and utilized for other repairs, therefore, the naval reservists and civilians were able to use these two methods to complete the assembly. However, the big takeaway for the cooler head assembly was the importance of having the proper electrodes available for all metal powders to be used to ensure that welding is always available to create large parts that are not possible to produce as a single print.

e. Print Designs

When tasked with printing the flange and cooler head, the team decided to design and print the holes for bolting the components onto the seawater system. However, this proved to be counter-productive because the XSPEE3D does not print holes to accurate dimensions. Not only did the holes need to be machined out by Reserve Component

Sailors, but the center of the holes was difficult to assess. As a result, the holes were slightly off, and the cooler head was not able to be installed for pressure testing. Further machining was required to widen several holes to allow for a successful installation for testing, resulting in a delay of approximately 12 hours. In the future, the team recommends all holes be added following the printing and heat-treating process [160]. A transfer punch can be used to quickly identify and mark the exact center of the holes needed for the assembly, ensuring successful hole placement initially and avoiding costly delays for re-machining.

6. Preliminary Findings

S24 was a great opportunity to demonstrate the application of advanced manufacturing (AdvM) technologies for all participants and is particularly noteworthy as being the first BDA/R exercise to incorporate M-AM into the “tool belt” available to the Navy. Important lessons were learned, especially in the areas of logistics, environmental planning and protection, operator training and the design and printing of larger, complex parts [160]. The logistics and environmental challenges encountered can be mitigated in the future by better planning; unfortunately, S24 was planned in a relatively short period of time and some items were dropped during the planning process. On top of that, the focus of most of the supporting entities was on the upcoming RIMPAC 2024 exercise happening immediately after S24. The challenges the team overcame to successfully print, assemble, and test the cooler head were very impressive, and, overall, an important step forward was made by incorporating MAM technologies into a BDA/R exercise. However, the lessons learned regarding larger and complex parts are important since most of the parts the DON will need in a wartime scenario will not be simple. Ingenuity of both service members and the supporting companies will be needed to find ways to expeditiously produce critical parts needed to keep assets ready and fix them if needed to get back into the fight [160]. A list of mitigating actions recommended by this report is as follows:

- Procure a stand-alone generator that can adequately power XSPEE3D and SPEE3DCell, as well as any M-AM machine with high power requirements, without relying on exercise infrastructure to operate the machines.

- Ensure event organizers understand the scale (weight and dimensions) of machines as well as site requirements.
- Conduct a clean air study on XSPEED and provide material safety data sheets to exercise organizers early to ensure there are no concerns regarding environmental impact.
- Ensure there are at least four days of dedicated training and setup time built into the schedule, before commencement of exercise events and after the machines have been placed in their dedicated positions.
- Develop concise and robust standard operating procedures to guide training, printing, and post-processing with the XSPEE3D and SPEE3DCell.
- Ensure tools and equipment are available to construct multi-component prints into a completed part.

B. TRIDENT WARRIOR 2024

Following on the successes of S24, TW 2024 commenced with CAMRE establishing the JAMC at MCBH Kaneohe Bay. The focus was to showcase the capability of plastic and metal AdvM technologies, which incorporate both subtractive and additive techniques together to produce parts with complex geometries and less material wastage [160]. Unlike S24, the team did not operate under a simulated wartime atmosphere. Although polymer printers were successfully implemented as part of TW24, only M-AM shall be discussed in detail in this section.

1. Exercise Overview

TW24 differed from S24 due to a much higher volume of both M-AM and polymer AM. Also, TW24 included participants spread across Oahu whereas S24 was localized to Ford Island. The laydown on Oahu for TW24 is shown in Figure 90 with assets deployed both afloat and ashore. The XSPEE3D and SPEE3DCell remained at MCBH Kaneohe Bay due to their size and powder feedstock. Joining the XSPEE3D for TW24 was the Snowbird

laser wire DED printer, which was leased by CAMRE for the exercise. Snowbird was deployed both ashore and afloat due to its smaller size and weight of 3.20 m x 2.44 m x 2.59 m container and 4,535.92 kg (10.5' x 8' x 8.5' and 10,000 lbs.) as well as the 316L SS feedstock vice powdered metals [160]. XSPEE3D and Snowbird parts were machined in various locations to include the SPEE3DCell at the JAMC, MCBH Kaneohe Bay, 25th Infantry Division (ID), USS SOMERSET, and Bear Machinery. One focus of TW24 that was missing from S24 was materials characterization—testing was performed both at Bear Machinery and NPS to verify metal parts were printed with nominal tensile strength, ductility, hardness, and elemental composition [160]. Overall, TW24 was a huge success for CAMRE and the DoD and paved the way for further AM experimentation which is going to lead to improvements in the DoD's overall AM strategy.



Adapted from [160], [186], [187].

Figure 90. JAMC focuses, details, key tests, and overview at TW 2024.

2. NPS Role in TW24

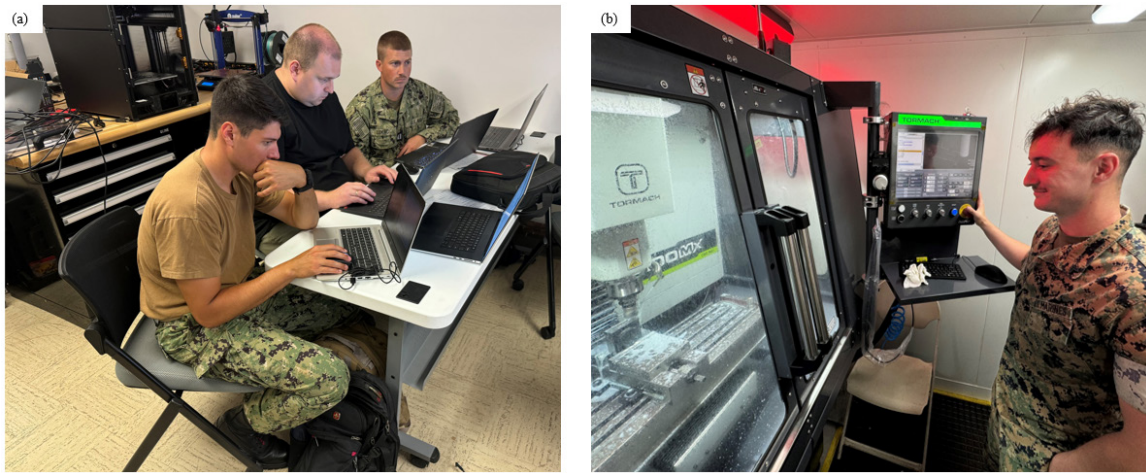
Overall, many more students from NPS participated in TW24 compared to S24. Ten students in total participated, with four going aboard USS SOMERSET and the other six staying ashore at the JAMC. NPS students were joined at TW24 by technical representatives from both SPEE3D and Snowbird Technologies to provide technical expertise in case troubleshooting and repairs of the machines were needed. Other members of the JAMC were as follows:

- Civilians from NAVSEA Corona and NIWCPAC
- Civilians from Bear Machinery LLC, a local machine shop in Kaneohe, HI
- United States Marine Corps (USMC) reservists from Marine Innovation Unit (MIU)
- USMC personnel from CLC-33
- U.S. Army (USA) personnel from 25th Infantry Division (ID)
- United States Navy (USN) personnel from USS SOMERSET and SAN DIEGO

With a wide variety of personnel from multiple branches of service and commands, command and control were essential. NPS students served as the officer in charge (OIC) of the ashore or afloat portion of the JAMC where they were assigned.

3. Training

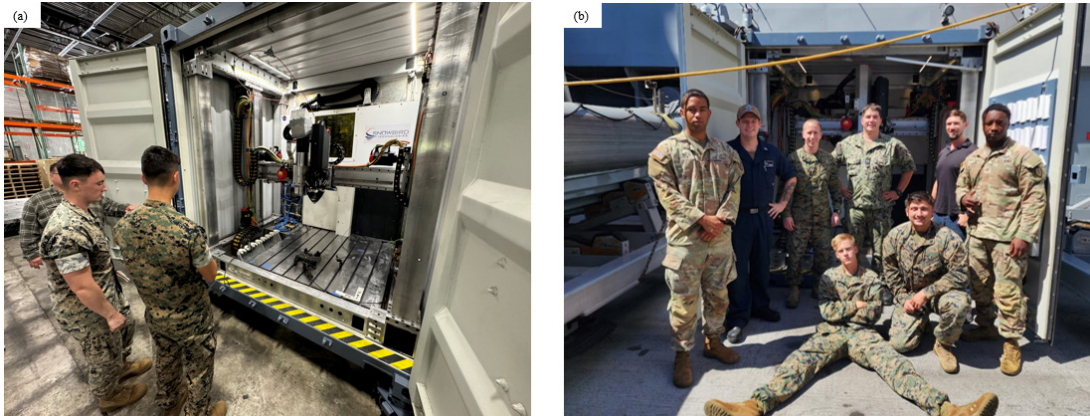
Training on the XSPEE3D started immediately following S24, and it continued during TW24 as more NPS students and other personnel became exposed to it. With assistance from SPEE3D contractors, NPS students and Marines from CLC33 served as the primary operators of both the XSPEE3D and SPEE3DCell as shown in Figure 91. All heat treatment operations and some of the post-processing machining for the XSPEE3D parts were performed with the SPEE3DCell. Parts were also machined at Bear Machinery and other shops on MCBH Kaneohe Bay.



(a) NPS students plan the XSPEE3D printer operations with assistance from Mr. Witold Spzunar from SPEE3D and (b) CPL Martin Lauterman from CLC33 operates the CNC machine in the SPEE3DCELL.

Figure 91. Training of personnel during TW24.

Initial training on the Snowbird printer was obtained in Jacksonville, FL in April 2024 when the lease contract for the machine was being finalized (Figure 92a). At the time, the Snowbird printer had a large list of discrepancies that required fixing for the machine to be successfully employed in TW24. With the help of NSWC Corona personnel, particularly Mr. Kevin Demesa and Mr. Jacob Lopez, the Snowbird software and hardware systems were upgraded and debugged from April–June 2024 before the machine was shipped to San Diego, CA for transportation to Oahu. During the ashore phase of TW24, the final issues with the Snowbird printer were resolved, the operators of the machine were trained, and the machine was loaded onto the USS SOMERSET. While underway, training of USS SOMERSET personnel and NPS students was provided by Mr. Zachary Wilson, who also provided oversight during troubleshooting and repair efforts (Figure 92b).



(a) Initial Snowbird training in Jacksonville, FL in April 2024 at the factory and (b) Snowbird training underway on USS SOMERSET during TW24. Adapted from [187].

Figure 92. Snowbird training.

4. Snowbird Printing

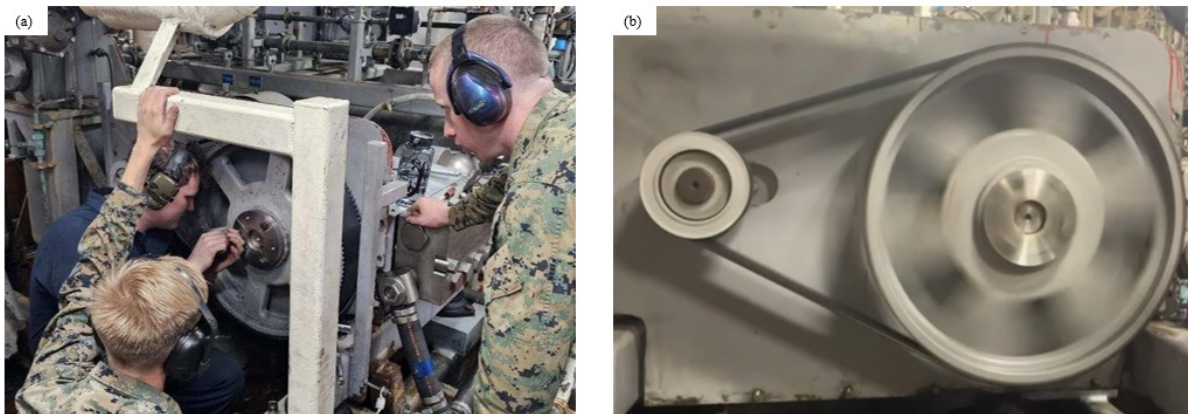
The Snowbird printer was used both ashore and afloat during TW24, and it was utilized to print a total of ten parts and six test coupons [160]. The Snowbird was optimized for 316L SS printing using a Meltio printhead mounted on a gantry system allowing for printing and 3 axis subtractive machining operations [160]. The Meltio printhead uses an array of six lasers to melt a wire and extrude through a copper welding tip. The entire process is highly analogous to Metal Inert Gas (MIG) welding and requires a constant argon gas flow during printing operations. Snowbird printing specifications are described in Table 15.

Table 15. Snowbird printer specifications.

Print Specification	Value
Metal alloys available for printing	316L SS
Build Volume	4 ft x 4 ft x 4 ft (64 cubic feet)
Relative Density	99.96%
Deposition Rate	183.3 g/min (maximum)
Spot size / layer height	1 mm
Power Requirements	3 phase, 208 V, 200 A

Adapted from [57], [188].

Overall, the Snowbird was highly successful during its time aboard USS SOMERSET, logging over 102 hours of printing without any mechanical or system failures [186]. A prioritized list of prints was designed and loaded onto the machine's hard drive prior to embarking the machine on USS SOMERSET. However, immediately upon getting underway, one of the ship's reverse osmosis (RO) pumps was placed out of commission (OOC) due to a failed bushing and a Navy casualty report (CASREP) was issued [160]. The ship's engineer approached the NPS student serving as the Snowbird OIC to print a replacement because the lead time of the part from the supply system was over 9 months. The JAMC team designed, printed, machined, and installed the new bushing in 9.5 days, clearing the CASREP and placing the RO pump back in service (Figure 93) [160]. The cost of the part through the supply system was \$23, which was lower than the estimated cost of production from Snowbird of \$257 [160]. However, the time savings are well worth the cost as the operations of the USS SOMERSET would be severely hampered with a RO pump OOC if a full contingent of Marines were embarked aboard [160].



(a) Installing the new bushing onto the OOC RO pump and (b) the successful retest of the RO pump with the bushing installed. Adapted from [186], [187].

Figure 93. RO pump repair.

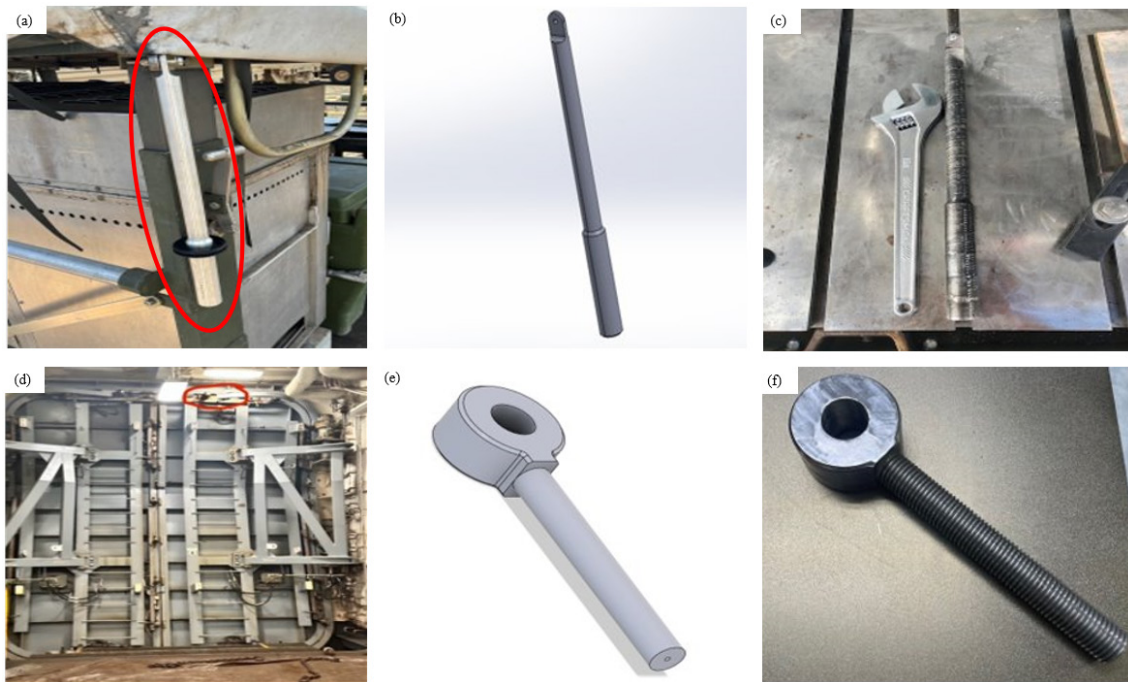
The Snowbird also printed several other readiness solutions that had an immediate impact on the joint force. While ashore, a support beam for the USA mobile field kitchen was printed and machined to restore the system to full functionality as shown in Figure 94a–c [160]. Although not the most complex part, it did have a lead time of over 60 days

in the supply system. Additionally, the part itself was not available in the supply system; therefore, the USA is required to buy the next higher assembly, at a cost of \$2,313.80 [160]. The part for the mobile kitchen was designed, printed, and machined in four days total at a cost of only \$45.30, a huge time and cost savings to the USA [160]. Another readiness solution for USS SOMERSET was an eyelet for the hangar door, which had cracked during use and was welded back together. The part was designed, printed and machined aboard USS SOMERSET as shown in Figure 94d–f. The cost and lead time for the part in the supply system was \$210.40 and over 4 months, and it was produced in four days at a cost of \$64.20 by the team aboard USS SOMERSET. Both case studies highlight the role M-AM can play in producing parts with a long lead time and/or high cost due to scarcity or the need to buy the next higher assembly. For the three case studies from Snowbird–RO pump, mobile kitchen, and LPD hangar door—a comparison of cost (in dollars) and time (in Ao), is summarized in Table 16. The OEM cost comes from the Federal Logistics (FEDLOG) system and includes all labor costs. The M-AM costs were determined based on printer feedstock costs only without labor considered, therefore, the M-AM costs presented in Table 16 are lower than actual costs. However, all three case studies show a huge Ao savings from the M-AM method, making it the obvious choice for a commanding officer who needs his/her equipment ready for use [160].

Table 16. Cost and Ao breakdown for Snowbird case studies.

Part	M-AM Cost (\$)	OEM Cost (\$)	M-AM Cost (Ao)	OEM Cost (Ao)
RO pump	\$257	\$23	9.5 days	> 270 days
Mobile field kitchen	\$45.30	\$2,313.80	4 days	> 60 days
LPD hangar door	\$64.20	\$210.40	4 days	> 120 days

Adapted from [160].

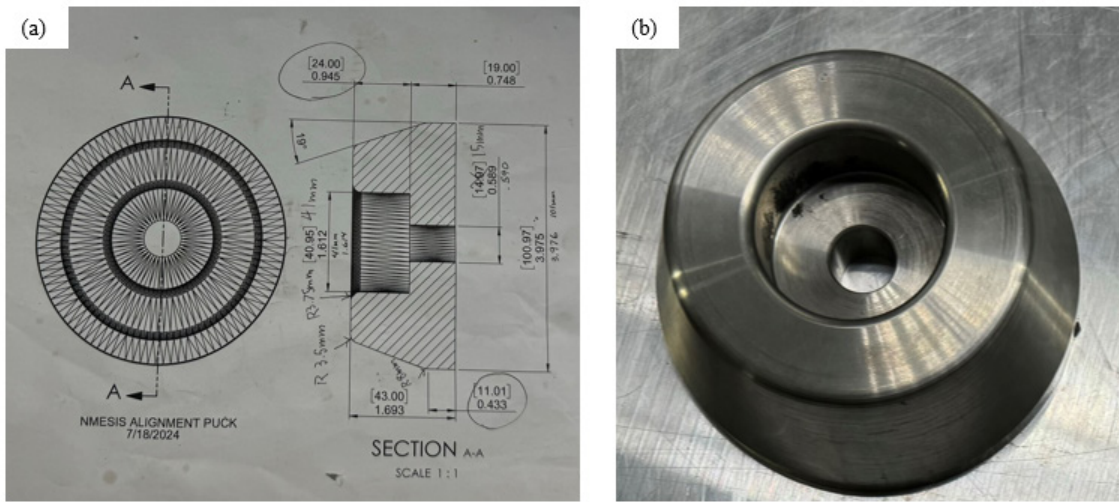


(a) Location, (b) CAD rendering, and (c) final printed (but not yet machined) mobile kitchen support piece. (d) Location, (e) CAD rendering, and (f) final printed and machined hangar door eyelet for USS SOMERSET.

Figure 94. Snowbird case studies.

5. XSPEE3D Printing

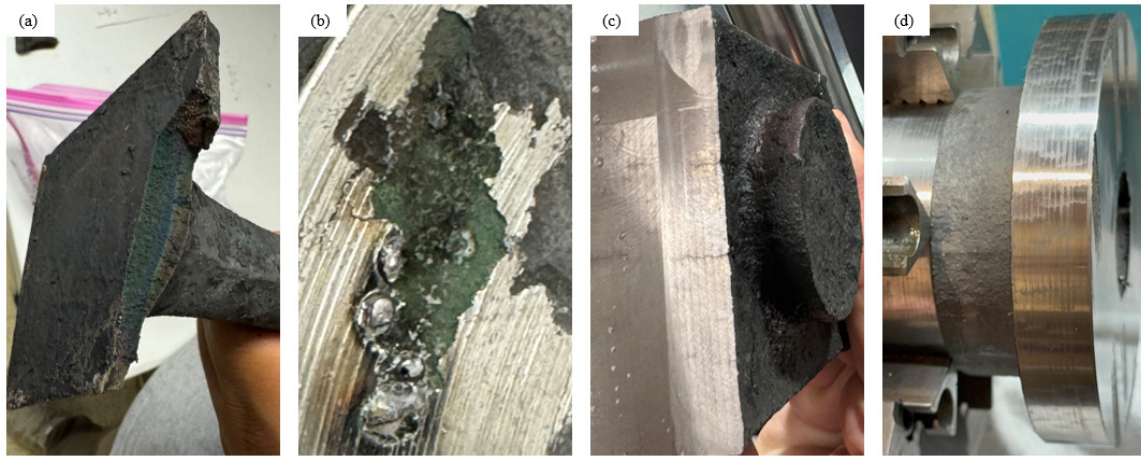
After the success of S24, the XSPEE3D was expected to play an integral role in the JAMC during TW24. A total of 31 parts were printed with XSPEE3D, of which 29 were 316L SS and the remaining two were AA 6061. Copper, AB, and NAB were not printed during TW24 because no parts were requested from those alloys. 316L SS was printed most frequently, which is not surprising due to the large amount of steel used throughout the joint force. One of the successful parts designed, printed, heat treated, and machined was an alignment puck for the USMC Joint Light Tactical Vehicle (JLTV) shown below in Figure 95. The puck was a great demonstration of the flexibility of the JAMC—the part was printed and heat treated by Marines under NPS student guidance and machined by Bear Machinery.



(a) Engineering drawings and (b) the final printed and machined JLTV alignment puck from 316L SS on XSPEE3D.

Figure 95. JLTV alignment puck.

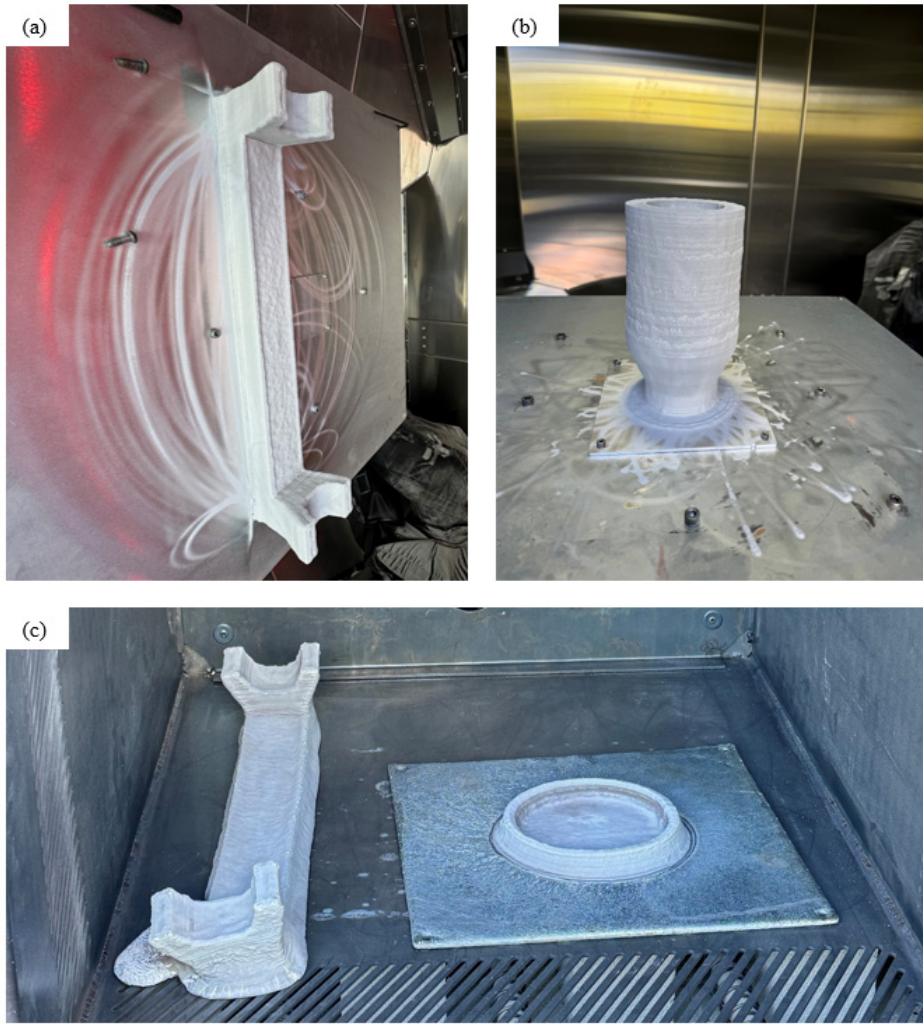
Unfortunately, the JLTV alignment is the only 316L SS component that was successfully printed, heat-treated, and machined using the XSPEE3D. Some of the other printed components had serious defects including internal discoloration and oxidation, surface corrosion, cracking, and possible interlayer oxidation. The most likely cause for these issues is the heat treatment—the furnace must be kept inert during the 316L SS heat treatment. Nitrogen from CLC33 was used to purge and maintain the furnace inert during the 316L SS heat treatments, and a poor seal or contaminated gas could have allowed enough oxygen into the furnace during heat treatment to cause some of the defects shown in Figure 96.



(a) Discoloration observed on the cross-section of a print, (b) chromium oxide formation on the surface of a print, (c) cracking across print layers during machining, and (d) clearly defined print layers, indicating interlayer oxidation, as a part is being machined.

Figure 96. XSPEE3D 316L SS print defects.

For a portion of TW24, the XSPEE3D was switched from 316L SS to AA 6061 based on a demand for aluminum parts. Thankfully, the clogging issues experienced in S24 did not occur and parts were able to be printed for the JAMC as shown in Figure 97. Although no issues were encountered during printing, there were other problems encountered with AA 6061, specifically in the heat treatment process. One of the AA 6061 prints, the bracket for the 7-ton USMC truck, slumped and partially melted during heat treatment, possibly due to the furnace reaching too high of a temperature on the bottom metal base plate. Unfortunately, the part was not useable and occurred late in TW24, so the replacement part was not able to be printed.



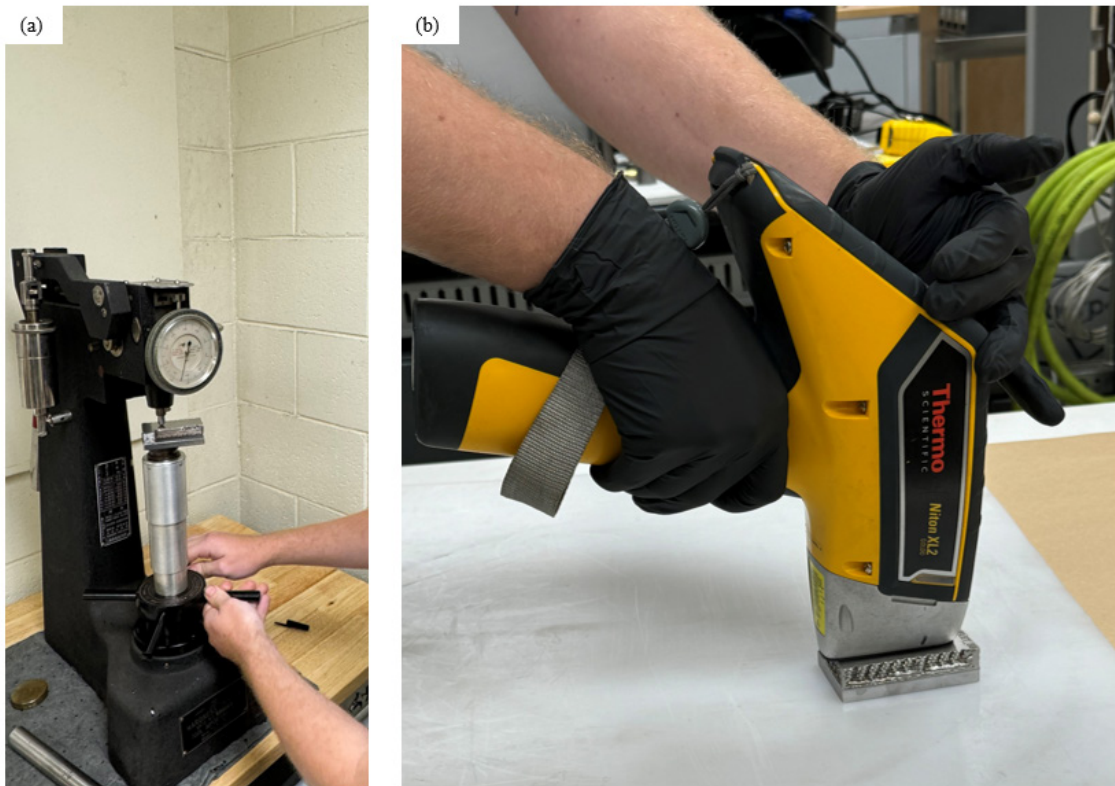
(a) Bracket for the USMC 7-ton truck, (b) USMC 5-inch gun cap, and (c) post heat treatment of the bracket and a generator exhaust cap showing slumping and partial melting of the bracket during the heat treatment.

Figure 97. XSPEE3D AA 6061 prints.

6. Materials Characterization

Materials characterization of samples from Snowbird and XSPEE3D were performed at both NPS and Bear Machinery [160]. Bear Machinery performed two analyses in support of TW24: hardness testing using a Misawa-Seiki Hardness Tester and composition analyses using a SciAps X-550 XRF detector [160]. The Misawa-Seiki can perform both Rockwell B and C scale hardness tests and is a relatively simple hand-cranked system (Figure 98a). The X-550 is a handheld XRF that utilizes a 5 W x-ray tube and a

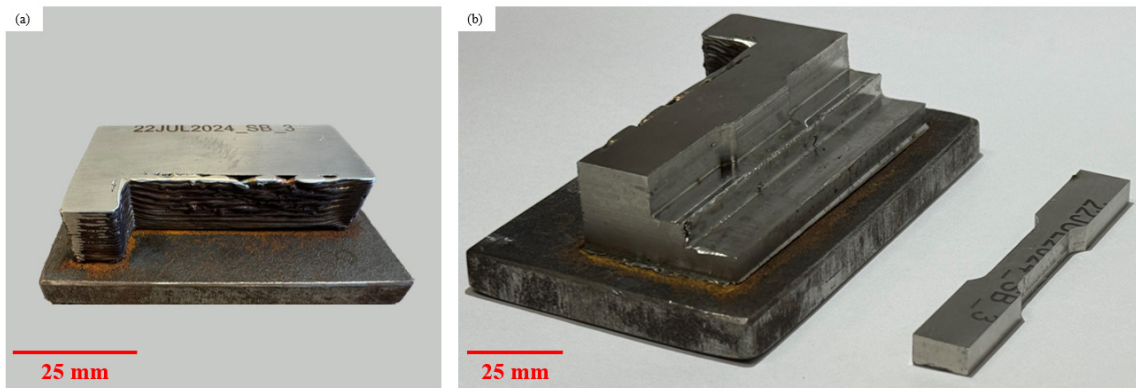
silicon drift detector [189]. The X-550 was chosen based on its speed, portability, and element range which are key attributes for expeditionary use (Figure 98b).



(a) Hardness testing and (b) XRF analyses performed at Bear Machinery

Figure 98. Hardness and XRF analyses performed at Bear Machinery.

During the exercise, dedicated test coupons were printed as often as possible from Snowbird and XSPEE3D [160]. However, operational parts took priority over the test coupons, so a test coupon was not printed every single day, which would have been desirable. However, test coupons were printed on Snowbird concurrently with some of the printed parts, which provides a degree of confidence that the printed parts are suitable for use [160]. One of the test coupons and the tensile specimen machined from it are shown in Figure 99.



(a) 316L SS test coupon from the Snowbird printer and (b) tensile specimen machined from the test coupon for tensile testing. Adapted from [160].

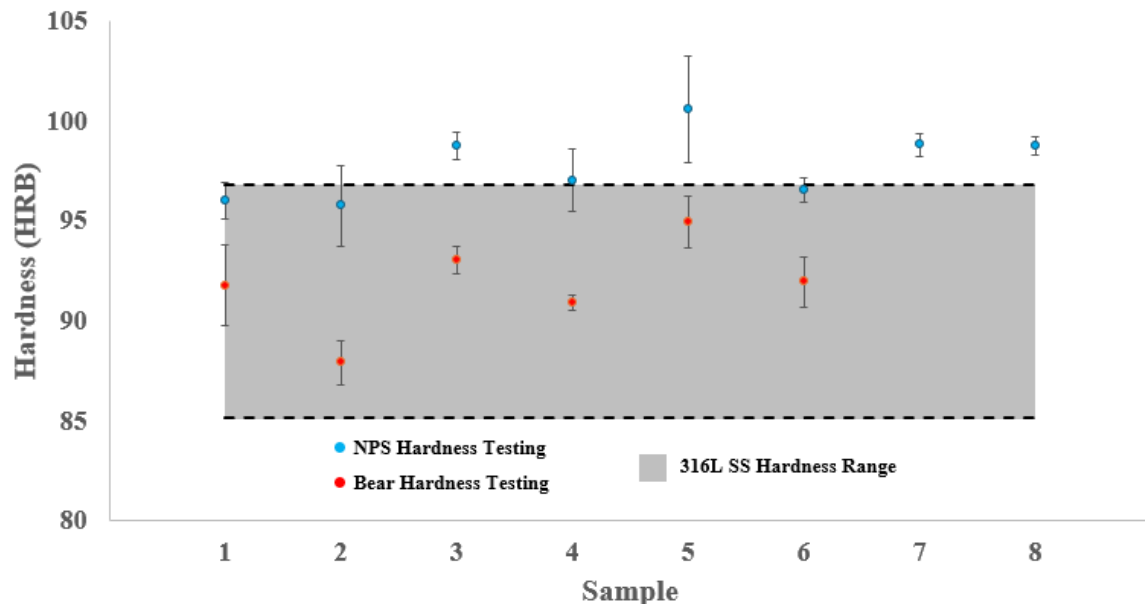
Figure 99. Test coupons from Snowbird printer.

Hardness testing was performed at both Bear Machinery and NPS, using the Rockwell B scale (HRB). The results of the tests are summarized in Figure 100 and show mostly consistent hardness values with small standard deviations, especially for the analyses performed by Bear. However, there are two key observations from this data:

- Hardness results at NPS were consistently higher than those obtained by Bear.
- All hardness results obtained by both Bear and NPS were above the minimum hardness specification for 316L SS prints from the Meltio wire DED system.

The NPS hardness tester is a Struers Durascan, which is an automated tester with an optical measuring system and is routinely calibrated. As a result, there is minimal human error present, unlike with the Misawa-Seiki at Bear Machinery; therefore, the NPS hardness results are assumed to be more accurate than those from Bear Machinery.

Sample Number	Printer	Identifier	NPS Average Hardness (HRB)	NPS Standard Deviation	Bear Average Hardness (HRB)	Bear Standard Deviation
1	Snowbird	June 24 SB	95.99125	0.890497579	91.75	2.046338193
2	Snowbird	July 16 USCG	95.75	2.019832914	87.875	1.082531755
3	Snowbird	LPD 25	98.73	0.667832314	93	0.661437828
4	Snowbird	July 22 1	96.98125	1.555212506	90.875	0.414578099
5	Snowbird	July 22 2	100.5625	2.662103257	94.9375	1.309520427
6	Snowbird	July 22 3	96.5425	0.606336334	91.9375	1.260890063
7	XSPEE3D	RO Bushing 1	98.77375	0.552583421	90.1875	0.242061459
8	XSPEE3D	RO Bushing 2	98.7275	0.470578102	92.75	0.829156198



Adapted from [160].

Figure 100. Hardness results for 316L SS prints.

XRF data for 316L SS printed from both Snowbird and XSPEE3D showed a consistent elemental composition amongst the eight samples tested, as shown in Figure 101. Standard deviation of the elemental weight percentage ranged from 0.004554 to 1.285837, indicating very consistent composition across the printed samples. Of note, samples 7 and 8, from the XSPEE3D, differed significantly from the composition of the other six samples from Snowbird. The calculated weight percent of Cu, Ni, Co, Fe, Mn, Cr, and V fell outside one standard deviation for samples 7 and 8, which can be seen by the diverging spectra lines in Figure 101.

Sample	Identifier	Sn	Mo	Cu	Ni	Co	Fe	Mn	Cr	V	Si	Nb
1	June 24 SB	0	2.33	0.154	11.91	0	63.477	1.734	18.392	0.082	1.638	0
2	July 16 USCG	0.01	2.351	0.158	12.026	0	63.399	1.712	18.323	0.066	1.716	0
3	LPD 25	0	2.103	0.181	11.245	0.257	63.447	1.898	18.432	0.103	2.303	0
4	July 22 1	0	2.106	0.212	11.534	0.288	63.701	2.02	18.426	0.068	1.599	0.024
5	July 22 2	0.011	2.16	0.214	11.506	0.27	64.317	1.876	18.543	0.082	0.956	0.026
6	July 22 3	0	2.136	0.184	11.228	0.292	63.421	1.912	18.429	0.057	2.295	0
7	RO Bushing 1	0	2.177	0	12.316	0.236	66.584	0.184	16.961	0	1.389	0
8	RO Bushing 2	0	2.166	0	12.246	0	66.464	0	17.039	0	1.451	0
Average		0.002625	2.191125	0.137875	11.75138	0.167875	64.35125	1.417	18.06813	0.05725	1.668375	0.00625
Standard Deviation		0.004554	0.089928	0.082129	0.403397	0.131052	1.285837	0.771878	0.619566	0.035471	0.423703	0.010837

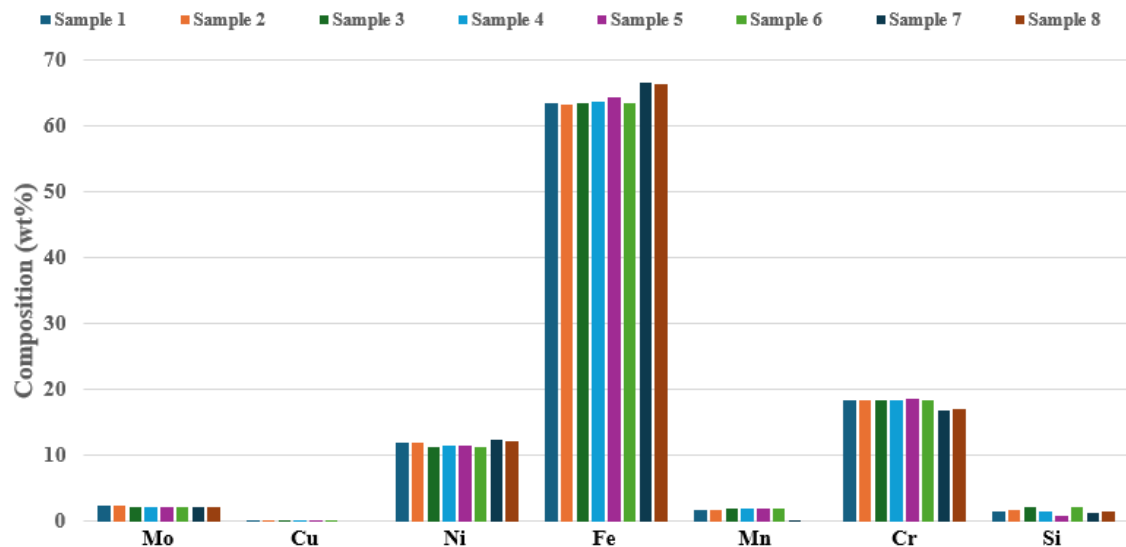
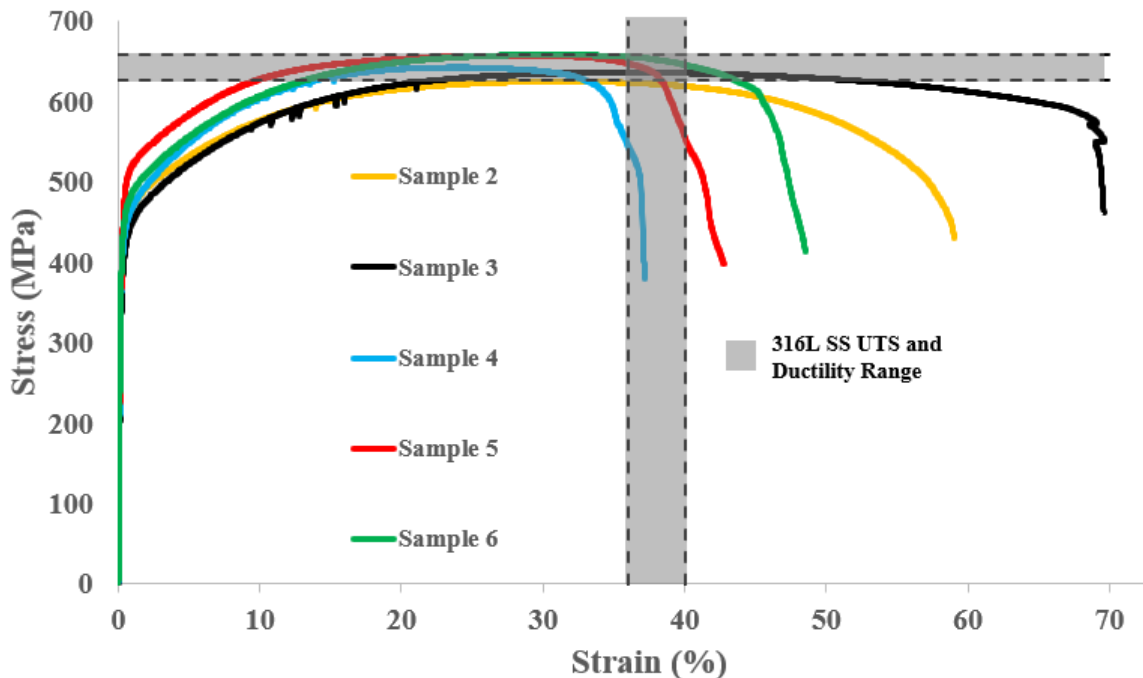


Figure 101. XRF results of all 316L SS prints.

Following hardness and XRF analyses, the test coupons were machined into tensile specimens in accordance with ASTM B557M-15 for subsize rectangular specimens as shown in Figure 99. Samples were machined out of the center of the test coupon to provide the best representation of the material. Following some filing and sanding to remove any burs or small pits / scratches that would be stress concentrations, the tensile specimens were tested using an Instron model 5982 tensile testing machine (100-kN load cell) to determine the UTS and ductility (Figure 102).

Sample Number	Printer	Identifier	Ultimate Tensile Strength (MPa)	Ductility (%)
2	Snowbird	July 16 USCG	625.34	59.08
3	Snowbird	LPD 25	636.36	69.65
4	Snowbird	July 22 1	642.89	40.03
5	Snowbird	July 22 2	657.74	51.54
6	Snowbird	July 22 3	658.67	48.54



Adapted from [160].

Figure 102. Tensile testing results.

All tensile specimens from the Snowbird test coupons exhibited classic ductile failure with $\sigma_{eng} = 644.2 \pm 12.74$ and $\varepsilon_{fail} = 53.77 \pm 10.01$. These average values are within the specifications range provided by Meltio for 316L SS, which are $\sigma_{eng} = 643 \pm 16$ (XY) and $\varepsilon_{fail} = 38 \pm 2$ (XY) [57]. However, Sample 2 did not fall within the specification band for UTS with a value of $\sigma_{eng} = 625.34$ MPa. This deficiency is most likely due to either human or instrument error during the tensile specimen cross-sectional area calculation, which is performed by hand using a pair of calipers before tensile testing [160]. Unfortunately, no tensile specimens were printed with XSPEE3D so no data for UTS or ductility is provided. Meltio and XSPEE3D 316L SS feedstock have different published

elemental compositions, which helps explain the differences seen from XRF analysis (Table 17). Another interesting observation is that the published hardness of XSPEE3D is only 67 by HRB, which is significantly lower than the measured hardness by both Bear Machinery and NPS.

Table 17. Wrought 316SS standard, XSPEE3D 316L SS powder, and Meltio 316L SS elemental composition comparison.

Property	Wrought 316L SS	Meltio 316L SS	XSPEE3D 316L SS
Composition	C (0.03%), Mn (2.0%), Si (1.0%), Cr (16–18%), Ni (10–14%), Mo (2–3%), Fe (bal)	C (0.02%), Mn (1.7%), Si (0.9%), Cr (18.5%), Ni (12%), Mo (2.7%), Fe (bal)	C (<0.03%), Mn (<0.05%), Si (<0.3%), Cr (16–18%), Ni (12–14%), Mo (2–2.5%), Fe (bal)
0.2% Yield Stress (MPa)	260	429 ± 6 (XY) 347 ± 11 (XZ)	240 (XY) 250 (Z)
UTS (MPa)	550	643 ± 16 (XY) 655 ± 28 (XZ)	479 (XY) 490 (Z)
Elongation (%)	35	38 ± 2 (XY) 41 ± 4 (XZ)	22 (XY) 23 (Z)
Hardness (HV / HRB)	225 / 96	198 / 92	123 / 67

Adapted from [57], [190], [191].

7. Lessons Learned

An accounting of the lessons learned during TW24 was compiled with the help and contributions of all the participants from the exercise, to be applied to TRIDENT WARRIOR 25 and other future events to advance the use of M-AM in the DoD [160].

a. Logistics

Support of sophisticated M-AM capabilities requires foresight and planning when it comes to expendables required to maintain them operational. Both Snowbird and

XSPEE3D require a dedicated power supply and gas supplies (argon for Snowbird and nitrogen for XSPEE3D) which must be supplied in addition to the machines. Another huge challenge is the size of the machines and the ability for them to be easily onloaded and offloaded onto a ship. The XSPEE3D, with dimensions of 6.10 m x 2.44 m x 2.59 m and 11,793.40 kg (20' x 8' x 8.5' and 26,000 lbs.), cannot be accommodated on many ships and piers. On the other hand, the Snowbird, with dimensions of 3.20 m x 2.44 m x 2.59 m and 4,535.92 kg (10.5' x 8' x 8.5' and 10,000 lbs.), can be accommodated by most DON shipboard and shore-based forklift and cranes.

b. Training and Personnel

The operation of sophisticated M-AM machines, such as XSPEE3D or Snowbird, is complicated and requires dedicated training and personnel to be successful. Without the knowledgeable NPS students, DON civilians, and technical representatives from SPEE3D and Snowbird, none of the success of TW24 would have been possible. In particular, the subtractive machining process is a very specific skill set that sometimes requires decades of experience to fully master [160]. Younger companies trying to break into the M-AM sector do not necessarily have that expertise in house, so finding and hiring the right personnel as employees or contractors is crucial to ensure their machines are as user-friendly as possible [160].

Dedicated training of at least one week is required for an exercise like TW24 to be successful. This time is necessary to overcome logistics hurdles, environmental concerns, and, most importantly, train the personnel who will use the machine on both operations and troubleshooting. Once the training time is invested in sailor, Marine or soldier, he or she must be given the time and schedule flexibility to dedicate him or herself to mastery of the machine without any other collateral duties or distractions.

c. Print Designs

One problem encountered in TW24 was the disconnect between the M-AM operators, who designed and printed the parts, and machinists, who were given the parts for finishing into the final product for installation. Many times, the printed part was not

designed to be “machinist friendly,” and the following examples were encountered during TW24:

- The part was printed too closely to final tolerance, which prevented the required excess material necessary to machine to final product [160].
- The part was printed with complex geometries such as holes or grooves which are much easier to machine. In many cases, the machinists had to use specialized tools and methods to refinish these geometries to the right dimensions, and it would have been simpler and faster to have printed the part without and let the machinists add these features after the print. [160]
- The part had no boss or other removable component to make it easy to mount parts on a lathe or CNC machine for machining [160].

Bear Machinery’s personnel were helpful in pointing out these issues to the rest of the TW24 team. On many occasions, a quick meeting between the operators and machinists could have saved hours of machining time [160].

d. Printer Acquisition

M-AM technology is evolving at a fast pace, and the DON’s acquisition process is not agile enough to keep up with it. However, the leases on M-AM technologies are advantageous because they have a faster execution time and allow for DON personnel to gain experience with the latest and greatest technologies. Until M-AM has completely matured or a specific M-AM technology is established as the standard for the DON, leases are a powerful tool for exercises such as TW24.

8. Preliminary Findings

TW24 was a huge success for the joint force—the JAMC orchestrated the largest distributed AdvM experiment ever attempted by the DoD, including simulated operations in an expeditionary and contested environment [160], [186]. With 309 total parts printed throughout the exercise, including 41 by the XSPEE3D and Snowbird, readiness solutions were produced for all DoD components except the U.S. Air Force (USAF). Based on the materials characterization data (hardness, XRF, and tensile), all metal parts are suitable for

use. Some key lessons learned were added to the ones already accumulated during S24, and these will be considered moving into the next exercise building upon TW24. Some key takeaways and future directions from TW24 are as follows:

- Logistics planning is of paramount importance: M-AM technologies require powder or wire feedstock, generators and fuel, and inert gas supplies to maintain operations.
- Training time for operators must be built into the operations plan and once trained, personnel should be allowed to operate with minimal collateral duties or distractions. M-AM technologies are complex and time demanding, and they cannot be mastered without a significant investment of time and energy.
- Leverage expertise in machining when possible—hours of time spent on machining a poorly designed part could have been saved with a quick 10-minute meeting between the operators and machinists [160].
- Leasing M-AM technology makes sense based upon the DON’s time-consuming acquisition process, which moves much slower than the pace at which M-AM is evolving. By the time a machine is purchased, chances are it will be obsolete.

THIS PAGE INTENTIONALLY LEFT BLANK

VIII. CONCLUSIONS

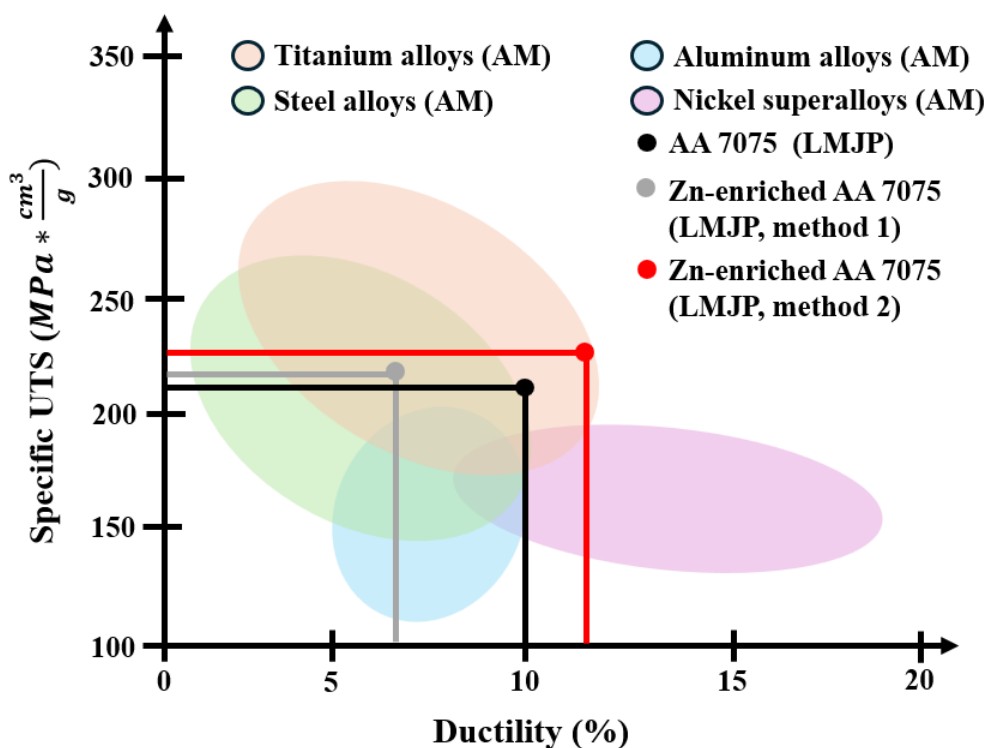
A synopsis of the research and operational objectives shall now be discussed based on the results presented in Chapters IV–VII.

A. RESEARCH OBJECTIVES

Broadly speaking, the goal of the laboratory research was to develop successful processes to produce high-end aluminum alloys and custom shapes using M-AM methods, specifically LMJP. Each of the three research objectives shall now be analyzed in retrospect of the results obtained:

- Print AA 7075 samples with comparable properties to that of the wrought alloy. Characterize the samples to verify fully dense, crack-free fabrication.
- Complete—pure AA 7075 samples were printed with an average UTS of 593.22 MPa and average ductility of 10.05%, exceeding the specifications for the wrought alloy. The specific strength of $211.11 \text{ MPa} * \frac{\text{cm}^3}{\text{g}}$ is higher than all other known aluminum alloys produced via AM methods, and well within the range of Ti alloys and steels (Figure 103).
- Identify and successfully utilize additives while printing AA 7075 to improve the materials properties beyond those achieved by pure AA 7075 via particle strengthening methods. Characterize and mechanically test the samples to verify additives were successfully incorporated and probe the microstructure to understand how the additives interacted with AA 7075.
- Complete—NB were unsuccessful, but Zn enrichment was partially successful. Zn-enriched AA 7075 was printed with an average UTS of 644.77 MPa at an average ductility of 11.76%. The specific strength of both enrichment schemes was higher (217.26 and $226.24 \text{ MPa} * \frac{\text{cm}^3}{\text{g}}$) than that achieved by AA 7075 and at the high end of Ti alloys range (Figure 103).

- Design and print custom infill aluminum components to further optimize strength-to-weight ratio. Initial printing to be done with aluminum alloy 4008 (AA 4008) to lay the groundwork for accomplishing with AA 7075.
- Partially complete—although a code was developed and used to some success to modify AA 4008 prints with ElemX, the custom infill is not optimized and no mechanical testing was completed.



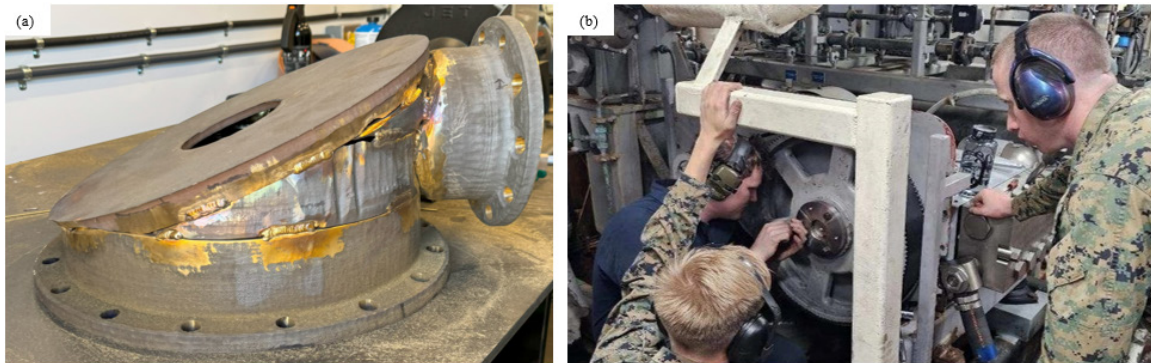
Adapted from [55].

Figure 103. Specific strength comparison of 7XXX aluminum printed via LMJP.

B. OPERATIONAL OBJECTIVES

The DON needs M-AM techniques right now to help in the critical areas of BDA/R and contested logistics; therefore, it is imperative to develop expertise in the use of M-AM for support of the Fleet today. Both operational objectives shall now be analyzed in retrospect of the results obtained:

- Utilize a M-AM technique for a simulated battle damage repair, where the part drawing is unavailable, and the original part is damaged beyond repair. The printed parts should be post-processed and retested to the maximum extent possible.
- Complete—Four parts were fabricated and successfully retested using the XSPEE3D cold spray metal printer during S24, including a heat exchanger cooler head (Figure 104a).
- Utilize various M-AM techniques to design, print, and certify parts for as many DoD components as possible. Certification shall be conducted both at NPS and locally to expedite the timeline to verify a part is suitable for use.
- Complete—the XSPEE3D and Snowbird laser wire DED system were employed to print a total of 41 parts and eight test coupons throughout TW24. Of those parts, two were used to close CASREPs on USS SOMERSET, providing an immediate readiness solution to the Fleet (Figure 104b). Parts from both printers were characterized at Bear Machinery in Kaneohe, HI and at the NPS laboratory with all test coupons except one passing all materials characterization and testing.



(a) Heat exchanger cooler head produced during S24 and (b) installation of the RO pump bushing during TW24.

Figure 104. Successful prints during S24 and TW24.

C. FUTURE DIRECTIONS

Based on the results achieved in Chapters IV–VII addressing the research and operational objectives above, a discussion on possible future work is provided.

1. LMJP of AA 7075 and Zn-Enriched AA 7075

With a methodology developed to successfully produce AA 7075 and Zn-enriched AA 7075 via LMJP, the next major step is to scale the process to produce useful parts for the DON. Additionally, the Zn enrichment did not hit the target UTS, indicating that the ZN content was insufficient and/or not homogeneously distributed throughout the prints. Therefore, adding more Zn and possibly Cu to improve the materials properties to that of AA 7068 should be explored. To better understand why the results of both Zn enrichment methods were inconsistent, a study on the mixing characteristics within the ElemX printer crucible would be useful, possibly using the Ansys Fluent MHD module for simulating magnetohydrodynamic forces and mixing. Another means of achieving additional strengthening is via a tailored heat treatment procedure, which could be studied utilizing the rapid nano-CT capability at the 18-ID FXI beamline.

2. Gradient Infill of Aluminum Alloys

Further refinement and application of codes to customize the print infill is needed to improve the reproducibility of the process. With that complete, printing fully customizable 7XXX series aluminum components should be achievable and have an immediate impact on the aerospace, marine, automotive, and other key industrial sectors, not to mention the DON. The water displacement method or CT scans could be used for a study to provide quantitative data on the gradient infill achieved using the code. Ultimately, the goal is producing parts similar to the ones shown in Figure 25 and performing mechanical testing.

3. Expeditionary Metal Additive Manufacturing

The DON must continue to invest in M-AM and AdvM technologies to improve capability in the areas of BDA/R and contested logistics. Proper use of M-AM and AdvM technologies can equate to huge savings in both Ao and money, improving readiness in

contested environments and augmenting fragile supply chains. A more systematic study of M-AM and AdvM technologies, with a focus on the materials properties of printed, heat treated, and machined parts (including the fatigue limit), would better inform DON leaders on the long-term benefits of these technologies to the Fleet.

THIS PAGE INTENTIONALLY LEFT BLANK

APPENDIX A. ELEMX STANDARD OPERATING PROCEDURE

Preparing the Nozzle

1.1 Nozzle Preparation utilizing Pre-filled Plugs

- | | |
|----------------------------------------------------------------------------------------------------------------------------------------------------------------------------------------------------------------------------------------------|---------------------------------------------------------------------------------------------------------------------------------------------|
| 1) Check the lower pump under microscope for any defects | Aluminum pre-filled plugs can be used instead of plasma treatment. More pre-filled plugs can be printed using the STL file on the computer. |
| 2) Sand the lower pump with 1000 grit sandpaper to $0.500\text{ mm} \pm 0.005$ | Take care not to touch the front face of the lower pump. |
| 3) Clean lower pump with compressed air. | Take care not to drop lower pump or shoot it across the room with the compressed air. |
| 4) Place the pre-filled plug in the upper pump and place the lower pump on top. Ensure no gap between the upper and lower pump. Apply a small amount of superglue in 3–4 spots at the junction to hold the assembly together. | |
| 5) After waiting about 5 min to dry, insert the upper/lower pump assembly into the heater element coils. Apply a small dab of superglue to hold in place. Verify upper/lower pump assembly fits snuggly and flush with the end of the coils. | |
| 6) While waiting for the glue to fully dry, proceed to section 2 to start up the ElemX. | Do not be in a hurry; allow glue to fully dry so a nozzle is not dropped and ruined. |

Start Up

2.1 Aligning Mainline Power & PC Start Up

- | | |
|-------------------------------------------------------------------------|-------------------------------------------|
| 1) Take the power selector switch on the back of the Xerox ElemX to ON. | Aligns mainline power to the Xerox ElemX. |
|-------------------------------------------------------------------------|-------------------------------------------|

2) Pull the emergency stop button out and turn a quarter-turn CCW.	Resets the emergency shutdown interlock.
3) Wait for the PC to start up then log in. Once logged in, the HMI should start up automatically. If not, select it from the desktop.	
4) Once the HMI is open, select NO ACCESS in the top right corner and log in with the user password used to log in to the PC.	
5) If not lit, press the green START button on the OBP.	Resets the HMI.
6) Press the JOG button on the OBP.	Shifts printer axis control to manual.
7) Press and hold the RESET button on the OBP for 5 seconds.	Clears start up alerts and warnings.
8) Press FEED START on OBP.	Permits operation of motion controls.

2.2 Installing Pump

1) Place the pump assembly into the print head and ensure the following: a) Thermocouples are properly routed (if no twisting can occur, it is properly routed). b) Heater contacts are secure. c) Shoulder bolts are flush, bottomed out, and tight.	Print quality can be negatively affected if the upper pump assembly and associated instrumentation is not installed properly. Excess vibration of loose print head components can lead to damage of the print head and upper pump assembly.
2) Select the METALS CONTROL tab on the HMI and verify the thermocouple position on the print head camera.	The upper pump is delicate and can be punctured by the thermocouple. Proper installation must be verified via the viewing camera to prevent damage to the thermocouple.

- 3) Place a catch tray for the Burn-In process in the center of the build plate and close the front door.

2.3 Energizing Chiller & Aligning Argon

WARNING: DO NOT EXCEED 100 PSI ON THE EXTERNAL ARGON REGULATOR. EXCEEDING 100 PSI INTO THE XEROX ELEMX COULD RESULT IN INTERNAL REGULATOR DAMAGE.

- 1) Align external argon source to Xerox ElemX and adjust regulator pressure to 40 ± 10 psi.
- 2) Press the COOLANT ON button on the OBP.
- 3) Select the THERMAL CONTROLS tab on the HMI. If EMERGENCY CHILLER STOP is flashing red, select the EMERGENCY CHILLER STOP. Click START CHILLER on the HMI.
- 4) Press the ARGON button on the OBP.
- 5) Observe as the argon flow indication increases to 7 ± 0.15 L/min. If argon flow does not reach 7 ± 0.15 L/min, verify external argon regulator outlet pressure.

DO NOT EXCEED 100 PSI. ARGON REGULATOR NORMALLY DOES NOT NEED TO BE ADJUSTED.

EMERGENCY CHILLER STOP may be flashing because of the shutdown procedure.

2.4 Energizing Heaters

- 1) Press the UPPER HEATER ENABLE and BUILD HEATER ENABLE buttons on the OBP. Wait until all three lights under the chiller on the HMI turn green.
- 2) Select the THERMAL CONTROLS tab on the HMI then select BED START HEATING and HEAD START HEATING on the THERMAL CONTROLS SCREEN. Observe both

temperatures increase. If temperatures do not increase, verify proper logon to the HMI and proper argon flow.

- 3) Wait for the head temperature to reach 825°C before proceeding. If not using “Plug,” turn off pre-fill plug in user diagnostics.
- 4) Between 700–800°C, observe the head temperature. An overheating alert may occur, resulting in the head temperature decreasing. If this occurs, select ALARM ACK and RESET on the OBP. Next, select the thermal control tab on the HMI and select HEAD START HEATING.

Attempting to fill the reservoir before print head temperature of 825 °C is reached WILL CAUSE DAMAGE TO THE UPPER PUMP.

Conduct fault steps without delay to not cool down lower pump and crack it.

2.5 Filling Reservoir

- 1) Select the METAL CONTROLS tab on the HMI.
- 2) Press the WIRE FEED button on the OBP.
- 3) Take the WIRE FEED knob to 80mm/min (75 %).
- 4) Select FILL MODE on the METAL CONTROLS screen and observe the filament move into the reservoir.
- 5) If the HMI switches from FILL MODE to MANUAL MODE, verify the reservoir level is below the set point of 121.0 mm then select FILL MODE to continue filling.

As the filament is fed into the reservoir, the laser level sensor can erroneously detect level out of range and shift from automatic feeding to manual feeding.

NOTE: if HMI keeps switching into “hold” mode, it is a laser issue. Press stop and allow melt pool level to stabilize. Switch to MANUAL wire

- feed, select 4TH AXIS on the OBP, then + on the OBP to jog the wire forward past the laser issue area. Do not exceed 121 mm
- 6) Once the melt pool is visible in the print head camera, take the WIRE FEED knob to 200 mm/min (100%).
 - 7) When the reservoir level reaches 121.0 mm, observe the HMI shift from FILL MODE to HOLD MODE.

2.6 Energizing the High Voltage Supply & Electronic Pulse Controller

- 1) Press the HV ENABLE button on the OBP, then wait 10 seconds.
 - 2) Press the EPC ENABLE button on the OBP.
- A ten second wait is required to ensure that the current demand does not exceed the interlock to prevent simultaneous energizing of HV and EPC.

2.7 Loading Pulse Width

- 1) Select the METAL CONTROLS tab on the HMI.
- 2) Select LOAD TIME on the METAL CONTROLS screen and observe the PULSE HIGH TIME read +0.1300

2.8 Burn-In

- 1) Verify work offsets are centered at 150X and 150Y by performing the following:
 - a) Select the OPERATE tab on the HMI.
 - b) Select the MACHINE icon on the OPERATE screen to display the MACHINE page.
- Not Necessary for Burn-In, but good to check before each print.
- Note: 150 for X and Y offsets might not be appropriate for every print. Change as needed to start the print off the center of the build plate if necessary.

- c) Select PARAMETERS then WORK OFFSETS.
- d) Select the G54...G57 icon and verify G56 and G57 values for X and Y are 150.
- f) Return to the main OPERATE page by selecting PARAMETERS then MACHINE

- 2) On the OBP, press the RESET button.

- 3) Take the FREQUENCY knob to 100%.

- 4) Select the METAL CONTROLS tab on the HMI.

- 5) Select BURN-IN on the METAL CONTROLS screen.

- 6) Verify the burn-in program is loaded by the following:
 - a) If not already there, select the OPERATE tab on the HMI.
 - b) Verify the correct code is listed as the current program (program title: BURN_IN_V8).
 - c) If the current program is not correct, press the AUTO button on the OBP.

- 7) Verify BUILD PLATE LOADED is green. If not, verify the build plate is loaded and secured then select BUILD PLATE LOADED.

- 8) Verify the FEED START button on the OBP is lit. If not, press the FEED START button.

- 9) Press the CYCLE START button on the OBP. If WIRE FEED ENABLE MISSING is received on the HMI, repeat step (8).

Note: if using a new upper pump, do two burn-ins to “season” the heater and improve jetting.

Feed start, then center plate

10) Verify adequate jetting using a strobe light set to 100 fps.

Jetting should appear as slow moving, consistent drops. Spraying, inconsistent drop size, or excessive deviation from vertical jetting are indications of poor nozzle performance and a new nozzle should be considered.

- 11) If no jetting occurs, perform the following:
- Verify the HV ENABLE and EPC ENABLE buttons on the OBP are lit.
 - Select the METAL CONTROLS tab on the HMI.
 - Verify the PULSE HIGH TIME is 0.130 ms.
 - On the OBP, press the CYCLE START button.

Wait until burn-in program is complete as sometimes the jetting angle is very poor and improves over the duration of the burn-in program.

2.9 Setting Drop Mass

- Place a zeroed collection tray under the print head and close the front door.
- Select the METAL CONTROLS tab on the HMI.
- Select CALIBRATE on the METAL CONTROLS screen.
- Take the FREQUENCY knob to 60% (300 Hz).
- Press the CYCLE START button on the OBP.
- When jetting has stopped and SYSTEM READY is displayed on the HMI, remove the collection tray and weigh it. The mass should be 1.45 ± 0.05 grams. If not, adjust the PULSE HIGH TIME as follows:

WARNING: Bed plate is hot! Wear PPE when removing collection trays and use tongs.

Up drafts generated by the hot print material may cause lighter-than-actual weight readings. Allowing time for the material to cool down will reduce fluctuations in weight readings.

- a) On the metal controls tab under “jet pulses,” increase/decrease the PULSE HIGH TIME by 0.001 ms per 0.05 grams under/over 1.45 grams by selecting plus or minus 0.5 μ s.
- 7) Once PULSE HIGH TIME has been adjusted, perform steps (1) though (10) until mass is 1.45 ± 0.05 grams.

Printing

3.1 Selecting a Part to Print

- 1) Select the OPERATE tab on the HMI.
- 2) On the OPERATE tab, select PART FOR SUBMISSION. A file explorer will open. Navigate to where the part .MPF file is stored and copy the file to the local disc.
- 3) Once the part is copied to the local disc, select the desired print mode PRINT OPTIMIZATION or ERROR DIFFUSION /FILTERING ONLY.
- 4) Select SUBMIT PART.
- 5) Verify the correct part is loaded on the HMI.

While printing from a network or portable media device is possible, momentary network interruption or portable media device removal will result cycle failure and a failed print.

Print optimization is recommended and ideal in most cases.

3.2 Printing Selected Part

- 1) Verify the desired part is loaded.
- 2) Verify bed plate temperature is stable at 475°C. If the bed plate temperature has overshot 475°C by more than 5°C, wait until the bed plate returns to 475°C before commencing print.

If bed plate temperature is heavily overshot, the bed plate will cool down while a print is in progress, which could lead to part de-lamination due to thermal contraction.

- 3) Ensure the actual bed plate temperature is > 400C at the bed plate surface with the contact thermometer to ensure proper adhesion to the build plate.
- 4) Verify the build plate is clear. Using a wire brush and wearing gloves, firmly score the build plate to ensure proper part adhesion.
- 5) Take the FREQUENCY knob to 100%.
- 6) On the OBP, push the CYCLE START button.

Be sure not to print in the same spot repeatedly to prevent premature wear of the nickel coating on the build plate.

3.3 Removing Printed Parts

- 1) When CYCLE COMPLETE is displayed on the OPERATE tab of the OBP, select BUILD PLATE LOAD/UNLOAD | PROCESS SHUTDOWN tab on the HMI.
- 2) Select UNLOAD PART. The print bed will move to the side door, and the side door will unlock.

NOTE: if build plate does not automatically move to right access door, select “jog” on OBP and manually move the build plate there using X and Y commands.

**WARNING: BUILD PLATE TEMPERATURE IS IN EXCESS OF 450°C.
EXERCISE
USE EXTREME CARE WHILE HANDLING.**

- 3) Open the side door then, using the build plate cart, lift the build plate and remove it from the print bay.
- 4) Slide the side door shut then select UNDOCK CART on the HMI.

If the build plate assembly is moved off the limit switch, clamps will automatically secure the plate. Reset cart slider, close the right access door, hold RESET for >5 sec, press RETURN BUILD PLATE TO CENTER, then return to step 2.

Revised with new build plate dunk cart.
Door Shut → Dunk part → Reset 5 sec

→ Load build plate button → Open door → Load plate in → close door.

CAUTION: EXCESSIVE FORCE MAY DAMAGE PRINTED PART.

- 5) Remove the part from the build plate by lowering the build plate into a pool of water or by spraying with a stream of water. Agitating the part with a rubber mallet may be necessary to remove the part from the print bed.
- 6) Once the part is removed from the build plate and the build plate is clear, remove excess water (if necessary) and lower the build plate back onto the heating element. On the HMI, select LOAD BUILD PLATE and open the right access door. Ensure the build plate is properly aligned. Close the right access door.
- 7) Select PLATE INSTALLED on the HMI and ensure the build plate latches properly grasp the build plate and build plate moves to the home position.
- 8) Select the OPERATE tab on the HMI and select BUILD PLATE LOADED.
- 9) To print additional parts, perform the following:
 - a) Verify the START button on the OBP is flashing green then press the START button.
 - b) On the OBP, press the HV ENABLE button, then wait 10 seconds.
 - c) On the OBP, press the EPC ENABLE button.
 - d) On the OBP, ensure BUILD HEATER ENABLE is selected. Select THERMAL CONTROLS tab on HMI then select BED START HEATING.

CAUTION: build plate may still be extremely hot. Misalignment of the build plate can result in the build plate latch arms not seating correctly. Ensure proper alignment of the build plate.

Wait until the bed temperature is stable at 475°C.
e) Proceed to section 3.1.

Shutdown

4.1 Emptying the Reservoir

- 1) Place the catch tray in the center of the build plate then shut the front door.
- 2) On the OBP, press the HV ENABLE button, then wait 10 seconds.
- 3) On the OBP, press the EPC ENABLE button.
- 4) Select the BUILD PLATE LOAD/UNLOAD | PROCESS SHUTDOWN tab on the HMI, then select RETURN BUILD PLATE TO CENTER.
- 5) On the OBP, push the CYCLE START and RESET buttons.
- 6) On the HMI, select EMPTY PRINT HEAD MOLTEN MATERIAL POOL.
- 7) Take the FREQUENCY knob to 80%.
- 8) On the OBP, press the CYCLE START button.
- 9) When no more material is being ejected from the print head, press the CYCLE STOP button on the OBP.

Move to Part Removal Procedure

Then go to OPERATE Tab

Then use Stroboscope

Then Reset

4.2 Securing Electronic Pulse Control and High Voltage Supply

- | | |
|--------------------------------------------------------------------------------------------------------------------------------------------------------------------------------------------------------------------------------------------------------------------|--|
| <ol style="list-style-type: none"> 1) Wire Feed Disable
 2) On the OBP, press the EPC ENABLE button, and observe the green light go out.
 3) On the OBP, press the HV ENABLE button and observe the green light go out. | |
|--------------------------------------------------------------------------------------------------------------------------------------------------------------------------------------------------------------------------------------------------------------------|--|

4.3 Print Head & Print Bed Cooldown

- | | |
|-------------------------------------------------------------------------------------------------------------------------------------------------------------------------------------------------------------------------------------------------------------------------------------------------------------------------------------------------|------------------------------------------------------------------------------------------------------------------------------------------|
| <ol style="list-style-type: none"> 1) Select the THERMAL CONTROLS tab. on the HMI then select HEAD STOP HEATING and BED STOP HEATING.
 2) When the print head temperature reads 50°C and lowering, press the can UPPER HEATER ENABLE and BUILD HEATER ENABLE button on the OBP and observe the green light go out. | <p>Securing power to the upper heater before temperatures are reduced below 50°C induce cooldown rates that could damage the heater.</p> |
|-------------------------------------------------------------------------------------------------------------------------------------------------------------------------------------------------------------------------------------------------------------------------------------------------------------------------------------------------|------------------------------------------------------------------------------------------------------------------------------------------|

4.4 Securing the Chiller & Argon Flow

- | | |
|------------------------------------------------------------------------------------------------------------------------------------------------------------------------------------------------------------------------------------------------------------------------------------------------------------------------------------------|------------------------------------------------------------------|
| <ol style="list-style-type: none"> 1) On the OBP, press the ARGON button and observe the green light go out.
 2) Secure external argon to the Xerox ElemX.
 3) Select the THERMAL CONTROLS tab on the HMI. When the print head temperature reached below 45°C, select EMERGENCY CHILLER STOP. | <p>DO NOT TOUCH THE ARGON REGULATOR KNOB WHEN SECURING ARGON</p> |
|------------------------------------------------------------------------------------------------------------------------------------------------------------------------------------------------------------------------------------------------------------------------------------------------------------------------------------------|------------------------------------------------------------------|

- 4) On the OBP, press the COOLANT ON and WIRE FEED buttons and observe the green lights go out.

4.5 Securing the HMI & Xerox ElemX Power

- 1) On the OBP, depress the red E-STOP button. Turn Feed Knob to 0 and Wire Feed to 50 (lowest)
 - 2) Select the EXIT tab on the HMI then select EXIT RUNTIME.
 - 3) Shutdown the PC by selecting shutdown from the start menu.
 - 4) Take the power selector switch on the back of the Xerox ElemX to OFF.
- Wait for black screen

Casualty Procedures

5.1 Fire

- 1) Depress the EMERGENCY STOP PUSH BUTTON.
- 2) Secure power to the Xerox ElemX by taking the power selector switch on the back of the Xerox ElemX to OFF.
- 3) Fight the fire.

5.2 Casualty: print head is stuck in the print position (down near the plate)

- 1) Press AUTO on the OBP.
- 2) Press and hold RESET for 5 sec.
- 3) Press FEED START on the OBP.
- 4) Ensure the frequency knob is at 100%.

APPENDIX B. AA 7075 POLISHING AND ETCHING RECIPE

Aluminum Alloy 7075 Sanding and Polishing Recipe (March 2024)					
Sanding Steps					
Surface	Force (lbf)	Speed (RPM)	Time (min)	Lubricant	Notes
P800 sandpaper	5	100	2.5	sink water	Sand the tops of the pucks to level them off in prep for microhardness or SEM
P800 sandpaper	1	100	2.5	sink water	Use increments of 2.5 min to ensure not too much material is sanded away
P1000 sandpaper	1	100	10	sink water	
P1500 sandpaper	1	100	15	sink water	
P2500 sandpaper	1	100	20	sink water	
P4000 sandpaper	1	100	30	sink water	P4000 has particle size of ~5 micron so first polishing step is with 3 micron diamond

**** Following all grinding, inspect surface and clean with IPA & cotton swab to remove all sand paper residue / debris ****

Polishing Steps					
Surface	Force (lbf)	Speed (RPM)	Time (min)	Lubricant	Notes
Struers DP-Dac	1	100	5	3 micron diamond	rinse cloth, samples, and sample holder with DI after polishing is complete to remove debris
Struers DP-Dac	1	100	5	3 micron diamond	"
Struers DP-Dac	1	100	5	3 micron diamond	"
Struers DP-Dac	1	100	5	3 micron diamond	"
Buehler MicroCloth	1	100	5	1 micon diamond	"
Buehler MicroCloth	1	100	5	1 micon diamond	"
Buehler MicroCloth	1	100	5	1 micon diamond	"
Buehler MicroCloth	1	100	5	1 micon diamond	"
Buehler MicroCloth	1	100	5	0.25 micon diamond	"
Buehler MicroCloth	1	100	5	0.25 micon diamond	"
Buehler MicroCloth	1	100	5	0.25 micon diamond	"
Buehler MicroCloth	1	100	5	0.25 micon diamond	"

Etching Steps			
Step	Process	Procedure	Notes
1	Etching	Fully submerge surface to be etched for 10 sec.	10 sec steps used to ensure surface is not over etched
2	Rinsing	After 10 sec, immediately retract and rinse sample with DI	
3	Drying	Use air compressor to dry surface, rinse with DI, dry, rinse with IPA, dry one last	Use high pressure (> 50 PSI) from a compressor vice canned air to ensure all etchant is removed.

**** for AA7075, 2 cycles of etching for 20 sec total found to be sufficient for a good quality surface etch suitable for optical microscopy!!! ****

THIS PAGE INTENTIONALLY LEFT BLANK

LIST OF REFERENCES

- [1] Xometry, “4 Types of Metal 3D Printing Processes and Their Materials,” Aug. 23, 2022. Available: <https://www.xometry.com/resources/3d-printing/types-of-metal-3d-printing/>
- [2] I. Gunduz, “Additive Manufacturing Science and Applications,” presented at the Naval Postgraduate School, Monterey, CA USA, Jul. 07, 2023.
- [3] M. Sokoluk, C. Cao, S. Pan, and X. Li, “Nanoparticle-enabled phase control for arc welding of unweldable aluminum alloy 7075,” *Nat Commun*, vol. 10, no. 1, p. 98, Jan. 2019, Available: <https://doi.org/10.1038/s41467-018-07989-y>
- [4] M. Zuo, M. Sokoluk, C. Cao, J. Yuan, S. Zheng, and X. Li, “Microstructure Control and Performance Evolution of Aluminum Alloy 7075 by Nano-Treating,” *Scientific Reports*, vol. 9, no. 1, p. 10671, Jul. 2019, Available: <https://doi.org/10.1038/s41598-019-47182-9>
- [5] J. H. Martin, B. D. Yahata, J. M. Hundley, J. A. Mayer, T. A. Schaedler, and T. M. Pollock, “3D printing of high-strength aluminium alloys,” *Nature*, vol. 549, no. 7672, Art. no. 7672, Sep. 2017, Available: <https://doi.org/10.1038/nature23894>
- [6] A. Bhagavatam, A. Ramakrishnan, and V. A. and G. P. Dinda, “Laser Metal Deposition of Aluminum 7075 Alloy,” *IJMSR*, vol. 2, no. 1, pp. 50–55, Oct. 2018, Available: <https://doi.org/10.18689/ijmsr-1000108>
- [7] Britannica, “Aluminum: Uses, Properties, & Compounds,” Jul. 24, 2024. Available: <https://www.britannica.com/science/aluminum>
- [8] ALFED, “Aluminium is the third most common element in the earth’s crust,” Oct. 15, 2020. Available: <https://alfed.org.uk/aluminium-is-the-third-most-common-element-in-the-earths-crust-2/>
- [9] S. Neuman, “Aluminum’s Strange Journey From Precious Metal To Beer Can,” *NPR*, Dec. 10, 2019. Available: <https://www.npr.org/2019/12/05/785099705/aluminums-strange-journey-from-precious-metal-to-beer-can>
- [10] G. J. Binczewski, “The Point of a Monument: A History of the Aluminum Cap of the Washington Monument,” *JOM*, vol. 47, no. 11, pp. 20–25, 1995, Available: <https://www.tms.org/pubs/journals/jom/9511/binczewski-9511.html>

- [11] ACS: Chemistry for Life, “Hall Process: Production and Commercialization of Aluminum,” *American Chemical Society National Historic Chemical Landmarks*. Available: <https://www.acs.org/education/whatischemistry/landmarks/aluminumprocess.html>. [Accessed: Oct. 21, 2024]
- [12] NASA, “NASA’s Perseverance Mars Rover Gets Its Wheels and Air Brakes – NASA,” Apr. 03, 2020. Available: <https://www.nasa.gov/solar-system/nasas-perseverance-mars-rover-gets-its-wheels-and-air-brakes/>
- [13] Aluminum Magazine: Everything About Aluminum, “The Future of Aluminium: Advancements and Innovations,” Feb. 23, 2024. Available: <https://aluminiummagazine.com/mag/magazine/the-future-of-aluminium-advancements-and-innovations.html>
- [14] L. Kolbeinsen, “The beginning and the end of the aluminium value chain,” *Matériaux & Techniques*, vol. 108, p. 506, Jan. 2020, Available: <https://doi.org/10.1051/matech/2021008>
- [15] Wright Brothers Aeroplane Company, “1903 Wright Engine,” 2011. Available: https://www.wright-brothers.org/Information_Desk/Just_the_Facts/Engines_&_Props/1903_Engine.htm
- [16] W. D. Callister and D. G. Rethwisch, *Materials Science and Engineering: An Introduction*, 9th ed. Hoboken, NJ: John Wiley & Sons, Inc., 2014.
- [17] R. J. D. Tilley, *Crystals and Crystal Structures*. Hoboken, NJ USA: John Wiley & Sons, 2020.
- [18] N. Tsymbal, “Introduction to Solid State Physics: Crystal Structure,” presented at the Physics 927, University of Nebraska-Lincoln, 2024.
- [19] T. Y. Ansell, “Crystal Structure and XRD,” presented at the Naval Postgraduate School, Monterey, CA USA, Jan. 05, 2023.
- [20] B. Ohl, “What is the Difference Between ‘Crystal Structure’ and ‘Bravais Lattice?’,” Nov. 24, 2022. Available: <https://msestudent.com/what-is-the-difference-between-crystal-structure-and-bravais-lattice/>
- [21] T. Y. Ansell, “Introduction to Crystallography,” presented at the Naval Postgraduate School, Monterey, CA USA, Jan. 04, 2023.
- [22] B. Ohl, “Face-Centered Cubic (FCC) Unit Cell,” *Materials Science & Engineering Student*, Nov. 24, 2022. Available: <https://msestudent.com/face-centered-cubic-fcc-unit-cell/>

- [23] B. Ohl, “Miller Indices for Crystal Directions and Planes,” *Materials Science & Engineering Student*, Nov. 24, 2022. Available: <https://msestudent.com/miller-indices/>
- [24] P. M. V. Raja and A. R. Barron, *Physical Methods in Chemistry and Nano Science*. Rice University: LibreTexts, 2024. Available: [https://chem.libretexts.org/Bookshelves/Analytical_Chemistry/Physical_Methods_in_Chemistry_and_Nano_Science_\(Barron\)](https://chem.libretexts.org/Bookshelves/Analytical_Chemistry/Physical_Methods_in_Chemistry_and_Nano_Science_(Barron))
- [25] Britannica, “Slip.” Available: <https://www.britannica.com/science/slip-crystals>. [Accessed: Oct. 22, 2024]
- [26] P. Ball, “A sense of dislocations,” *Nature Mater*, vol. 14, no. 10, pp. 968–968, Oct. 2015, Available: <https://doi.org/10.1038/nmat4443>
- [27] M. A. Meyers and K. K. Chawla, *Mechanical Behavior of Materials*, 2nd ed. New York, NY, USA: Cambridge University Press, 2009.
- [28] Howard Precision Metals, “Differences Between Cast and Wrought Aluminum Alloys,” Oct. 19, 2022. Available: <https://www.howardprecision.com/differences-between-cast-and-wrought-aluminum-alloys/>
- [29] Southwest Aluminum. “What are the differences between wrought and cast aluminum?” Apr. 01, 2020. Available: <https://www.southwest-aluminum.com/info/what-are-the-differences-between-wrought-and-c-44453499.html>
- [30] K. L. Kelty, “Influence of the as-printing and post-printing processes on the mechanical properties of liquid metal jetted 3D parts,” M.S. thesis, Dept. of MAE, NPS, Monterey, CA USA, 2022.
- [31] Warner Brothers Foundry Company, “Advantages of Alloys Over Pure Metal,” Aug. 25, 2021. Available: <https://www.wbcastings.com/blog/advantages-of-alloys/>
- [32] Aluminum Guide, “Aluminium alloys classifications,” Oct. 01, 2018. Available: <https://aluminium-guide.com/classifications-aluminium-alloys/>
- [33] R. Marker, “Understanding Aluminum Alloys,” *Aluminum Fabrication*, Apr. 22, 2024. Available: <https://www.allmetalsfab.com/understanding-aluminum-alloys/>
- [34] Smiths Metal Centres, “3003 Aluminum Alloy,” Biggleswade, United Kingdom, 2020. Available: <https://www.smithmetal.com/3003.htm>
- [35] Smiths Metal Centres, “5052 Aluminum Alloy,” Biggleswade, United Kingdom, 2020. Available: <https://www.smithmetal.com/5052.htm>

- [36] Aluminum Guide, “6061 Aluminium Alloy,” Oct. 12, 2013. Available: <https://aluminium-guide.com/alyuminium-alloy-6061/>
- [37] World Material, “7075 Aluminum Alloy Properties, AA 7075-T6, T7351, T651, Density, Composition, Yield Strength.” Available: <https://www.theworldmaterial.com/al-7075-aluminum-alloy/>. [Accessed: Aug. 18, 2024]
- [38] J. R. Davis, *Aluminum and aluminum alloys*. Materials Park, OH: ASM International, 1993.
- [39] R. Cornell and H. K. D. H. Bhadeshia, “Aluminium-Silicon Casting Alloys,” *University of Cambridge*. Available: <https://www.phase-trans.msm.cam.ac.uk/abstracts/M7-8.html>. [Accessed: May 11, 2023]
- [40] Total Materia, “AlMgSi Alloys,” Oct. 2014. Available: <https://www.totalmateria.com/page.aspx?ID=CheckArticle&LN=EN&site=KTN&NM=348>
- [41] J. Joys, R. Kasler, and L. R. Thomas, “Atomised aluminium alloy powders for metal Additive Manufacturing,” *Metal Additive Manufacturing*, vol. 2, no. 3, pp. 73–76, Sep. 01, 2016. Available: <https://www.metal-am.com/articles/selecting-atomised-aluminium-alloy-powders-for-the-metal-3d-printing-process/>
- [42] J. Hu, W. Zhang, D. Fu, J. Teng, and H. Zhang, “Improvement of the mechanical properties of Al–Mg–Si alloys with nano-scale precipitates after repetitive continuous extrusion forming and T8 tempering,” *Journal of Materials Research and Technology*, vol. 8, no. 6, pp. 5950–5960, Nov. 2019, Available: <https://doi.org/10.1016/j.jmrt.2019.09.070>
- [43] C. Fletcher, “Metallography Guide for Xerox 4008 Aluminum Wire,” Xerox, Norwalk, CT USA, White Paper 01/22, 2022.
- [44] T. DebRoy *et al.*, “Additive manufacturing of metallic components – Process, structure and properties,” *Progress in Materials Science*, vol. 92, no. March 2018, pp. 112–224, Available: <https://doi.org/10.1016/j.pmatsci.2017.10.001>
- [45] M. Ziolkowski and T. Dyl, “Possible Applications of Additive Manufacturing Technologies in Shipbuilding: A Review,” *Machines*, vol. 8, no. 4, Art. no. 4, Dec. 2020, Available: <https://doi.org/10.3390/machines8040084>
- [46] G. Langelandsvik, O. M. Akselsen, T. Furu, and H. J. Roven, “Review of Aluminum Alloy Development for Wire Arc Additive Manufacturing,” *Materials*, vol. 14, no. 18, Art. no. 18, Jan. 2021, Available: <https://doi.org/10.3390/ma14185370>

- [47] S. Srivatsav, V. Jayakumar, and M. Sathishkumar, “Recent developments and challenges associated with wire arc additive manufacturing of Al alloy: A review,” *Materials Today: Proceedings*, vol. 46, pp. 8561–8566, Jan. 2021, Available: <https://doi.org/10.1016/j.matpr.2021.03.542>
- [48] E. A. Starke and J. T. Staley, “Application of modern aluminum alloys to aircraft,” *Progress in Aerospace Sciences*, vol. 32, no. 2, pp. 131–172, Jan. 1996, Available: [https://doi.org/10.1016/0376-0421\(95\)00004-6](https://doi.org/10.1016/0376-0421(95)00004-6)
- [49] Kaiser Aluminum, “Alloy 7068,” Foothill Ranch, CA USA, MMPDS-04, Oct. 2019. Available: <https://www.kaiseraluminum.com/search/?search=Kaiser%20Aluminum%20Alloy%207068>
- [50] Smiths Metal Centres, “7068 Aluminum Alloy,” Biggleswade, United Kingdom, 2020. Available: <https://www.smithmetal.com/7068.htm>
- [51] MatWeb, “Aluminum 7068-T6; 7068-T651 Rod & Bar.” Available: <https://www.matweb.com/search/datasheet.aspx?matguid=c31454fe42574158b23efcc6abb0a6b9>. [Accessed: Jul. 16, 2024]
- [52] MatWeb, “Aluminum 7075-T6; 7075-T651.” Available: <https://www.matweb.com/search/datasheet.aspx?MatGUID=4f19a42be94546b686bbf43f79c51b7d&ckck=1>. [Accessed: Jul. 16, 2024]
- [53] M. Minnicino, D. Gray, and P. Moy, “Aluminum Alloy 7068 Mechanical Characterization,” U.S. Army Research Laboratory, Aberdeen Proving Ground, MD, Technical ARL-TR-4913, Aug. 2009.
- [54] V. Anand, A. J. Kaufman, and N. J. Grant, “Rapid Solidification of a Modified 7075 Aluminum Alloy by Ultrasonic Gas Atomization,” Dept. of Materials Science and Engineering, MIT, Cambridge, MA USA, N00014-78-C-0385, Mar. 1980. Available: <https://apps.dtic.mil/sti/citations/ADA085141>
- [55] Y. Zhu *et al.*, “Ultrastrong nanotwinned titanium alloys through additive manufacturing,” *Nat. Mater.*, vol. 21, no. 11, pp. 1258–1262, Nov. 2022, Available: [10.1038/s41563-022-01359-2](https://doi.org/10.1038/s41563-022-01359-2)
- [56] Wieland Diversified, “HY 80 Steel,” 2021. Available: <https://www.wieland-diversified.com/hy-80-100-steels/hy-80-steel/>
- [57] Meltio, “Meltio Stainless Steel 316L,” Jaen, Spain, ER316LSI, Aug. 2024. Available: <https://meltio3d.com/metal-3d-printing-materials-guide/>

- [58] A. Mauduit, S. Pillot, and H. Gransac, “Study of the suitability of aluminum alloys for additive manufacturing by laser powder bed fusion,” *UPB Sci. Bull. Ser. B Chem. Mater. Sci.*, vol. 79, pp. 219–238, Dec. 2017, Available: https://www.researchgate.net/publication/321679030_Study_of_the_suitability_of_aluminum_alloys_for_additive_manufacturing_by_laser_powder_bed_fusion
- [59] C. Mulvaney, M. Domack, C. Domack, K. Taminger, and J. FitzGerald, “Hot Cracking Behavior and Beam-Induced Grain Refinement in Electron Beam Freeform Fabricated Al 7075,” NASA, Langley Research Center Hampton, VA, NASA/TP—20230005342, Jun. 2023. Available: <https://ntrs.nasa.gov/citations/20230005342>
- [60] A. Wimmer, H. Panzer, C. Zoeller, S. Adami, N. A. Adams, and M. F. Zaeh, “Experimental and numerical investigations of the hot cracking susceptibility during the powder bed fusion of AA 7075 using a laser beam,” *Prog Addit Manuf*, Oct. 2023, Available: <https://doi.org/10.1007/s40964-023-00523-7>
- [61] S. Kou, *Welding Metallurgy*, 3rd ed. Hoboken, NJ: John Wiley & Sons, Inc., 2003.
- [62] J. Brehm, J. Buckner, C. Profazi, and A. Hickman, “Incipient Melting in AA7075,” Sandia National Lab, Albuquerque, NM USA, SAND2022-9908, Jul. 2022. doi: 10.2172/1876952. Available: <https://www.osti.gov/biblio/1876952>
- [63] J. Beddoes, “Design of solution heat treatments for aerospace alloys,” *Canadian Metallurgical Quarterly*, vol. 50, no. 3, pp. 215–221, Jul. 2011, Available: <https://doi.org/10.1179/1879139511Y.0000000004>
- [64] S. Kou, “Predicting Susceptibility to Solidification Cracking and Liquation Cracking by CALPHAD,” *Metals*, vol. 11, no. 9, Art. no. 9, Sep. 2021, Available: <https://doi.org/10.3390/met11091442>
- [65] A. P. Babu, S. K. Kairy, A. Huang, and N. Birbilis, “Laser powder bed fusion of high solute Al-Zn-Mg alloys: Processing, characterisation and properties,” *Materials & Design*, vol. 196, p. 109183, Nov. 2020, Available: <https://doi.org/10.1016/j.matdes.2020.109183>. [Accessed: Jul. 30, 2024]
- [66] B. Fields *et al.*, “Investigation of an additively manufactured modified aluminum 7068 alloy: Processing, microstructure, and mechanical properties,” *Materials Science and Engineering: A*, vol. 891, no. 145901, pp. 1–17, Jan. 2024, Available: <https://doi.org/10.1016/j.msea.2023.145901>
- [67] A. Bhagavatam, A. Ramakrishnan, and V. A. and G. P. Dinda, “Laser Metal Deposition of Aluminum 7075 Alloy,” *IJMSR*, vol. 2, no. 1, pp. 50–55, Oct. 2018, doi: 10.18689/ijmsr-1000108. Available: <https://madridge.org/journal-of-material-science-and-research/ijmsr-1000108.php>.

- [68] E. S. Alley, “Strengthening Mechanisms: Particle Strengthening,” presented at the Naval Postgraduate School, Monterey, CA USA, Jul. 05, 2023.
- [69] J. E. Hatch, *Aluminum: Properties and Physical Metallurgy*, 2nd ed. Metals Park, Ohio USA: American Society for Metals, 1984.
- [70] F. B. Darsono and S. T. Koin, “The Effect of T6 Heat Treatment on 7075 Aluminum on its Hardness and Tensile Strength,” *IOP Conf. Ser.: Mater. Sci. Eng.*, vol. 1096, no. 1, p. 012042, Mar. 2021, Available: <https://doi.org/10.1088/1757-899X/1096/1/012042>
- [71] R. E. Smallman and A. H. W. Ngan, *Modern Physcial Metallurgy*, 8th ed. Waltham, MA: Elsevier Science, 2014.
- [72] L. Fischer, “Nano-Dispersion Strengthening of Aluminum,” University of Colorado, 2004. Available: <https://studylib.net/doc/7521525/nano-dispersion-strengthening-of-aluminum---multi>
- [73] J. Osten *et al.*, “Development of Precipitation Hardening Parameters for High Strength Alloy AA 7068,” *Materials*, vol. 13, no. 4, Art. no. 4, Jan. 2020, Available: <https://doi.org/10.3390/ma13040918>
- [74] J. Hatch, *Aluminum: Properties and Physical Metallurgy*, 2nd ed. American Society for Metals, 1984.
- [75] R. Clark *et al.*, “On the correlation of mechanical and physical properties of 7075-T6 Al alloy,” *Engineering Failure Analysis*, vol. 12, no. 4, pp. 520–526, Aug. 2005, Available: <https://doi.org/10.1016/j.engfailanal.2004.09.005>
- [76] J.-P. Immarigeon, R. T. Holt, A. K. Koul, L. Zhao, W. Wallace, and J. C. Beddoes, “Lightweight materials for aircraft applications,” *Materials Characterization*, vol. 35, no. 1, pp. 41–67, Jul. 1995, Available: [https://doi.org/10.1016/1044-5803\(95\)00066-6](https://doi.org/10.1016/1044-5803(95)00066-6)
- [77] Metals and Materials International. “Strength of a 3D Printed Al 7068 Alloy Under Micro-Pillar Compression.” Available: <https://link.springer.com/article/10.1007/s12540-022-01171-2>. [Accessed: Jul. 16, 2024]
- [78] K. Ma *et al.*, “Mechanical behavior and strengthening mechanisms in ultrafine grain precipitation-strengthened aluminum alloy,” *Acta Materialia*, vol. 62, pp. 141–155, Jan. 2014, Available: <https://doi.org/10.1016/j.actamat.2013.09.042>
- [79] L. F. Mondolfo, *Aluminum Alloys: Structure and Properties*. London, United Kingdom: The Butterworth Group, 1979.

- [80] M. Rosso, I. Peter, and C. Castella, “Influence of Heat Treatment Parameters on the Metallurgical Quality of EN AW 7068 Extruded Bars,” in *Light Metals 2015*, M. Hyland, Ed., Cham: Springer International Publishing, 2016, pp. 229–235. doi: 10.1007/978-3-319-48248-4_40. Available: https://doi.org/10.1007/978-3-319-48248-4_40
- [81] N. Birbilis, M. K. Cavanaugh, and R. G. Buchheit, “Electrochemical behavior and localized corrosion associated with Al₇Cu₂Fe particles in aluminum alloy 7075-T651,” *Corrosion Science*, vol. 48, no. 12, pp. 4202–4215, Dec. 2006, Available: 10.1016/j.corsci.2006.02.007
- [82] O. Gharbi, S. Kairy, P. Lima, D. Jiang, J. Nicklaus, and N. Birbilis, “Microstructure and corrosion evolution of additively manufactured aluminium alloy AA7075 as a function of ageing,” *npj Materials Degradation*, vol. 3, Dec. 2019, Available: <https://doi.org/10.1038/s41529-019-0101-6>
- [83] *Materials Characterization*, vol. 10. Metals Park, Ohio: ASM International, 2019. Available: <https://dl.asminternational.org/handbooks/edited-volume/7/Materials-Characterization>
- [84] Struers, “Hardness Testing,” Ballerup, Denmark, 62140510, Sep. 2017. Available: <https://www.struers.com/en/Knowledge/Hardness-testing#>
- [85] E. S. Alley, “Mechanical Testing-Macro and Micro Hardness,” presented at the Naval Postgraduate School, Monterey, CA USA, Apr. 21, 2023.
- [86] C. Harris, “What is the Formula for Rockwell Hardness?,” Ames, Jul. 11, 2023. Available: <https://amesportablehardnesstesters.com/what-is-the-formula-for-rockwell-hardness/>
- [87] Struers, “Rockwell Hardness Testing (HR).” Available: <https://www.struers.com/en/Knowledge/Hardness-testing/Rockwell#>. [Accessed: Aug. 15, 2024]
- [88] Struers, “Vickers hardness testing insight | Struers.com.” Available: <https://www.struers.com/en/Knowledge/Hardness-testing/Vickers#application>. [Accessed: Aug. 15, 2024]
- [89] Ametek, “Brinell Hardness Testing.” Available: <https://www.hardnesstesters.com/test-types/brinell-hardness-testing>. [Accessed: Aug. 15, 2024]
- [90] Ametek, “Rockwell Hardness Testing.” Available: <https://www.hardnesstesters.com/test-types/rockwell-hardness-testing>. [Accessed: Aug. 28, 2024]
- [91] N. E. Dowling, *Mechanical Behavior of Materials: Engineering Methods for Deformation, Fracture, and Fatigue*, 4th ed. Essex, England: Pearson Education Limited, 2013.

- [92] D. Brandon and W. Kaplan, *Microstructural Characterization of Materials*, 2nd ed. The Atrium, Southern Gate, Chichester, West Sussex PO19 8SQ, England: John Wiley & Sons, Inc., 2008.
- [93] Evident, “Anatomy of a Microscope – Numerical Aperture and Resolution.” Available: <https://www.olympus-lifescience.com/en/microscope-resource/primer/anatomy/numaperture/>. [Accessed: Sep. 16, 2024]
- [94] T. Y. Ansell, “Electron Microscopy,” presented at the Naval Postgraduate School, Monterey, CA USA, Jan. 31, 2023.
- [95] ThermoFisher Scientific, “Transmission Electron Microscopy vs. Scanning Electron Microscopy,” *ThermoFisher Scientific*. Available: <https://www.thermofisher.com/us/en/reference-components/MSD-reference-components/instruments-reference-components/materials-science-form.html>. [Accessed: Oct. 22, 2024]
- [96] ThermoFisher Scientific, “The Difference Between SEM and Optical Microscopes.” Available: <https://www.thermofisher.com/us/en/home/materials-science/learning-center/applications/sem-optical-microscopes-difference.html>. [Accessed: Sep. 16, 2024]
- [97] R. Shimizu, “Quantitative Analysis by Auger Electron Spectroscopy,” *Jpn. J. Appl. Phys.*, vol. 22, no. 11R, p. 1631, Nov. 1983, Available: <https://doi.org/10.1143/JJAP.22.1631>
- [98] T. Y. Ansell, “X-ray Generation,” presented at the Naval Postgraduate School, Monterey, CA USA, Mar. 2023.
- [99] C. Suryanarayana, “Microstructure: An Introduction,” in *Aerospace Materials and Material Technologies, Aerospace Material Technologies*, in 2. Singapore: Springer, 2016, pp. 105–123. Available: https://doi.org/10.1007/978-981-10-2143-5_6
- [100] T. Y. Ansell, “Transmission Electron Microscopy,” presented at the Naval Postgraduate School, Monterey, CA USA, Mar. 01, 2023.
- [101] MyScope, “Transmission Electron Microscopy.” Available: https://myscope.training/TEM_Image_formation_basics. [Accessed: Nov. 20, 2024]

- [102] J. I. Otamendi, “Fabrication and Characterization of Multilayered Assemblies based on Polyelectrolytes and Hybrid Systems with Carbon Nanomaterials for Applications in Nanofiltration and as Smart Surfaces,” Ph.D dissertation, Universidad del País Vasco, Leioa, Bizkaia, Spain, 2016. Available: https://www.researchgate.net/publication/316275263_Fabrication_and_Characterization_of_Multilayered_Assemblies_base_d_on_Polyelectrolytes_and_Hybrid_Systems_with_Carbon_Nanomaterials_for_Applications_in_Nanofiltration_and_as_Smart_Surfaces
- [103] S. Burgess, “What is Standardless Quantitative Analysis?,” *Nanoanalysis*, Nov. 29, 2019. Available: <https://nano.oxinst.com/library/past-blogss/what-is-standardless-quantitative-analysis>
- [104] JEOL: Solutions for Innovation, “Can I Trust My Quantitative EDS Data?,” Nov. 02, 2020. Available: <https://www.jeolusa.com/RESOURCES/Electron-Optics/Documents-Downloads/can-i-trust-my-quantitative-eds-data>
- [105] B. D. Cullity and S. R. Stock, *Elements of X-ray Diffraction*, 3rd ed. India: Pearson Education Limited, 2014.
- [106] Delphi Precision Imaging, “What Is 3D X-Ray / Industrial CT?” Available: <https://www.delphiprecisionimaging.com/what-is-ct-dr>. [Accessed: Nov. 19, 2024]
- [107] North Star Imaging (NSI) An ITW Company, “System Manual,” Rogers, MN USA, Version 0, Jan. 2022. Available: <https://4nsi.com/product/x5000-industrial-3d-x-ray-inspection-system/>
- [108] X. Xiao *et al.*, “Full-field X-ray Imaging, a Workhorse Microscopy Beamline at NSLS II for Material Science Researches,” *Microscopy and Microanalysis*, vol. 25, no. S2, pp. 386–387, Aug. 2019, Available: <https://doi.org/10.1017/S1431927619002666>
- [109] P. J. Withers, “X-ray nanotomography,” *Materials Today*, vol. 10, no. 12, pp. 26–34, Dec. 2007, Available: [https://doi.org/10.1016/S1369-7021\(07\)70305-X](https://doi.org/10.1016/S1369-7021(07)70305-X)
- [110] Brookhaven National Laboratory, “NSLS-II | Beamline 18-ID (FXI) Full Field X-ray Imaging.” Available: <https://www.bnl.gov/nsls2/beamlines/beamline.php?r=18-ID>. [Accessed: Sep. 17, 2024]
- [111] D. S. Coburn *et al.*, “Design, characterization, and performance of a hard x-ray transmission microscope at the National Synchrotron Light Source II 18-ID beamline,” *Review of Scientific Instruments*, vol. 90, no. 5, p. 053701, May 2019, Available: <https://doi.org/10.1063/1.5088124>

- [112] T. Y. Ansell, “Current Status of Liquid Metal Printing,” *Journal of Manufacturing and Materials Processing*, vol. 5, no. 2, Art. no. 2, Jun. 2021, Available: <https://doi.org/10.3390/jmmp5020031>
- [113] L. Gasman, “Additive aerospace considered as a business.,” in *Additive Manufacturing for the Aerospace Industry*, Elsevier Inc., 2019, pp. 327–340. Available: <https://doi.org/10.1016/B978-0-12-814062-8.00017-0>
- [114] G. Turichin, “Additive Manufacturing of large parts,” *Additive Manufacturing*, Available: <https://doi.org/10.1016/B978-0-12-818411-0.00001-X>
- [115] D. Thomas and A. Gleadall, “Advanced metal transfer additive manufacturing of high temperature turbine blades,” *The International Journal of Advanced Manufacturing Technology*, vol. 4, no. 2, pp. 87–96, Jun. 2022, Available: <https://doi.org/10.1007/s00170-022-09176-2>
- [116] A. Boshetto *et al.*, “Selective Laser Melting of a 1U CubeSat structure. Design for Additive Manufacturing and assembly,” *Acta Astronautica*, vol. 159, pp. 377–384, 2019, Available: <https://doi.org/10.1016/j.actaastro.2019.03.041>.
- [117] G. Z. Yu, D.-T. Chou, D. Hong, A. Roy, and P. N. Kumta, “Biomimetic Rotated Lamellar Plywood Motifs by Additive Manufacturing of Metal Alloy Scaffolds for Bone Tissue Engineering,” *ACS Biomater. Sci. Eng.*, vol. 3, no. 4, pp. 648–657, Apr. 2017, Available: <https://doi.org/10.1021/acsbiomaterials.7b00043>
- [118] D. Klobčar, S. Balos, M. Bašić, A. Djuric, M. Lindič, and A. Šćetinec, “WAAM and Other Unconventional Metal Additive Manufacturing Technologies,” *Advanced Technologies & Materials*, vol. 45, pp. 1–9, Dec. 2020, Available: <https://doi.org/10.24867/ATM-2020-2-001>
- [119] Xometry. “Metal Injection Molding (MIM): Process, Uses, Advantages, and Disadvantages.” Available: <https://www.xometry.com/resources/injection-molding/metal-injection-molding/>. [Accessed: Jul. 28, 2024]
- [120] H. Ye, X. Y. Liu, and H. Hong, “Fabrication of metal matrix composites by metal injection molding—A review,” *Journal of Materials Processing Technology*, vol. 200, no. 1, pp. 12–24, May 2008, Available: <https://doi.org/10.1016/j.jmatprotec.2007.10.066>
- [121] J. Kim, A. Wakai, and A. Moridi, “Materials and manufacturing renaissance: Additive manufacturing of high-entropy alloys,” *Journal of Materials Research*, vol. 35, no. 15, pp. 1–21, Jun. 2020, Available: <https://doi.org/10.1557/jmr.2020.140>
- [122] I. Gunduz, “Additive Manufacturing Methods: Nozzle Based Approaches,” presented at the Naval Postgraduate School, Monterey, CA USA, Jul. 05, 2023.

- [123] RAMLAB, “What is DED? – DED fully explained by the RAMLAB knowledge hub.” Available: <https://www.ramlab.com/resources/ded-101/>. [Accessed: Jul. 28, 2024]
- [124] W. Jin, C. Zhang, S. Jin, Y. Tian, D. Wellmann, and W. Liu, “Wire Arc Additive Manufacturing of Stainless Steels: A Review,” *Applied Sciences*, vol. 10, no. 5, Art. no. 5, Jan. 2020, Available: <https://doi.org/10.3390/app10051563>
- [125] Iván Tabernero, A. Paskual, P. Álvarez, and A. Suárez, “Study on Arc Welding Processes for High Deposition Rate Additive Manufacturing,” *Procedia CIRP*, vol. 68, pp. 358–362, Jan. 2018, Available: <https://doi.org/10.1016/j.procir.2017.12.095>
- [126] WAAM3D, “DED-Based Additive Manufacturing and WAAM’s Continued Rise,” Oct. 25, 2023. Available: <https://www.waam3d.com/blog-posts/ded-based-additive-manufacturing-and-waams-continued-rise>
- [127] B. V. Nair, “Safety management in metal Additive Manufacturing: Observations from Industry,” *Metal Additive Manufacturing*, vol. 5, no. 1, pp. 137–143, 2019, Available: <https://www.metal-am.com/articles/safety-management-in-metal-3d-printing/>
- [128] Meltio, “The benefits of a Wire-based 3D Printing Process,” Sep. 19, 2023. Available: <https://meltio3d.com/the-benefits-of-a-wire-based-3d-printing-process/>
- [129] D.-G. Ahn, “Directed Energy Deposition (DED) Process: State of the Art,” *Int. J. of Precis. Eng. and Manuf.-Green Tech.*, vol. 8, no. 2, pp. 703–742, Mar. 2021, Available: <https://doi.org/10.1007/s40684-020-00302-7>
- [130] N. W. Twisselman, “Functionally Graded Aluminum Metal Matrix Composite Cold Spray Coatings on Aluminum 7075 Substrate,” M.S. thesis, Dept. of MAE, NPS, Monterey, CA USA, 2023.
- [131] T. Schmidt *et al.*, “From Particle Acceleration to Impact and Bonding in Cold Spraying,” *J Therm Spray Tech*, vol. 18, no. 5, pp. 794–808, Dec. 2009, Available: <https://doi.org/10.1007/s11666-009-9357-7>
- [132] R. N. Raoelison *et al.*, “Cold gas dynamic spray technology: A comprehensive review of processing conditions for various technological developments till to date,” *Additive Manufacturing*, vol. 19, pp. 134–159, Jan. 2018, Available: <https://doi.org/10.1016/j.addma.2017.07.001>
- [133] H. Assadi, F. Gärtner, T. Stoltenhoff, and H. Kreye, “Bonding mechanism in cold gas spraying,” *Acta Materialia*, vol. 51, pp. 4379–4394, Sep. 2003, Available: [https://doi.org/10.1016/S1359-6454\(03\)00274-X](https://doi.org/10.1016/S1359-6454(03)00274-X)

- [134] O. C. Ozdemir, C. A. Widener, D. Helfritch, and F. Delfanian, “Estimating the Effect of Helium and Nitrogen Mixing on Deposition Efficiency in Cold Spray,” *J Therm Spray Tech*, vol. 25, no. 4, pp. 660–671, Apr. 2016, Available: <https://doi.org/10.1007/s11666-016-0394-8>
- [135] R. Osthus, “What is Cold Spray | VRC Metal Systems | Box Elder, SD,” Apr. 20, 2021. Available: <https://vrcmetalsystems.com/what-is-cold-spray/>.
- [136] S. Chowdhury *et al.*, “Laser powder bed fusion: a state-of-the-art review of the technology, materials, properties & defects, and numerical modelling,” *Journal of Materials Research and Technology*, vol. 20, pp. 2109–2172, Sep. 2022, Available: <https://doi.org/10.1016/j.jmrt.2022.07.121>
- [137] A. Mauduit, S. Pillot, and H. Gransac, “Study of the suitability of aluminum alloys for additive manufacturing by laser powder bed fusion,” *UPB Sci. Bull. Ser. B Chem. Mater. Sci.*, vol. 79, pp. 219–238, Dec. 2017, Available: https://www.researchgate.net/publication/321679030_Study_of_the_suitability_of_aluminum_alloys_for_additive_manufacturing_by_laser_powder_bed_fusion
- [138] K. Kumar Jha, R. Kesharwani, and M. Imam, “Microstructural and micro-hardness study on the fabricated Al 5083-O/6061-T6/7075-T6 gradient composite component via a novel route of friction stir additive manufacturing,” *Materials Today: Proceedings*, vol. 56, pp. 819–825, Jan. 2022, Available: <https://doi.org/10.1016/j.matpr.2022.02.262>
- [139] I. Gunduz, “Additive Manufacturing Methods: Parallel Methods Part 3 Selective Laser Sintering/Melting (SLS, SLM), Powder Bed Fusion (PBF),” presented at the Naval Postgraduate School, Monterey, CA USA, Jul. 10, 2023.
- [140] S. Heiland, B. Milkereit, K.-P. Hoyer, E. Zhuravlev, O. Kessler, and M. Schaper, “Requirements for Processing High-Strength AlZnMgCu Alloys with PBF-LB/M to Achieve Crack-Free and Dense Parts,” *Materials (Basel)*, vol. 14, no. 23, p. 7190, Nov. 2021, Available: <https://doi.org/10.3390/ma14237190>
- [141] S. Z. Uddin, L. E. Murr, C. A. Terrazas, P. Morton, D. A. Roberson, and R. B. Wicker, “Processing and characterization of crack-free aluminum 6061 using high-temperature heating in laser powder bed fusion additive manufacturing,” *Additive Manufacturing*, vol. 22, pp. 405–415, Aug. 2018, Available: <https://doi.org/10.1016/j.addma.2018.05.047>
- [142] V. Sukhotskiy, P. Vishnoi, I. H. Karampelas, S. Vader, Z. Vader, and E. P. Furlani, “Magnetohydrodynamic Drop-on-Demand Liquid Metal Additive Manufacturing: System Overview and Modelling,” presented at the International Conference of Fluid Flow, Heat and Mass Transfer, Jun. 2018, Available: <https://doi.org/10.11159/ffhmt18.155>.

- [143] S. Farooqi, “One Drop at a Time: Xerox 3D Prints with Liquid Metal,” *Engineering.com*, Feb. 12, 2021. Available: <https://www.engineering.com/one-drop-at-a-time-xerox-3d-prints-with-liquid-metal/>
- [144] L. Chen and G. Yang, “Epitaxial Growth and Cracking Mechanisms of Thermally Sprayed Ceramic Splats,” *J Therm Spray Tech*, vol. 27, no. 3, pp. 255–268, Feb. 2018, Available: <https://doi.org/10.1007/s11666-018-0692-4>
- [145] A. C. Brown, P. Conradie, and B. D. De, “Development of a stereolithography (STL) input and computer numerical control (CNC) output algorithm for an entry-level 3-D printer,” *South African Journal of Industrial Engineering*, vol. 25, no. 2, pp. 39–47, Aug. 2014, Available: <https://doi.org/10.10520/EJC165149>.
- [146] F. W. Baumann, M. Schuermann, U. Odefey, and M. Pfeil, “From GCode to STL: Reconstruct Models from 3D Printing as a Service,” *IOP Conf. Ser.: Mater. Sci. Eng.*, vol. 280, no. 1, p. 012033, Dec. 2017, Available: <https://doi.org/10.1088/1757-899X/280/1/012033>
- [147] F. Marbun, R. A. M. Napitupulu, C. S. Manurung, S. Simanjuntak, and Y.-C. Kao, “Slicing Methodology of A CAD File for 3D Printing,” *IOP Conf. Ser.: Mater. Sci. Eng.*, vol. 852, no. 1, p. 012074, Jul. 2020, Available: <https://doi.org/10.1088/1757-899X/852/1/012074>.
- [148] R. Ye, “What is G-code: Definition, Function, Types & Uses,” *Rapid Prototyping & Low Volume Production*, Jul. 25, 2023. Available: <https://www.3erp.com/blog/g-code/>
- [149] CNCSOURCED, “G-Code vs. M-Code: What’s The Difference?,” Feb. 13, 2024. Available: <https://www.cncsourced.com/guides/g-code-vs-m-code-whats-the-difference/>
- [150] RepRap, “G-code,” Sep. 25, 2024. Available: https://reprap.org/wiki/G-code#G0_.26_G1:_Move
- [151] Xerox Corporation, “Xerox ElemX 3D Printer Operator Manual,” 702P08509, Jun. 2021. Available: https://www.support.xerox.com/en-gb/product/xerox-elemx/downloads?language=en_GB
- [152] K. I. Misch, “Fabricating Porous Metal Structures Capable of Capillary Action Through Additive Manufacturing,” M.S. thesis, Dept. of MAE, NPS, Monterey, CA USA, 2024.
- [153] V. Wang, “Stochastic low density liquid metal printing,” M.S. thesis, Dept. of MAE, NPS, Monterey, CA USA, 2023.
- [154] S. Magnuson, “Navy Must Go All In on Additive Manufacturing, Official Says,” *National Defense*, Mar. 2023.

- [155] D. Maurer, “Timely Actions Needed to Improve Planning and Develop Capabilities for Battle Damage Repair,” Government Accountability Office, Washington, DC, USA, Report to Congressional Committees GAO Report No. GAO-21-246, Jun. 2021.
- [156] D. Maurer, “Services Continue Efforts to Rebuild Readiness, but Recovery Will Take Years and Sustained Management Attention,” United States Government Accountability Office, Washington, DC, USA, Statement for the Record to the Subcommittee on Readiness and Management Support, Committee on Armed Services, U.S. Senate GAO Report No GAO-21-225T, Dec. 2020.
- [157] Meltio, “US Navy installs on board the first Phillips Additive Hybrid,” Jan. 16, 2023. Available: <https://meltio3d.com/us-navy-installs-on-board-the-first-phillips-additive/>
- [158] Naval Sea Systems Command Office of Corporate Communications, “Metal 3D Printer Installed on USS Bataan,” Nov. 04, 2022.
- [159] Naval Sea Systems Command Public Affairs, “NAVSEA Improves Readiness of USS Bataan with New 3D Printing Capability,” Aug. 15, 2023.
- [160] Z. Vrtis, S. Cohick, M. Tisdall, and E. Gunduz, “Enhancing Military Operational Readiness Through Advanced Manufacturing Technologies: Insights from Recent Exercises,” *The Phalanx*, vol. 57, no. 3, pp. 34–39, Fall 2024. Available: <https://www.mors.org/Publications/Phalanx/Current-Issue>
- [161] ASTM. “Standard Test Methods for Tension Testing Wrought and Cast Aluminum- and Magnesium-Alloy Products (Metric).” Danvers, MA USA, Oct. 01, 2015.
- [162] ASTM. “Standard Test Methods for Tension Testing of Metallic Materials.” Danvers, MA USA, Feb. 01, 2021.
- [163] BNNano, “Boron Nitride NanoBarb.” Available: <https://www.bnnano.com>. [Accessed: Jul. 12, 2023]
- [164] L. Thomson and S. Wilcenski, “Transforming Composite Materials with Boron Nitride NanoBarbs,” Nov. 26, 2020. Available: <https://www.azonano.com/article.aspx?ArticleID=5600>
- [165] S. Stokes, “Dispersion and Precipitation Strengthening of Additively Manufactured Aluminum Alloys,” Thesis, Naval Postgraduate School, Monterey, CA, 2024.
- [166] San Francisco, CA USA. *Fundamentals Of Filing*, (1942). Available: <https://www.youtube.com/watch?app=desktop&v=P5Kp0WEGawY&feature=youtu.be>

- [167] SAE International, “Heat Treatment of Wrought Aluminum Parts.” Warrendale, PA USA, Aug. 2020.
- [168] ANSI. “ASTM E8/E8M-21 – Standard Test Methods for Tension Testing of Metallic Materials.” Available: <https://webstore.ansi.org/standards/astm/astme8e8m21>. [Accessed: Feb. 13, 2024]
- [169] M. Ge *et al.*, “One-minute nano-tomography using hard X-ray full-field transmission microscope,” *Applied Physics Letters*, vol. 113, p. 083109, Aug. 2018, Available: <https://doi.org/10.1063/1.5048378>
- [170] D. Gürsoy, F. De Carlo, X. Xiao, and C. Jacobsen, “TomoPy: a framework for the analysis of synchrotron tomographic data,” *J Synchrotron Rad*, vol. 21, no. 5, pp. 1188–1193, Sep. 2014, Available: <https://doi.org/10.1107/S1600577514013939>
- [171] N. I. Kennedy, “Investigating Methods to Produce In-Situ Alloys in Metal Additive Manufacturing,” M.S. thesis, Dept. of MAE, NPS, Monterey, CA USA, 2023.
- [172] D. Zimmerman, “Battle of Midway: Repairing the Yorktown After the Battle of the Coral Sea,” *Defense Media Network*, May 26, 2012. Available: <https://www.defensemedianetwork.com/stories/youve-got-three-days-repairing-the-yorktown-after-coral-sea/>
- [173] J. DeFarcy, “Commander Task Group 56.1 Battle Damage Assessment / Repair and Tow Exercise,” *Faceplate*, vol. 27, no. 2, pp. 11–14, Nov. 2023, Available: <http://www.navsea.navy.mil/Home/SUPSLV/00C3-Diving/Faceplate-Magazine/>
- [174] J. DeFarcy, “CTG 56.1 Battle Damage Assessment / Repair and Tow Exercise,” CTG 56.1, Manama, Bahrain, After Action Report After Action Report, May 2023.
- [175] MDSU TWO, “ATLANTIC THUNDER 22 ExBDR,” Virginia Beach, VA USA, Apr. 2022.
- [176] M. Beautyman, “Ship Wartime Repair and Maintenance & Afloat Salvage Training Aboard Former Bonhomme Richard (LHD 6),” NAVSEA 00C, Washington, DC, After Action Report After Action Report, Jul. 2021.
- [177] C. Wilkins, “SWARMEX 22–3 EX-DENVER,” MDSU ONE, JBPHH, Hawaii, After Action Report SWARMEX 22–3, Jun. 2022.
- [178] Smit, “USS Chancellorsville (CG-62) Emergency Repair,” Final Report SUS212160-01, Jul. 2022.
- [179] Litton Ship Systems, “USS TARAWA LHA-1,” Litton Ship Systems, California, USA, Booklet of General Plans LD845002, 1977.

- [180] SPEE3D, “Owner’s Manual: XSPEE3D,” Melbourne, Australia, 3.3.1-022, 2024. Available: <https://portal.spee3d.com/documentation/>
- [181] SPEE3D, “Aluminium Bronze Select,” Melbourne, Australia, Material Datasheet, Apr. 2023. Available: <https://portal.spee3d.com/documentation/>
- [182] Columbia Metals Ltd, “Copper Nickel 90/10.” Available: <https://columbiametals.com/product/copper-nickel-90-10-4/>. [Accessed: Jun. 12, 2024]
- [183] SPEE3D, “CuAl10 Bronze Heat Treatment,” Melbourne, Australia, Version 2, Feb. 2024. Available: <https://portal.spee3d.com/documentation/>
- [184] AMPCO Metal, “Technical Data Sheet – AMPCO-TRODE 10,” AMPCO Metal, Material Datasheet 10, 2015. Available: www.ampcometal.com
- [185] AMPCO Metal, “Technical Data Sheet – AMPCO-TRODE 46,” AMPCO Metal, Material Datasheet 46, 2015. Available: www.ampcometal.com
- [186] S. Cohick, “Trident Warrior 2024 Initiative Final Experiment Report – Advanced Manufacturing for Contested Logistics,” Naval Information Warfare Center – Pacific, Monterey, CA, Final Report TW FIMS number 16844, Aug. 2024.
- [187] M. Radigan, “Trident Warrior 24,” presented at the CAMRE, Naval Postgraduate School, Aug. 02, 2024.
- [188] SAMMTECH Mobile Manufacturing, “Snowbird Additive Mobile Manufacturing Technology,” Snowbird Technologies, Jacksonville, FL, Technical, 2024.
- [189] SciAps, “SciAps X-550 Specifications,” SciAps, Andover, MA, Technical, 2024.
- [190] *Metals Handbook: Properties and Selection: Stainless Steels, Tool Materials and Special-Purpose Metals*, 9th ed., vol. 3. Metals Park, Ohio: American Society for Metals, 1980.
- [191] SPEE3D, “316L Stainless Steel Select,” Melbourne, Australia, Material Datasheet, Apr. 2023. Available: <https://portal.spee3d.com/documentation/>

THIS PAGE INTENTIONALLY LEFT BLANK

INITIAL DISTRIBUTION LIST

1. Defense Technical Information Center
Fort Belvoir, Virginia
2. Dudley Knox Library
Naval Postgraduate School
Monterey, California



DUDLEY KNOX LIBRARY

NAVAL POSTGRADUATE SCHOOL

www.nps.edu

WHERE SCIENCE MEETS THE ART OF WARFARE